2D and 3D optical nanoscopy of single molecules at cryogenic temperatures

Reenu Baby

université de BORDEAUX

THÈSE PRÉSENTÉE

POUR OBTENIR LE GRADE DE

DOCTEUR DE

L'UNIVERSITÉ DE BORDEAUX

ÉCOLE DOCTORALE DES SCIENCES PHYSIQUES ET DE L'INGÉNIEUR

SPÉCIALITÉ : LASER, MATIÈRE ET NANOSCIENCES

Par Reenu BABY

2D AND 3D OPTICAL NANOSCOPY OF SINGLE MOLECULES AT CRYOGENIC TEMPERATURES

Soutenue le : Mardi 17 Juillet 2018

Commission d'examen :

M. Lionel CANIONI	Professeur (Univ. Bordeaux)	Président
M. François TREUSSART	Professeur (Univ. Paris-Saclay)	Rapporteur
M. Pierre GILLIOT	Directeur de Recherche (CNRS)	Rapporteur
Mme. Stéphanie BUIL	Maître de conférences Univ. Versailles St-Quentin-en-Yvelines	Examinateur
M. Jean-Baptiste TREBBIA	Chargé de Recherche (CNRS)	Co-encadrant
M. Brahim LOUNIS	Professeur (Univ. Bordeaux)	Directeur de thèse

Abstract:

In this thesis, we present the development of a cryogenic super-resolution optical nanoscopy that can resolve molecules at nanometric distances, called the Excited State Saturation (ESSat) Microscopy.

ESSat microscopy is a scanning confocal imaging technique based on the optical saturation of the zero phonon line of a single fluorescent molecule. It uses a patterned illumination beam that contains a 'zero-intensity' region at the focus of the microscope objective with a large intensity gradient around. We achieved a sub-10 nm resolution in the lateral direction and 22 nm resolution in the axial direction with extremely low excitation intensities of few tens of $kWcm^{-2}$. Compared to other super-resolution imaging techniques, like STED, RESOLFT, etc., our technique offers a unique opportunity to super-resolve single molecules with overlapping optical resonances and that are much closer than the diffraction limit. In addition, it is possible to determine the orientation of molecular dipoles from the fluorescent ESSat images. Since coherent dipole-dipole coupling interactions between single quantum emitters have a very high coupling efficiency at short distance much smaller than the diffraction limit, it is important to resolve them well below it. ESSat microscopy thus paves a way to disclose the rich spatial and frequential signatures of the coupled system and to manipulate their degree of entanglement.

Keywords: optical microscopy, single molecule, optical saturation, super-resolution

Résumé:

Dans cette thèse, nous présentons le développement d'une méthode de nanoscopie optique super-résolue en trois dimensions pour résoudre des émetteurs quantiques uniques à température cryogénique. Cette méthode, appelée microscopie à saturation d'état excité (ESSat), est une technique d'imagerie confocale à balayage basée sur la saturation optique de la raie sans phonon de l'émetteur. Elle utilise un faisceau d'illumination structurée comprenant une zone d'intensité nulle au foyer de l'objectif de microscope, avec un gradient d'intensité important autour. En imageant des molécules fluorescentes aromatiques individuelles à 2 K, nous avons atteint une résolution de 28 nm dans la direction latérale et 22 nm dans la direction axiale, avec de faibles intensités laser d'environ dix $kWcm^{-2}$, soit cinq ordres de grandeur inférieures à celles utilisées à température ambiante dans les méthodes de nanoscopie basées sur la déplétion par émission stimulée. Notre technique offre une opportunité unique de super-résoudre des molécules uniques séparées par des distances nanométriques et avec des résonances optiques qui se recouvrent. De plus, la méthode fournit une détermination directe de l'orientation des dipôles moléculaires à partir des images ESSat de fluorescence. La microscopie ESSat ouvre ainsi la voie à des études approfondies des interactions cohérentes dipôle-dipôle optiques entre émetteurs quantiques individuels, qui nécessitent des distances relatives nanométriques. En particulier, cette méthode permettra d'étudier les riches signatures spatiales et fréquentielles du système couplé et de manipuler leur degré d'intrication.

Mots-clés: microscopie optique, super-résolution, molécule unique, saturation optique, mise en forme de phase, basse température.

Acknowledgement

This thesis is carried out in the Nanophotonics group of Laboratoire Photonique, Numérique et Nanosciences (LP2N), a joint research unit between Institut d'Optique Graduate School (IOGS), University of Bordeaux and CNRS. It gives me great pleasure in expressing my gratitude to all those people who have supported me in completing this thesis.

Foremost, I owe my deepest gratitude to my supervisor Prof. Brahim Lounis for his continuous support for my Ph.D. study. I would like to thank him for his valuable guidance, motivation and immense knowledge. It has been a great experience to work with him.

My sincere gratitude to François Treussart and Pierre Gilliot for their interest in my work and for being referees of my thesis. I would also like to thank Lionel Canioni and Stéphanie Buil for serving as my committee members. Thank you all for your time and valuable feedback.

I would like to thank Jean-Baptiste Trebbia for his constant support, encouragement and insightful comments. He has been of great help in building the optical setup, performing experiments, analyzing data, doing numerical calculations and writing this thesis. It would never have been possible for me to complete this work without his incredible help.

My special thanks to Philippe Tamarat. I consider it as a privilege to work with him during this thesis. His patience and positive attitude towards work is highly inspiring. I would like to thank him for proofreading my manuscript and for all the valuable discussions.

I thank my fellow lab mates in the Nanophotonics group for sharing these years with me and for the stimulating discussions and for all the fun, we have had in the last few years.

I am indebted to the members of the mechanical and electronic workshops of LP2N for their continual service throughout my Ph.D., especially in engineering the new sample can for the cryostat. Many thanks to all the staffs at Institut d'Optique d'Aquitaine (IOA) for helping me with the administrative procedures.

I gratefully acknowledge the funding source that made my Ph.D. work possible. I was funded by LAPHIA (Laser & Photonique en Aquitaine), an initiative of excellence of the University of Bordeaux.

Finally, very big thanks to my family for all their love and unbelievable encouragement throughout my Ph.D. Thank You.

Reenu BABY
Talence, July 2018

Contents

Introduction

Optical microscopy, in particular, fluorescence microscopy, is a widely used type of microscopy that uses visible light to magnify samples hundreds of times their original size and to resolve their finest details. However, the wave nature of light limits the ultimate resolution achievable with an optical microscope. Light originating from a point object does not converge to a single point at the image plane but spreads out in space to a finite-sized volume, called the point spread function (PSF). The three-dimensional spatial extent of the PSF determines the smallest dimension that can be resolved in the image. The resolution is limited by diffraction as $0.61\lambda/NA$ in the image plane and $2n\lambda/NA^2$ on the optical axis, where λ is the wavelength of light used, $NA=n \sin\alpha$ is the numerical aperture of the objective, n the refractive index of the microscope medium and α the half-angle of the maximum cone of light that can enter or exit the objective [1]. For a visible light excitation of 500 nm and for an oil immersion objective (typically of NA $\sim$ 1.4), the diffraction limit in the lateral direction is $\sim$ 200 nm and the axial resolution is $\sim$ 700 nm.

The conventional far-field fluorescence microscopy techniques include wide-field microscopy [2] and confocal microscopy [3]. In wide-field microscopy, the whole sample is exposed simultaneously with an illumination light using an objective. The light is then collected from the planes above and below the plane of focus as well. This lack of depth determination will significantly blur the image and is the main limitation for wide-field 3D imaging. In contrast, for confocal microscopy, a focused laser beam is scanned through the sample. Also, a confocal pinhole is used in the detection path to reject the out-of-focus fluorescence, so that only the fluorescence stemming from the illuminated focal volume is detected with a photodetector. Thus, confocal microscopy is capable of collecting a series of optical sections, which can be further processed into a three-dimensional image. Moreover, since the detected signal is the square of the excitation PSF, the confocal microscopy offers a $\sqrt{2}$ times better resolution than a wide-field system with an infinitesimal pinhole diameter.

Various other techniques have been developed to improve the resolution and the image contrast, depending on the applications. With multiphoton microscopy [4], where fluorophores are excited with multiple photons of lower energy (usually in the wavelength range 700-1000 nm), deep imaging is possible within a tissue (up to 500 μm). Other techniques such as total internal reflection (TIRF) microscopy [5] and 4π-microscopy [6] are used to improve the axial resolution. TIRF microscopy is a wide field technique, where evanescent waves are used to excite fluorophores, leading to an axial resolution of 100 nm at the sample interface. On the other hand, 4π-microscopy

uses two counter propagating light beams to excite the fluorophore. At the focus, the two beams interfere constructively to create a narrow focal maximum with sidelobes. Thus, the lateral resolution is unaffected while a 3 to 7 fold improvement in axial resolution is achieved. Finally, structured illumination microscopy (SIM) [7], which is a modified wide field microscopy can achieve a twofold resolution enhancement in all directions, thus a factor of 8 in volume. In summary, all these methods could push the resolution to its limits but couldn't break the diffraction limit.

Over the last two decades, different super-resolution microscopy techniques were developed to surpass the diffraction limit. This is done by temporally or spatially modulating the excitation or activation light (patterned illumination method) and by utilizing the emission properties of the fluorescent probes (stochastic imaging method). The techniques such as stimulated emission depletion (STED) microscopy [8], reversible saturable optical fluorescence transition (RESOLFT) microscopy [9], saturated structured illumination microscopy (SSIM) [10] fall into patterned illumination methods, since they use spatially modified beams and optical saturation to effectively reduce the size of the PSF. The stochastic imaging methods include photoactivated localization microscopy (PALM) [11], stochastic optical reconstruction microscopy (STORM) [12] and universal points accumulation for imaging in nanoscale technology (uPAINT) [13] etc. These techniques use photoswitchable fluorescent probes and sequential collection of the emission from distinct fluorophores that are well separated. All these methods allow imaging single molecules, biological cell structures, protein complexes that are previously unobservable.

However, further advancement in an optical microscope has to be explored in order to study the nanometer scale interaction between single quantum emitters, which is the ultimate motivation of the work presented in this manuscript. In 2016, Zhang et al. [14] reported the imaging of coherent dipole-dipole coupling of two individual molecules separated by a few nanometers using a method based on scanning tunnelling microscopy. However, to study the optical properties, we need a method capable of manipulating and probing the optical transitions. The aim of this PhD work is to develop a low-temperature optical nanoscopy method that allows resolving single molecules close to each other or to other nanostructures, in the view of studying their nanometer-scale interactions, which are at the heart of various protocols of quantum computation technologies [15].

A signature of coupled quantum emitters is the appearance of a two-photon resonance at high excitation intensities [16]. This was first observed in 2002 with a cryogenic single molecule technique [17]. Under intense laser illumination, both molecules are excited with a two-photon transition when the laser frequency is at halfway from the molecular low-intensity resonances. This effect is evidenced by the onset of a new excitation peak in the fluorescence excitation spectrum of the coupled system when the laser intensity is raised (see Figure A).

The optical dipole-dipole interaction between molecules modifies their resonance frequencies and the damping of their dipole oscillations and has an inverse dependence on the cube of the distance between the individual molecules. In practice, it manifests itself when the distance between two molecules is less than ~10 nm. In order to determine the coupling constants, it is important to resolve individual molecules with a nanometer scale resolution in three-dimensions. In addition, the sign of the coupling energy is determined by the orientation of the two molecular dipoles. Thus, it is essential to know the exact position as well as the orientation of the individual molecules to determine their interaction energy.

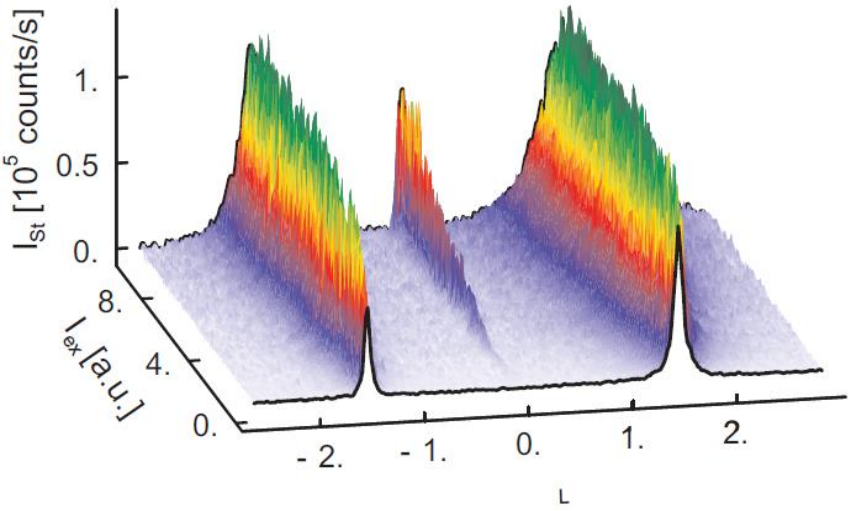

Figure A: Signature of an optical dipole-dipole coupling between two molecules: Evolution of the fluorescence excitation spectrum of the coupled-system with excitation intensity. Figure adapted from [17].

The standard localization methods based on confocal microscopy will fail to distinguish two quantum emitters with overlapping optical resonances and that separated by a distance of ~10 nm. Therefore, we need a 3D super-resolution microscopy that can resolve single quantum emitters in such a configuration, and furthermore unveil the rich spatial and frequential signatures of the coupled system. We aim at developing a technique that can determine the dipole orientation as well, from the spatial distribution of the fluorescence super-resolution images recorded. Moreover, when the excited molecular states are maximally coupled with a zero decay rate for the subradiant antisymmetric state, a normal TEM_{00} beam cannot be used to excite such states. We need an excitation beam with opposite electric fields at the two sides of the beam, for which a doughnut beam is an excellent option. Such metastable state with infinite lifetime opens up with the application of quantum memory for the realization of quantum computers [18].

During the course of this Doctorate work, we developed a low-temperature super-resolution imaging technique that can fulfil all the requirements for studying the coherent optical dipole-dipole coupling interaction, called the Excited State Saturation (ESSat) Microscopy. ESSat microscopy is a cryogenic technique to image single molecules embedded in the solid matrix with a sub-10nm optical resolution, which exploits the non-linearity of the fluorescence signal of single molecule excited on their ZPL.

Outline of the thesis

Chapter I: The chapter starts with an introduction to the basic concepts of the diffraction theory. Firstly, it discusses the initial developments in microscopy that can enhance the image contrast, including confocal microscopy, two-photon microscopy, etc. Then, the chapter moves into details of some of the important super-resolution imaging techniques developed so far at room temperature along with their advantages and limitations.

Chapter II: The chapter presents the main optical properties of single molecules at low temperature, in particular how the linewidth and saturation intensity of a single molecule is modified in comparison with their room temperature values. The use of low temperature allows having the highest possible quality factor for the zero-phonon-line by drastically reducing the dephasing due to phonons. This gives us a much lower power requirement for performing a super-resolution imaging technique based on optical saturation.

Chapter III: In this chapter, we describe the cryogenic ESSat microscopy in two dimensions. The principle of 2D-ESSat microscopy along with the obtained results and the challenges we faced are presented. With 2D-ESSat microscopy, we could achieve a 4 nm resolution in the lateral direction with an excitation intensity of 1.3 $kW.cm^{-2}$. By incorporating a modulation technique, we could achieve a resolution of 9 nm along the XY plane with a much higher image contrast.

Chapter IV: A nanoscopy in three-dimension is required for our studies. Therefore, we extend ESSat microscopy into three dimensions, which is developed in this chapter. The modifications we made to get the axial resolution and the results we achieved are discussed in detail. We also investigate the influence of different parameters, such as the high NA of the used objective, the polarization chosen for the incident beam, the aberrations in the optical system, on the laser intensity distribution in the focal region. We show that we can achieve a resolution of 28 nm in the lateral direction and 22 nm in the axial direction with modulated 3D-ESSat microscopy, with an excitation intensity of 9.8 $kW.cm^{-2}$ and a modulated-Gaussian beam intensity of 75 $W.cm^{-2}$. Moreover, we discuss the methods that can be used for the determination of the dipole orientation directly from the recorded 3D-ESSat images.

Finally, the thesis ends with a general conclusion of all the results we obtained along with the limitations and the prospects of this work.

Chapter 1

Fluorescence Microscopy and Super-Resolution Microscopy

For a very long time, microscopy has been a critical tool for imaging structures that are far too small to see with the naked eye. A lot of effort has been put forward to improve the performances, including contrast, magnification, depth of field and resolution. Different microscopic techniques were developed like electron microscopy, X-ray microscopy, optical microscopy, … Among these techniques, the most widely used is the optical microscopy. It has immense applications in different fields like chemistry, biology, and physics. In chemistry, optical microscope provides information about the chemical structure and morphology of materials like liquid crystals [19] and organic compounds [20]. It can also monitor materials that undergo catalysis, ligand binding, adsorption, optical activity or other reactions [21]. In biology, the observation of cells [22], such as neurons [23] or virus [24] [25], permits to understand their biological functions as well as their organizations at the micrometre scale. It is also used for detecting and tracking proteins at the single emitter level to reveal their dynamics and their roles in the normal or pathological functioning of a cell [26]. From the physical point of view, the photophysical and spectral properties of nano-objects such as molecules [27], quantum dots [28] [29], NV centres [30] [31] and carbon nanotubes [32] [33] are studied.

An optical microscope gives the magnified image of the sample by probing it with visible light (400-700 nm). However, if the numerical aperture (N.A.) of the objective is kept constant, higher magnification cannot bring more information into the image. Instead, it will blur the image. Tremendous efforts have been made to distinguish between smaller and closer nano-objects, which give the resolution of the microscope. Thus, it is the resolution that gives the richness of details and sharpness in the image. However, NA is limited, which restricts the resolution. Therefore, other approaches in microscopy called the scanning probe microscopes such as a near-field optical microscope (NSOM) were pursued to achieve better resolution.

NSOM surpasses the diffraction limit constraints by exploiting the properties of evanescent waves or non-propagation fields. Numerous examples using an optical fibre that funnels light down to the nanometric dimension could be cited [34] [35] [36]. However, such techniques are limited by

their relatively slow imaging speed. Moreover, they have extremely shallow working distance, making them a surface probe technique. Hence, we need far-field techniques to extract three-dimensional information from thick samples. Therefore, any attempt to increase the resolving power of a far-field microscope is valuable and creates an immense potential [37]. In the last decade, abundant studies have been undertaken to find ways to circumvent the diffraction problem and overcome these limits. These endeavours resulted in the rise of the field of 'super-resolution optical microscopy' and emergence of many high-resolution techniques.

This chapter starts with an introduction to the diffraction scalar theory to introduce the notations and the relevant parameters addressed in chapters 3 and 4 of the thesis. In section 1.2, we will present different methods to enhance the imaging contrast by reducing the detection volumes, such as confocal microscopy, total internal reflection fluorescence microscopy (TIRF), 4π-microscopy, etc... In sections 1.3 and 1.4, I will present various super-resolution imaging techniques that strive to push imaging from the microscopic regime to the nanoscopic regime in two dimensions and three dimensions, respectively. Along with, I will enumerate the advantages and disadvantages of each of the techniques.

1.1 Diffraction Limited Optical Resolution

Diffraction of light imposes the ultimate limit in optical resolution. When light passes through the circular aperture of an objective, it will diffract forming the diffraction pattern with a central disk of light having a finite diameter, encircled by a fading series of concentric rings known as the Airy pattern [1]. The core of the Airy pattern, inside the first minimum, is often called the 'Airy Disk,' named after Sir George Airy. The lateral resolution of an optical microscope can be defined as the radius of the Airy disk.

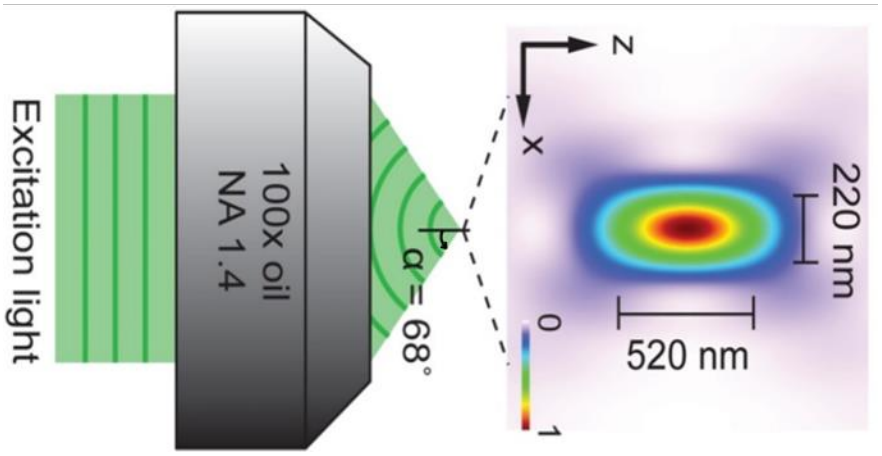

Figure 1.1: The focusing of light with an optical microscope forming an ellipsoidal diffraction-limited distribution. λ=550 nm, NA = 1.4. The FWHM in the lateral and axial directions are 220 nm and 520 nm, respectively. Figure adapted from [38].

The light intensity also varies along the optical axis (z-axis) in an analogous way, forming a 3D-Airy disk. This three-dimensional representation of the diffraction pattern of light is called the Point Spread Function (PSF). In a confocal microscope, the shape of the point spread function resembles that of an ellipsoid.

The expression of the PSF can be derived from the propagation of an optical field through a lens. Refer to Figure 1.2 and consider a plane wave propagating through a converging lens. A lens is positioned at z = 0, and the focal plane is at z = f. Thus, the electric field distribution $\mathrm{E_2(x_2, y_2, z)}$ in the image plane can be written according to Huygens-Fresnel principle as,

$$\mathrm{E_2(x_2, y_2, z)} = -\frac{\mathrm{i}}{\lambda}\iint \mathrm{E_1(x_1, y_1, 0)}\frac{\exp(-\mathrm{ikr})}{\mathrm{r}}\cos(\mathbf{n}, \mathbf{r})\,\mathrm{dx_1 dy_1}, \tag{1.1}$$

where $\mathrm{E_1(x_1, y_1, 0)}$ is the light field on the diffraction plane, $\cos(\mathbf{n}, \mathbf{r})$ is the cosine of the angle between the unit normal vector ($\mathbf{n}$) of the diffraction plane and the observation direction ($\mathbf{r}$). Under paraxial approximation, $\mathrm{z} \approx \mathrm{f}$ and $\cos(\mathbf{n}, \mathbf{r}) \approx 1$.

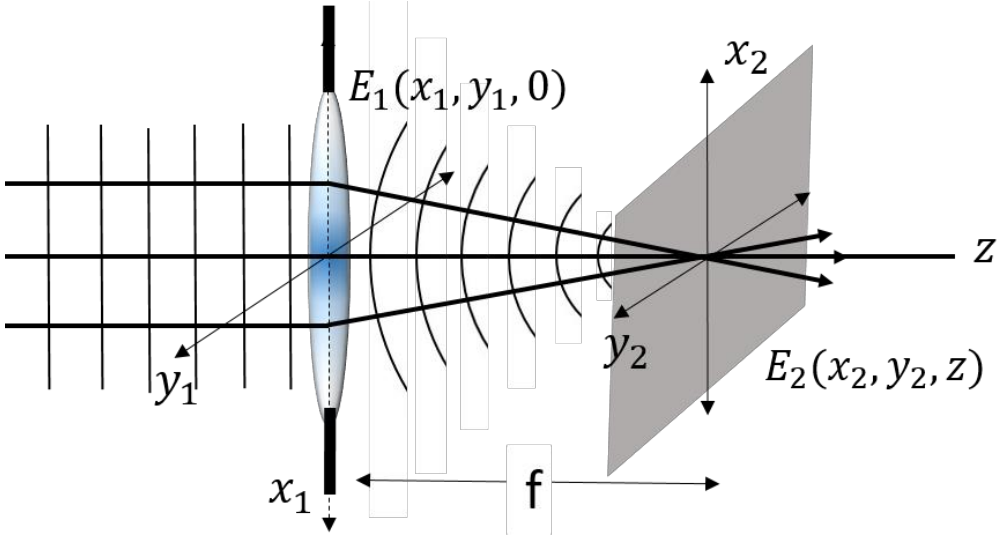

Figure 1.2: Focusing of a plane wave propagating through a converging lens. $\mathrm{E_1(x_1, y_1, 0)}$ is the aperture plane and $\mathrm{E_2(x_2, y_2, z)}$ is the focal plane.

Solving Equation 1.1, the PSF can express in terms of wavelength, λ and numerical aperture, NA as,

$$\mathrm{PSF(r)} = \mathrm{h(r)} = \left[\frac{2\mathrm{J_1(k\,NA\,r)}}{\mathrm{k\,NA\,r}}\right]^2. \tag{1.2}$$

The size of the PSF along the axial and the lateral direction gives the corresponding resolution limit.

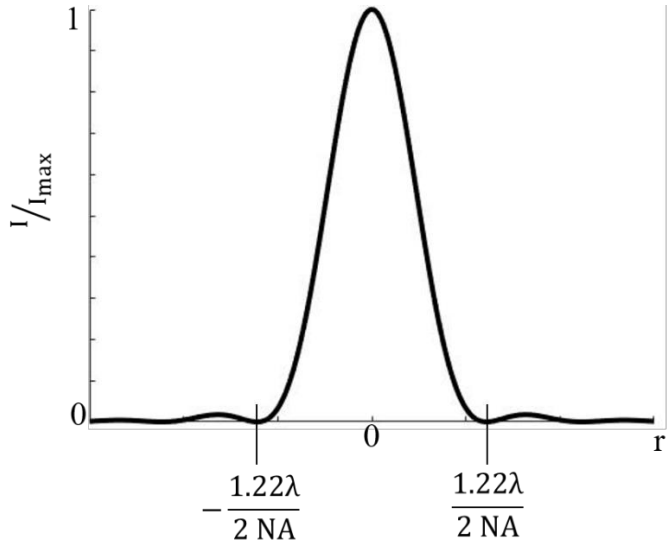

Figure 1.3: Intensity graph of the diffraction pattern obtained for a circular aperture. First minima occur at $r = \pm 1.22\lambda/2$ NA. I_{max} is the intensity at centre (r=0).

The distance between the centre bright spot and the first diffraction minimum (lateral spatial resolution) is given by,

$$\Delta r = \frac{1.22\lambda}{2NA}. \tag{1.3}$$

This distance is equal to the radius of the central disk of the Airy pattern. Thus, two point sources are considered resolved, if the distance between their Airy disks is greater than this value. Otherwise, the Airy disks merge and are considered not resolved.

The resolution in the axial dimension (z-axis) is even worse than that of lateral dimension and can be written as:

$$\Delta z = \frac{2\lambda}{NA^2}. \tag{1.4}$$

Therefore, while imaging highly convoluted features, the diffraction-limited image displays poor axial sectioning capability and lowered contrast in the imaging plane.

There are a few different definitions for the resolution limit since it is based on how a viewer perceives an image. Traditionally, the resolution of an imaging system is described by the Rayleigh criterion [39] [40]. The Rayleigh criterion states that the minimum distance between two objects to resolve them laterally is reached when the central disk of the Airy pattern of one coincides with the first minimum of the other. In other terms, the Rayleigh criterion is satisfied when the distance between the images of two closely spaced point sources is almost equal to the width of the point-spread function.

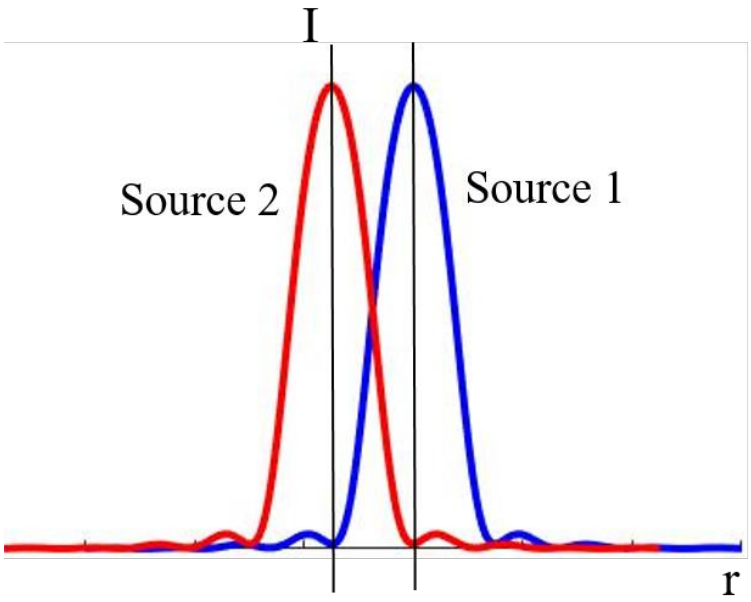

Figure 1.4: The graphical demonstration of the Rayleigh criterion. Blue and the red lines represent the intensity of the two neighbouring point sources. For the two point sources to resolve, the peak of the central maximum of one should be at least at the first minimum of the other.

Both the lateral and axial resolution limits depend upon two factors: numerical aperture of the objective and the optical wavelength. Consequently, we can reduce the diffraction-limited spot by either decreasing the imaging wavelength or increasing numerical aperture (i.e., use an imaging medium with a larger refractive index or larger collection angles). Assuming ideal conditions, with NA of 1.5, we end up with a resolution of $\Delta x \approx 160$ nm and $\Delta z \approx 550$ nm, for $\lambda = 400$ nm.

The NA can be increased by using immersion objectives, where the air gap between the sample and objective lens is replaced with a higher refractive index material. Immersion objectives are of two types. One is the liquid immersion objectives with a numerical aperture as high as 1.65 depending on the refractive index of the medium and the substrate [41] [42]. However, with such objectives, the resolution is still limited to about 140 nm in the lateral direction and around 500 nm along the axial direction [42]. Second is the solid immersion objectives, where the liquid is replaced by a solid immersion lens (SIL) made out of high index glasses ($n \sim 2$) or other materials with an index as large as 3.3 [43] [44]. Thus, solid immersion microscopy can achieve significantly higher spatial resolution than a liquid immersion microscopy. However, the field of view of SIL microscopy is often limited to few tens of μm because of out of axis aberrations, which restricts the applications [45].

Therefore, it is impossible to resolve sample in the nanoscale regime with the conventional optical microscopy. With the strong incentive to image smaller features, the barrier of the diffraction limit has pushed quite far, and these exploratory ideas have led to the discovery of new science and technology at the nanoscale. The upcoming sections discussed the variety of such techniques.

1.2 Fluorescence Microscopy

Fluorescence microscopy is the most popular contrasting optical microscopic technique [46]. It requires fluorophores that absorb light in a specific wavelength range, and re-emit with a lower energy. Thus, fluorescence emission is shifted to a longer wavelength, called the Stokes shift. This allows efficient separation and detection of fluorescent signals from the illumination light. Therefore, fluorescence microscopy has high contrast, sensitivity and a dark background.

The main components of a fluorescence microscope are an illumination source, optical filters, an objective and a detector [47]. To excite fluorophores in the sample, an intense light source with a wavelength close to its absorption maximum is required. A broad-spectrum source along with an excitation filter can be used to permit the range of excitation wavelength to incident on the sample. Another commonly used illumination source is lasers since they have very narrow spectra. An emission filter is used to separate fluorescence signal from the scattered excitation light and other background signals. For detection, high quantum efficiency photodetectors like avalanche photodiodes (APD), photomultiplier tube (PMT) or camera are used. All these developments make fluorescence microscopy a powerful imaging tool for single molecule imaging [48] [49].

Several far-field microscopy configurations have demonstrated to fulfil the basic requirements for single-molecule detection. In this section, we will see different fluorescence microscopy methods that can have an increase in the resolution by engineering the illumination. Successful microscopy techniques are based on confocal microscopy, multiphoton microscopy and wide-field methods such as total internal reflection microscopy.

1.2.1 Confocal Microscopy

One of the possibilities for improving the resolution is by laser scanning confocal microscopy. It is one of the most significant advances in optical microscopy, invented by Minsky in 1955 [3]. In contrast to conventional wide-field illumination, where the full field of view is illuminated and imaged onto a camera, scanning confocal microscopy uses spatial filtering to ensure that only a diffraction-limited focal volume is illuminated and only light from this focal volume can reach the detector. This is done using a pinhole in the detection path [50].

The fluorophores in the sample are illuminated with a focused laser beam. A pinhole is located at the confocal image plane of the focus to collect only the light from the focal point of the sample. Since the objective and the pinhole have the same point of focus, this microscopy is named “confocal” [51]. The main advantage of confocal microscopy is the elimination of out of focus background. The sample is scanned by either moving the sample or more commonly by a set of rotating mirrors that reflect the laser beam in the x- and y-direction of the sample plane. Thus, in a scanning procedure, a single diffraction limited spot is scanned across a sample. Through effectively suppressing the out-of-focus light, the method permits higher contrast and offers the ability to create optical sectioning to study very thin (less than 1 μm) sections of thick samples. By recording a number of such optical sections, and focusing the microscope slightly on individual

sections, it is possible to record a stack of images, thereby generate 3D images. Consequently, it allows imaging deep within thick samples such as cells and tissues.

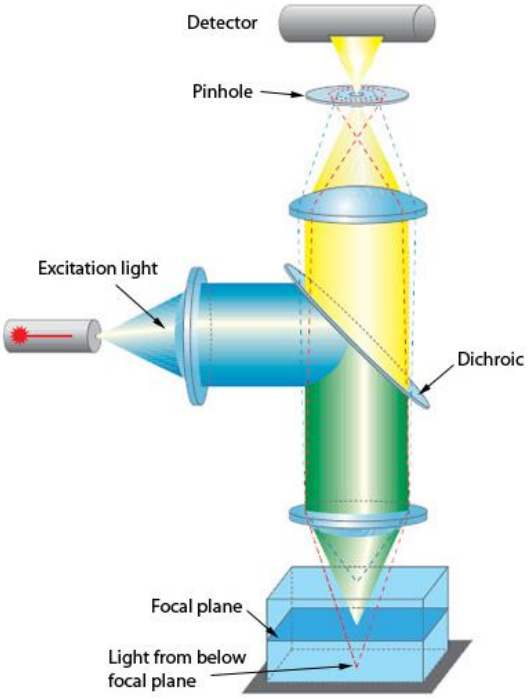

Figure 1.5: Diagram of a confocal microscope. An objective focuses the laser beam on the sample. A pinhole is set in the detection path and is conjugated with the focused laser spot to reject the out-of-focus fluorescence. Figure extracted from [52].

While an increase in image quality succeeds, there is no true enhancement of resolution possible with a confocal microscope. The confocal PSF can be written as,

$$\mathrm{PSF}_{\mathrm{conf}}(\mathrm{r}) = \left[\frac{2\mathrm{J}_1(\mathrm{k\,NA\,r})}{\mathrm{k\,NA\,r}}\right]^4. \tag{1.5}$$

Approximating the excitation PSF by a Gaussian distribution, the confocal PSF gives another Gaussian PSF with FWHM smaller by a factor of $\sqrt{2}$. That is, the attainable lateral size of the PSF can be improved by this factor. The use of high NA and pinhole improves the axial resolution as well. But, it is always two to three times worse than the lateral resolution because of the blurring effect of the PSF. The narrower and the smaller side-lobes of confocal PSF are desirable features; a narrow PSF means a sharper image, and smaller side-lobes mean less imaging artefacts. Thus, confocal microscopy reduces the size of the three-dimensional focal spot; but still cannot break the diffraction limit [53].

1.2.2 Two-photon excitation Microscopy

In two-photon excitation microscopy, two photons are simultaneously absorbed by the fluorophore. This requires less energetic photons but higher laser illumination. The longer wavelength radiation makes it less damaging and allows penetrating more deeply into the sample, typically 5-20 times deeper than in confocal microscopy [4]. Images are generated with a focused laser scanned over the sample as in the case of confocal microscopy. In two-photon excitation microscopy, fluorescence absorption rate varies quadratically with the excitation intensity. This allows exciting the fluorophore in a tiny diffraction-limited focal volume. The absence of out-of-focus light makes the image distinct and easy to interpret. Figure 1.6 shows the case of two-photon microscopy [54], where two excitation photons from a pulsed laser combine to excite a fluorescent molecule.

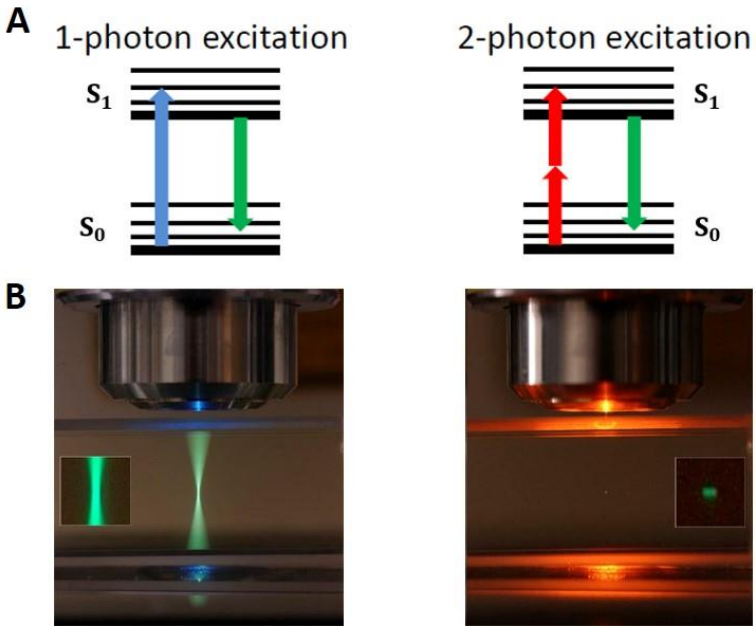

Figure 1.6: Single-photon and two-photon excitations. In the single-photon excitation case, one photon of the energy hν can excite fluorophores. The excitation takes place along the propagation of the light, both before and after the focal plane. In the two-photon excitation case, two photons of energy $h\nu/2$ act together to excite fluorophores. The excitation occurs only in the focal volume. The one-photon excitation is done by exciting the sample by a scanning blue (488nm) laser and the two-photon excitation by scanning IR pulse laser (Zeiss NLO system). (The image was taken using a Nikon D1X camera by Steve Ruzin and Holly Aaron, UC Berkeley)

The resolution of two-photon microscopy is lower than in confocal microscopy, because of the longer wavelength used for excitation. The point spread function in two-photon excitation microscopy is given by:

$$\mathrm{PSF_{TP}}(\mathrm{r}) = \left[\frac{2\mathrm{J_1}(\mathrm{k\ NA\ r})}{\mathrm{k\ NA\ r}}\right]^4. \tag{1.6}$$

This is the same mathematical expression as that of a confocal microscopy. However, λ is twice as long for two-photon microscopy, which gives PSF approximately the same as wide-field microscopy. Even though two-photon microscopy produces images with lower resolution than confocal microscopy, because of better penetration and reduced photobleaching it has found immense use in biomedical research [55].

1.2.3 Structured Illumination Microscopy (SIM)

Both the techniques discussed before are scanning microscopes. A focused laser beam is scanned over the sample using a galvanometer mirror and the light from each pixel of the sample is then detected by a single photon-detector. This method is time-consuming. The typical acquisition rate of a home-built laser scanning microscopy for acquiring 40 × 40 pixel images (pixel size of 50 nm) is less than few tens of frames per second [56] [57]. Therefore, wide-field approaches are favoured for faster imaging requirements. The spatial resolution of wide-field fluorescence microscopy can improve by up to a factor of two using structured illumination microscopy (SIM) demonstrated by Gustafsson [7]. This is done by collecting information from frequency space outside the diffraction-limited region. The working principle of SIM can understand clearly by looking at in Fourier space. In the Fourier space, low-resolution information resides close to the origin (inside the circle in Figure 1.8.B), while higher resolution information with high spatial frequencies resides further away. The Abbe's diffraction limit for the maximum detectable spatial frequency is given by,

$$f_0 = 2\frac{NA}{\lambda} \tag{1.7}$$

All higher frequencies will be lost. SIM produces super-resolution by bringing the frequency spectrum of the object that is beyond f_0 into the passband of the detection system.

SIM uses Moiré effect to improve the resolution of fluorescence microscopy. The microscopic configuration of SIM is shown in Figure 1.7. A movable grating is used to generate the first order diffracted laser beams, which interfere at the focal plane of the objective creating sinusoidal illumination pattern. This high frequency of the excitation pattern overlaps with the high-frequency spatial distribution of the sample, producing Moiré fringes. Such fringes can shift high-frequency features of the sample to lower frequencies, making them observable under the microscope. [7] [58] [59]. Hence, we can get information that is not accessible by a conventional microscope. With a single image, it is not possible to separate the contributions from the observed image. Thus, by taking multiple images of a sample with different orientation of the structured illumination by moving the diffraction grating, one can reconstruct the full image. A set of 9 images are required to obtain a 2D-SIM image.

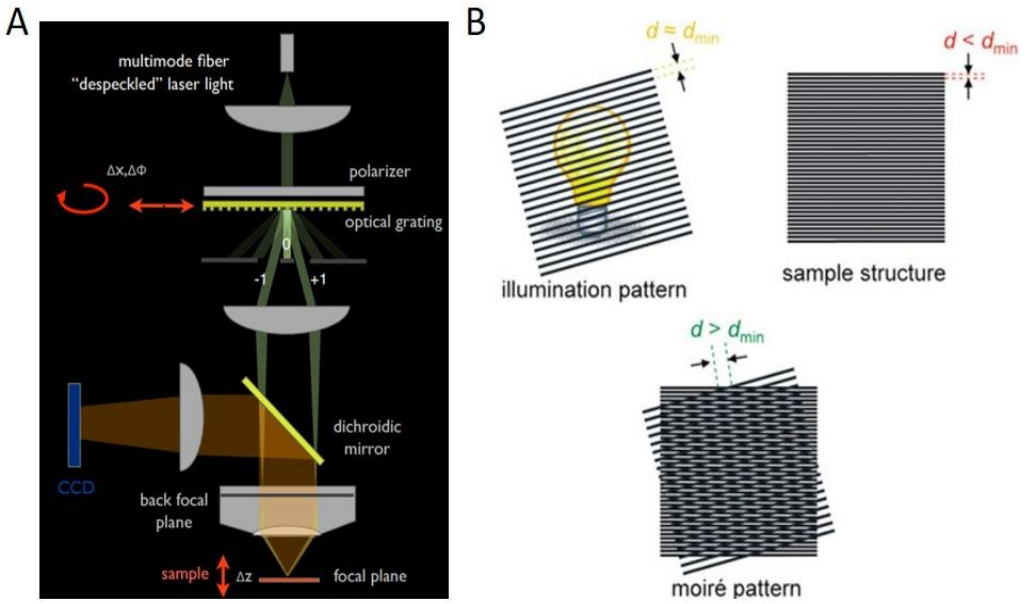

Figure 1.7: (A) Microscope configuration of SIM. Laser light is scrambled using a rotating holographic diffuser in order to remove spatial coherence and coupled into a multimode optical fibre. The collimated light from the fibre then directed to a fused silica linear transmission phase grating, which diffracted the beam into a large number of orders. A beam block in the intermediate pupil plane discarded all diffraction orders except +1 and -1. The beams are then focused near opposing edges of the back focal plane of the objective. The objective lens will then recollimate the beams and made them intersect each other on the focal plane of the objective lens, where they interfered to form a 2D illumination pattern. (B) Generation of Moiré fringes. The sample is illuminated by this excitation pattern and the spatial frequency mixing results in Moiré pattern, which is collected by the same objective and deflected by a dichroic mirror to a cooled charge-coupled device camera. An emission filter placed in front of the camera is used to reject the scattered excitation light. The orientation and phase of the illumination pattern were controlled by rotating and laterally translating the grating. For this purpose, the grating was mounted on a piezoelectric translator, which in turn was mounted on a motorized rotation stage. Figure extracted from [60] and [61].

To maximize the resolution, it is necessary for the illumination to contain as high spatial frequencies f_1 as possible. But, the illumination light field is also limited by diffraction. Thus f_1 cannot be larger than the maximum detectable spatial frequency, f_0. Thus, the resolution limit for SIM can be at most $\approx 2f_0$, that is, we can get all information within a circle twice as large as the physically observed region. Besides the potential of much faster image acquisition, these microscopes are much simpler and cheaper than confocal ones. The drawback to this technique is the need of a computer reconstruction algorithm for image reconstruction, which can be time-consuming.

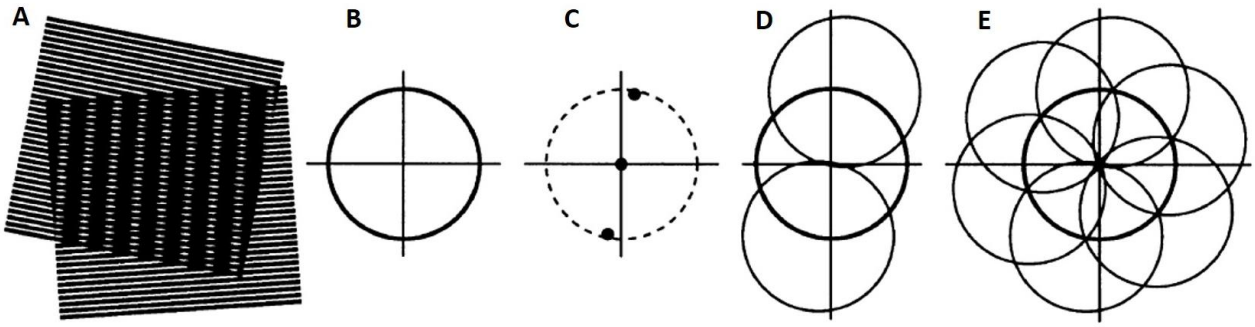

Figure 1.8: Super-resolution by SIM. (A) Moiré pattern produced by the superposition of two line patterns. (B) The resolution limit of the conventional optical microscope in reciprocal space. The set of low-resolution information that it can detect defines the central circular region. The region outside the circle contains the high spatial frequency components, which cannot be resolved. (C) A sinusoidally stripped illumination pattern has only two Fourier components. The positions of the two side components are limited by the same circle that defines the observable region (dashed). (D)The visible region thus contains, moved information that originates in two offset regions, along with the normal information. (E) From a sequence of such images with different orientations and phases of the illumination pattern, it is possible to recover information from an area twice the size of the usually observable region, resulting in twice the normal resolution. Figure extracted from [7].

1.2.4 Total Internal Reflection Fluorescence Microscopy

Total internal reflection fluorescence (TIRF) microscopy [5], developed by Daniel Axelrod is a powerful method to restrict the excitation and detection of fluorophores to a thin region of the sample. With this approach, we can eliminate the fluorescence background from outside the focal plane and can effectively improve the signal-to-background ratio.

TIRF microscopy exploits the unique properties of an evanescent wave, which decays exponentially with the penetration depth. It usually ranges from 30 to 300 nm and depends on the incident angle, wavelength, and the refractive index of the sample and coverslip. Typically, the contact area between a specimen and a glass coverslip is utilized as the interface for TIRF microscopy. Only the fluorophores within the penetration depth are excited, and the fluorophores in the rest of the sample are hardly excited. This permits the creation of images with the exceptional signal-to-background ratio.

There are two main configurations of TIRF microscopy, called prism-type TIRF microscopy and objective-type TIRF microscopy. In the case of prism-type TIRF microscopy, the prism attached to the coverslip's surface guides the focused light beam towards the coverslip-sample interface. Objective type TIRF microscopy uses an oil-immersion objective with an NA $\geq$ 1.4 to excite fluorescence and to collect the emitted light. The higher the NA of the objective, the lower the

possible penetration depth of the evanescent field, as the incident angle become flattered. The prism strongly limits the access to the specimen, and it is difficult to change media. In objective type method, the angle of incidence of the laser light can be changed by placing the laser spot in the different areas of the back focal plane of the objective. This allows changing the penetration depth accordingly.

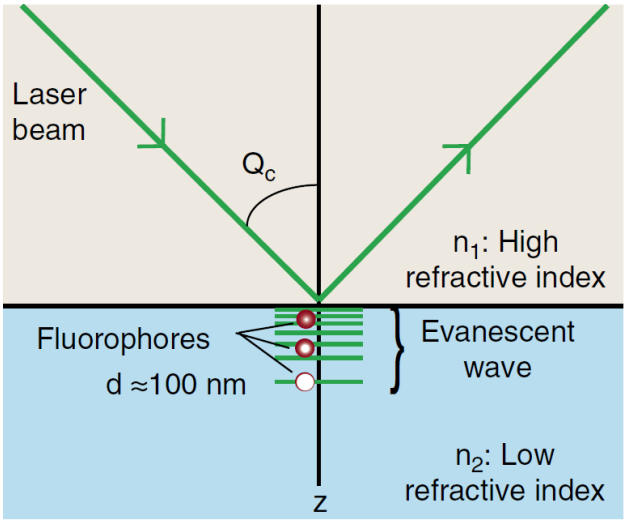

Figure 1.9: Illustration of the basic concept of TIRF microscopy. The evanescent electromagnetic field will selectively excite the fluorophores nearest the glass surfaces (typically $\leq$ 100 nm) and the microscope optics can collect secondary fluorescence from these emitters.

Even though TIRF microscopy is limited to image at the interface, it is well suited for an extensive number of applications, like imaging cell surfaces and the observation of membrane-associated processes like cell adhesion [62], hormone binding, molecule transport and several exocytotic and endocytotic processes [63]. Moreover, the excellent signal to noise ratio in TIRF microscopy allows for the first direct observation of the catalytic activity of a single enzyme molecule [64]. Live-cell imaging represents one of the most promising applications of the TIRF microscopy [65]. Additionally, TIRF Microscopy can be used for determining the orientation of plasmonic nanostructures [66].

1.2.5 4Pi Microscopy

4Pi Microscopy belongs to a class of super-resolution microscopy with a strategy to reconfigure the conventional objective geometry and light collection. We have seen in Section 1.1 that the numerical aperture plays a crucial role in determining the resolution. For higher resolution, the sample should be illuminated as well as the fluorescent light from the sample should be collected under the maximum possible solid angle. Usually, these two angles are identical, because the objective is used for both the excitation and the collection. The angle is a solid angle of 2π since we illuminate the sample at one side and collect the fluorescence from one side of the sample. If we could utilize total solid angle of 4π, i.e. illuminate spherically and collect spherically, we would get perfectly symmetric imaging properties in all three dimensions in the specimen volume.

However, this needs a 90^0 semi-aperture angle, which is not realistic. By using two opposing lenses, this angle approaches the limit of 4π (hence the name 4π microscopy) [67] [68].

4π microscope aims to increase the axial resolution, which is conventionally much lower than the lateral part. In 4Pi microscopy, two counter-propagating beams illuminate a sample using two objectives opposite to each other, so that they have a common focus, where they interfere constructively [69]. This gives rise to a 3-7 fold narrower main peak along the optical axis, and therefore axial resolution can be increased to 80-160 nm [70]. The lateral resolution remains unaffected. Hence, similar to confocal microscopy, a single small volume of the sample can image. However, the sample should be thin and optically homogeneous, for the two counterpropagating waves to maintain alignment during scanning.

Besides the difficulties in the realization, the drawback of the 4Pi microscopy includes the side-lobes of the interference pattern next to the focal spot, which introduces imaging artefacts. A deconvolution procedure has to be done to remove those side-lobes.

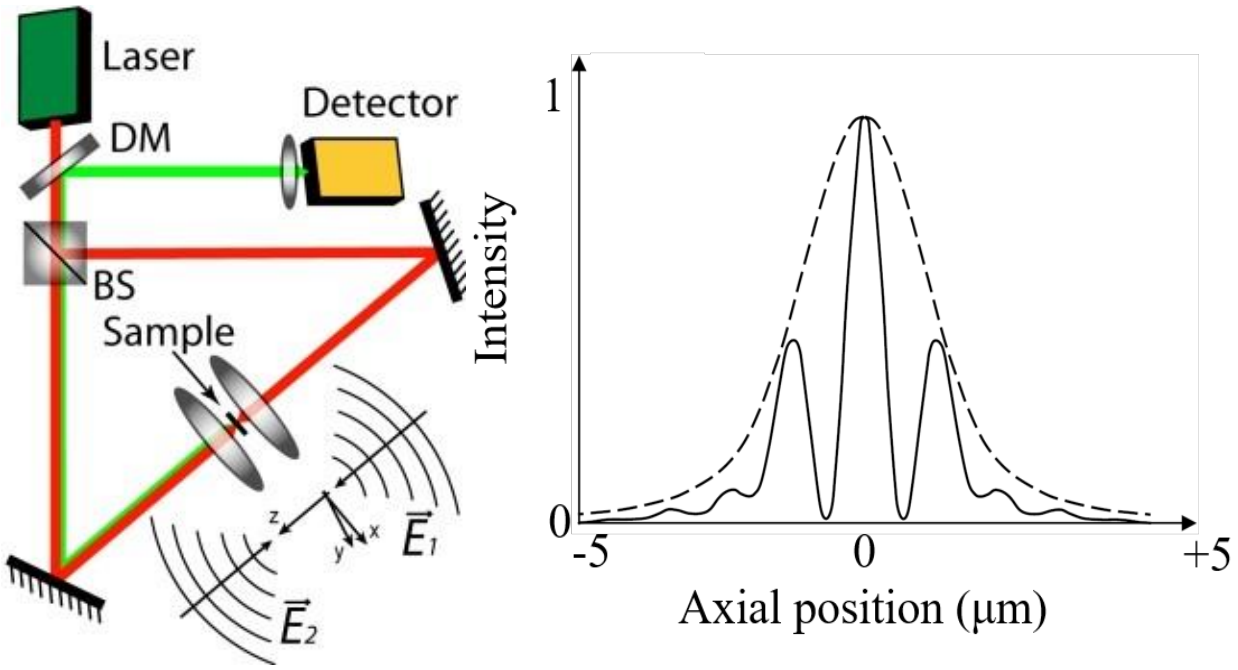

Figure 1.10: The optical principle and performance of 4π confocal fluorescence microscopy. (A) Schematic diagram of the optical principle. Light from a laser is split into two beams, which illuminate the specimen from opposing sides. The focus points of the microscope objectives coincide, producing a point spread function that has a standing wave pattern in the optical axis direction (z). In the lateral dimension, the PSF is identical to that obtained with one-sided illumination. Scanning is done by moving the specimen, whereas the laser beams are fixed. (B) Depth response to a planar, infinitely thin, fluorescent layer. The corresponding wave for ordinary confocal microscopy is shown with dashed line. The standing wave pattern caused by the two counter-propagating laser beam is clearly seen. Figure adapted from [71].

1.3 Super-Resolution Microscopy

The resolution limit in microscopy formulated by Abbe lets generations of scientists believes that studying single molecules and resolving sub-wavelength structures were not achievable. Laser scanning confocal microscopy, multiphoton microscopy, TIRF, SIM and others mentioned in the previous section have been widely used to enhance spatial resolution along both the lateral and axial axes. But, all these techniques remain limited in achieving substantial improvements. Rather than breaking the diffraction limit, the primary advantage of these techniques is the reduction of background signal originating from out-of-focus light.

The resolution limit imposed by the diffraction of light can be surpassed by the involvement of fluorophore photophysics or photochemistry. The awarding of the 2014 Nobel Prize in Chemistry to Eric Betzig, Stefan Hell and William E. Moerner for their pioneering work in "super-resolution fluorescence microscopy" marks a clear recognition that the old beliefs have to be reconsidered. Although there are different super-resolution methods, all of them ultimately separate densely packed emitters or features in the same way. One or few of the distinct fluorophores are allowed to emit, while the neighbours are reserved silent. They have circumvented these assumptions in different ways. One way is based on localization of single fluorophores, discussed in section 1.3.1. These techniques rely on photoswitching or photoactivation of fluorophores to enable sequential collection of emission from active single fluorophores. Another method is by effectively reducing the size of the PSF using specifically engineered illumination patterns and by exploiting saturation-based nonlinear optical effects, discussed in section 1.3.2. These main methodologies make it possible to attain resolution well beyond the diffraction limit of light. In this section, I present an overview of various most popular super-resolution fluorescence imaging methods and will consider their fundamental and practical challenges that lie ahead.

1.3.1 Super-resolution by single-molecule localization (Stochastic imaging of single molecules)

Single molecule localization techniques for sub-diffraction-limited imaging take advantages of growing capabilities in single-molecule imaging and precise position localization of molecules. Given that enough photons are detected, localization precision can be turned into resolution by temporally separating fluorescence signals from closely spaced molecules, so that they can be localized separately [72]. Initial implementations of this concept included photoactivated localization microscopy (PALM) [73] [11] [12] [74], and stochastic optical reconstruction microscopy (STORM) [75] [76] [77].These techniques rely on stochastic switching of special fluorescent molecules between their fluorescent and non-fluorescent states or other mechanisms to activate individual molecules within the emission PSF at different times. Images with enhanced resolution are then reconstructed from the measured positions of individual fluorophores, by finding, the centres of their diffraction limited PSFs. Typically; this is achieved by approximating the diffraction-limited Airy disk as a two-dimensional Gaussian function. The accuracy of the localizing a single emitter improves proportionally to the square root of the number of photons collected and is given by the standard error of the mean, s.e.m as:

$$s.e.m. = \frac{\sigma}{\sqrt{N}} \tag{1.8}$$

where σ is the standard deviation of the Gaussian fit, N is the number of photons collected. With fluorescence imaging with one-nanometer accuracy (FIONA), the localization accuracy on Myosin V molecular motor is made as accurate as 1.5 nm by collecting approximately 5000 -10000 photons per spot per image with an acquisition time of 0.5 s [78]. Because a large number of imaging cycles are required to probe all the fluorophores within the field, imaging speed and time resolution is usually limited to this approach. In addition, these methods rely on fluorophores being photoactivable, which is not the case for most natural fluorophores. Nevertheless, stochastic imaging systems can be easily adopted because of their relatively simple optical instrumentation and sample preparation. PALM/STORM can also accomplish 3D-imaging by adding astigmatism into the imaging system [75], by defocusing light [79], by using a double-helical point spread function [80], or by using interferometry [81]. A resolution localization of 10-20 nm in all three dimensions was achieved [80] (Discussed in Section 1.4.1).

PALM and STORM:

Photoactivated localization microscopy (PALM) and Stochastic Optical Reconstruction Microscopy (STORM) have the same fundamental working principle. Both are wide-field super-resolution imaging techniques. While PALM uses photoconvertible or photoactivatable fluorescence proteins or organic fluorophores [11] [12], which can undergo only one or several cycles of activation before being permanently photobleached, STORM [82] [76] [83] utilizes reversibly photoswitchable organic fluorophores or probes.

The fluorescent emission of such molecules is controlled such that, at any point in time, only a single one, or a sparse subset, of the fluorophores in a given region of the sample is in "on" state. This is achieved by using a weak activation light intensity. To enable parallel recording of many individual emitters, allowing each to be localized with high precision, the activated fluorescent molecules must be separated by a distance that surpasses the diffraction limit. Localization is done by fitting the PSF intensity to a mathematical model such as a Gaussian function [78]. After localizing molecules in the first subset, they are deactivated to the dark state, and a new similar subset is activated to the fluorescent state. Typical excitation power required is about 50 mW for a $60\ \mu m \times 60\ \mu m$ scan area. These newly activated fluorescent molecules are localized similarly. By repeating this cycle of activation, localization, and deactivation, the positions of an arbitrary number of closely spaced fluorophores is determined, and a high-resolution image is constructed from the measured positions of the fluorophores. It is important that the activated state of the photoswitchable molecule must lead to the successive emission of sufficient photons to enable precise localization before deactivating. Thus, the resolution of the final image is not limited by diffraction but by the accuracy of each localization and the localization density. The imaging procedure of PALM and STORM are shown in the Figure 1.11 and Figure 1.12, respectively.

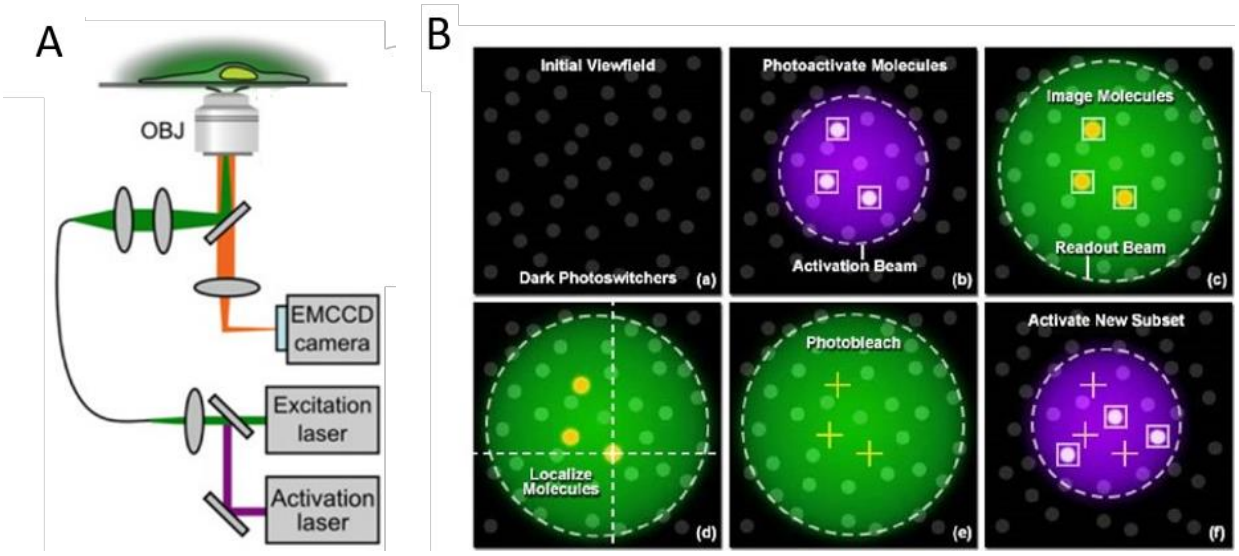

Figure 1.11: PALM instrumentation and working principle. (A) Experimental set-up for 2D single-color PALM. The sample is activated and excited using the same objective lens (OBJ)and the emitted fluorescence is directed onto an EMCCD camera. (B)Working principle of PALM. Figure extracted from [84].

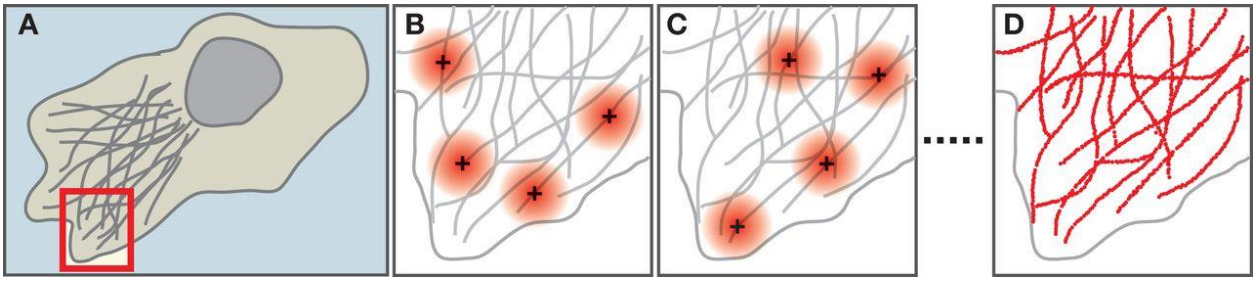

Figure 1.12: The STORM imaging procedure: (A) Schematic of a cell in which the structures of interest are labelled with photoswitchable fluorophores. Initially, all fluorophores are in the nonfluorescent state. The inset indicates the area shown in figure B-D. (B) An activation cycle: a subset of fluorophores is activated to the fluorescent state such that their images do not overlap. The image of each fluorophore appears as a diffraction limited spot, and the position of each activated fluorophore is determined by fitting Gaussian and finding the centroid of the spot (Black Cross). (C) A second activation cycle: A different subset of fluorophores is activated, and their positions are determined as before. (D) After a sufficient number of fluorophores has been localized, a high-resolution image is constructed by plotting the measured positions of the fluorophores. The resolution of this image is not limited by the diffraction but by the accuracy of each fluorophore localization and by the number of fluorophore positions obtained. Figure adapted from [85].

Several properties of photoswitchable fluorophores determine their suitability for PALM and STORM method. The brightness of the fluorophore is crucial for single-molecule detection and precise localization. Also, non-ideal switching characteristics such as residual fluorescence emission from the dark state and spontaneous reactivation from the dark state to the fluorescent

state can present challenges when imaging densely labelled samples. Since more the number of photons, higher the precision, it is important to select a fluorescent molecule with high photon emission rates. A widely used fluorescent protein that displays photoswitching characteristics suitable for PALM is mEosFP [86]. Fluorophores commonly used for STORM include photoswitchable fluorescent proteins and organic dyes, like Cyanine, Rhodamine, etc. Organic dyes tend to be brighter than fluorescent proteins, allowing for higher localization precision [85]. On the other hand, fluorescent proteins have the advantage of being genetically encoded, making it easier to label intracellular proteins in living cells. With high labelling efficiencies and samples with a good signal-to-noise ratio, the localization precision of PALM and STORM can be brought down to 10 nm laterally [81] [87].

Universal Point Accumulation for Imaging in Nanoscale Topography (UPAINT):

With STORM and PALM, a sub-diffraction resolution can be attained and cellular components can be visualized with astonishing details. However, these methods have difficulties to access densely labelled regions due to spontaneous photoswitching, which prevents imaging individual fluorophores in these regions. Moreover, they failed in attaining super-resolved images of native proteins or endogenous molecules at nanometer resolution on live cells. universal Point Accumulation for Imaging in Nanoscale Topography (uPAINT) is an extremely versatile super-resolution imaging technique circumventing these issues [88].

uPAINT utilizes the real-time imaging of low concentration high-affinity fluorescent ligands as they bind to and interact with random membrane biomolecules in living cells. It does not require prior labelling or photoactivation of single molecules. A wide field fluorescence microscope working in oblique illumination is used for uPAINT. Oblique illumination selectively excites fluorescent ligands that have bound to their target and not those present in solution above the cellular membrane (Figure 1.13 A). Thus, any biomolecule that labelled with a fluorescent ligand can be studied [13].

The experimental setup of uPAINT microscopy is shown in the Figure 1.13 B. A CW laser is used for excitation through the fluorescence epiport of the microscope and illuminate a wide field area of 10-20 μm in diameter of the sample by focusing the beam in the back aperture of the objective. The focused beam is translated with respect to the optical axis on the periphery of the back aperture of the objective in order to obtain an oblique illumination. Illumination intensities of a few kW/cm^2 excite the fluorescent ligands that are bound to the cell surface of interest. The mobility of the ligand is drastically decreased, allowing its detection with a sensitive and rapid EM-CCD camera for several milliseconds, until photobleaching occurs. However, it is not possible to track the behaviour of single molecules over long times.

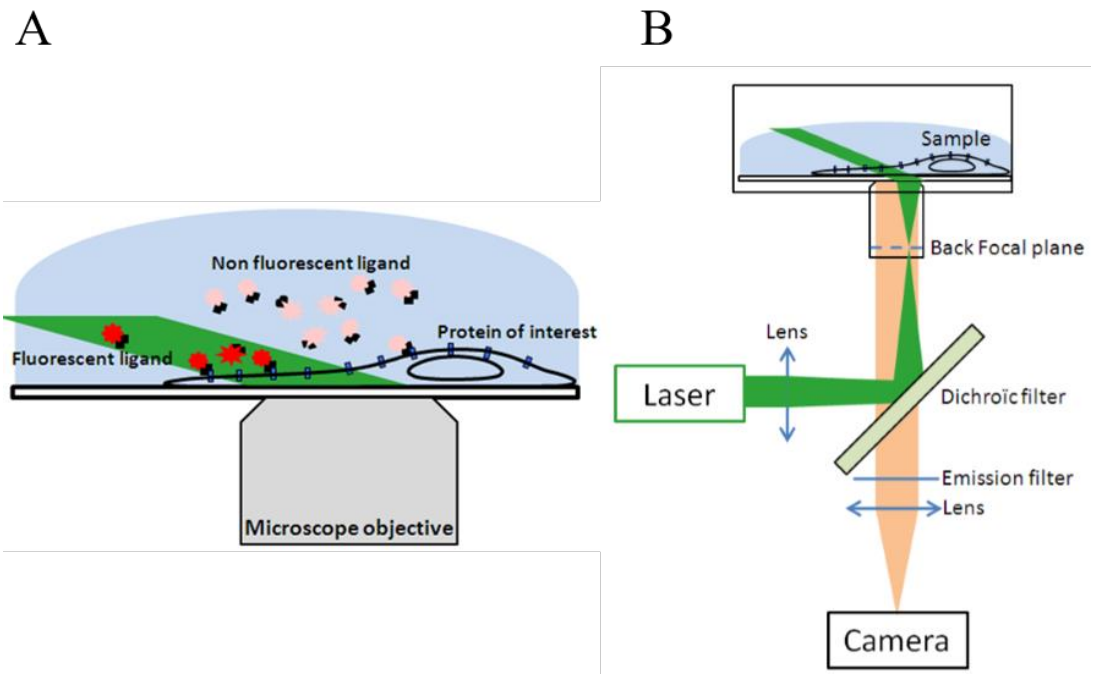

Figure 1.13: (A) Principle of uPAINT: uPAINT is based on the real-time imaging and tracking of single fluorescent ligands while they label their membrane biomolecules targets. A low concentration of fluorescent ligands is introduced into the extracellular medium such that a constant rate of membrane molecules is being labelled during the imaging sequence. Oblique illumination of the sample is used to excite predominantly fluorescent ligands, which have bind to the cell surface while not illuminating the molecules in the above solution. (B) Schematics of the optical setup for uPAINT. Figure adapted from [13].

A typical localization precision of 40-50 nm resolution is achieved for 50 ms integration time with the uPAINT method [89]. Moreover, it can also provide dynamic information on the single protein level revealing localization-specific diffusion properties of membrane biomolecules by generating a significant amount of information about each cell. However, since the fluorescent ligands cannot penetrate into the plasma membrane of a living cell, it is not possible to study the intracellular protein dynamics of biomolecules with uPAINT technique.

1.3.2 Super-resolution by spatially patterned excitation (ensemble based imaging)

In this technique, resolution enhancement is achieved by spatially modulating the fluorescence behaviour of the molecules in the diffraction-limited region, such that not all of them emit simultaneously, by using nonlinear optical effects and high-intensity laser. The most popular ones among the ensemble based imaging techniques are stimulated emission depletion (STED) microscopy, reversible saturable optical fluorescence transitions (RESOLFT), ground state depletion microscopy (GSD) and saturated structured illumination microscopy (SSIM).

Stimulated Emission Depletion Microscopy:

Stimulated emission depletion microscopy (STED), as the name says, exploits "stimulated emission" to create sub-diffraction PSF. This nonlinear technique functions like an improved confocal laser-scanning microscope. STED uses two illuminating beams. The first beam is a usual Gaussian beam, which illuminates the emitter and excites it. The size of the spot will be diffraction-limited. The second beam, STED beam, passes through a singular optic, which produces a doughnut-shaped beam that has a minimum at the axial centre [90]. STED beam has a longer wavelength compared to the excitation beam. Figure 1.14.A shows the energy levels involved in the excitation and emission of a fluorescent molecule, which constitutes a simplification of the Jablonski diagram. The fluorophores are excited from the ground state S_0 to higher vibronic states of their first excited electronic state S_1, which relaxes to the lowest vibronic state of S_1 within few picoseconds. De-excitation of S_1 down to S_0 occurs within nanoseconds and may be accompanied by the spontaneous emission of a fluorescence photon. This spontaneous emission can be suppressed via stimulated emission by depleting the state S_1 by optically forcing the molecule into S_0 immediately after excitation. This is done with the doughnut-shaped STED beam. Because of the doughnut distribution, most of the stimulated emission will take place at the periphery of the original pulse and none in the exact centre [91] [92]. Thus, only molecules in the centre of the STED beam are able to emit fluorescence. The spontaneous fluorescence photons are only detected and the stimulated photons are removed using a filter at the frequency of the depletion beam. With increasing intensity of the STED beam, the excited state S_1 is more and more likely depleted, i.e., the molecule is spending almost no time in this state. This narrows the PSF and results in a resolution beyond the diffraction limit [93]. Thus, the physical mechanism behind STED microscopy is a competition between stimulated emission and spontaneous emission.

It was experimentally proved that the resolving power increases with the square root of the saturation level of STED. Therefore, for the calculation of resolution in STED microscopes the Abbe equation, the diameter of the PSF, Δr_{STED}, is replaced with the following [94]:

$$\Delta r_{STED} \approx \frac{\lambda}{2NA} \frac{1}{\sqrt{1 + \frac{I}{I_s}}}, \tag{1.9}$$

where λ is the wavelength, NA is the numerical aperture of the objective, I is the maximal focal intensity applied for STED and I_s is the saturation intensity of the fluorophores. By sending an intensity high enough the size of the PSF can be made arbitrarily small [95]. And, when I/I_s is increased toward infinity, resolution (Δr_{STED}) approximates to zero; hence resolution is now independent of diffraction [96]. The theoretical principles of STED microscopy were first introduced in 1994 by Hell and Wichmann [91].

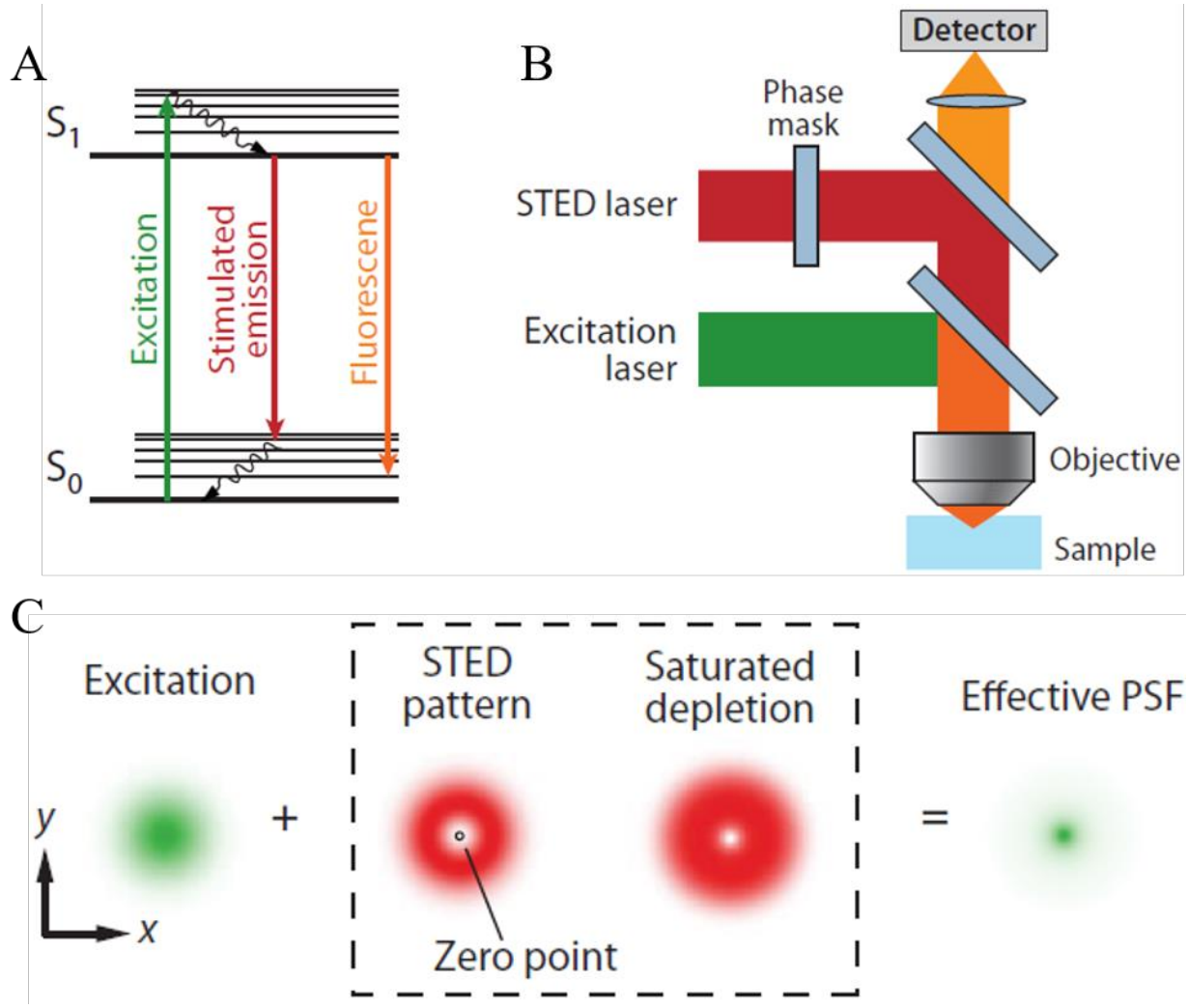

Figure 1.14: The principle of STED microscopy. (A) Jablonski diagram of the molecular states and transitions involved in STED microscopy. An excitation laser excites an emitter from the ground state S_0 to s higher vibrational level of the excited state S_1. The emitter can emit fluorescence from the lowest vibrational level of S_1 by spontaneous emission. The emitter can emit fluorescence from the lowest vibrational level of S_0 by stimulated emission. (B) Schematic drawing of a STED microscope. The excitation laser and STED laser are combined by dichroic mirrors and focused by an objective on the sample. A phase mask is placed in the light path of the STED laser to create a specific pattern at the objective focal point. A detector records the fluorescence. (C) Enhanced resolution with STED microscopy. In the xy plane, a doughnut-shaped STED laser is applied with the zero point overlapped with the maximum of the excitation laser focus. With saturated depletion, fluorescence from regions near the zero point is suppressed, leading to a decreased size of the effective PSF. Figure adapted from [97].

With STED microscopy, 50-70 nm resolution is commonly reached [8], while it is possible to reach much higher resolution under optimized conditions. When combined with time-resolved readout and computer algorithms for the fitting of point spread functions, STED has produced images with resolution down to 2.4 ± 0.3 nanometers with NV centres in diamond [98]. Signal

levels and possibly specimen damage set the practical resolution limit. Moreover, the optical systems are much more complicated and expensive.

Reversible Saturable Optical Fluorescence Transitions (RESOLFT):

There are other mechanisms capable of suppressing undesired fluorescence emission other than stimulated emission. A more general scheme using reversible saturable or switchable optical transitions to achieve super-resolution has been formalized with the name Reversible Saturable Optical Fluorescence Transitions (RESOLFT) microscopy [99]. This concept makes use of fluorescent probes that can be reversibly photoswitched between a fluorescent on state and an off state, called the reversible switchable fluorescent proteins (rsFPs).

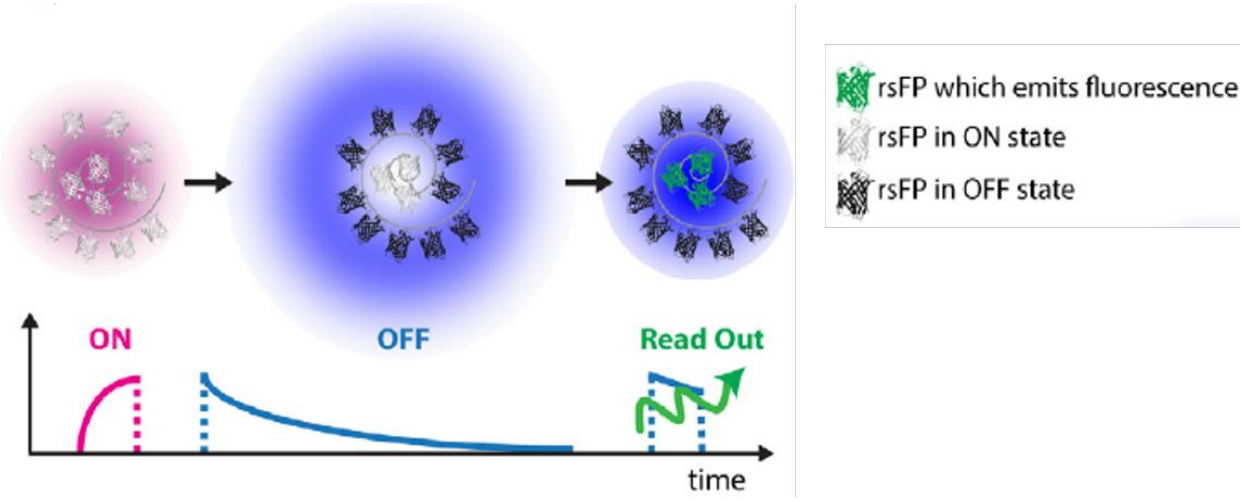

Figure 1.15: RESOLFT with reversibly switchable proteins. Scheme of the switching of fluorescent state for RESOLFT imaging of the rsEGFP is depicted. Each step is performed with different colours and duration depending on the absorption spectra of both states of a chosen rsEGFP. Figure adapted from [100].

The gain in spatial resolution is achieved in the same way as in STED, which uses a depletion laser to drive fluorophores at the periphery of the excitation into the dark state by increasing the degree of saturation, I/I_S. Unlike STED, which features a high I_S value ($\sim 10^7$ W/cm^2) and thus requires an intense depletion laser (often$> 10^9$ W/cm^2), RESOLFT nanoscopy requires a much lower laser intensity. This is because of the long-lived photoinduced off states, which also leads to a lower residual fluorescence level. The off state can be the triplet state as in ground state depletion microscopy, or the dark state of a reversibly photoswitchable fluorophore. The dark state includes isomerization states (cis-trans) or hydrated-dehydrated molecular configurations or other optically bistable transitions in fluorophores [9]. The saturation intensity can be reduced by $\sim 10^3$ compared to STED by using triplet off state [101] [102]. Alternatively, the switching between conformational fluorophore states [103] [104] [105] [106] gives a factor of $> 10^6$. Suitable candidates for saturable switches are encountered in photochromic compounds and photoswitchable GFP-like proteins [99] [103] [106], which could ultimately achieve super-resolution under realistic physical conditions.

Both RESOLFT and STED technique certainly requires scanning, but not necessarily with a single beam or a point-like zero. A point scanning technique compromises the temporal resolution, especially in the large field of view since the states of the rsFPs need to be populated and depopulated several times. The limited temporal resolution of STED and RESOLFT can overcome by using multiple zeros [107] [108] or dark lines [109] [110] in conjunction with conventional CCD-camera detection, provided the zeros or the dark lines are further apart from the minimal distance required by the diffraction resolution limit of conventional CCD camera imaging.

Ground State Depletion (GSD) Microscopy:

Ground State Depletion (GSD) fluorescence microscopy comes under the RESOLFT concept, with the potential of achieving far field lateral resolutions of 10-20 nm with low laser intensities compared to STED. The method was introduced by Hell [101]. The basic principle of GSD is based on the transitions that switch the fluorescence dyes to be in the fluorescent (on) and dark (off) states. The dark state employed is a long-lived state, say, for example, triplet state.

GSD Microscopy uses a high-intensity doughnut light to transfer a majority of fluorophores from the excited state to a stable and a reversible dark state, triplet state T_1. Triplet state has a lifetime in the range of a hundred milliseconds to several seconds. The single fluorophores that remain in the excited state are then stochastically emitted for a short time. The fluorescence signals produced by these fluorophores switching between dark and bright states are recorded over time. The high-intensity excitation light is used in such a way that almost all fluorophores in the sample are turned dark, leaving only single, well-separated fluorophores emitting fluorescence, which is a requirement for the localization procedure.

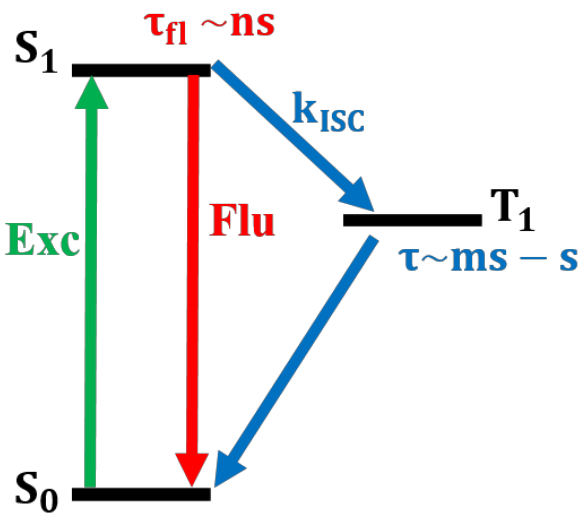

Figure 1.16: Switching a regular fluorophore using its dark states in GSD (optical shelving). Repetitive excitation (Exc) of the singlet ground state S_0 to the first excited singlet state S_1 elicits fluorescence (Flu) emission and switches a molecule to the triplet state T_1 with long lifetime (τ).

The position of individual fluorophores is determined in each image with nanometer resolution. Since only a few fluorescent molecules can be analyzed in each frame, it is necessary to acquire

thousands of images to detect the entire set of hundreds of thousands of fluorophores labelling a biological structure. This leads to imaging times in the range typically 2-10 min per super-resolution image.

For successful implementation, GSD microscopy requires either special fluorophores with high triplet yield or other metastable states. The broad range of fluorophores suitable for GSD imaging includes not only AlexaFluor 488, AlexaFluor 532, Rhodamins 6G, AlexaFluor 647, but also a range of Atto and Chromeo dyes. GSD could achieve a localization of about 7.6 nm for nitrogen vacancy in diamonds with doughnut beam intensity, $I_D = 910I_S$ [111].

Saturated Structured Illumination Microscopy (SSIM):

In SIM, the highest spatial frequency possible for the illumination beam determines how wide the objective passband of the imaging system can be enlarged. Unfortunately, the highest spatial frequency that illumination source can contain is itself limited by diffraction ($f_0 = 2NA/\lambda_{em}$). This limits the resolution of SIM with linear photo-responses to about two times the diffraction-limited resolution. The same nonlinear phenomena, saturation of the excited state is used to overcome this two-fold limitation, and the technique is called saturated structured illumination microscopy (SSIM) [10].

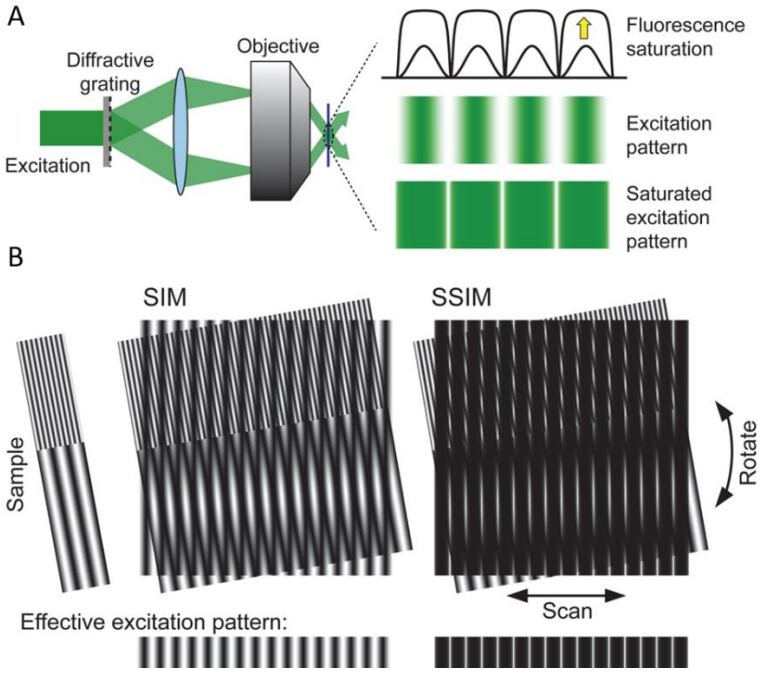

Figure 1.17: Comparison between SIM and SSIM. (A) Generation of the saturated excitation pattern. As the intensity of the patterned illumination beam is increased above the saturation intensity of the fluorophore, the effective excitation pattern will not remain sinusoidal. It will become flat, but without any fluorescence from the zero of the valley. (B) Multiplication of the saturated illumination pattern with the image gives Moiré fringes with higher-order spatial frequencies. Figure adapted from [38].

The patterned illumination pattern is generated by the same way as for SIM, by interfering light beams from a single laser using a diffraction grating. Under strong excitation intensity, fluorophores will show the nonlinear optical saturation. This saturation leads to the clipping of the peaks of excitation pattern and therefore it becomes flat (Figure 1.17 A). However, the fluorescence emission is still absent from the zero points in the valleys. This gives the saturated excitation pattern (Figure 1.17 B). Thus, the role of nonlinear optical saturation is to generate high-frequency harmonics into the illumination pattern, which contain spatial frequencies that are multiples of f_1.

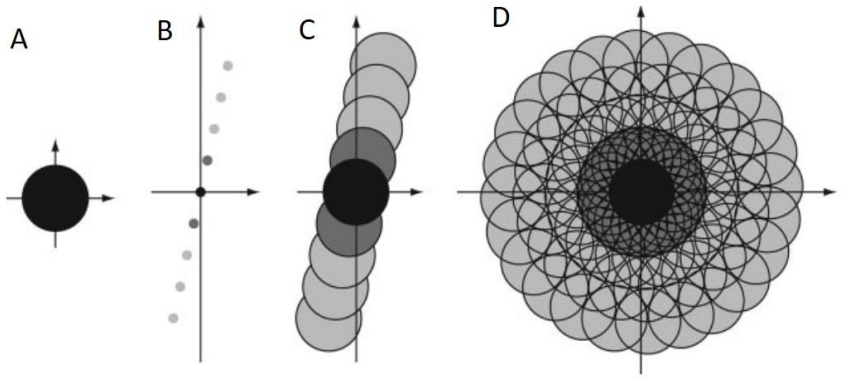

Figure 1.18: Principle of SSIM. (A)The region of frequency space that is observable by conventional microscopy. (B) The illumination pattern has three frequency components: one at the origin (black) and two at $\pm f_0$(dark grey) as in SIM. Along with this, we have spatial frequencies at multiples of f_0 under saturation. Theoretically infinite number of additional components appear in the effective excitation; the three lowest harmonics are shown here (light grey). (C) Observable regions for SSIM based on those three lowest harmonics. (D) Corresponding observable regions with illumination pattern rotated to different pattern orientations. With this much larger region of observable spatial frequencies, an increased spatial resolution can be obtained. Figure adapted from [10].

The saturated illumination pattern is now mixed with the high-frequency spatial features of the sample forming the Moiré fringes. Similar to SIM, the gridlines (saturated illumination pattern) are rotated several times to generate data for a single image, which is retrieved mathematically during post-acquisition processing (Figure 1.18). This process can effectively bring sub-diffraction-limited spatial features into the detection range of the microscope. The resolution limit of SSIM is bounded by signal-to-noise ratio and the photostability of the fluorophores used. SSIM has demonstrated a 50 nm resolution for a bright and photostable DNA stain molecular probes that emit 50,000 photons per molecule [10].

Minimal Emission Fluxes (MINFLUX) Microscopy :

MINFLUX is the newly developed fluorescence microscope that can optically separate molecules, which are only nanometers apart from each other [112]. They could achieve a lateral resolution of 1 nm. Thus, this method achieves resolution more than 100 times better than conventional optical

microscopy and beat the super-resolution methods discussed before, like STED and PALM/STORM.

MINFLUX took the advantages of STED and PALM/STORM in an entirely new thought. The doughnut beam in the STED microscope defines precisely the position in space where the corresponding fluorescing molecule is located. However, we need a high-intensity laser to confine the molecule in nanometer resolution at the doughnut center. On the other hand, the stochastic approaches like PALM/STORM switch the fluorophores on and off at random locations and at the single molecule level. Even though PALM/STORM is working at the single-molecule level, they do not know the exact position of the molecule in space. The position is determined by collecting as many fluorescence photons as possible on a camera and estimating the centroid of the fluorescence diffraction pattern. But, the unknown orientation of the fluorophore emission dipole limits in achieving molecular (one nanometer) resolution [113].

MINFLUX uses a doughnut-shaped laser beam, like STED, to determine the precise position of fluorophores and is randomly switched as in the case of PALM. Using the PALM principle, images can be taken with 100 times better resolution. In contrast to STED, doughnut beam is used for excitation, not for stimulated emission, and the molecule is excited only if it is on the doughnut ring. The emitter is probed with the local intensity minimum of doughnut beam, thereby minimizes the need of fluorescence photons for localization precision. Later, the maximum likelihood estimator (MLE) is used to locate the exact position of the molecule with high precision.

MINFLUX offer faster acquisition and lower light signal as it works with a doughnut beam. So now, it is possible to record the fast occurring changes in molecules, with 100 times better temporal resolution than other super-resolution techniques. Added to that, MINFLUX can be used in combination with other super-resolution techniques like light sheet microscopy. However, there are some practical limitations for MINFLUX. The background and aberrations in the system can blur the intensity minima, which defines the molecule.

1.4 Three-dimensional super-resolution

All these far-field fluorescence microscopic techniques discussed in the previous section have led to extensive improvements in image resolution, achieving a resolution of 20-30 nm in the lateral dimensions. However, to study coupling interaction between molecules, or between molecules and metallic structures, and for resolving most organelles and cellular structures, high-resolution in all three dimensions is required and it remains a challenge. With confocal or multiphoton microscopy, we can perform three-dimensional imaging, but with an axial resolution of about 500-800 nm, two or three times worse than the achievable lateral resolution. It is the 4Pi microscopy, which could achieve the best 3D resolution in light microscopy until lately with an axial resolution $\sim$100 nm. Here, in this section, we will show various optical imaging techniques exceeding conventional resolution in all three dimensions.

1.4.1 Three-dimensional imaging by single-molecule localization

Astigmatism imaging:

Stochastic optical reconstruction microscopy can be extended to three-dimension using optical astigmatism [114] [115]. An image with an axial resolution of 50-60 nm has been reported in the literature [75]. In this method (Figure 1.19), a cylindrical lens is placed in the imaging path to create two slightly different focal planes for the x and y directions. The lateral position of the fluorescent dye is then determined from the centroid of its image, by fitting a 2D elliptical Gaussian function. With the axial position, the ellipticity and orientations of a fluorophore's image will vary. At the centre of the two focal planes, the image will appear round and on either side, it will be an ellipsoidal shape. From the fit of the images and the orientation of the ellipse, the z-position can be determined explicitly.

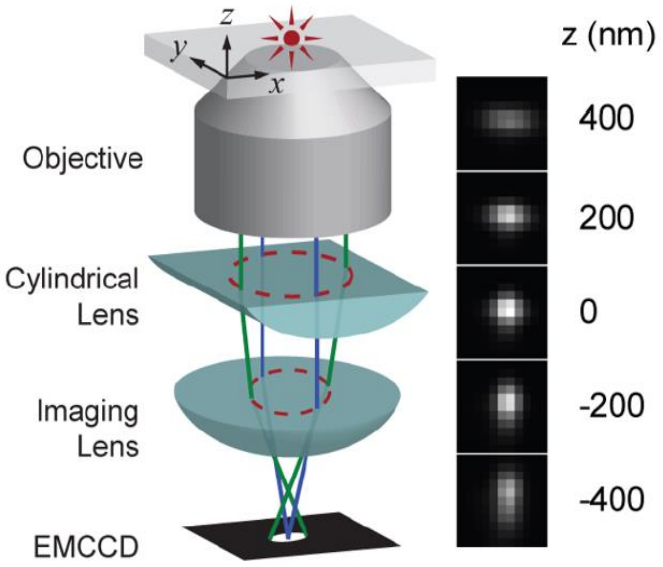

Figure 1.19: Three-dimensional localization of individual fluorophores in 3D-STORM microscopy. A cylindrical lens is used to image a fluorescent dye at different axial planes and from the ellipticity of the image, the axial position is determined precisely. The right panel shows the image of a fluorophore at various z positions. Figure adapted from [75].

However, this better axial localization is achieved at the expense of fluorescence signal. The astigmatic PSFs expand in size with defocus, resulting in reduced signal levels. This will reduce transverse position sensitivity than a focused system. Therefore, in photon-limited applications, while defocusing, the signal is lost in the noise.

Biplane Imaging:

In biplane (BP)FPALM, a combination of double-plane detection scheme with fluorescence photoactivation localization microscopy (FPALM) is used to enable 3D-super localization with good speed or sensitivity. This can image thick samples over a depth of several micrometres with

a resolution of 25 nm laterally and 50 nm axially [79]. As the name suggests, it is a FPALM microscope with two axially separated parallel object planes (~ 350 nm away) that are imaged simultaneously, providing two sections of the PSF. In the detection path, the focused light is split by a NPBS cube and is directed towards an EM-CCD camera. This simultaneous detection of two planes has two significant advantages. First, the imaging process is hastened by making axial scanning unnecessary for volumes less than ~ 1μm thick. Second, it removes localization artefacts present in scanning-based systems caused by the rapid blinking and bleaching common to single molecules. By combining the signal from the two recorded sections of interest, a 3D raw data stack consisting of two planes can be reconstructed [116].

The lateral localization accuracy for the 3DSTORM method varies with the axial position for a depth of ~ 1μm. Therefore, for a homogeneous lateral localization, the depth range in such method must be in the range of ~ 500 nm. Moreover, since the orientation of the dipole also adds up to the ellipticity of the fluorescence image, the sensitivity of ellipticity to find the axial position is far less for it. On the other hand, the lateral and axial resolution values of (BP)FPALM do not have a dependence on the localization depth range of ~ 1 μm. Therefore, it is capable of 3D imaging of volumes ≤ 1 μm thickness without scanning. By taking multiple optical sections, it is possible to have a three-dimensional image of samples with higher depth range. A 3D imaging of a sample with a depth range of 4 μm is achieved with (BP)FPALM [79].

Double-Helix PSF imaging:

In double-helical PSF imaging, the PSF is engineered to have a double helix (DH) shape along the z-axis of the microscope. The DH-PSF has two dominant lobes in the image plane, and the angle of the line connecting them with respect to the horizontal direction is related to the axial position of the emitter. This angular information can thus be used to extract the axial location of the emitters with high precision [117].

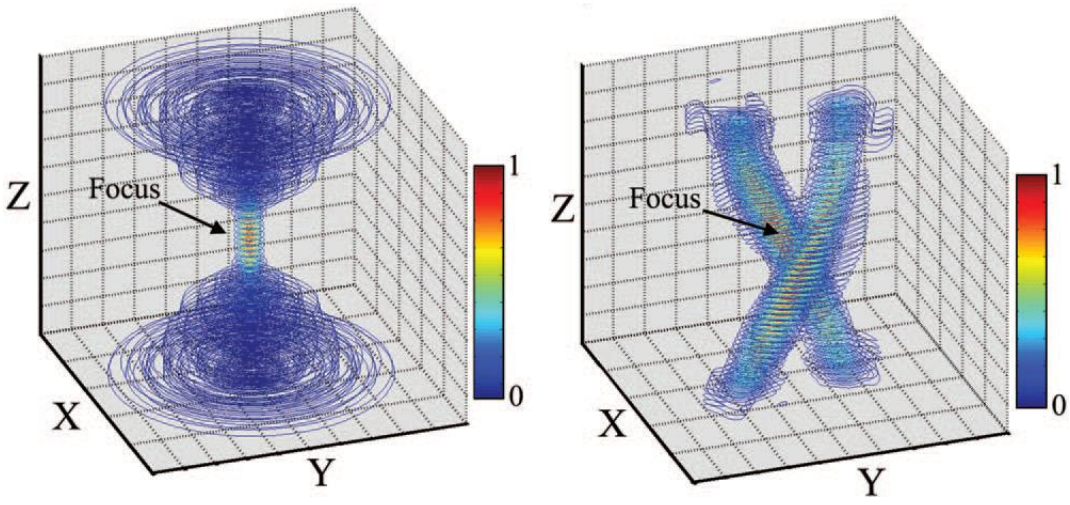

Figure 1.20: Three-dimensional image of the (A) standard PSF and the (B) DH-PSF with the contour lines. The standard PSF barely changes along the focal region, beyond which the PSF

rapidly expands in size. The DH-PSF exhibits two lobes that continuously rotate along the axial (Z) dimension. Figure adapted from [118].

With sufficient fluorescence detected counts, on the order of 100-1000 per fluorescent probes, z-resolution single fluorescent molecules in a thick sample are localized in single 500 ms acquisitions with 10 to 20 nm precision over a large depth of field (2 μm) by finding the centre of the two DH-PSF lobes [80].

iPALM:

Interferometric photoactivated localization microscopy (iPALM) [108] is a combination of lateral PALM with single photon multi-phase interferometry. To adapt interferometry principle, iPALM make use of the interference of a single fluorophore with itself. To provide two paths for the fluorescent signal to traverse, iPALM use two opposing objectives one on either side of the sample, similar to 4π microscopy. This has the added benefit of accumulating almost all the emitted fluorescence from the sample, making it concretely photon-efficient technique. The signal from both objectives is recombined with a 3-way beam splitter (Figure 1.25) [119]. The 3-way beam splitter results in the self-interference of photons and produces three beams of varying intensities. The beam splitter then directs the beam to three synchronized camera simultaneously, producing interference images on each of them. The path length difference taken by the fluorescent photon while passing through the two objectives has a strong dependence on the relative single molecule fluorescence intensities seen by each camera. By standardizing a model fluorophore position against the image intensities in each camera, the axial position can be determined precisely.

The iPALM approach yields an axial localization of about 10 nm for typical fluorescent probes, actually twice the lateral resolution, 20 nm [81]. This resolution capability offers to study the molecular scale architecture of a cell, including determination of 3D localization of specific proteins and their interaction. Although iPALM microscopy provides better axial resolution than other super-resolution methods that are based on biplane detection, or “engineered” point spread function techniques including astigmatic approach; several limitations remain. In addition to the requirement that the sample is sandwiched between two microscope objectives, the technical complexity of the iPALM experimental apparatus is high and is also limited in the available temporal resolution than other super-resolution modalities such as SIM. Also, due to opposing objectives, the thickness of the sample to be imaged should be less than 15 – 20 μm. These problems currently limit widespread adoption of this method.

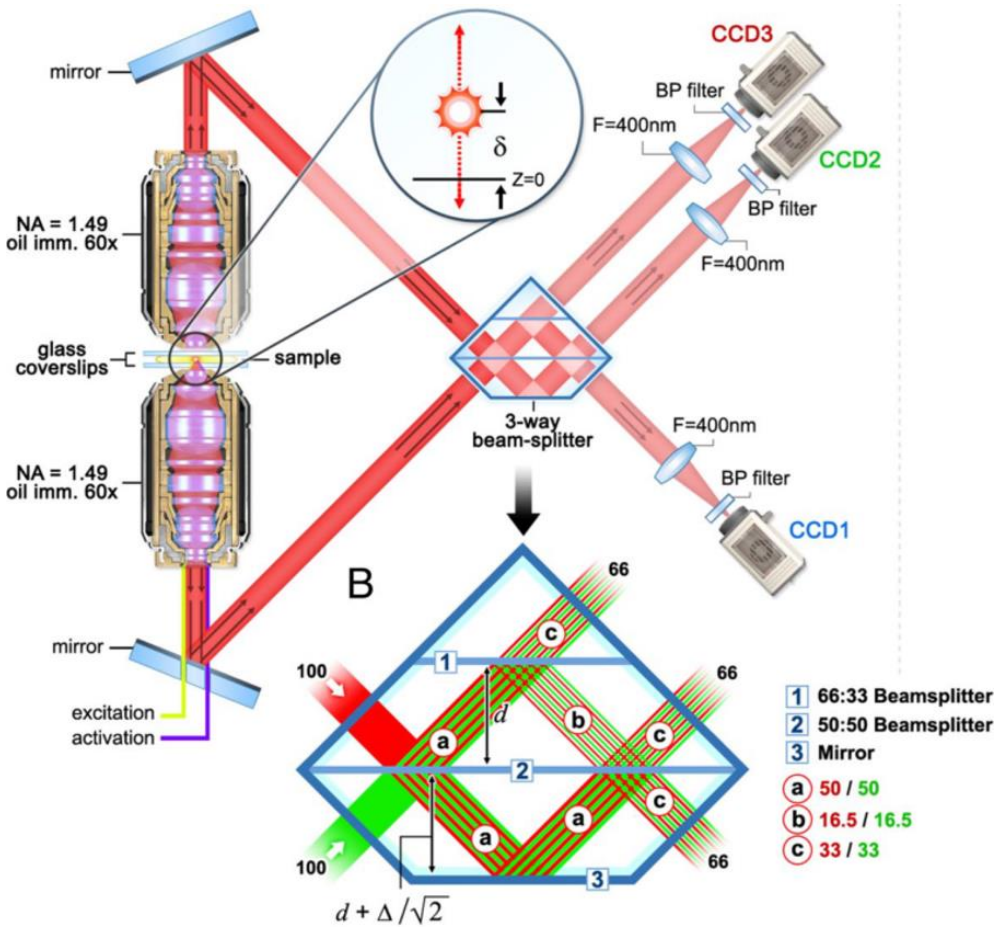

Figure 1.21: Experimental setup of iPALM Microscope. The fluorescence photons from the sample are collected by the two objectives and will travel in the two paths depending on the fluorophores axial position. The two signals are then combined using a 3-way beam splitter which causes self-interference of the photons and produces three beams of varying intensities which are subsequently detected by CCD cameras. Figure adapted from [81].

1.4.2 Three-dimensional imaging using patterned excitation

Selective Plane Illumination Microscopy (SPIM):

Selective Plane Illumination Microscopy (SPIM) or light sheet fluorescence microscopy (LSFM) uses a light sheet to illuminate the sample from the side in a well-defined volume around the focal plane of the objective [120]. A cylindrical lens or a scanning laser beam in combination with an illumination objective is used to generate the light sheet. The light sheet has a hyperbolic profile. The sample is illuminated at the beam waist of the light sheet as shown in Figure 1.22. Thus, only the focal plane of the sample inside the light sheet is exposed to laser light and is imaged all at once by the camera. This reduces the photodamage and provides optical sectioning with high frame rates. The thickness of the light sheet and the NA of the objective defines the axial resolution.

Using a conventional wide-field technology, the fluorescent signal is collected by the objective aligned perpendicular to the plane of illumination. By moving the sample across the light sheet, a series of optical sections are imaged, which are then reconstructed to form three-dimensional images. Thus, SPIM allows imaging thick and live samples in three-dimensions for prolonged duration with excellent resolution while being minimally invasive.

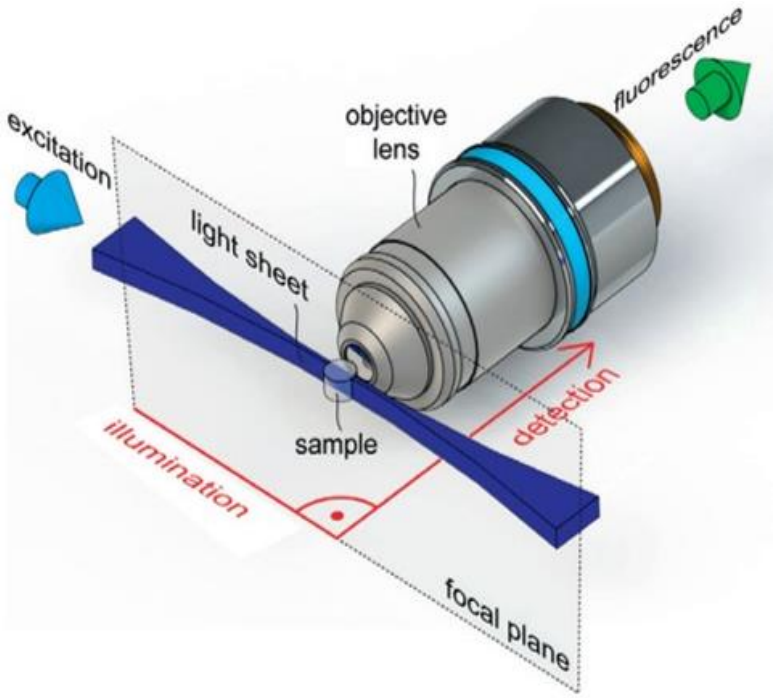

Figure 1.22: Illustration of light sheet fluorescence microscopy (LSFM) setup. The light sheet which is produced by a cylindrical lens is projected onto the sample from one side with an objective. The light sheet will illuminate the entire 2D focal plane. The fluorescent signal is collected by the objective placed perpendicular to the light sheet and the illuminated area is imaged all at once. Figure adapted from [121].

The limitation of SPIM is that it requires complicated two-objective setup. Later, Galland [122] introduced the concept of single-objective SPIM (so-SPIM) (Figure 1.23). In soSPIM, light sheet is created by reflection from a 45^0 mirror, and the fluorescent signal is collected through the same objective used for illumination. So-SPIM can produce 3D optical sectioning with capabilities ranging from single molecule detection at the cellular level to whole-embryo imaging.

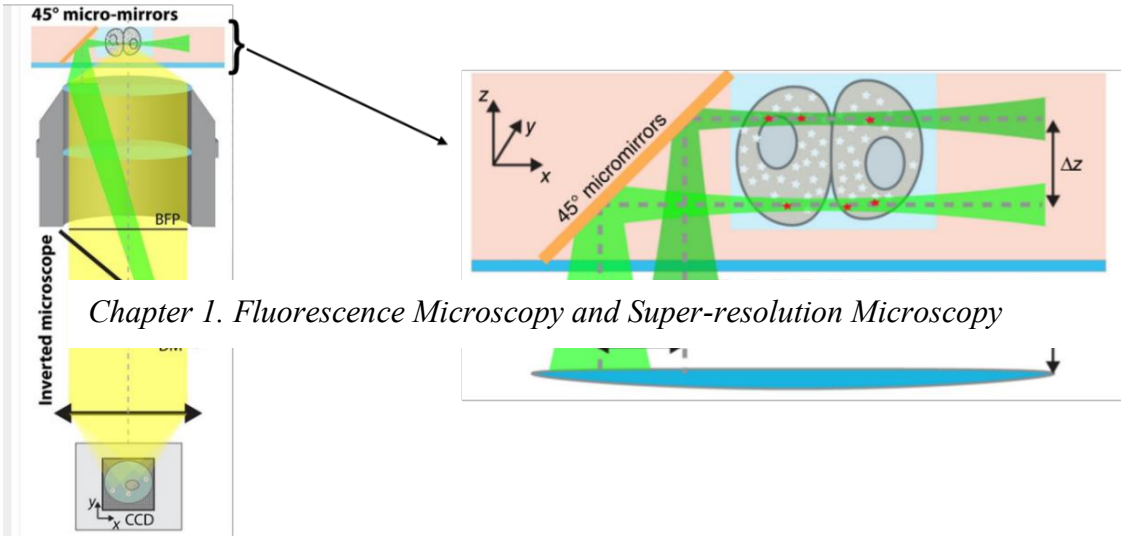

Figure 1.23: Principle of so-SPIM Microscopy. The excitation beam entering an inverted microscope objective illuminates the sample after passing through a 45^0 micromirror, forming a light sheet. The micromirror is mounted on the sample holder. Three-dimensional images are taken by translating the excitation beam along the mirror (Δx) and by positioning the objective in the axial direction (Δz). Figure adapted from [122].

Isotropic Single Objective (ISO) Microscopy:

The 4Pi microscopy using two objective lenses facing each other can confine axial dimension three times narrower than that obtained with a single lens [68]. However, the complexity in adjusting the two objective lenses and two optical paths make the technique very difficult to implement. Isotropic single-objective (ISO) microscopy is an alternative approach to achieve the focal spot similar for 4Pi microscopy but using single objective lens [123] [124].

For ISO focusing, two modifications are made on the confocal microscopy. First, a phase-only spatial light modulator (SLM) is introduced between the dichroic mirror and the objective. The phase pattern on the SLM is such that the incident beam is shaped in order to focus simultaneously at two points (Figure 1.24.A). The phase pattern is calculated using electromagnetic time reversal theory [124]. By changing this pattern, it is possible to scan axially for about 10 μm, depending upon how far objective is optimized to focus from its focal plane. Second, a mirror is placed equidistant between the two focal points. This makes the light to focus at the first point and then reflected back by the mirror to overlap the second focal point with the first one (Figure 1.24.B). Similar to 4Pi microscopy, a quasi-isotropic central spot surrounded by side lobes are formed through the interference of the direct and mirror reflected field. The diameter of the spot is about $\lambda/2$, that is, super-resolved in the axial direction. This illumination scheme can also be incorporated with other imaging techniques in order to have three-dimensional super-resolution without much experimental complexity [125].

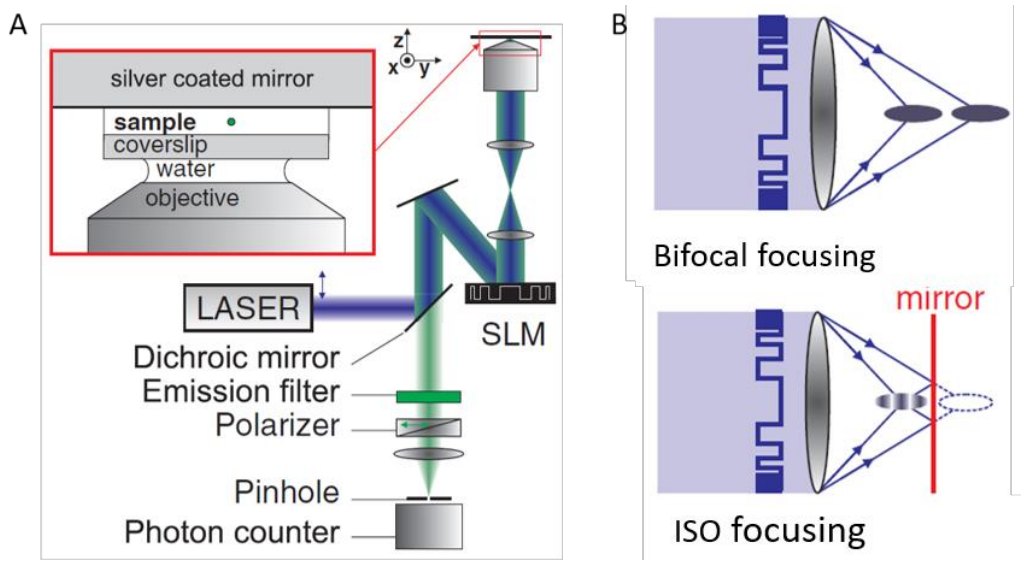

Figure 1.24: (A) Experimental setup of the isotropic single objective microscope. (B) The concept of ISO focusing with mirror. Figure adapted from [123].

ISO Microscopy also suffers from the problems with the high sidelobes. Using high NA objective, the amplitude of the side lobes can be diminished to a large extent. Added to that, mechanical drifts of the mirror is critical for the experiment precision. This can cause deterioration in the PSF shape. However, it is found that measurements for 15 to 20 min can be taken without any PSF deterioration and without using any additional stabilizing system.

3D STED Microscopy:

Stimulated emission depletion (STED) microscopy allows far-field fluorescence imaging with diffraction-unlimited resolution. A helicoidal phase mask creates the most commonly used diffraction profile for STED. This gives a highly anisotropic effective PSF that is narrowed in the lateral (XY) plane but remains diffraction limited in the axial (Z) direction. Consequently, these STED images are super-resolved only in the lateral direction, but not along the axial direction. Later, STED is extended to three-dimensional (3D) imaging by incorporating certain modifications in STED microscopy, like PSF engineering, combining STED with axial superresolution microscopes like 4Pi microscopy, TIRF, etc. Here, I present different adaptations in STED microscopy which allows 3D superresolution.

i) 4pi + STED: The elongation in the axial PSF of the STED can be reduced by employing 4Pi microscopy in combination with STED microscopy [126] [104]. The sample is placed at the common focus of two opposing lenses in a so-called "4Pi" geometry to reduce the focal spot size. This allows the creation of sharp central minimum in the axial direction of the depletion focus and has enabled 33 nm axial resolution [104]. However, this approach suffers from high experimental complexity.

ii) isoSTED: To generate an isotropic depletion profile, two depletion patterns featuring a common focal zero is utilized: one for lateral $STED_{xy}$ and another for axial $STED_z$. The $STED_{xy}$ beam is the usual doughnut-shaped generated using a helical phase mask and the $STED_z$ beam is formed with a phase mask consisting of a central area with a π-phase retardation. Such a phase mask produces a ring-shaped profile in the focal plane and dark central field with symmetric bright spots along the optical axis [127] [128].

isoSTED provides a direct three-dimensional imaging of dense samples with a resolution of 43 nm in the lateral and 125 nm in the axial direction [129], well below the diffraction limit. However, the $STED_z$ depletion profile exhibits axially repetitive interference minima above and below the focal plane. These sidelobes create artefacts, so-called ghost images, and degrade image quality. Deconvolution process [130] [131] can mitigate this phenomenon, but requires an additional image post-processing step and is limited to images with good signal-to-noise ratio.

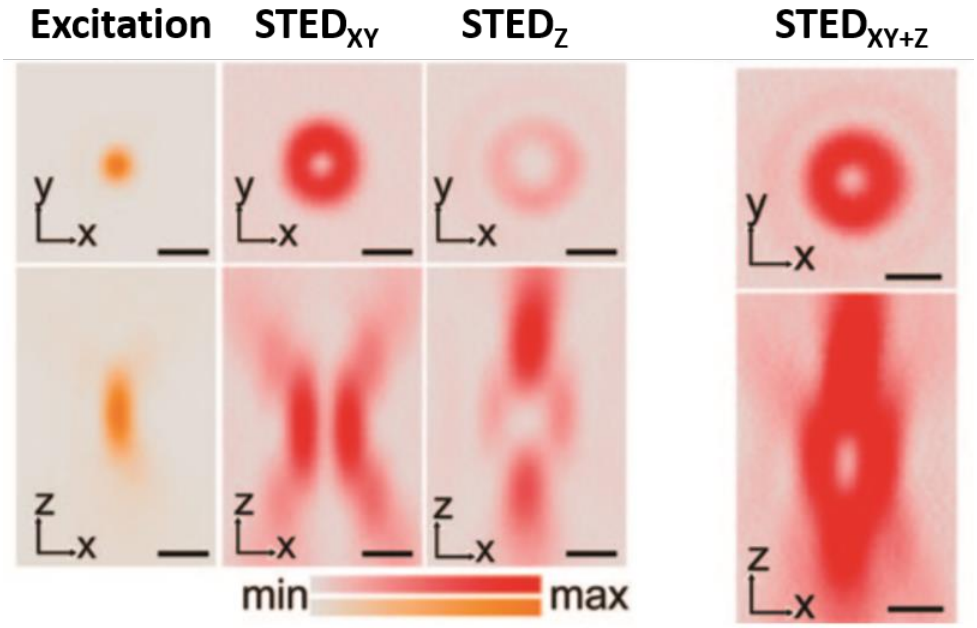

Figure1.25: Focal intensity distributions of excitation and STED beams. From left to right: Excitation, STED beam for lateral superresolution, STED beam for axial superresolution, and STED beam of isoSTED which is the combination of both lateral and axial STED beams. Figure adapted from [129].

iii) TIRF-STED: The major advantage of TIRF microscopy is that it can provide sub-diffraction axial sectioning by limiting excitation to the immediate vicinity of the sample-substrate interface. STED microscopy can be facilitated TIRF illumination to have 3D super-resolution, by combining the lateral resolution enhancement achieved by stimulated emission depletion with the optical section capabilities of total internal reflection [132]. This combination enables observation volumes of sub-100 nm diameter in all three dimensions. This decoupling of axial from lateral resolution improvement provides additional flexibility in instrument design. STED can be optimized solely for best resolution in the focal plane while TIR takes care of limiting observation

to the immediate vicinity of the coverslip. Because of the limited excitation to a small portion of the sample, TIRF-STED can reduce photobleaching of fluorophores and phototoxicity to living samples. Thus, the important potential advantages of TIRF-STED lies in imaging live samples. Nevertheless, TIRF-STED has the limitation that the strong axial confinement occurs only on one surface of the sample.

iv) Double Helix-STED: DH-STED approach allows the discrimination of fluorescent emitters spaced closer than diffraction limit and the precise localization of individual emitters in the axial dimension with a resolution about 25 nm [133]. If the emitters are resolved by lateral superresolution, the DH-PSF can enable depth localization of the emitter with high, uniform precision through an extended depth of field, thereby providing axial information with a single lateral scan. However, the emitters separated axially by a distance closer than the conventional depth of focus cannot be distinguished laterally. This drawback is compensated by the simplicity and accuracy of the technique.

3D-SIM:

SIM can also be extended to three dimensions with a lateral and axial resolution of 100 nm and 300 nm, respectively [134] [7] [60] [135]. This can be done by creating structured illumination pattern with the interference of multiple light sources in the axial direction [69], the lateral direction [7], or both [60], resulting in three-dimensional Moiré pattern. Similar to lateral SIM, multiple images are then acquired with illumination pattern at different phases and orientations, which then reconstructed to form a three-dimensional high-resolution image [58]. These microscopes are much simpler and cheaper than confocal ones. They do not require special fluorescent probes as in PALM or STORM or extreme light intensities as in STED. Moreover, 3D-SIM is readily extensible to multicolor imaging. The drawback to this technique is that it uses a computer reconstruction algorithm that data collection can take a long time, which makes it too slow for live imaging.

1.5 Conclusion

The diffraction limit imposed by a conventional optical microscopy is no longer limiting our imaging tools. Super-resolution imaging techniques have developed based on the ability to control a small subset of fluorophores to fluoresce, while neighbouring fluorophores are forced to be in the non-fluorescent state. This can be achieved either by stochastically imaging or by patterned illumination. Stochastically imaging methods like PALM, STORM, uPAINT etc., are specific to certain types of photoswitchable and photoactivable proteins or dyes. They can improve resolution to tenths of nanometers. The patterned illumination techniques like STED, RESOLFT, etc., need photostable fluorophores and could achieve resolution of about few nanometers by increasing the excitation intensity well above the saturation intensity.

Thus, it is possible to visualize dynamic molecular structures, single molecules and nanostructures with a much higher resolution than the diffraction limit. There are still challenges to be faced to see features at their correct size and to study various nano-metric interactions. Thus, there needs further development in the field of super-resolution microscopy techniques. This PhD work is intended to develop a new super-resolution microscopic technique called ESSat Microscopy to study such dipole-dipole interactions.

Chapter 2

Single Molecules at Low Temperatures

Optical experiments at the single molecule level have grown over the past two decades into a very powerful technique with new and unexpected achievements in different fields of science. Different kinds of spectroscopy and microscopy techniques were employed to detect single molecules in the condensed phase at liquid helium temperature and room temperature. It was the revolutionary actions of Moerner [136] and Orrit [137] that laid the foundation for this research field. With the very rapid adoption by many other researchers, single molecule experiments have evolved to a new frontier in science with high impact in a broad range of disciplines, spanning from physics [138] to biology [139] [140], and including chemistry [141], material sciences [142] [143] and quantum optics [144] [145].

Single molecule detection allows the determination of their fundamental properties, such as their energy levels and transitions [146] [147] [148]. It is also possible to find the symmetry and deformations of molecules by studying the Stark effect in such systems [149] [150]. In addition, several photophysical properties of single molecules like spectral shifts, blinking dynamics, lifetime variations and polarization changes that are extremely sensitive to their local nano-environments could be studied [146] [147].

Single-molecule spectroscopy and microscopy have allowed a reconsideration for long-standing questions in biophysics, biochemistry, and biology [151] [152]. They give to scientists the opportunity to look at and study conformational dynamics and interactions of an individual molecule in biological processes, through the labeling of biomolecules, which cannot be studied on the bulk scale [64]. The motion and action of several types of proteins can be followed at the single protein level. More and more, we are getting closer to following the action of single molecules directly in living cells.

Single molecules were also used as single photon sources for potential applications in quantum cryptography and quantum computation [153] [154]. They were also used as point-like probes in optical microscopy [155] local reporters of position [156] and for observing magnetic resonance transition [157] [158].

Another important role of single molecule is in the development of nanoplasmonics. Plasmonic particles improve the single molecule response and can control the emission characteristics [159] [160] [161]. All these experiments show that the near-field interaction between metallic nanostructures and single emitters is of huge benefit to enhance the detection sensitivity.

Finally, there are several recent research works on the investigation of the nonlinear response of single molecules. Coherent nonlinear interactions between single molecules and light fields with lower intensities down to few photon levels have been reported [162]. This leads to the advent of coherent nonlinear spectroscopy of a single molecule, which allows optical switching with minimal photons and are thus favorable for applications in quantum engineering [163]. Moreover, a nonlinear localization microscopic technique based on Rabi oscillations of single emitters showed superior localization accuracy as well as higher acquisition speed, compared to conventional linear schemes [164].

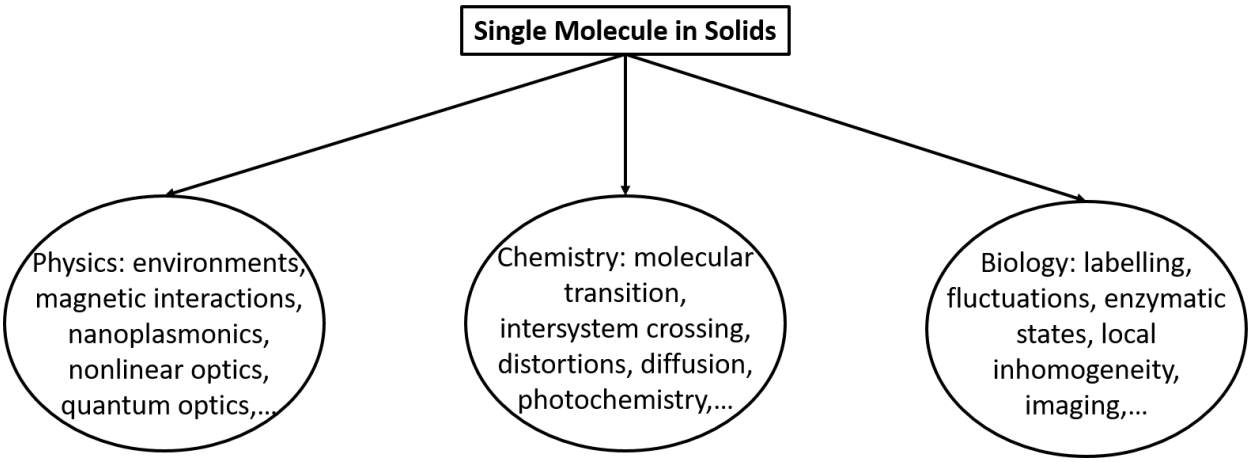

Figure 2.1: Some scientific problems in physics, chemistry, and biology that have explored with single- molecule spectroscopy and microscopy.

This chapter deals with the properties of single molecules embedded in solid at low temperature. The importance of detecting single molecules will be discussed in section 2.1. In section 2.2, I will introduce the energy level scheme of a single molecule in a solid matrix and the important physical principles that allow getting down to the single-molecule level. Later in section 2.3, the methods of single molecule detection are detailed. After that, saturation of single molecule is explained with emphasize on the saturation parameter in section 2.4. This is followed by the different molecular-matrix systems suitable for single molecule detection in section 2.5. Finally, in section 2.6, I will list out the different photophysical phenomena that are relevant to single molecules.

2.1 Introduction

In 1989, W.E Moerner and L. Kador [136] detected single molecules embedded in the condensed phase at liquid helium temperature (T = 2 K) for the first time. They detected single pentacene molecules in a p-terphenyl crystal using a sophisticated frequency double modulation absorption

spectroscopy. Soon after in 1990, M. Orrit and J. Bernard [137] introduced single molecule detection by fluorescence excitation, which offers excellent signal-to-noise ratio. The latter method becomes the standard technique as it is easier to perform and detection of single molecules is straightforward.

Single-molecule experiments completely remove the traditional ensemble averaging over large populations of molecules probed at the same time. This allows studying the individual behavior and fluctuations on a molecule-by-molecule basis, which is completely obscured by conventional measurement techniques: fluctuations in photon counts, photon antibunching, blinking, quantum jumps, spectral jumps, etc. Studies of these fluctuations give us the relevant information about the dynamical processes arising in the condensed phase as well as the distribution of molecule's local environment. Thus, single molecules can be used as nearly point-like reporters of their nano-environment. In this respect, single molecule detection has opened up a qualitatively new field of research.

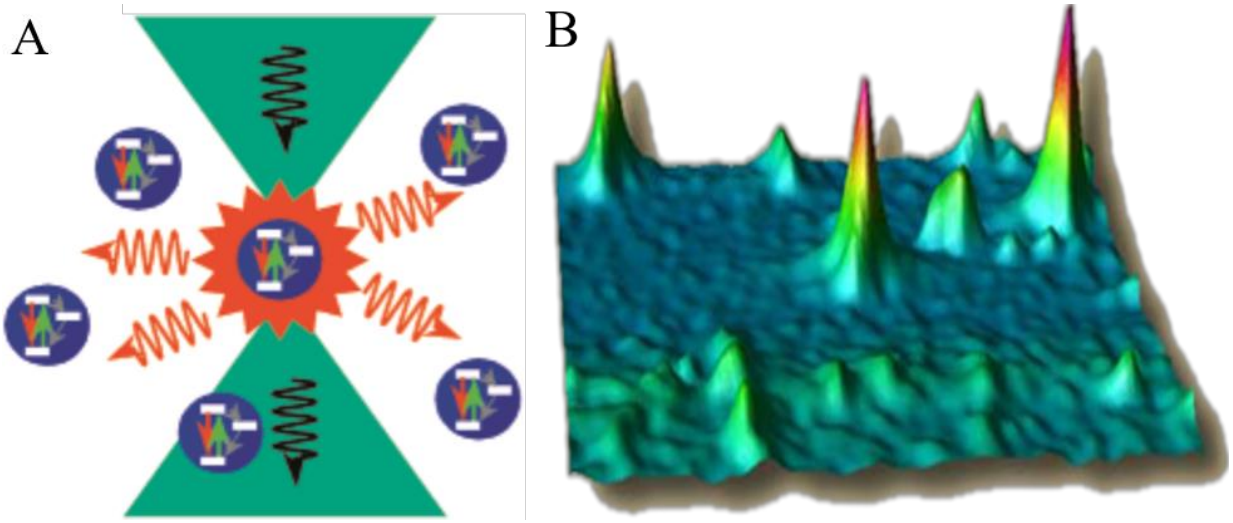

Figure 2.2: (A) Schematic of an optical beam pumping a single resonant molecule, which subsequently removes photons from the excitation beam and emits fluorescence. Figure adapted from [47]. (B) A two-dimensional image of single molecules of pentacene in a p-terphenyl crystal at T= 1.5 K excited with a single mode laser. Figure adapted from [165].

In fluorescence excitation microscopy, a single molecule is probed by exciting the molecule of interest at its resonant wavelength using a laser beam, and the resulting transitions to the vibrational levels of the ground state are detected. The scattered excitation light is blocked by using sharp-edged filters. By scanning the frequency of the excitation laser and recording the number of fluorescence photons emitted, the images of the single molecule can be recorded directly. But molecules are usually hidden deep in a condensed phase solid and they are bathed in the phonon vibrations of the solid. Therefore, molecules interact with the electric, magnetic and the random stress and strain fields of the host matrix. Thus, single-molecules have to be detected from billions to trillions of solvent or host molecules and in the presence of measurement noise. This is possible by exploiting certain optical properties of fluorescent molecules at low temperature, detailed in the next section.

2.2 Physical principles

2.2.1 Jablonsky Diagram

There are two important factors, which facilitate single molecule microscopy and spectroscopy at low temperature, known as inhomogeneous broadening and peak absorption cross-section. To understand these factors, we need to look at the energy level scheme of single molecules embedded in a matrix. Figure 2.3 shows the energy level diagram of a molecule, known as the Jablonsky diagram [166] [167].

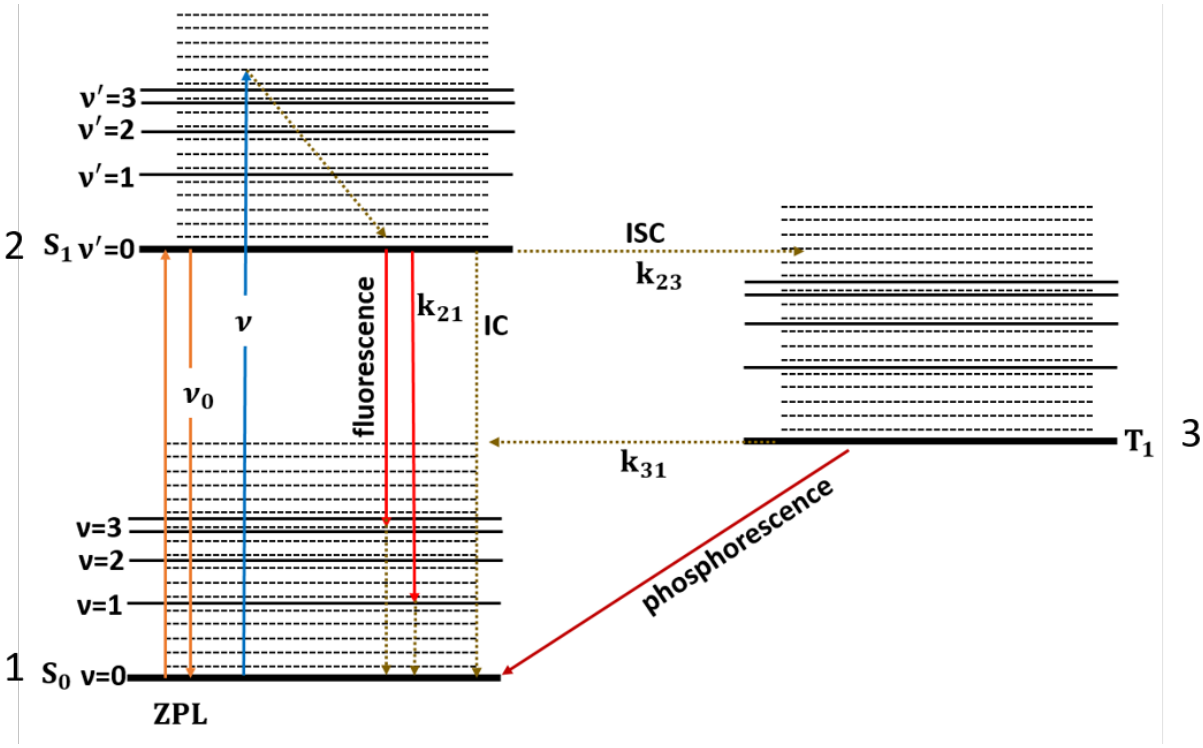

Figure 2.3: Jablonski diagram of a single molecule embedded in a host matrix. The thickest lines indicate the lowest energy levels of each state. The set of ν -lines represent vibrational levels. The thinnest lines denote the phonon states of the host. The radiative transitions are shown with solid lines. Inter-system crossing (ISC) transitions, internal conversion (IC) and vibrational relaxation are shown with dotted lines. ν- frequency of the absorbed laser light, ν_0- frequency of the purely electronic transition (zero-phonon line). k_{21}, k_{23} and k_{31} are the rates of the singlet-singlet, singlet-triplet, and triplet-singlet transitions, respectively.

It is modeled by a three-level system consisting of electronic singlet ground state S_0, first electronic singlet excited state S_1, and the lowest triplet state T_1. Each of these states possesses vibrational levels on top. Since these molecules are embedded in a solid-state matrix, there are no rotational levels. The assumption that the molecule is in the electronic and vibrational ground state prior to laser excitation holds at low temperature, where no other states are thermally populated. Various transitions are possible. Solid arrows indicate the radiative transitions and dashed arrows the non-radiative ones. In the experiments presented in this work, the molecule is excited from the lowest

vibrational level of S_0 to the lowest vibrational level of S_1, i.e. $S_0^{v=0} \rightarrow S_1^{v=0}$. This purely electronic transition is referred as the zero phonon line (ZPL) [47].

The population of lattice vibrations (phonons) have a strong dependence on temperature. At liquid helium temperature, the probability to absorb on electronic transitions without involving phonons is maximal. Dephasing process of the transition dipole due to phonons also vanish, resulting in a sharp and intense zero-phonon-line (ZPL), whose linewidth is given by the excited state's lifetime and is of the order of $\Gamma_{hom} \sim 10^{-3} cm^{-1}$. This linewidth is called the homogeneous linewidth. Thus, the ZPL provides the intrinsic characteristics of an individual impurity molecule.

The excitation lineshape is also composed of vibronic replica and phonon side bands (PSB) [168] which arise from the direct electron-phonon coupling (see Figure 2.4). The phonon sideband is shifted to a higher frequency in absorption and to a lower frequency in fluorescence. The phonon wings at low temperature commonly stretch to ~ 100 cm^{-1}, five orders of magnitude broader than that of ZPL. Thus, PSB will not show up in the typical scan range of a single molecule excitation spectrum. The distribution of the phonon sideband depends on the electron-phonon coupling, and is represented by the Debye-Waller factor (α_{DW}) [169] [170]. The Debye-Waller factor is a measure of the relative intensity distribution of the zero-phonon line and the phonon sideband, and is written as,

$$\alpha_{DW} = \frac{I_{ZPL}}{I_{ZPL} + I_{PSB}}. \tag{2.1}$$

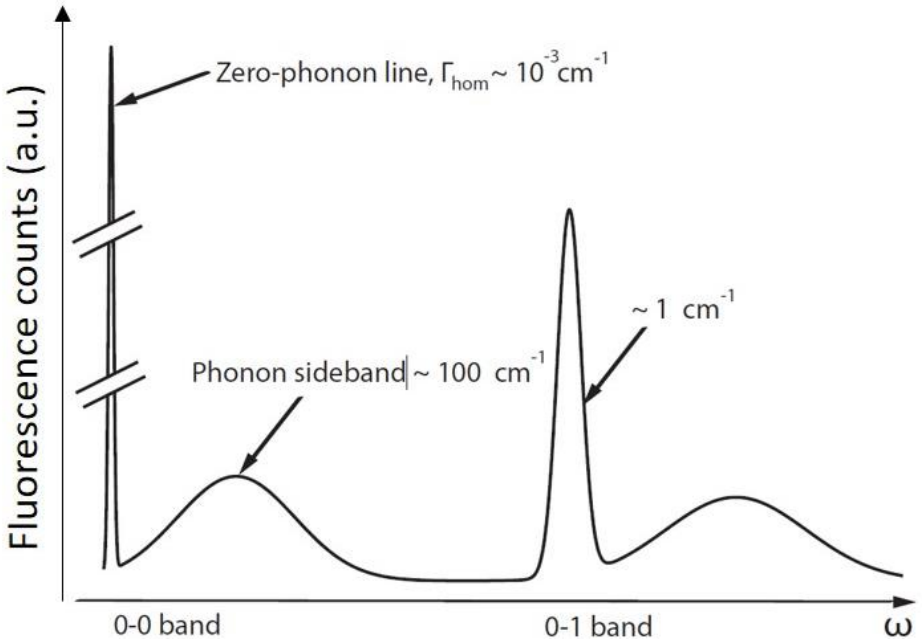

Figure 2.4: Schematic absorption spectrum of a single molecule at low temperature showing zero phonon line (ZPL) and one vibronic band.

The temperature and the properties of the molecular-matrix system determine the value of the Debye-Waller factor. It decreases exponentially with temperature and achieves its maximum value at $T \leq 2$ K, of the order of 0.25 for aromatic molecules in molecular crystals.

The internal vibration contribution results in another factor called the Franck-Condon factor (α_{FC}) [171] [172] [173]. It is the nuclear term determined by the intermolecular properties, and it expresses the transition probabilities between vibrational levels of two electronic system. It implies that any transition from the ground state to the excited state undergoes no momentum transfer, i.e. the normalized molecular coordinate is not changed, and the transition proceeds vertically.

For rigid molecules, the geometry change in the molecular system is small between the ground state and the excited state, and so the Debye-Waller factor and the Franck-Condon factor are maximized.

Other optical transitions exist from the lowest vibrational level of S_0 to the higher vibration levels of S_1, i.e. $S_0^{v=0} \rightarrow S_1^{v\neq 0}$. The vibronic levels $S_1^{v\neq 0}$ have a very short lifetime in the picosecond timescale. Therefore, a rapid non-radiative relaxation brings the molecule into the lowest vibrational level of S_1, from which it will decay radiatively back to S_0. The linewidth of a vibronic transition is typically of the order of $1\ \mathrm{cm}^{-1}$, three orders of magnitude broader than that of the zero-phonon line.

There are three decay channels from the vibrational ground state of the first electronically excited singlet state S_1. The molecule can decay back to the $S_0^{v=0}$ by emitting a photon with the same energy as the absorbed photon, called the "resonance fluorescence". Alternatively, decay via the very short-lived ($\tau \approx$ ps) vibrational levels to the higher vibrational level of S_0, by the emission of a red-shifted photon, is called the "Stokes-shifted fluorescence". Further relaxation from this level to the vibrational (and electronic) ground state releases further energy from the molecule, which usually emitted as heat or phonons. The third way of decay is by the non-radiative transition to the triplet state T_1 via intersystem crossing (ISC) with a probability of about 10^{-6} (this will vary from system to system). This transition is accompanied by a change of spin of the promoted electron and referred to as the intersystem crossing (ISC). The change of spin is quantum mechanically forbidden in the electric dipole approximation [174]. Nevertheless, there is always a weak interaction of the wave functions of different multiplicities making a transition between singlet and triplet possible. This effect called spin-orbit coupling is weak in hydrocarbons. Therefore, the triplet state has a relatively long lifetime ranging from micro to milliseconds. Radiative relaxation from T_1 to S_0, called phosphorescence, is also weakly allowed. Thus, the molecule can be considered as "dark" for the time it is in the triplet state. Suitable candidates for single molecule spectroscopy and microscopy, therefore, must fulfill the requirement that k_{23}/k_{21} and k_{23}/k_{31} are small. For instance, for the terrylene molecule in p-terphenyl crystal, typically $k_{23}/k_{21} = 10^{-6}$ and $k_{23}/k_{31} = 0.27$ [149]. In the present work, triplet transitions are not relevant in the description of the optical properties of single molecules and therefore neglected in all upcoming descriptions.

2.2.2 Inhomogeneous Broadening

At liquid helium temperatures, dephasing of the transition dipole owing to the phonons is drastically reduced. Thus homogeneous width of the ZPL approaches the lifetime-limited value of

some tens of MHz [175]. The quality factor of such a narrow transition is very large, nearly 10^8. This extremely high-quality factor of single-molecule lines in solids leads to exquisite sensitivity to nanoscopic changes in the molecular environment [176] [177]. Thus, a small defect in the matrix environment or other inhomogeneities such as stress, dislocations, point defects or statistically varying electric fields modifies the energy required for an electronic transition in each molecule, producing a detectable shift of their resonance frequency, even if the molecules are chemically the same. The resulting distribution of this homogeneously broadened absorption lines is called inhomogeneous broadening [149]. This situation is depicted schematically in Figure 2.5. Because of the collective, statistical nature of the molecules, the inhomogeneous broadening has a Gaussian shape. It may amount to FWHM of $\nu_{\mathrm{inhom}} \approx 10^2 - 10^3\ \mathrm{cm}^{-1}$ $(3 - 30\ \mathrm{THz})$ in disordered solids like glassy solutions or polymers, and only a fraction of a wavenumber (less than 1 GHz), for unstressed sublimated crystals, where all impurities have very similar environments [178]. Several combinations of molecules and host materials are known in which single molecule lines can be observed [179] [148].

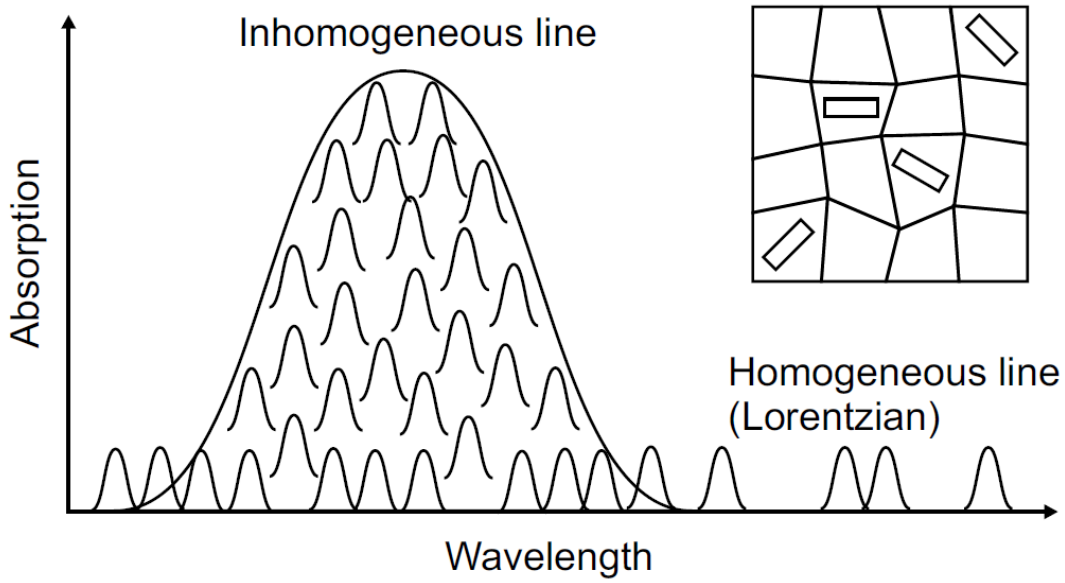

Figure 2.5: Schematic representation of an inhomogeneously broadened absorption band of dopant molecules in a solid at low temperatures. The inhomogeneous band is composed of the contributions of homogeneously broadened absorption lines of all molecules. The distribution of center resonance frequencies caused by random strains and imperfections in the solid as shown in the upper right corner. Figure adapted from [180].

The ZPL Lorentzian lineshape for a single molecule fluorescence excitation can be written as [181]:

$$\mathrm{I}(\nu) = \mathrm{I}(\nu_0)\frac{{\Delta\nu_{\mathrm{hom}}}^2/4}{(\nu - \nu_0)^2 + \left(\frac{\Delta\nu_{\mathrm{hom}}}{2}\right)^2}, \tag{2.2}$$

where $I(\nu)$ is the radiation intensity at ν, $I(\nu_0)$ is the maximum intensity which corresponds to the intensity at the resonance frequency (ν_0) and $\Delta\nu_{hom}$ denotes the full width at half maximum (FWHM) of the homogeneously broadened Lorentzian lineshape. Figure 2.6 shows the fluorescence excitation spectrum of terrylene molecules in a p-terphenyl single crystal at 1.8 K. The spectrum shows many distinct Lorentzian spectra, each of them representing single molecules.

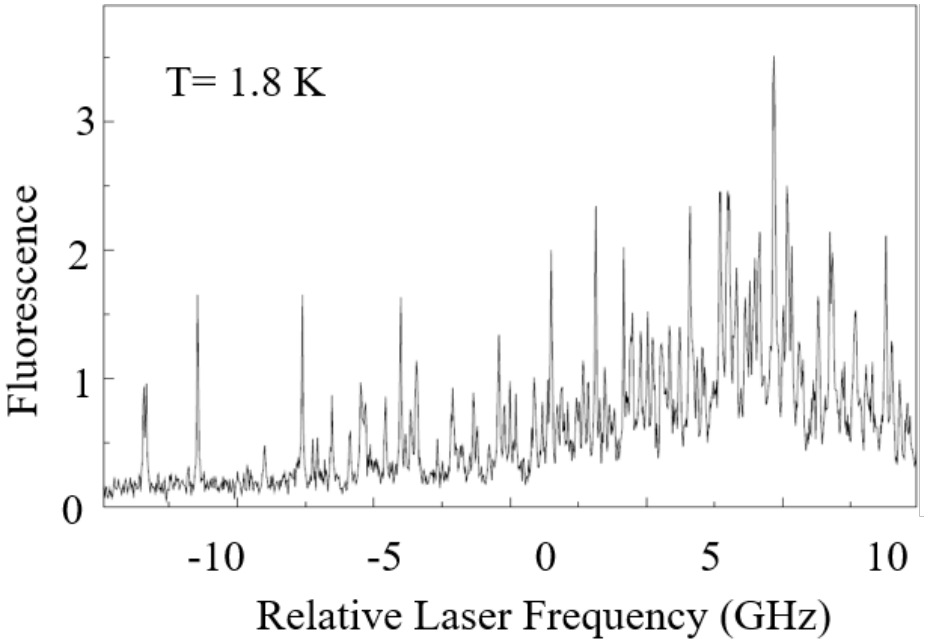

Figure 2.6: Fluorescence excitation spectrum at 1.8 K of terrylene in a p-terphenyl single crystal in the spectral region of site X_2 (~ 578.5 nm). The narrow features are the excitation lines of single terrylene molecules. Figure adapted from [149].

All processes that lead to a broadening of a single emitter define the homogeneous linewidth. To determine the homogeneous broadening in the frequency domain, we correlate the linewidth of the transition to the lifetime of the upper state:

$$\Delta\nu_{hom} = \frac{1}{\pi T_2} = \frac{1}{2\pi T_1} + \frac{1}{\pi T_2^*}. \tag{2.3}$$

Here T_1 represents the decay time of the excited state (fluorescence lifetime), T_2 the total dephasing time of the optical transition and T_2^* the pure dephasing time. T_1 is essentially independent on temperature while T_2^* shows a strong dependence on temperature. The actual value of T_2^* at a given temperature depends on the excitation of low-frequency phonons that couple to the electronic transitions of the dye molecule. At low temperature ($T \leq 2K$) and in crystalline matrices, T_2^* approaches infinity and does not contribute to the linewidth, as host phonons and local modes are mostly quenched. Thus, the linewidth is solely determined by the lifetime of the excited state and is called the natural linewidth $\Delta\nu_{nat}$.

$$\Delta\nu_{nat} = \frac{1}{\pi T_2} = \frac{1}{2\pi T_1}. \tag{2.4}$$

This is the fundamental lower band for the linewidth and can be as narrow as few tens of MHz.

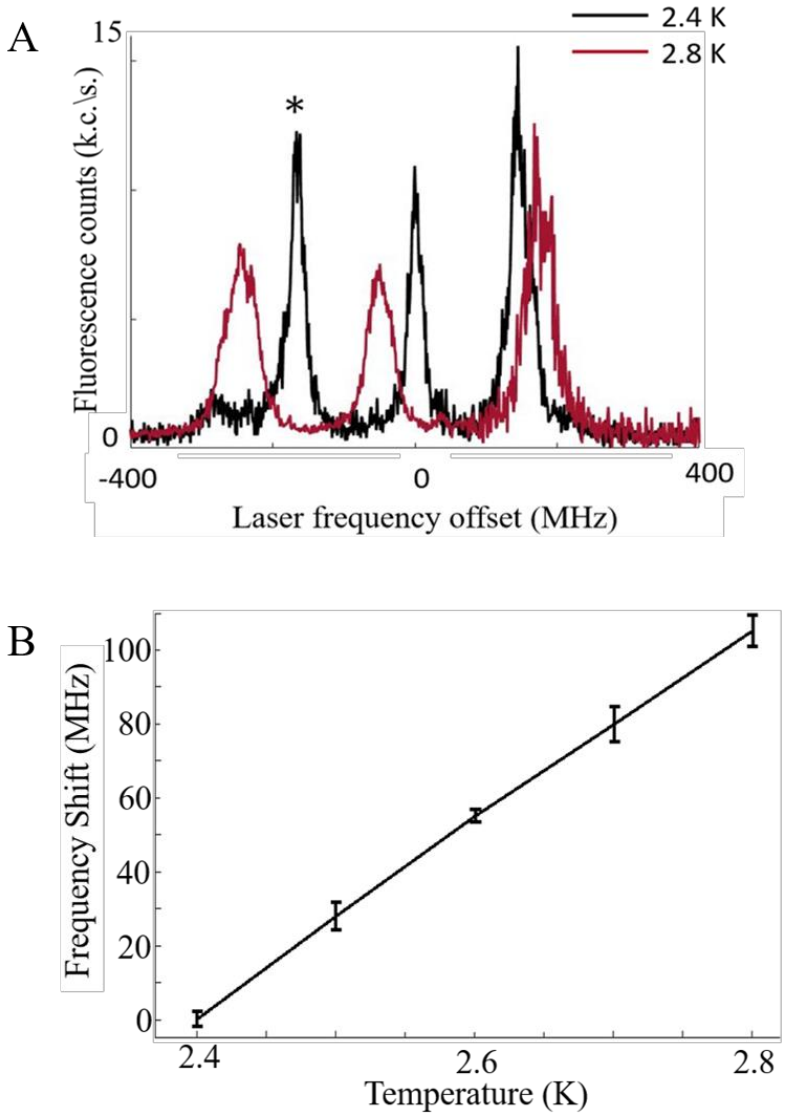

Figure 2.7: Experimentally obtained temperature dependence of three different DBATT molecule in an octadecane host matrix. (A) The fluorescence excitation spectrum for two different temperatures, 2.4 K (black curve) and 2.8 K (red curve). With 0.4 K change in the temperature, we can see the broadening of the linewidth as well as a very noticeable frequency shift between the lines. Two molecules are blue shifted, and one is red shifted with increasing temperature. (B) Dependence of the frequency shift with respect to temperature for a single molecule. The molecule (marked by * in A) shows a shift of $\sim$ 105 MHz with 0.4 K temperature rise. Excitation intensity: 110 $\mathrm{W/cm^2}$.

An increase in temperature activates phonon modes of the matrix and the low frequency molecular vibrations and thus strongly affects T_2^*. This leads to a broadening and a frequency shift of the homogeneous absorption line. From Figure 2.7, the dramatic broadening of the linewidth of single DBATT molecules in octadecane host matrix is clearly visible, when the temperature raised from

2.4 K to 2.8 K. The maximum signal from the molecule also decreases correspondingly. The temperature dependence study of the optical linewidth and frequency shift of individual molecules [182] [183], shows that the increase in linewidth is exponentially activated with temperature. With regard to the frequency shift, we have observed molecules shifting to lower frequency as well as molecules shifting to higher frequencies.

2.2.3 Peak absorption cross-section

A central role in single molecule experiments in solids is played by the peak absorption cross-section of the guest molecule on the ZPL [183]. It explains the huge signal of single molecules above the background. It is defined as the effective area of a homogeneous incoming beam from which the molecule will absorb every photon. In the limit of low laser intensities, the absorption cross-section at resonance σ of the zero-phonon line of single molecules in a solid can be written as,

$$\sigma = \alpha_{FC}\alpha_{DW}\frac{3\lambda^2}{2\pi}\frac{T_2}{2T_{1,rad}}\cos^2\theta, \tag{2.5}$$

where λ is the wavelength and $T_{1,rad}$ the radiative lifetime of the excited state. α_{FC} and α_{DW} are Franck-Condon and the Debye-Waller factors. The $\cos^2\theta$ factor takes into account the angle θ between the transition dipole moment and the laser-field polarization.

The peak absorption cross section has an inverse dependence on ν_{hom}, so that the narrow linewidth of a ZPL translates into a very large peak absorption cross section. For allowed transitions of rigid molecules, the value of σ becomes extremely large, approaching the ultimate limit of $3\lambda^2/2\pi$. Taking the value of Debye-Waller factor as 0.1 for DBATT molecule, we get the absorption cross-section at low temperature as 1.6×10^{-10} cm^2 at λ = 589 nm. Therefore, typical values of the absorption cross-section of a single molecule at 2 K are at the order of 10^{-10} cm^2. They are about 10^6 times larger than the absorption cross-section of dye molecules at room temperature, which is about 10^{-16} cm^2. Moreover, they are four orders of magnitude larger than the physical area of the single molecule. Thus, even though any dimension of a single molecule is much smaller than the optical wavelength, the effective area of the molecule for optical absorption is huge, almost as high as the squared wavelength of light.

2.3 Single Molecule Detection

Detecting single molecules requires methods that are both sensitive and selective. The method used must effectively detect the single molecule of interest while eliminating all background sources. By exploiting the inhomogeneous broadening and peak absorption cross-section at low temperature, we can quickly detect single molecules from the collection of millions of host molecules and other impurity molecules in the sample. Either one of the two methods or their combination can achieve this. The two approaches include spatial selection and spectral selection.

In both cases, the fluorescence from a single molecule can usually be detected with a signal-to-noise ratio limited by shot noise.

- Spatial selection: The sample is diluted such that the number of molecules is reduced in the observation space to about 10^{-9} mol/L, so that single molecules can be addressed by confocal fluorescence microscopy. The laser beam is focused into a diffraction-limited spot to facilitate the spatial selection of single molecules.
- Spectral selection: At liquid helium temperatures, the entire sample spectrum consists of single absorber lines which are about $10^3 - 10^4$ times narrower than the whole spectrum (depending on the molecule-matrix system). Individual molecules in the sample can then be selectively excited by the use of a single-mode tunable laser (with a line much narrower than the molecular linewidth). By scanning over the wings of the inhomogeneously broadened line, we can spectrally select single molecules with much ease. However, some form of spatial selection should be employed to reduce the probability that more than one molecule will be in resonance with the laser.

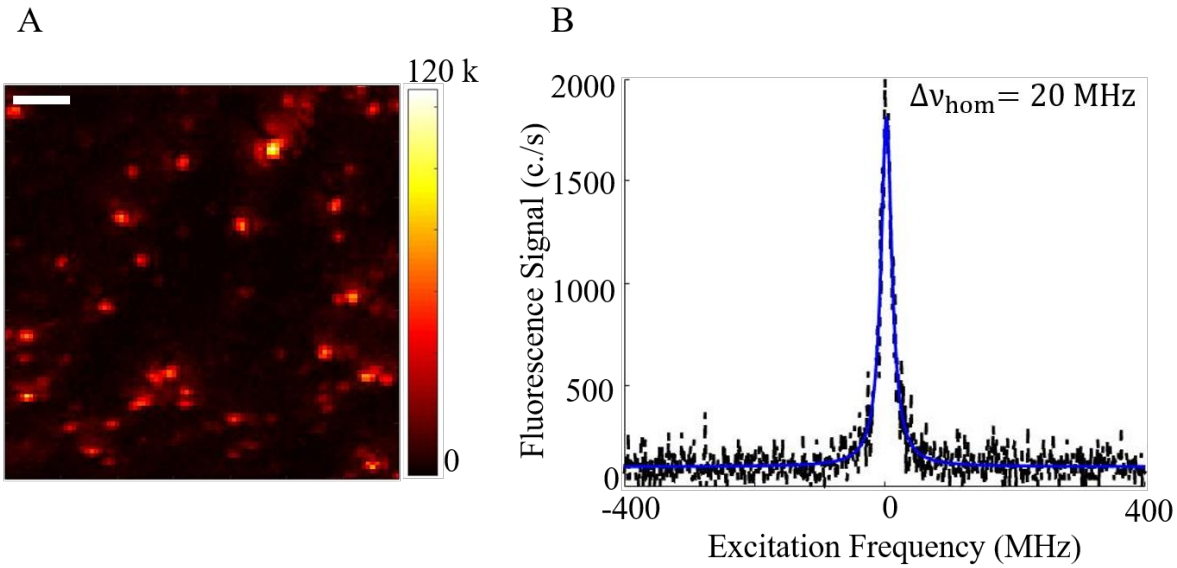

Figure 2.8: (A) Confocal fluorescence microscopy raster scan of single DBATT molecules in an octadecane matrix at T= 2 K, recorded for an excitation intensity, I = 50 W/cm^2. Scale bar: 2 µm. (B) Fluorescence excitation spectrum of single DBATT molecule in an octadecane matrix at 2 K with a lifetime limited linewidth. T= 2K. Excitation Intensity = 2 W/cm^2.

2.4 Optical saturation of single molecules

Under low excitation intensities, the number of photons absorbed by a molecule varies linearly with the excitation intensity. When the excitation intensity is increased, the molecular signal will saturate gradually. Once the molecule is fully saturated, it will not absorb more photons with the further increase in the excitation intensity. The signal from the molecule thus changes nonlinearly with the intensity. The intensity at which the signal is half of the fully saturated signal is called the

saturation intensity. It depends on the molecule as well as its orientation in the matrix. Thus, saturation data provide valuable information on the three-dimensional orientation of the transition dipole moment of a single molecule [184].

The analytical expression describing the population and coherence dynamics of a single molecule can be obtained by solving optical Bloch equations [185] [186]. For a single molecule at low temperature, three electronic states are relevant: the ground singlet state S_0, the excited singlet state S_1, and the first triplet state T_1. The non-radiative transitions between the vibrational sub-levels of the electronic states are very fast. Therefore, we are allowed to replace the vibrational multiplicities of the ground singlet state by their lowest levels. Triplet state will not be considered, since ISC can be neglected for well-chosen molecules. Accordingly, we have the density matrix, ρ for our two-level system as,

$$\rho = \begin{bmatrix} \rho_{11} & \rho_{12} \\ \rho_{21} & \rho_{22} \end{bmatrix}, \tag{2.6}$$

where ρ_{11} is the ground state population, ρ_{22} is the excited state population, and ρ_{12} and ρ_{21} describe the molecular coherence related to the dipole. In the rotating frame, the time evolution of the matrix elements for a two level system will turn from the optical Bloch equations as:

$$\begin{aligned} \frac{d\rho_{11}}{dt} &= \Gamma\rho_{22} + \frac{1}{2}i\Omega(\rho_{21-}\rho_{12}), \\ \frac{d\rho_{22}}{dt} &= -\Gamma\rho_{22} - \frac{1}{2}i\Omega(\rho_{21-}\rho_{12}), \\ \frac{d\rho_{12}}{dt} &= \frac{1}{2}i\Omega(\rho_{22-}\rho_{11}) - \left(i\delta + \frac{\Gamma}{2}\right)\rho_{12}, \\ \frac{d\rho_{21}}{dt} &= -\frac{1}{2}i\Omega(\rho_{22-}\rho_{11}) - \left(i\delta + \frac{\Gamma}{2}\right)\rho_{21}, \end{aligned} \tag{2.7}$$

where Ω is the Rabi frequency, $\hbar\Omega = |\mu_{12}.E_0|$, μ_{12} is the transition dipole moment of the molecule, E_0 is the electric field at the position of the dipole emitter, $\Gamma = 1/2\pi T_1$ is the radiative decay rate and δ is the laser's detuning with respect to the molecule's resonance, $\delta = \omega - \omega_0$, where ω is the laser frequency, and ω_0 is the resonance transition frequency of the molecule. In the limit $t \gg 1/\Gamma$ the populations reach their steady-state values, where, $\dot{\rho_{11}} = \dot{\rho_{22}} = 0$. The steady-state solution of the Bloch equation gives us the population of the excited state:

$$\rho_{22} = \frac{\frac{|\Omega|^2}{4}}{\delta^2 + \frac{|\Omega|^2}{2} + \frac{\Gamma^2}{4}} = \frac{1}{2}\,\frac{s}{1+s}, \tag{2.8}$$

where

$$s = \frac{\frac{|\Omega|^2}{2}}{\delta^2 + \frac{\Gamma^2}{4}}, \tag{2.9}$$

is the saturation parameter. Thus the excited state population is at most $1/2$, which is approached in the saturation limit ($s \gg 1$). From the Equation (2.9), we can write the on-resonance saturation parameter as,

$$s_0 = s(\delta = 0) = 2\frac{|\Omega|^2}{\Gamma^2} = \frac{I}{I_S}. \tag{2.10}$$

Considering $I = c\varepsilon_0 E_0^2/2$, as the intensity of the excitation laser and the expression for the radiative decay rate in vacuum,

$$\Gamma = \frac{{\omega_0}^3 {\mu_{12}}^2}{3\pi\varepsilon_0\hbar c^3}, \tag{2.11}$$

one finds,

$$I_S = \frac{h\nu}{2\sigma(0)T_1}, \tag{2.12}$$

is the saturation intensity, $I = c\varepsilon_0 E_0^2/2$ is the intensity of the excitation laser, and $\sigma(0)$ is the cross-section at low light intensity. The dependence of the absorption cross-section on the excitation intensity of the molecule is given by:

$$\sigma(I) = \frac{\sigma(0)}{1 + I/I_S}. \tag{2.13}$$

The steady state solution for the intensity of the red-shifted fluorescence shows a Lorentzian shaped resonance line with a maximum intensity

$$R(I) = R_\infty \frac{I/I_S}{1 + I/I_S} \tag{2.14}$$

and the full width at half maximum

$$\Delta\nu_{hom}(I) = \Delta\nu_{hom}(0)\sqrt{1 + I/I_S}. \tag{2.15}$$

We have experimentally studied the optical saturation of single molecules. Figure 2.9 shows the nonlinear fluorescence saturation of a DBATT molecule embedded in an octadecane matrix. Fluorescence excitation spectra for different excitation intensities ranging between 0.01 kW/cm^2 to 1.28 kW/cm^2 are plotted. The increase in the linewidth, as well as the saturation of the signal, is visible with an increase in the excitation intensity. The saturation intensity of different single molecules at low temperature is usually between 1 W/cm^2 and 5 W/cm^2, and the homogeneous linewidth is in the range of 20-50 MHz. The variation in the homogeneous linewidth is due to their local nano-environment, which is specific for each molecule and reflects residual spectral diffusion or dephasing processes. The saturation intensity strongly depends on the molecular orientation with respect to the laser polarization. It is typically 10^5 times lower at 2K than that obtained at room temperature.

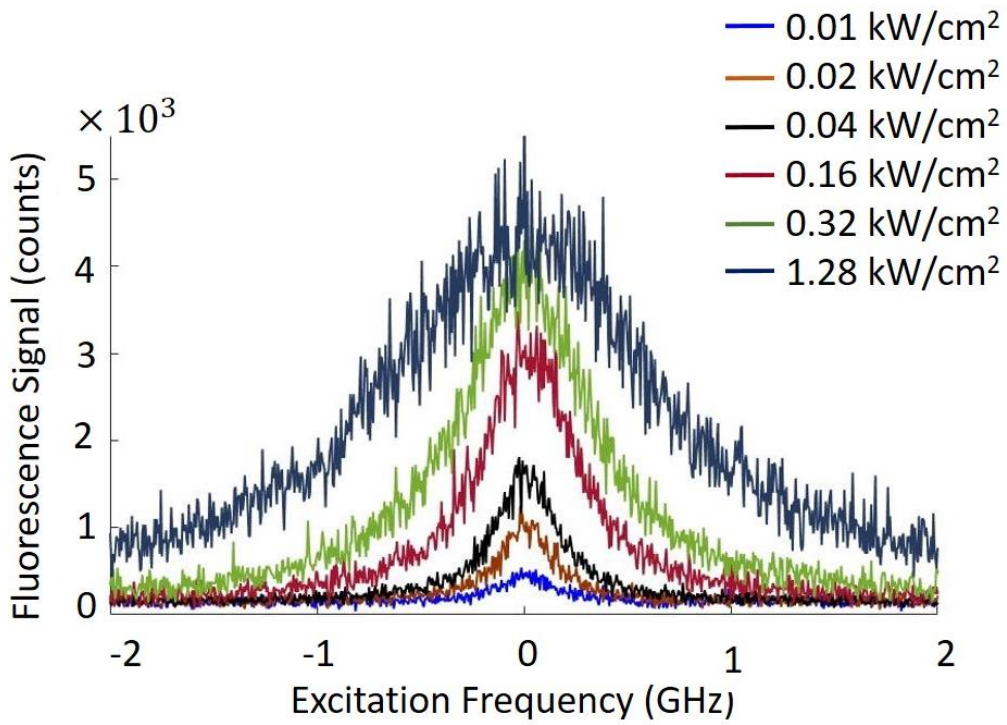

Figure 2.9: Fluorescence excitation spectra of single DBATT molecules in an octadecane matrix at 2 K for different excitation intensities varying from 0.01kW/cm^2 to 1.28 kW/cm^2. The nonlinear saturation of the signal and the broadening of the linewidth is clearly visible from the spectra.

Figure 2.10 (A) shows the experimental evolution of the full width at half maximum of a DBATT molecule in an octadecane matrix with the excitation intensity. Blue circles indicate the data points. The solid black line shows the fit of the experimental data points with Equation 2.15, yielding the homogeneous linewidth, $\Delta\nu_{hom}(0) = 25$ MHz and the saturation intensity, $I_S = 120$ W/cm^2. Figure 2.10 (B) shows the evolution of the fluorescence signal of the same molecules as a function of the excitation intensity. Fitting with Equation 2.14 yields the same saturation intensity as before. This high saturation intensity is due to the dipole orientation of the molecule.

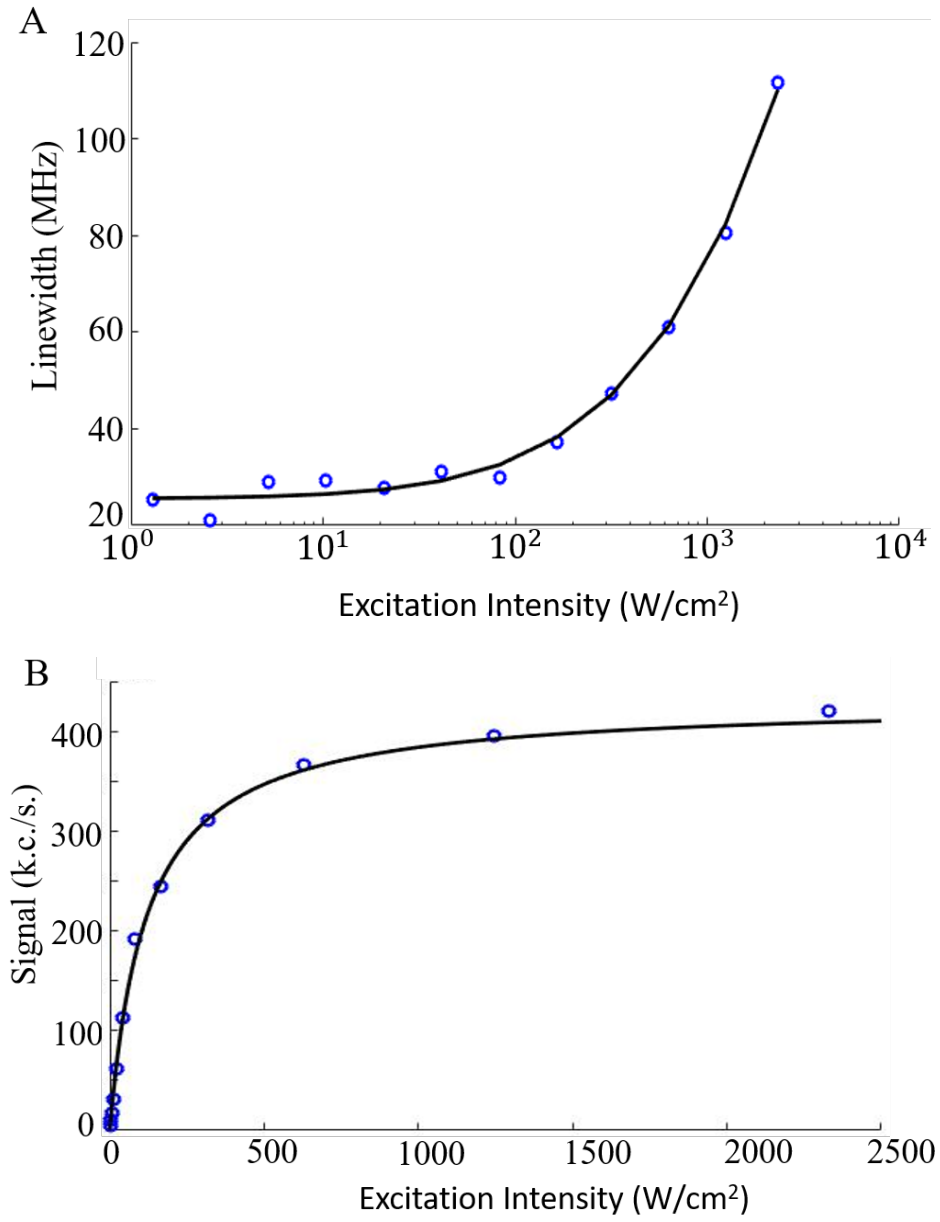

Figure 2.10: Experimental data showing the nonlinear optical saturation of a single molecule fluorescence at 2 K. (A) Broadening of the linewidth with excitation intensity. (B) Saturation of the fluorescence signal with excitation intensity. The circles indicate the experimental data and the solid lines show the fits with Equation 2.15 (A) and 2.14 (B).

2.5 Molecule-matrix systems

Another essential requirement for single molecule spectroscopy is the selection of appropriate guest-host systems [179] [148]. The most common guest impurity molecules are from the class of rigid conjugated hydrocarbons like pentacene, perylene, terrylene, tetra-butyl-terrylene, diphenyloctatetraene, dibenzoterrylene and dibenzanthanthrene (DBATT). Figure 2.11 shows

their chemical structures. These molecules have strongly allowed singlet-singlet transitions and excellent emission properties, i.e. a quantum efficiency approaching unity. Moreover, because of their rigid, planar aromatic structure, they have reduced intersystem crossing rates and large triplet decay rates, which minimizes the triplet bottleneck. Triplet bottleneck results in premature saturation of the emission rate from the molecule and reduction of the absorption cross-section. Such aromatic molecules also feature the weak Franck-Condon distortion required to guarantee a strong electronic transition. Also, the large aromatic hydrocarbons (except 'e' and 'f') place the lowest electronic transition in the mid-visible.

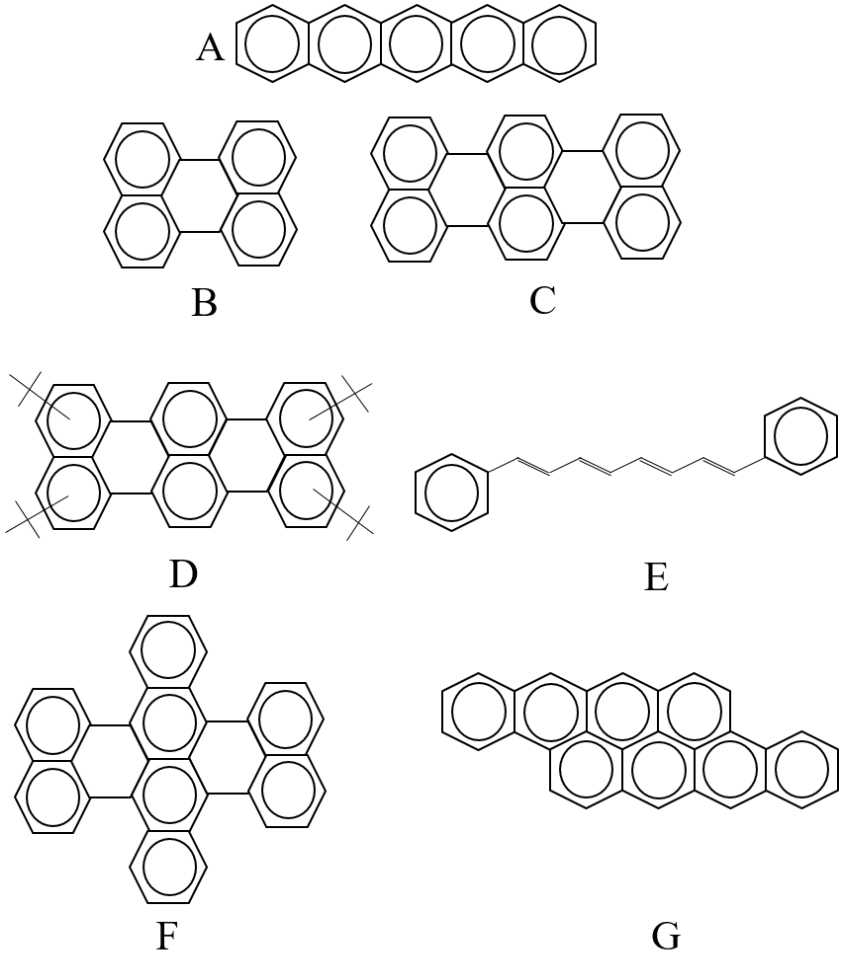

Figure 2.11: Structures of some of the molecules that have been studied by single-molecule experiments. (A) Pentacene, (B) perylene, (C) terrylene, (D) tetra-t-butyl-terrylene, (E) diphenyloctatetraene, (F) dibenzoterrylene and (G) dibenzanthanthrene (DBATT).

The host material is decided by the need to maintain a weak electron-phonon coupling, an excellent photostability for the fluorescent molecule as well as a weak spectral hole burning. In addition, it should be unaffected by the excitation and emission wavelength of the impurity molecule under study. The host matrix suitable for a particle molecule may not fit for others. Single crystals are often stable matrices, as they have a regular well-defined structure. Therefore, impurity molecules in such crystals all have a very similar local environment of matrix molecules. On the contrary,

polymers have a very irregular structure. This leads to variations in the local environment of the guest molecules and in this case, the interaction strength between the molecules and their local environment is spread. The most commonly used alkane host matrices include hexadecane, octadecane, nonane, and tetradecane. They yield relatively stable single-molecule spectra, with a slow, light-driven spectral shifting in several cases.

2.6 Photophysical features of single molecules

There are different single molecule signatures, which do not have a counterpart on large ensembles. These effects give us the verification of single molecule detection. Such effects can be investigated by studying the interaction between single quantum systems and coherent light. In this section, we will see some of such peculiarities shown by single molecules.

2.6.1 Blinking

One of the first effects reported when single fluorophores were studied was the emission of fluorescence in bursts rather than continuously [187] [188]. This blinking is almost invariably observed [189] in all kinds of fluorophores including fluorescent proteins [190] and under diverse environmental conditions and has, therefore, become one of the assurances of single-molecule observation. The blinking is attributed to temporal transitions of the molecule to non-fluorescent dark states and has been examined regarding the on and off time histograms as well as by correlation analysis of the fluorescence emission. These studies have shown that transitions to and from dark states occur on a large range of timescales, i.e. from microseconds up to minutes [190]. Depending on the nature of these non-fluorescent states, several mechanisms have been proposed and have been supported by experimental evidence.

One of the most obvious dark states is the triplet state T_1, which is populated through intersystem crossing [191]. If the dark state lasts for more than 100 ms, it cannot be explained with regard to triplet formation, but is claimed to be due to intermolecular energy transfer or to photochemical changes like photo-induced isomerization [192], conformational changes or reversible oxidation [193]. These processes may also be responsible for spectral diffusion [194] and spectral jumps [195] that are frequently observed in single-molecule fluorescence experiments.

2.6.2 Spectral Diffusion

Spectral diffusion is the time-dependent fluctuation in spectral features of a single molecule that shifts its center resonance frequency [165]. This is due to the configurational changes in the local environment, which affect the electronic transition frequency through the molecule-matrix coupling. A theoretical study of the spectral diffusion trajectories postulated specific defects that can produce this behavior [196] [197], confirming the relevance of single molecule experiments for probing the local nano-environment. Spectral shifts are observed for all type of hosts including crystalline, polymers and polycrystalline Shpol'skii matrices.

2.6.3 Photobleaching

Photobleaching is the light-induced destruction of fluorophores, which is a serious problem while imaging samples for long duration or when high powers are required. It leads to an abrupt and irreversible termination of the fluorescence emission from a single molecule. One step-photobleaching is a peculiar property of single molecules, because, if there were more than one molecule, a gradual reduction in the signal would be expected as individual molecules bleached away. There is zero photobleaching for single molecules at 2K. Although the mechanism of photobleaching is not entirely understood, it is thought that it involves electronic transitions to triplet states because triplet states have longer lifetimes and are more reactive. Another assumption is that it is due to photo-oxidation by highly reactive singlet ($^1\Delta_g$) oxygen [198]. To prevent reactions with oxygen, anti-photobleaching agents can be introduced to reduce the amount of oxygen in the sample. However, many of these are toxic to live cells.

2.6.4 Photon antibunching

Photon antibunching is a phenomenon arising from the fact that one fluorophore emits only one photon at a time [199]. For a single molecule system, the detection of a photon emitted projects the molecule in the ground state. The molecule needs to be re-excited before a second photon can be detected. Thus, there is a finite time delay between photon emissions. This characteristic property of single photon source is called photon antibunching.

Since the probability of detecting two photons simultaneously is lower than the probability of detecting them at different times, the second order correlation function [200] defined by

$$g^{(2)}(\tau) = \frac{\langle I(t)I(t+\tau)\rangle}{\langle I(t)\rangle^2}, \tag{2.16}$$

follows the inequality:

$$g^{(2)}(0) < g^{(2)}(\tau). \tag{2.17}$$

Furthermore, for the case of a beam consisting of individual photons stemming from a single molecule, there will be a no-event observation at $\tau = 0$. This leads to the non-classical result of $g^{(2)}(\tau) = 0$. In the case of a source formed by a pair of single-photon emitters, the value of $g^{(2)}(0)$ becomes 0.5 [201]. Thus, an antibunching dip $g^{(2)}(0) < 0.5$ is a conclusive signature of the quantum nature of light arising from a single emitter. In practice, $g^{(2)}(0)$ does not reach zero due to stochastic (poissonian) noise.

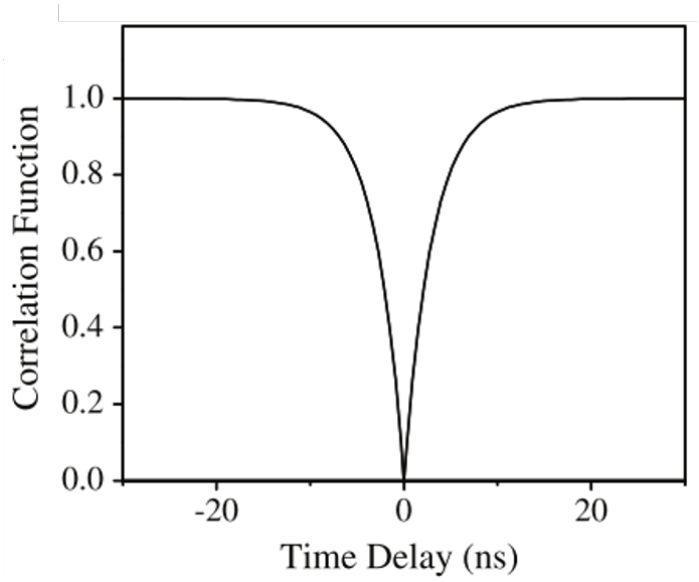

Figure 2.12: $g^{(2)}$ function for a single-photon source under continuous excitation. The graph shows a dip with a zero value at zero time delay, which is a clear signature of photon antibunching. A Hanbury-Brown and Twiss interferometer is used to build the correlation function. Figure adapted from [202].

2.7 Conclusions

There is a six orders of magnitude higher absorption cross-section for single molecules at low temperature when compared to that of room temperature. Moreover, the intersystem crossing rate and the electron-phonon coupling are very low. Thus, experiments at liquid helium temperature (2K) allow working with extremely sharp and intense zero-phonon-lines. The zero dephasing due to phonon vibrations provides coherence of the dipole moments and the ability to reveal truly quantum mechanical effects and probe local fluctuations in the molecular nano-environment. Together with the observation of discrete quantum jumps and discrete blinking, the detection of single photon emitters is tightly connected to the field of quantum optics.

The nonlinear properties of single molecule fluorescence signals, together with reduced saturation intensities at low temperature could be exploited to develop new super-resolution microscopy methods, with much lower power requirement than room temperature techniques like STED. The ability to resolve several molecules separated by tens of nanometers at liquid helium temperature would also open up thorough studies of the coherent dipole-dipole interaction.

Chapter 3

Two-Dimensional Excited State Saturation (ESSat) Microscopy

In Chapter 1, we have seen different super-resolution imaging techniques that have been developed in various labs. All those techniques have their own advantages and can accomplish the specific needs they are intended for. Most of them have applications in imaging biological cells and are aimed to get better and better resolution. Resolution of about 20-30 nm in the lateral direction and about 50-60 nm in the axial direction is now routinely achievable with those techniques.

The motivation for this Ph.D. work is to study the coherent coupling between two molecular dipole moments associated with optical transitions. In 2002, Sandoghdar [17] observed this by performing cryogenic single molecule spectroscopy under a scanning probe electrode. They found two identical molecules separated by 9 ± 2 nm and with close resonances. Besides the original resonances of the individual molecules, a third resonance shows up at high intensities in the midway between them, as an evidence for the two-photon excitation of a coupled two-molecule system and thus the dipole-dipole coupling between them. However, this experiment was not a reproducible approach to study quantitatively the coupling interaction between single molecules.

We develop a new super-resolution imaging technique, called Excited State Saturation (ESSat) Microscopy, to overcome this problem. ESSat is a cryogenic super-resolution imaging technique with a patterned illumination approach, which exploits the nonlinearity of the fluorescence signal excited on the zero-phonon-line. It also takes advantage of the high absorption cross-section of single molecules at low temperatures (2K) and their high photostability.

This chapter is devoted to the ESSat microscopy in two dimensions. We will describe the working principle of direct-ESSat Microscopy and the theoretical resolution achievable in Section 3.1. The effect of high numerical aperture of the objective is discussed in Section 3.2. In section 3.3, a different approach of ESSat Microscopy called the modulated-ESSat microscopy is explained. The experimental details, including the sample, cryostat, vortex phase mask, scanning system and the optical setup are discussed in Section 3.4. The effects of aberrations and their corrections employed in the experiment are then described in Section 3.5. Later in section 3.6, I will show the results

obtained with ESSat microscopy in the direct approach and with the modulation. Finally, I will conclude the chapter with the limitations and perspectives of the two-dimensional ESSat Microscopy in Section 3.7.

3.1 Direct-ESSat Microscopy

3.1.1 Principle

Excited State Saturation (ESSat) Microscopy attains super-resolution by exploiting the nonlinear optical saturation of the excited state of single molecules. It is based on scanning confocal fluorescence microscopy of single molecules excited on their zero-phonon-line at liquid helium temperature.

For the direct-ESSat microscopy, a Laguerre-Gaussian beam of the first order is used for illumination. A Laguerre-Gaussian beam has a higher order transverse mode, which can be obtained from the solutions of the paraxial wave equation in cylindrical coordinates. A light beam in the Laguerre-Gauss (LG_p^l) mode carries an orbital angular momentum lh/2π per photon (p is the radial index and l is the axial index). Unlike a Gaussian beam, for which the phase is identical at all points of the transverse plane of the beam, a Laguerre-Gaussian beam has a phase that winds as a function of the angle in this plane. If we join the points of equal phase as the wave propagates, the trajectory is described by a winding helix and is characterized by a phase profile,

$$A(\varphi) = \exp(in\varphi), \tag{3.1}$$

where φ is the angle made around the optical axis and n is the topological charge. In the transverse plane, the phase smoothly advances with angle in counter-clockwise direction for LG_0^{+1} and clockwise direction for LG_0^{-1}. When focusing such a beam, due to the twisting in the phase front, the phase in the beam center has "all phases". This gives rise to an optical singularity that produces a vanishing amplitude at the center of the focal point, due to the destructive interference of all the phases [203]. Therefore, the beam profile of a first-order Laguerre-Gaussian beam (LG_0^1) in the image focal plane of a lens has a "doughnut-shape".

The simulated images of the beam with wavelength λ = 589 nm in the focal plane of an objective with NA=0.95 is shown in Figure 3.1. The simulations are done by considering the vectorial diffraction theory (not taken into account in Figure 1b. of [204]), which is discussed in Section 3.2.

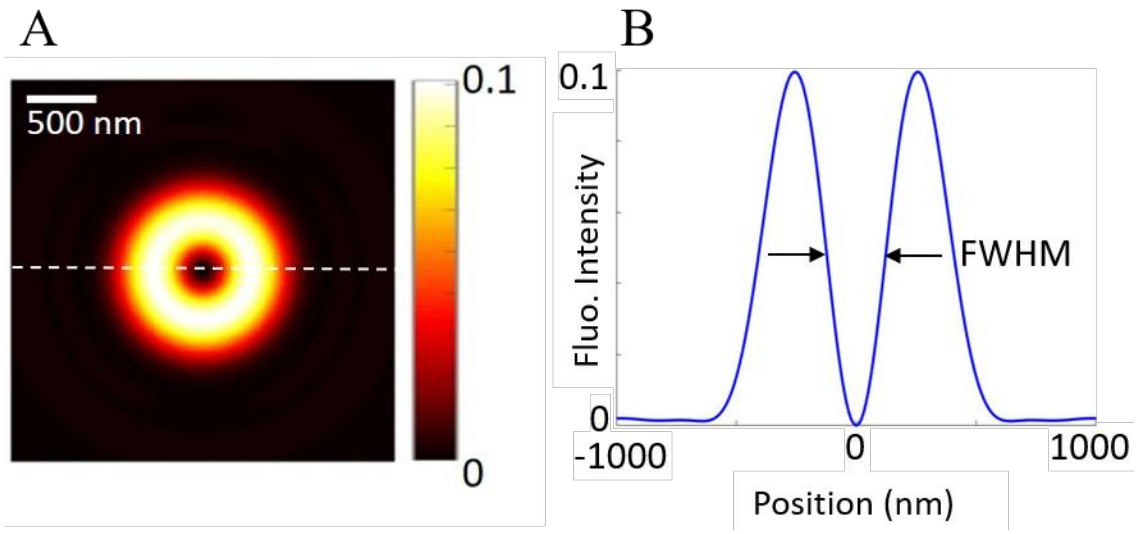

Figure 3.1: (A) Simulated image of a single molecule excited with a Laguerre-Gaussian beam. The excitation intensity is 10 % of saturation intensity; $I_D = 0.1I_S$. I_D is defined as the maximum intensity of the doughnut beam. The peak to peak distance between two opposite intensity maxima of the doughnut profile is around 560 nm. (B) Cross-section profile of the image A along the central dashed white line. The FWHM of the central dip of the doughnut image defines the resolution of the image. The fluorescence signal is given in unit of R_∞, the fluorescence signal given by a molecule at full saturation.

At low excitation intensity, well below the saturation, the fluorescence signal from the molecule will be proportional to the excitation intensity. Thus, the fluorescence image of a molecule will reproduce the excitation beam profile, thus will have a doughnut shape. The resolution can then be defined as the FWHM of the central dip of the doughnut image, and it will be diffraction limited.

Now, if we increase the excitation intensity, we have an optical saturation of the fluorescence signal of the molecule. This leads to the broadening of the image and sharpening of the central dip in the doughnut image. Thus, the FWHM of the doughnut dip can be reduced nonlinearly with excitation intensity. The simulated images of single molecule excited with a doughnut-shaped beam for different excitation intensity and their corresponding cross-sectional profiles are shown in Figure 3.2. From the cross-sectional profiles (Figure 3.2.B), we can see that the width of the central dark dip of the doughnut beam is drastically reduced above the saturation intensity. Therefore, we can have a resolution enhancement by increasing the excitation intensity.

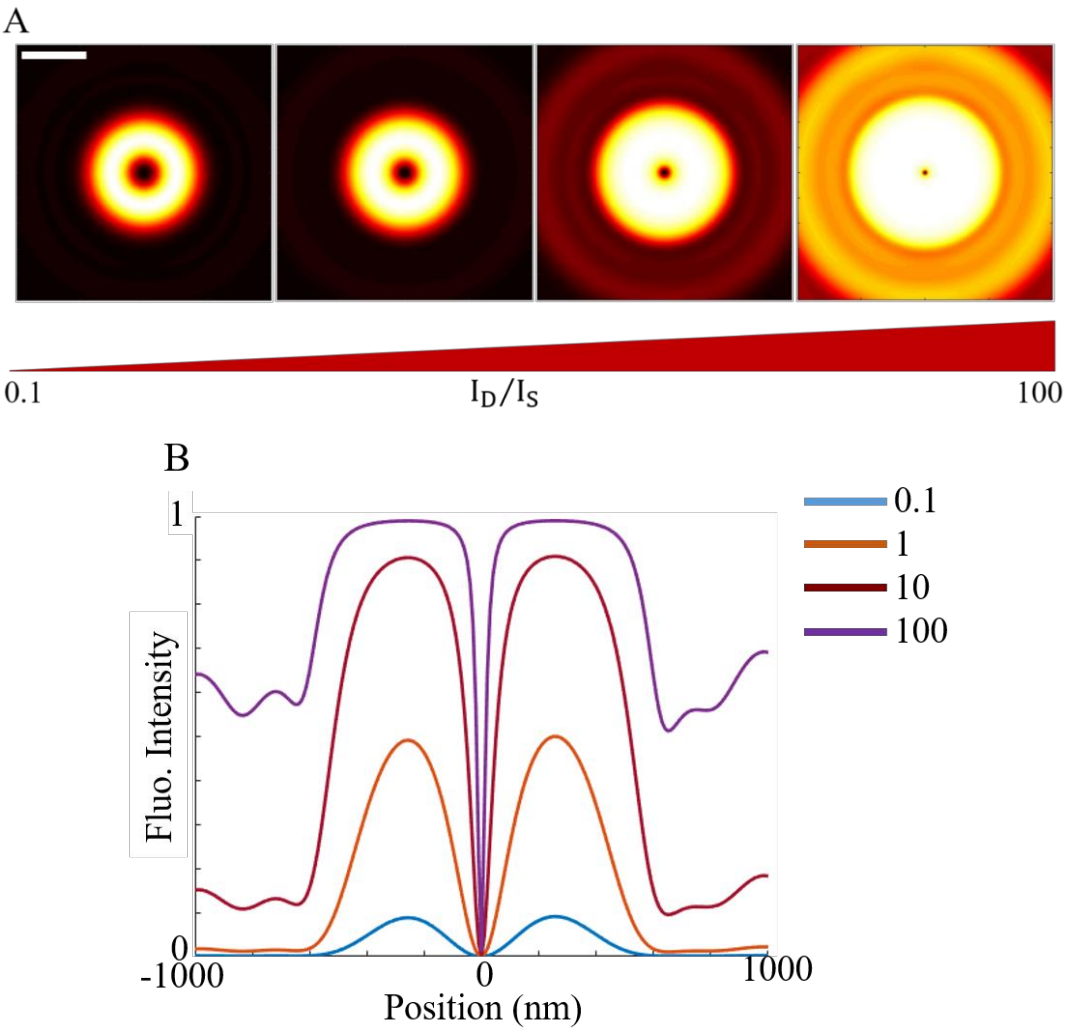

Figure 3.2: (A) Simulated images of molecule excited with a doughnut beam for different saturation parameters ($I_D/I_S = 0.1, 1, 10, 100$). Scale bar is 500 nm. (B) Cross-sectional profiles of the fluorescence intensity along the center. The fluorescence signal is given in unit of R_∞. The FWHM of the central dip is reduced drastically above the saturation.

3.1.2 Theoretical resolution with a doughnut beam

In the paraxial approximation, the helical beam focuses with a distribution of light intensity forming a doughnut-shaped beam, which can be described as [205]:

$$I_{donut}(r) = eI_D \frac{4r^2}{d^2} \exp\left(-\frac{4r^2}{d^2}\right) \tag{3.2}$$

where I_D is the maximal intensity of the doughnut beam and d is the diameter, i.e. the distance between two opposite intensity maxima of the doughnut beam. The analytical expression for the resolution Δr as a function of the excitation intensity I_D, is obtained by approximating the intensity

distribution of the doughnut beam with a sine function near the optical axis [94]. Therefore, we can write the intensity distribution as:

$$I_{donut}(r) = I_D \sin^2\left(\frac{\pi r}{d}\right) \tag{3.3}$$

The maximal fluorescence emission rate in a doughnut image is therefore $R(I_D)$. Assuming the fluorescence emission rate R(I) is half of $R(I_D)$ at $r = r_0$, the resolution $\Delta r = 2r_0$ is given by:

$$\Delta r = \frac{2d}{\pi} \arcsin\left[\frac{1}{\sqrt{2 + I_D/I_S}}\right] \tag{3.4}$$

This relation of the resolution of direct-ESSat microscopy with the excitation intensity is shown in Figure 3.3.

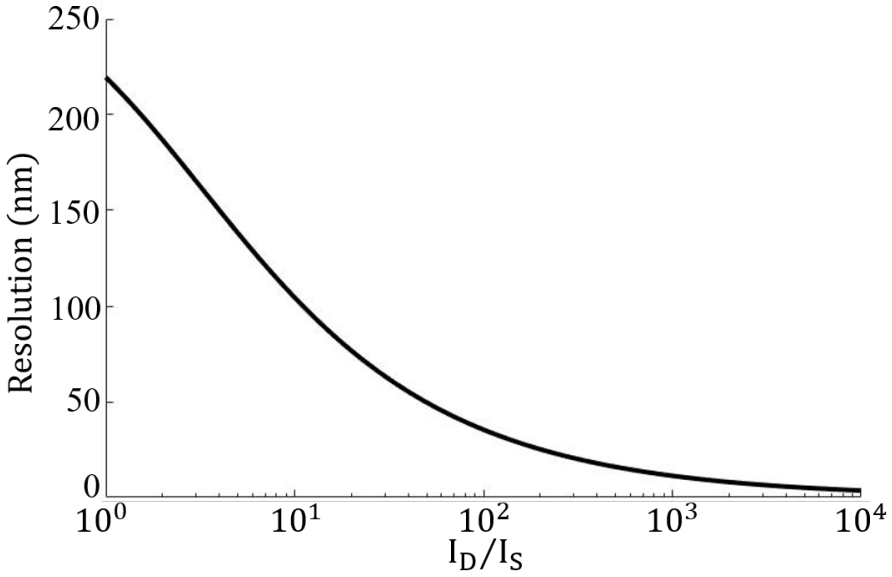

Figure 3.3: Theoretical resolution of the direct-ESSat microscopy as a function of the doughnut-excitation beam intensity.

As the excitation intensity is much higher than the saturation intensity ($I_D \gg I_S$), Equation 3.4 can be simplified as

$$\Delta r = \frac{2d}{\pi\sqrt{I_D/I_S}} \quad . \tag{3.5}$$

That is, the resolution of the microscope no longer limited by the wavelength or the numerical aperture of the objective. Instead, it has dependence on the ratio of saturation intensity, I_S and the excitation intensity, I_D. Thus by increasing the excitation intensity beyond the saturation intensity, we can have a significant resolution enhancement. Since the saturation intensity at cryogenic temperature for a well-chosen host-guest system is in the order of 1 W/cm^2, an excitation intensity on the order of few kW/cm^2 is enough to achieve nanometric resolution.

3.2 Effect of high NA objective

Even though numerical aperture of the objective does not limit the resolution of ESSat-Microscopy, it does have an influence in the image formation. Since Abbe's diffraction limit has an inverse dependence on the numerical aperture (NA) (Equation 1.10 and 1.11), we can get smaller diffraction limited spots by using higher NA objectives. However, when working with an optical system with high NA objective (NA approximately larger than 0.7), there are certain phenomena, which need to be considered, such as apodization, asymmetric focusing behavior, aberrations, depolarization etc. [206]. Hence, the paraxial approximations taken in the scalar diffraction theory (Section 1.1) does not hold anymore and the derived results from scalar diffraction theory by Huygens and Fresnel are not able to exactly reflect the behavior of the light field distribution in the vicinity of the focal point.

In the 1950s, Richard and Wolf proposed a complete mathematics representation of the electromagnetic field distribution in the focal region of a high NA objective. They considered the vectorial properties of the electromagnetic field and the derivation is based on vectorial Debye approximation [206] [207] [208]. Therefore, while doing super-resolution imaging with a high NA objective, we have to take into account the vectorial property of the incident light field.

3.2.1 Vectorial Diffraction Theory

According to Debye theory (or Debye approximations), the field in the focal region is a superposition of plane waves whose propagation vector falls inside the geometrical cone formed by drawing straight lines from the focal point through the aperture edge. On the other hand, the non-vectorial diffraction theory includes the contribution of light waves outside the geometrical cone as well.

The focusing of light waves with a high numerical aperture objective is shown in Figure 3.4. For a high numerical aperture objective lens, the beam wavefront after the lens is a spherical surface. The electric field distribution on this spherical surface (W) at point $P_1(x_1, y_1, z_1)$ can be defined as,

$$\mathbf{E_1}(x_1, y_1, z_1) = \mathbf{E}'(x_1, y_1, z_1)\frac{\exp(ikf)}{f} \tag{3.6}$$

where f is the radius of the spherical surface. The function $\exp(ikf)/f$ denotes the convergence of a spherical wave with radius f to the focal point, O and the function $\mathbf{E}'(x_1, y_1, z_1)$ represent the angular field distribution on the spherical wavefront.

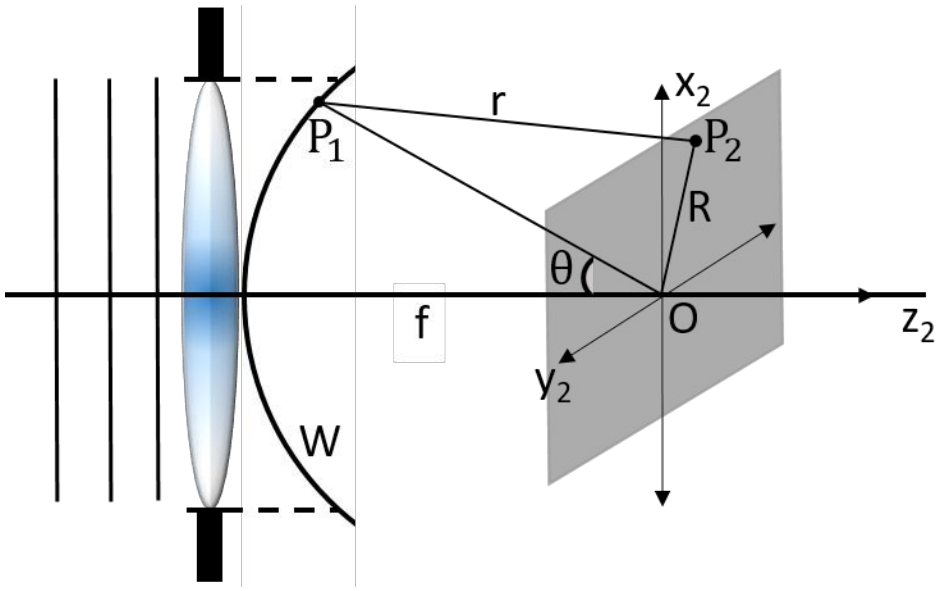

Figure 3.4: Focusing of light waves by a high numerical aperture objective. The beams are focused with a large convergence angle, θ (larger than 70°). The electric field is denoted as $\mathbf{E_1}(x_1, y_1, z_1)$ on the spherical surface and $\mathbf{E_2}(x_2, y_2, z_2)$ in the observation plane.

The electric field distribution at an arbitrary point P_2 on the observation plane can be written as:

$$\mathbf{E_2}(x_2, y_2, z_2) = \frac{i}{\lambda}\iint_{\Sigma} \mathbf{E_1}(x_1, y_1, z_1)\frac{\exp(-ikr)}{r}\cos(\mathbf{n}, \mathbf{r})\, dx_1 dy_1 \tag{3.7}$$

where r is the distance between an arbitrary point in the diffraction plane and that in the observation plane. The factor cos(**n**, **r**) is the cosine of the angle between the unit normal vector (**n**) of the diffraction plane and the observation direction (**r**).

Substituting the expression for $\mathbf{E_1}(x_1, y_1, z_1)$ from Equation 3.6, we get,

$$\mathbf{E_2}(x_2, y_2, z_2) = \frac{i}{\lambda}\iint_{\Sigma} \mathbf{E}'(x_1, y_1, z_1)\frac{\exp[-ik(r-f)]}{rf}\cos(\mathbf{n}, \mathbf{r})\, dx_1 dy_1 \tag{3.8}$$

Certain approximations have to be taken into account in order to solve Equation 3.8. One is to consider the point P_1 not so far from the optical axis. This leads to approximate the distance difference of r and f as,

$$r - f = \mathbf{s} \cdot \mathbf{R} \tag{3.9}$$

where **s** is the unit vector from the point P_1 in the diffraction plane to the focal point (O) and **R** is the vector from the focal point to the point P_2 on the observation plane. This approximation replaces the spherical wavelets by plane wavelets. Another approximation is that of the elemental area, $dx_1 dy_1$ is expressed as $f^2 d\Omega$, where $d\Omega$ is the solid angle corresponding to the area. Third, as in the paraxial approximation cos(**n**, **r**) is approximated as 1. This results in using f, the focal length instead of r. With these approximations, called the Debye approximation, we can modify Equation 3.8 and can have Debye integral as:

$$\mathbf{E_2}(x_2, y_2, z_2) = \frac{i}{\lambda}\iint_{\Omega} \mathbf{E}'(x_1, y_1, z_1)\exp(-ik\mathbf{s}\cdot\mathbf{R})d\Omega \tag{3.10}$$

The Debye integral can be solved for a circular objective by introducing a spherical coordinate system with the origin at the focal point (O). In spherical coordinate system, the diffraction plane coordinates can be written in terms of θ and φ. Thus, $E'(x_1, y_1, z_1)$ is replaced by $E'(\theta, \varphi)$.

Transforming to cylindrical coordinates for P_2, Equation 3.10 becomes,

$$\mathbf{E_2}(r_2, \psi, z_2) = \frac{i}{\lambda}\iint_{\Omega} \mathbf{E}'(\theta, \varphi)\exp[-ik\, r_2\, \sin\theta\cos(\varphi - \psi) - ikz_2\cos\theta]\sin\theta\, d\theta\, d\varphi \tag{3.11}$$

with

$$\mathbf{E}'(\theta, \varphi) = A_1(\theta, \varphi)\, A_2(\theta, \varphi)\, A_3(\theta, \varphi)\, \mathbf{a}(\theta, \varphi) \tag{3.12}$$

where $A_1(\theta, \varphi)$ is the phase distribution of the input beam at the entrance pupil of the objective lens, $A_2(\theta, \varphi)$ is the apodization factor of the focusing system, $A_3(\theta, \varphi)$ describes the aberrations introduced by the focusing system and $\vec{a}(\theta, \varphi)$ is the polarization unit vector of the incident electromagnetic field. Substituting $\mathbf{E}'(\theta, \varphi)$, Equation 3.11 becomes,

$$\mathbf{E_2}(r_2, \psi, z_2) = \frac{i}{\lambda}\oiint A_1(\theta, \varphi).A_2(\theta).A_3(\theta, \varphi).\exp[-ikr_2\sin\theta\cos(\varphi - \psi)]\ \exp(-ikz_2\cos\theta)\,.\,\mathbf{a}(\theta, \varphi).\sin\theta.d\theta.d\varphi \tag{3.13}$$

This equation is the Debye integral for a diffraction field in the focal region of a high numerical aperture objective with a circular aperture.

The simulation figures shown in Figure 3.1 and 3.2 are calculated with Equation 3.13. The phase distribution of the first order Laguerre Gaussian beam $A_1(\theta, \varphi)$ is taken as $\exp(i\varphi)$, the apodization factor $A_2(\theta, \varphi)$ as $\sqrt{\cos\theta}$ [209], considering an aberration-free system $A_3(\theta, \varphi)$ is taken as 1 and the polarization $\mathbf{a}(\theta, \varphi)$ as left circularly polarized (the same as the vortex orientation).

3.2.2 Influence of incident polarization

The focal intensity distribution of the first-order Laguerre- Gaussian beam by a high NA objective also varies with the polarization of the incident light [210] [211]. First, let's consider the case of a linearly polarized Laguerre Gaussian beam. Figure 3.5 shows the simulated images of the intensity distribution at the focal plane when a linearly polarized beam in the E_x direction (A) and E_y direction (B) is focused with an objective of NA 0.95. In both cases, the images present a distorted doughnut shape, with a non-zero residual intensity at the center. For NA=1, the minimum intensity can reach 48.8 % of the maximum intensity [210] and therefore could significantly reduce the signal-to-noise ratio (SNR). Besides, the profile also lost its rotational symmetry, i.e. the focal spot is elongated along the direction of polarization. The FWHM of the total intensity distribution for

the x-linearly polarized beam is about 610 nm along the x-axis and about 420 nm along the y-axis. The values are swapped for the y-linearly polarized beam.

This degradation of the image is the effect of high NA objective [212]. Because of the tight focusing, the beam converges significantly and the polarization direction rotates consequently. Therefore, the effective polarization after the objective has a component along the x-axis, y-axis, and z-axis as well. The component along the y-axis is negligible, but that in the z-axis is not negligible. This rather strong z-component in the focal point leads to the residual intensity at the center of the image. The asymmetry in the image is also due to the significant contribution of the axial component of the electric field. With higher NA objectives, this asymmetry becomes stronger.

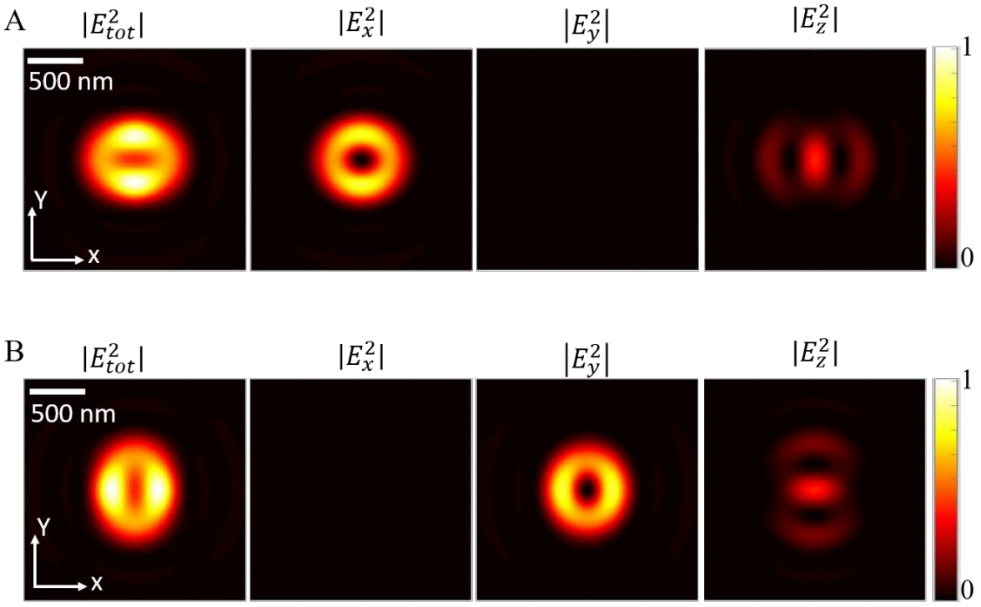

Figure 3.5: Simulated images of the doughnut beam intensity distribution at the focal plane (xy plane) when a linearly polarized light in the E_x direction (A) and E_y direction (B) is focused using an objective with NA of 0.95, taking into account depolarization effects. The figures give the intensity distribution due to the different components of the electric field (E_x^2, E_y^2 and E_z^2) and due to the total electric field E_{tot}^2. λ = 589 nm.

On the other hand, it is possible to have an undisturbed doughnut profile with a high NA objective by using circularly polarized light [213]. Even here, it is very important to have the orientation of the circularly polarized light identical to that of the orientation of the vortex phase. If not, we will get a minimum stronger than that obtained by using a linearly polarized light, despite the nice rotational symmetry (Figure 3.6.A). As in the case of a linearly polarized incident light, the non-zero minimum is due to the strong axial electric field component due to tight focusing. When the orientations of the helix and the polarization are different, the z-components at each point are along the same direction (towards +z). This results in an effectively strong E_z-component at the focus. On the other hand, when they have the same orientations, the total E_z-component at each point comprises equal and opposite E_z-components. Thus, all the E_z-component effectively cancels at

the focus, forming a good zero-minimum at the center. We thus either change the orientation of the circular polarization or change the orientation of the vortex phase by changing the sign of the topological charge n, in order to have the same orientation for both.

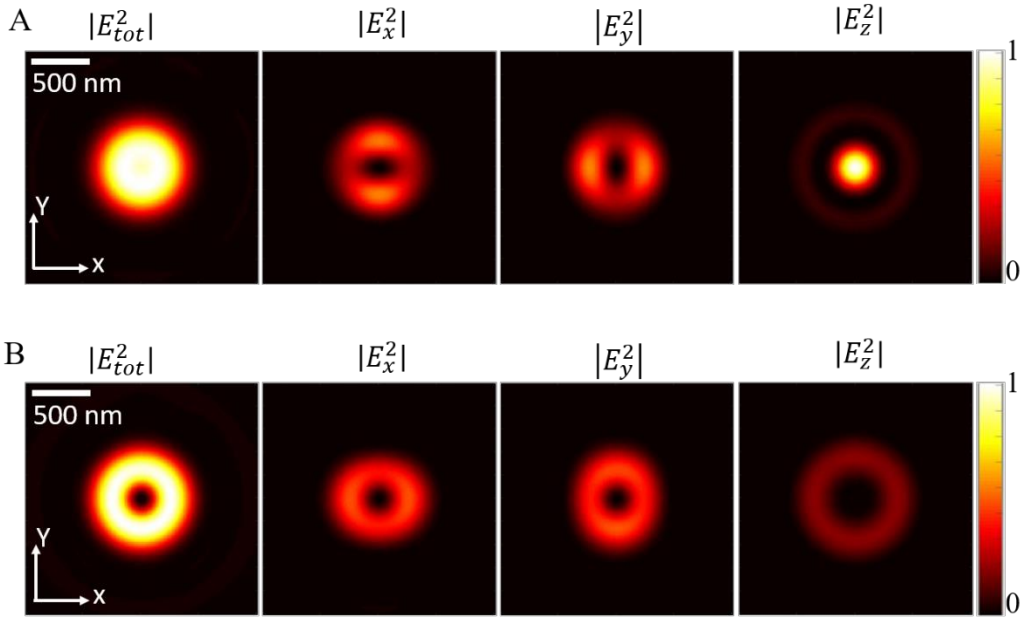

Figure 3.6: Effect of the orientation of the circular polarization with respect to the helicity of the vortex phase. (A) When the beam has an orientation of circular polarization opposite to that of the vortex, the beam profile will no longer be a doughnut. The central zero vanishes and we have a bright intensity at the center. (B) When the beam circular polarization has same orientation as that of the vortex, the beam profile is a perfect doughnut with a symmetric central zero and with a high-intensity gradient around. λ = 589 nm, NA=0.95.

Therefore, polarization plays a crucial role in the shape of the doughnut-shaped focused beam for an objective with a high numerical aperture (NA > 0.7). In our experiment, the beam is left circularly polarized to have the same orientation as that of the vortex phase, creating a reduced minimum at the center.

3.3 Modulated ESSat Microscopy

3.3.1 Principle

A super-resolved image of a single molecule with direct-ESSat microscopy gives a signal minimum surrounded with a high-intensity gradient all around. The location of the molecule is given by the fluorescence minimum. If there are two molecules in the focal volume, the high-intensity ring of one will act as a background for the other and vice versa. It is thus difficult to resolve two molecules with a high contrast using direct-ESSat microscopy. Therefore, modulated-ESSat microscopy is introduced to restore the positive images of single molecules and thereby to attain better image contrasts.

In modulated-ESSat microscopy, a temporally modulated Gaussian beam is superimposed with the doughnut beam to excite the molecules, and the amplitude of the fluorescence signal modulation is recorded. Figure 3.7 shows the principle of modulated-ESSat microscopy. The blue and orange lines are respectively the fluorescence profiles of the molecule, excited with only the doughnut beam, and only the Gaussian beam. As with direct-ESSat microscopy, a molecule is highly saturated with the doughnut beam, while the Gaussian beam has a maximal intensity equal to the saturation intensity I_S. Since the Gaussian beam is temporally modulated, it induces a fluorescence signal modulation. When the molecule is at the center of the doughnut beam, the molecule will not be saturated. It will be solely affected by the modulated-Gaussian beam and thus provide a maximal amplitude in the fluorescence signal modulation. Once the molecule is at the ring of the doughnut beam, it will be highly saturated and therefore essentially insensitive to the modulated-Gaussian beam. Thus, the amplitude of the fluorescence signal modulation will be reduced. Overall, the amplitude of the fluorescence signal modulation depends strongly on the position of the molecule with respect to the doughnut beam. The black curve in the Figure 3.7.B shows the amplitude of the fluorescence signal modulation, plotted as a function of the position of the molecule. Henceforth, we can get an effective PSF much smaller than the diffraction limit.

The intensity distribution of a Gaussian beam can be written as:

$$I_{Gaussian} = I_G \exp\left(-\frac{2r^2}{w_0^2}\right) \tag{3.14}$$

where I_G is the maximal intensity and w_0 beam waist.

We consider a single cosine modulation of the Gaussian beam:

$$I_{Gaussian}(r,t) = I_G \frac{1+\cos(2\pi\nu t)}{2} \exp\left(-\frac{2r^2}{w_0^2}\right) \tag{3.15}$$

where ν is the modulation frequency.

At moderate Gaussian beam intensity ($I_G \leq I_S$), the detected fluorescence count rate from a single molecule can be modeled as:

$$S = S_0 + \Delta S \frac{1+\cos(2\pi\nu t)}{2} \tag{3.16}$$

where S_0 is the fluorescence signal of the molecule due to the doughnut beam excitation and ΔS is the amplitude of the fluorescence intensity modulation induced by the modulated Gaussian beam.

The amplitude of the fluorescence signal modulation is extracted using a demodulation method based on a lock-in amplifier. For that, we apply a reference signal at the modulation frequency of the Gaussian beam (ν) and multiply it with the amplitude of the fluorescence signal modulation. The DC signal component at the locked frequency is then extracted by removing all the high-frequency noise using a low-pass filter.

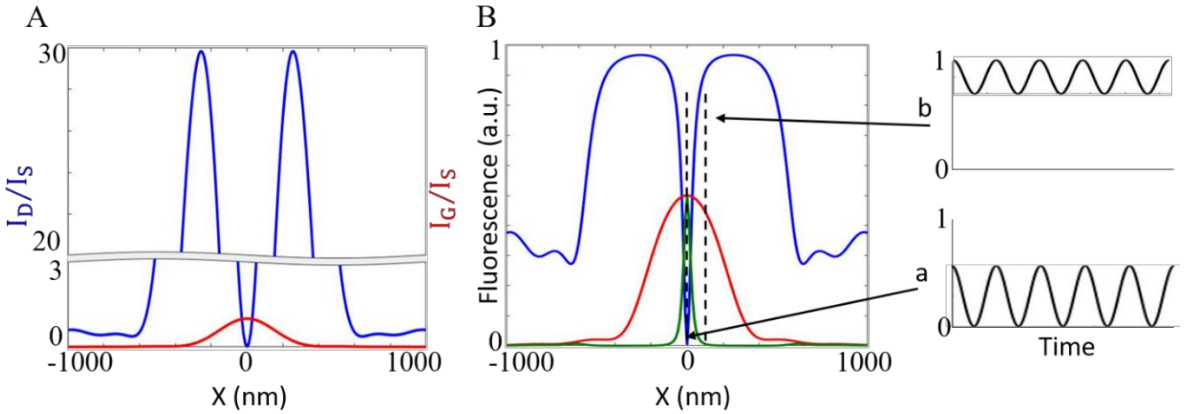

Figure 3.7: Principle of modulated-ESSat microscopy. (A) Intensity profile of the doughnut beam at $I_D = 30I_S$ (blue) and the Gaussian beam at $I_G = I_S$ (red). (B) Fluorescence signal (green) of the molecule excited by the doughnut beam and the modulated Gaussian beam. The doughnut beam saturates the molecule except at the centre. Therefore, when the molecule is at the center of the doughnut beam, the amplitude of the fluorescence intensity modulation is the highest. At the periphery, since the molecule is saturated, there is little effect of the modulated Gaussian beam. The insets 'a' and 'b' indicate the amplitude of the fluorescence intensity modulation at the center and at the periphery of the doughnut beam, respectively. The green curve shows the effective amplitude of the fluorescence signal modulation as a function of the position of the molecule. This effective PSF is much smaller than the diffraction limited PSF.

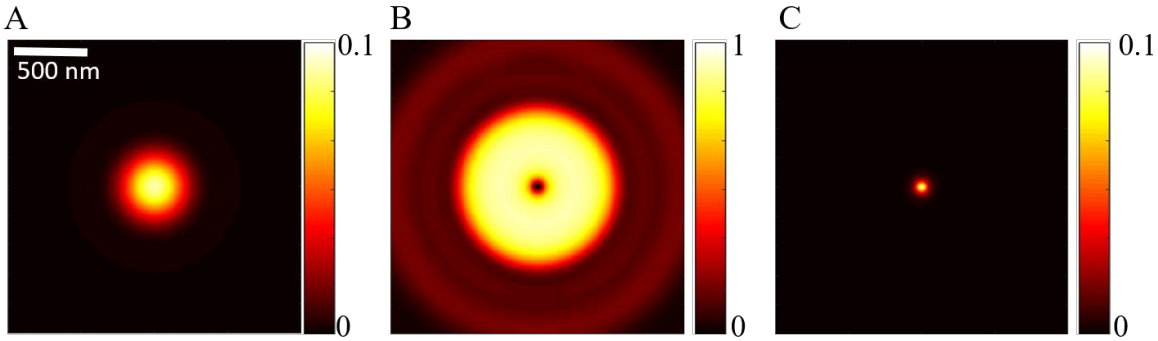

Figure 3.8: Simulations of modulated-ESSat imaging. (A) and (B) represents images of a molecule excited with a Gaussian beam and a doughnut beam, respectively. (C) Modulated-ESSat image showing an effective positive signal much smaller than the diffraction limit. $I_G = 0.1I_S$, $I_D = 10I_S$. The fluorescence signal is given in the unit of R_∞.

Figure 3.8 displays simulated images obtained with the modulated-ESSat microscopy. Figure 3.8.A and 3.8.B show the images of a molecule excited with the Gaussian beam and the doughnut beam, respectively. The Gaussian beam has an intensity $I_G = 0.1I_S$ and the doughnut beam of $I_D = 10I_S$. By overlapping these two beams and extracting the amplitude of the fluorescence signal modulation, a modulated-ESSat image is derived and shown in Figure 3.8.C. The modulated-ESSat image gives us a well-defined positive signal with an effective PSF much smaller than the diffraction-limited PSF. Thus, modulated-ESSat microscopy gets rid of the background issues

inherent to the direct-ESSat microscopy method, and can be easily employed for resolving two or more molecules separated by sub-wavelength distances.

3.3.2 Theoretical resolution with modulated-ESSat microscopy

The amplitude of the fluorescence intensity modulation can be expressed as [204]:

$$\Delta R(r) = R[I_{donut}(r) + I_{Gaussian}(r)] - R[I_{donut}(r)] \tag{3.17}$$

Considering the case where $r \ll d$, we have $I_{Gaussian}(r) \approx I_{Gaussian}(0) = I_G$. In the center of the doughnut beam, the amplitude is maximal and equal to $R(I_G)$.

The resolution can be defined as the FWHM of $\Delta R(r)$ and is given by:

$$\Delta r = \frac{2d}{\pi}\sqrt{\frac{A(I_G)}{I_D/I_S}} \tag{3.18}$$

with

$$A(I_G) = \sqrt{(1 + I_G/I_S) + (1 + I_G/2I_S)^2} - (1 + I_G/2I_S) \ . \tag{3.19}$$

As for direct-ESSat microscopy, the resolution depends on the inverse of $\sqrt{I_D/I_S}$ and can be considerably reduced when $I_D \gg I_S$. In addition, it is directly proportional to $\sqrt{A(I_G)}$, which has a dependence on I_G/I_S as shown in Figure 3.9. At $I_G \gg I_S$, $\sqrt{A(I_G)}$ becomes 1 and the resolution of the modulated-ESSat microscopy becomes the same as that of the direct-ESSat microscopy. For lower values of I_G, $\sqrt{A(I_G)}$ is less than 1, resulting in a better resolution. However, the signal-to-noise ratio of modulated-ESSat images will be lower. Therefore, in practice, the value taken for I_G is the order of tens of I_S or even higher and $\sqrt{A(I_G)}$ ~1.

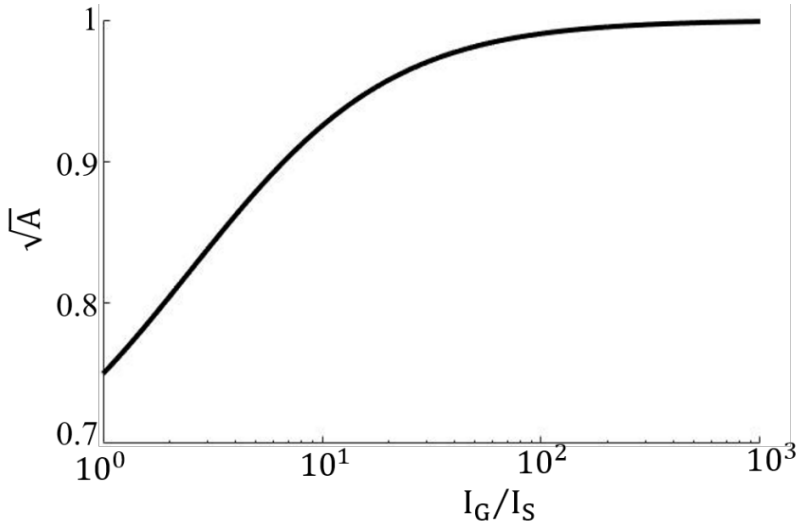

Figure 3.9: Evolution of $\sqrt{A}$ with I_G/I_S.

3.4 Experimental setup

3.4.1 Sample

The quantum emitters we choose are single fluorescent aromatic molecules of dibenzanthanthrene (DBATT) embedded in an octadecane Shpol'skii matrix. The chemical structures of the molecule and the matrix are shown in Figure 3.10. This host-guest combination has a fluorescence yield close to unity. At liquid helium temperature (2K), dephasing by acoustic phonons is negligible ($T_2 = 2T_1$), and the DBATT molecules exhibit excited-state lifetime-limited linewidths of approximately 20 MHz around 589 nm.

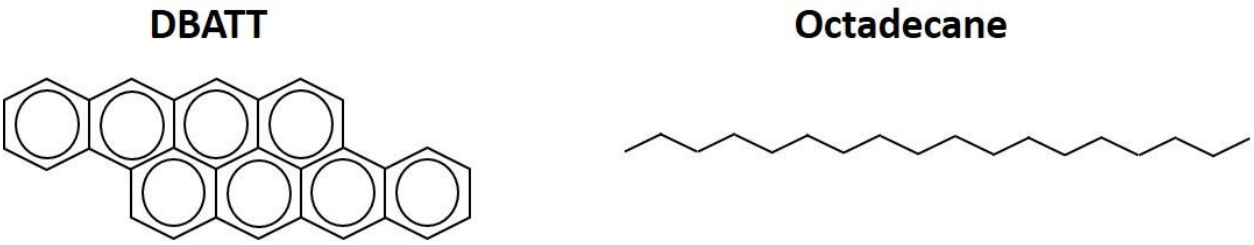

Figure 3.10: Chemical structure of the host-guest system used for the experiment: the DBATT aromatic molecule and the octadecane matrix.

The sample, a drop of a dilute solution of DBATT in octadecane (concentration well below 10^{-7} M), is placed on a glass coverslip and spread to form a thin film with thickness less than 10 μm. The coverslip is then glued onto the sample plate, which is mounted on a computer controlled 2D-scanning stage inserted in the cryostat.

3.4.2 Scanning System

The scanning stage consists of an X-Y piezoelectric scanner and X-Y-Z stepper positioner. The scanner used is an ANSxy50 attocube open-loop scanner that is compatible with cryogenic temperature conditions. The scanning unit consists of a non-magnetic Titanium construction for XY translation. The scanner has a typical scan range of 15×15 μm^2 at 2K and has a repeatability of 0.1%. The scanner is connected to the voltage output of a scan-controller (ANC200), which amplifies input control voltages by a factor of 15. At room temperature, Output voltages of 150 V are used to drive the scanner at low temperature (2 K), while 60 V are used at room temperature. The attocube scanners are calibrated using parallel gold electrodes patterned with a period of 10 μm.

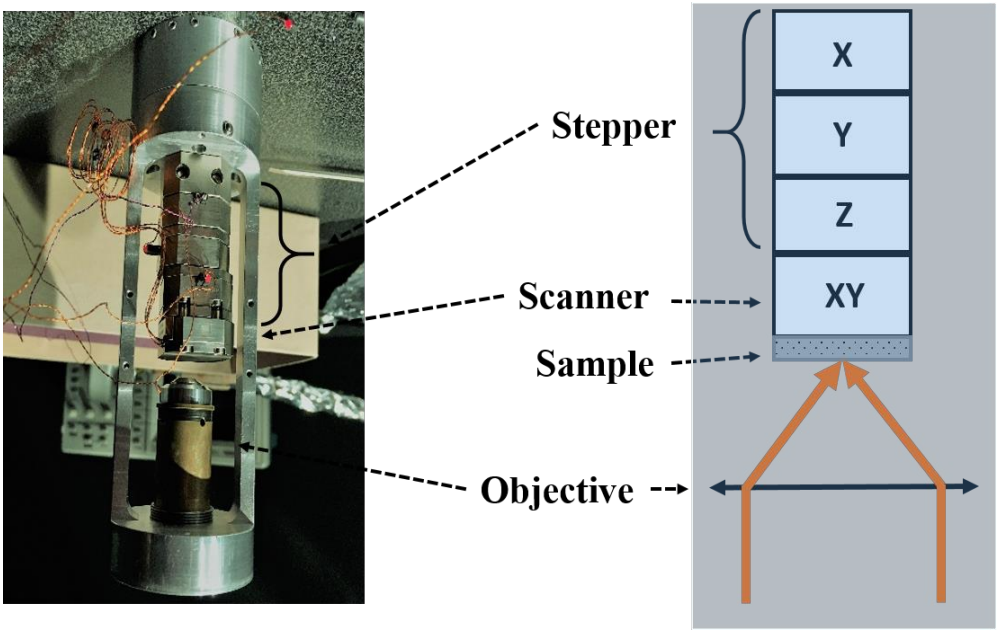

Figure 3.11: Scheme and picture showing the piezo scanner and stepper positioners over which the sample is mounted along with the objective. The scanners and positioners are connected to their controller via insulated twisted copper wires. This microscopy stack is inserted in the variable temperature insert of a liquid helium cryostat.

The stepper positioners used are attocube positioners, the ANPz50 for the axial (vertical) control the and two ANPx51 for the lateral (horizontal) movements. These positioners work on the simple principle of the "table-cloth-trick". By applying a suitable voltage asymmetric pulses onto the piezo, we can move the positioner with nanometer resolution. Step size varies linearly with the applied voltage with a slight dependence on the step frequency. Moreover, the step positioner shows repeatability better than 5 % for a given frequency and applied voltage. The step size of the ANPz51 varies from 250 nm to 2 µm at 300 K and 10 nm to 500 nm at 2 K. This positioner is used for focusing the laser beam onto the sample and has a travel range of 2.5 mm. For horizontal movements, the ANPx51 can travel over 3 mm, with a step size of the order of 250 nm at 300 K and 10 nm at 2K. Thus, after focusing, we can move the sample to the desired position in the horizontal plane using these step positioners, which can perform single stepping for fine positioning as well as continuous stepping for coarse positioning.

3.4.3 Cryostat

The main part of the experimental setup is the liquid helium cryostat, inside which we insert the sample and the scanning system. It is a Vapour-Shielded Optical Bath cryostat (Optistat SXM from Oxford instruments). It consists of a liquid helium reservoir, radiation shields and a variable temperature insert (VTI). A scheme of the cryostat is shown in Figure 3.12.

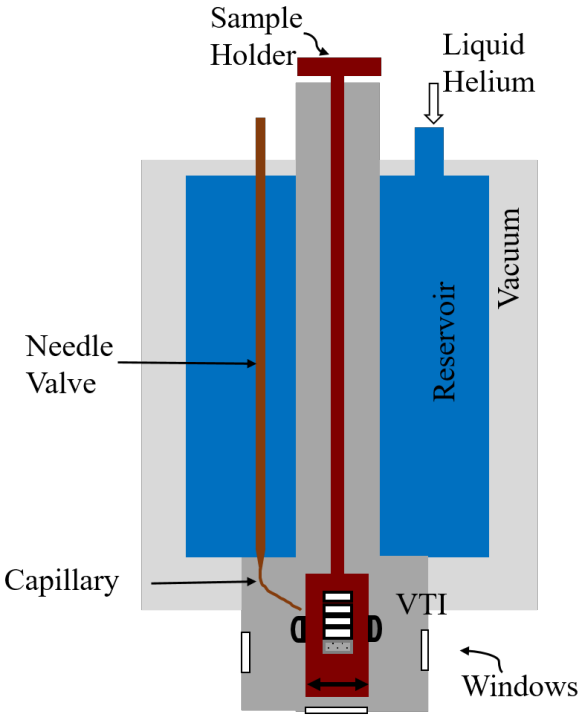

Figure 3.12: Scheme of the cryostat used for the experiment. Liquid helium filled inside the reservoir is supplied to the VTI through the needle valve. A temperature controller controls the needle valve and a heating resistance in order to stabilize the temperature of the VTI. The helium gas contained in the VTI is pumped in order to reach a pressure of several mbars, and thus a base temperature of 2K. The sample along with the piezo scanners and the objective are inserted into the cryostat using a long sample holder.

Liquid helium is filled into the reservoir using a helium transfer tube. Before filling helium, the reservoir is pre-cooled with liquid nitrogen, in order to reduce helium consumption. The evaporated liquid helium is sent out of the reservoir through the exhaust ports at the top of the cryostat. The reservoir and VTI are connected by a capillary, which can be opened or closed by a needle valve. The needle valve thus optimizes the helium flow to the VTI and also stabilizes the temperature. A thermistor is also placed at the bottom of the sample space and a temperature controller can adjust the temperature. The whole system is isolated by a high vacuum installation.

For these experiments, the temperature of the VTI is cooled down to T = 2K by pumping the helium gas at a pressure of a few mbars. The sample, along with the piezo system and the objective are mounted on a long sample rod loaded into the cryostat. The cooling procedure takes about three hours and the cryostat maintains the temperature for about 10 hours. The experiments can be performed continuously over several days or weeks, as long as the helium reservoir is refilled.

3.4.4 SLM and Vortex Phase Mask

The doughnut beam required in this experiment can be generated from a TEM_{00} beam with spiral phase plates [214], or diffractive optical elements such as those contained in a spatial light

modulator (SLM) [215] [216] [217], or with conventional mode converters [218]. In this experiment, we used a computer-generated hologram on a Liquid Crystal on Silicon (LCOS) SLM by Hamamatsu. Its active area consists of an LCD display containing 1280 × 1024 pixels. Each pixel is filled with liquid crystal. Initially, the liquid crystals are aligned parallel. By applying an electric voltage, the liquid crystals can be tilted. Since they are birefringent materials, this tilt changes the refractive index of the medium, which changes the optical path length within the liquid crystal cell. The change in the path length induces a corresponding phase difference between light beams. Thus, it is possible to change the phase in accordance with the applied electric voltage. Every pixel could be given a digital value from 0 to 255, which corresponds to a phase delay applied to the part of the light beam that falls on that particular pixel. Thus, the SLM is able to give any arbitrary phase pattern to a light beam.

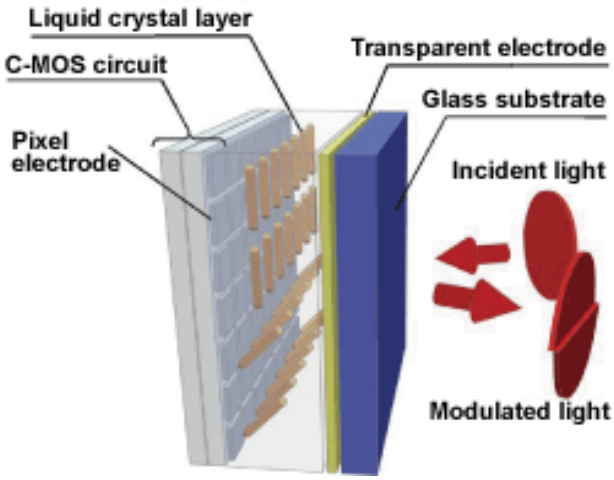

Figure 3.13: LCOS-SLM Configuration. The main part of a LCOS-SLM consists of an array of electrodes, parallel-aligned liquid crystals, and a transparent electrode. By applying a voltage to each pixel, it is possible to modify the orientation of the liquid crystals. Since they are birefringent materials, this changes the refractive index of the medium. Thus, the phase of the incident light can be locally tuned as desired by changing the applied voltage.

Imprinting a helical ramp phase with a central singularity [219] allows the direct formation of the doughnut-shaped beam. For this, we convert the values of the phase mask to the corresponding SLM pixel values. The light incident on the SLM will pass twice through the liquid crystals and is modulated according to the voltage map applied to the pixel electrodes. By connecting the SLM to a computer, we can easily display the SLM as an external monitor. Additionally, the SLM can be controlled by custom software written in LABVIEW.

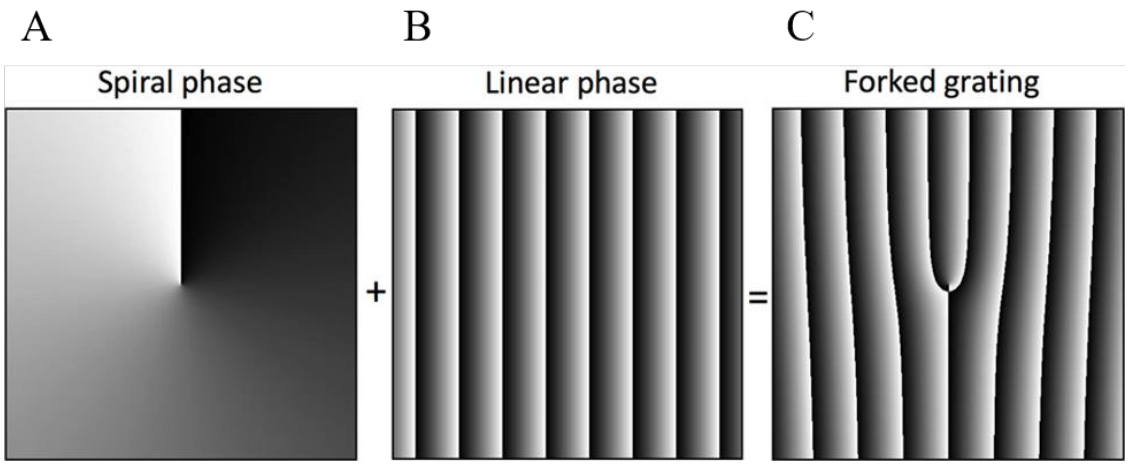

Figure 3.14: (A) Image showing the phase distribution of the cross-section of the beam in greyscale, where phase is represented from 0 (black) to 2π (white) The position of 0 is arbitrary as the phase of a wave only has a meaning if it is compared to the phase of a different part of the beam. (B) Blazed Grating. (C) The final hologram pattern (forked grating) to produce a LG beam. [220][221].

There are certain important things to note while using spatial light modulators. First, the SLM will only effectively modulate light that is polarized in the direction of the orientation of the liquid crystal. In this experiment, the light has to be polarized in the horizontal direction. Second, the pixel value that corresponds to a full 2π phase delay depends on the wavelength of the incident light, as the SLM used is able to modulate light in the wavelength interval of 400-700 nm. The flatness distortion is represented with a value from 0 to 255 (8bits) in the correction pattern and it corresponds to a phase from 0 to 2π. For 589 nm, the 2π value, which is 178, is determined by optimizing the doughnut beam profile at the focal plane of the objective. This means that the possible phase values at every pixel are $2n\pi/178$, with n an integer. Even if above-mentioned factors are satisfied, the SLM will not be 100% efficient, because only 93% of its surface is covered with liquid crystals. Therefore, light reflected from the regions without liquid crystal will be unmodulated, which induces a residual intensity at the doughnut center. To remove this unmodulated beam, a blazed grating (Figure 3.14.B) is applied along with the vortex mask. The grating diffracts 80% of light to the first order. Therefore, the SLM is tilted slightly, to select the modulated first order diffraction pattern and the unmodulated zeroth order beam is blocked.

3.4.5 Optical setup

The experimental setup for Excited State Saturation (ESSat) Microscopy is shown in Figure 3.15.A tunable single frequency CW dye laser emitting in the range 550-650 nm is used for excitation. The laser beam has a spectral linewidth of 1 MHz and is tuned to 589 nm to excite the sample (DBATT molecules). The laser beam is passed through a noise eater in order to stabilize the laser output power. An excitation filter is used to remove the light radiation with wavelength larger than the excitation wavelength required. This can considerably reduce the background noise in the

image. The laser beam is then coupled into a single mode polarization maintaining fiber. Afterwards, a $\lambda/2$ wave-plate (HWP) rotates the polarization by 90° so that the direction of polarization matches with the SLM-LCD orientation. A telescope arrangement is used to increase the size of the beam to fully exploit the SLM surface and to overfill the back focal plane of the objective. Then the linearly polarized light beam is incident on the LCOS-SLM (Hamamatsu X13138) for modulation. A vortex phase mask is imprinted on the SLM using a computer-generated hologram. After modulation, the light is passed through an iris to block the zeroth order unmodulated beam. Light is then polarized circularly so that all vectorial fields at the focal point interfere destructively and creates the minimum field at the center of the focus of the objective, forming a doughnut pattern. Circular polarization of light will also excite all the molecules uniformly irrespective of the orientation of their dipole projection in the sample plane.

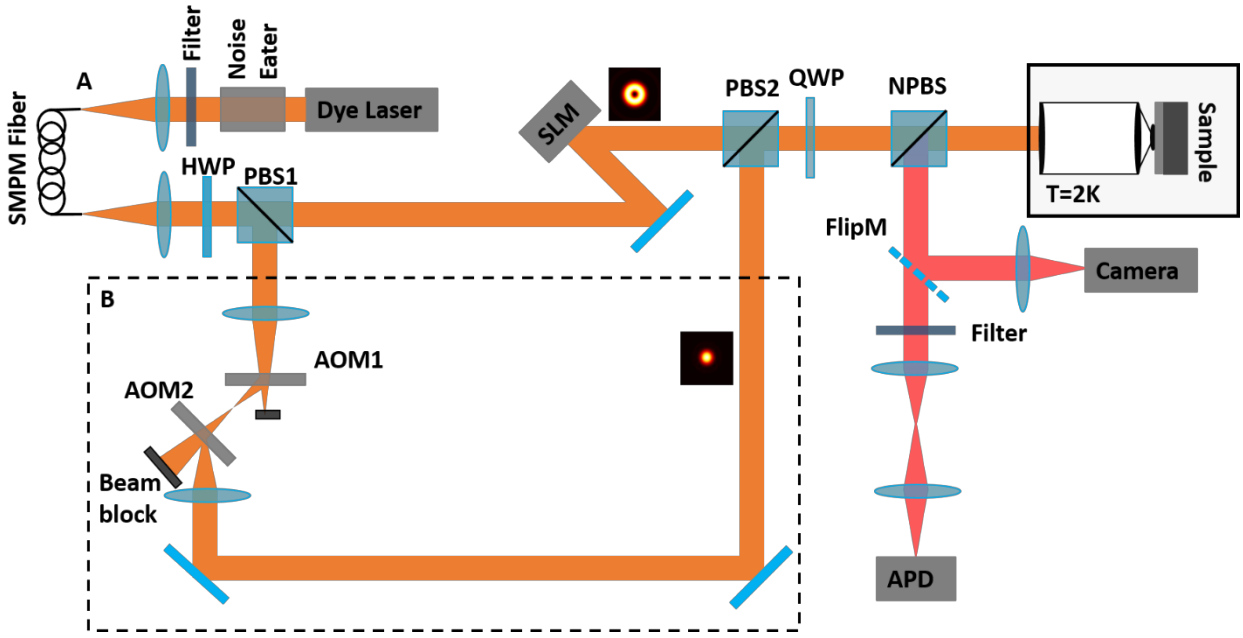

Figure 3.15: Experimental setup of the (A) direct-ESSat microscope and (B) modulated-ESSat part of the microscope.

During scanning, the DBATT molecules are excited with the doughnut-shaped beam at the zero-phonon line and the fluorescence signal is collected by the objective, then partially extracted by a non-polarizing beam splitter (NPBS) onto the path of detection. In order to characterize the spatial intensity profile of the beam, the reflected beam can be imaged on a camera using a flipping mirror. The camera used is a black and white DCC1545M high-resolution CMOS camera with 1280 × 1024 pixel resolution and a maximum full frame rate of 25 fps. Single molecule images are created by conjugating the point illumination source at the sample to the APD. Before focusing on a silicon avalanche photodiode (APD), the fluorescence signal passes through an emission filter, which eliminates the back-scattered excitation light. The emission filter used is Semrock FF01-629/56 bandpass filter. The avalanche photodiode is a single photon counting module (SPCM-AQRH-14) with an active area having diameter 180 µm, which can detect photons over the 400 nm to 1060 nm wavelength range, with a peak photon detection efficiency of about 65 % and a maximum

count rate around 20 million counts per second. The signal from the detector is then analysed with a computer, which constructs a two-dimensional image as an array of intensities for each spot scanned across the sample.

The modulation part of the microscope is shown in Figure 3.15. B. A part of the laser beam is reflected using a polarizing beam splitter to a different path. The beam then passes through two acousto-optic modulators (AOM). The acousto-optic modulators are used to modulate the amplitude of the Gaussian beam at a rate of 1 kHz at diffraction orders +1 and -1. In order to remove the beating between the doughnut beam and Gaussian beam over the integration time of the detector (few ms), the RF frequencies sent to the AOMs are differed by 1 MHz. This small frequency difference compared to the molecular linewidth (20 MHz) will also help in producing very similar degrees of excitation of the molecule. The beam is then directed into the microscope with another polarizing beam splitter and then into the cryostat where the sample is mounted. The reflected signal is then collected by the same objective and recorded using the APD, as in direct-ESSat microscopy.

3.5 Characterization of the doughnut beam

3.5.1 Zernike's polynomial for aberration correction

The size and shape of the doughnut beam have a critical role in ESSat microscopy. It determines the ultimate resolution of the setup. Therefore, it is important to investigate the effects of aberrations on the structural modifications of the doughnut focal spot. Aberrations in the system may result in a non-perfect zero in the doughnut center, energy flow to the higher annular rings, shifting the central minimum from the center of the PSF and anisotropic intensity distribution. Different types of aberrations arise in an imaging system due to misalignment or by focusing through a mismatched refractive index interface or due to the effect of objective [222], etc. The objective we use is not dedicated to low-temperature experiments. Therefore, strong aberrations, in particular astigmatism, arises due to the different thermal expansion coefficients of the different elements of the objective, once cooled down to 2 K. The problems due to aberrations can be corrected by using Zernike polynomials [223].

The Zernike polynomials are an infinite set of polynomials that are orthogonal over the interior of a unit circle [224]. They have been introduced by the Dutch scientist Fritz Zernike and can be applied to describe mathematically the deviation in a three-dimensional wavefront [225]. The complex Zernike polynomials Z_l^m are formed from the orthogonalization of the basis set $\{r^l e^{im\theta}\}$ such that $l = 0,1,2, \ldots$, and $m = 0,1,2, \ldots$, with the stipulation that $[l - |m|]$ is even and $|m| \leq l$. Any wavefront profile can be decomposed into a weighted sum of these polynomials. Figure 3.16 shows the first fifteen wavefront modes for the corresponding Zernike polynomials.

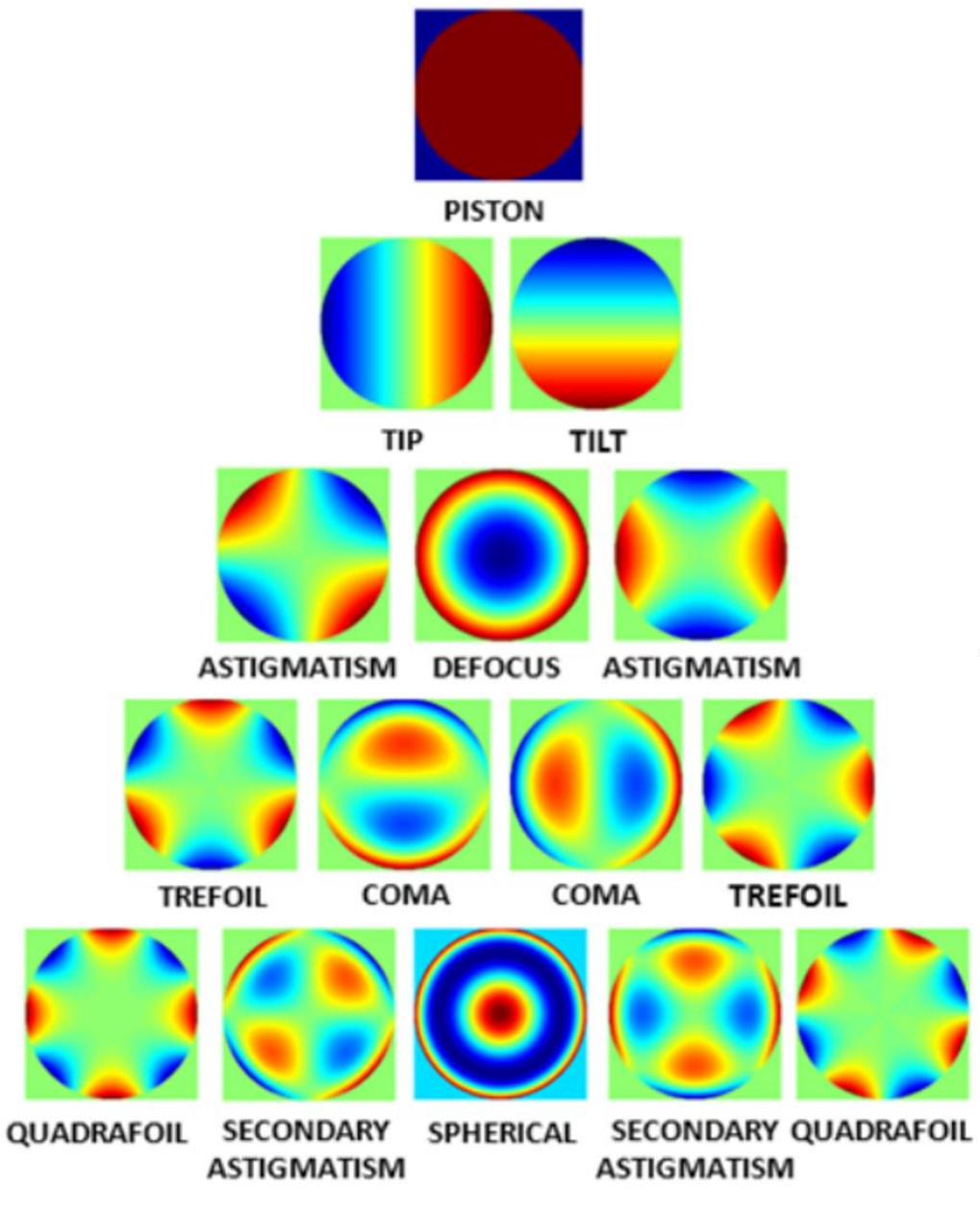

Figure 3.16: Wavefront models for the first fifteen Zernike polynomials. Figure adapted from [226].

Aberrations are corrected by applying a compensation phase mask on the SLM along with the vortex phase mask and the blazed grating. The compensation phase mask is a linear combination of the Zernike polynomials. We use the first eight polynomials that corresponds to horizontal tilt, vertical tilt, oblique astigmatism, defocus, vertical astigmatism, vertical trefoil, vertical coma and horizontal coma, respectively, since they represent the most common aberrations or their possible combinations in an imaging system.

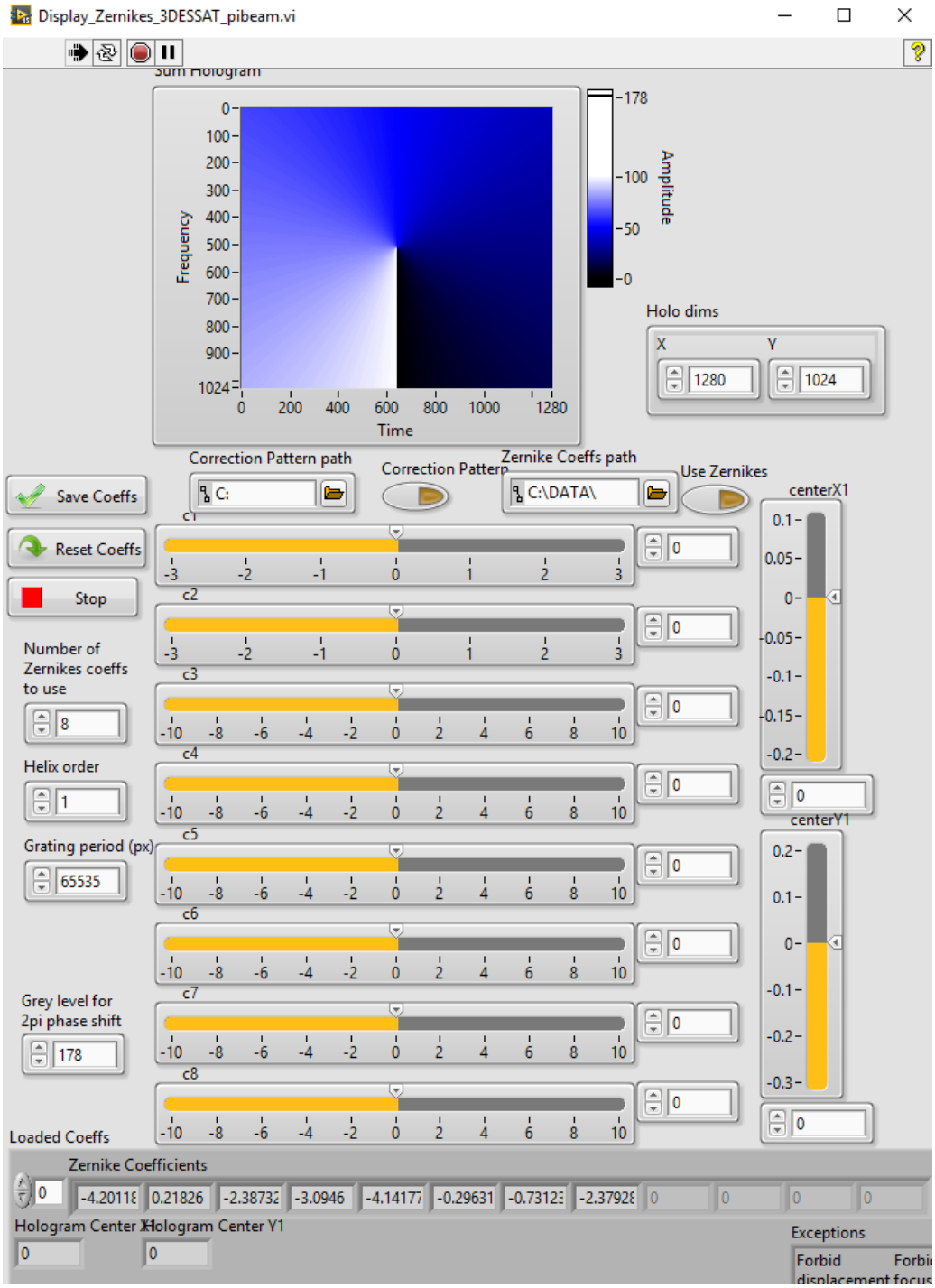

Figure3.17: Interface of the LabVIEW program for aberration correction and for optimization of the doughnut beam profile.

The aberrations due to misalignment mainly astigmatism and spherical aberrations are corrected at room temperature by imaging fluorescence beads and optimizing the image profiles. Cooling down to 2 K introduces aberrations effects on the beam because of the thermal constraints in the objective. Such aberration effects are removed to a large extent by modifying the coefficients of

Zernike polynomials on the SLM, such that a good quality profile is obtained. For this, we take the camera images of the beam reflected from a gold mirror placed at the focal plane of the objective. The gold mirror is chosen because of its flat surface properties as well as its minimum depolarization effects. Spherical aberrations while imaging the sample are corrected by optimizing the corresponding Zernike coefficients. It is also possible to displace the hologram in the x- and y-direction for compensating small alignment errors. The interface of the LabVIEW program for aberration correction and optimization of the doughnut beam is shown in Figure 3.17.

Figure 3.18 shows the camera images from the reflection of a gold mirror at the focal plane of the objective at room temperature, at 2 K without aberration correction and with aberration correction, respectively. The aberrations due to the cooling are effectively removed with the Zernike polynomials. Figure 3.18.C gives a symmetric doughnut beam profile with a good quality central minimum. We could optimize the Zernike polynomial and could get a central minimum intensity less than 1 % of the peak intensity.

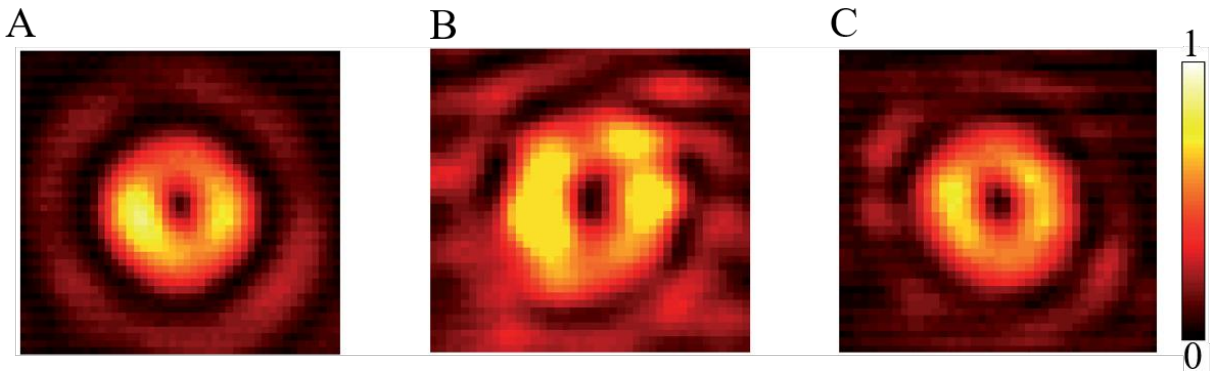

Figure 3.18: Optimization of the doughnut beam with the SLM. Camera images of the doughnut beam, reflected on a gold mirror at the focal plane of the objective, at room temperature (A), at 2 K without aberration correction (B) and at 2K with aberration correction (C).

3.6 Experimental results

3.6.1 Results of 2D-ESSat Microscopy

Figure 3.19.A shows the results obtained by exciting a single molecule with a Gaussian beam or with a doughnut-shaped beam. As the excitation intensity of the doughnut beam increases from left to right, the central dip of the doughnut images is sharpened. Figure 3.19.B shows the FWHM of the doughnut dip as a function of the laser intensity.

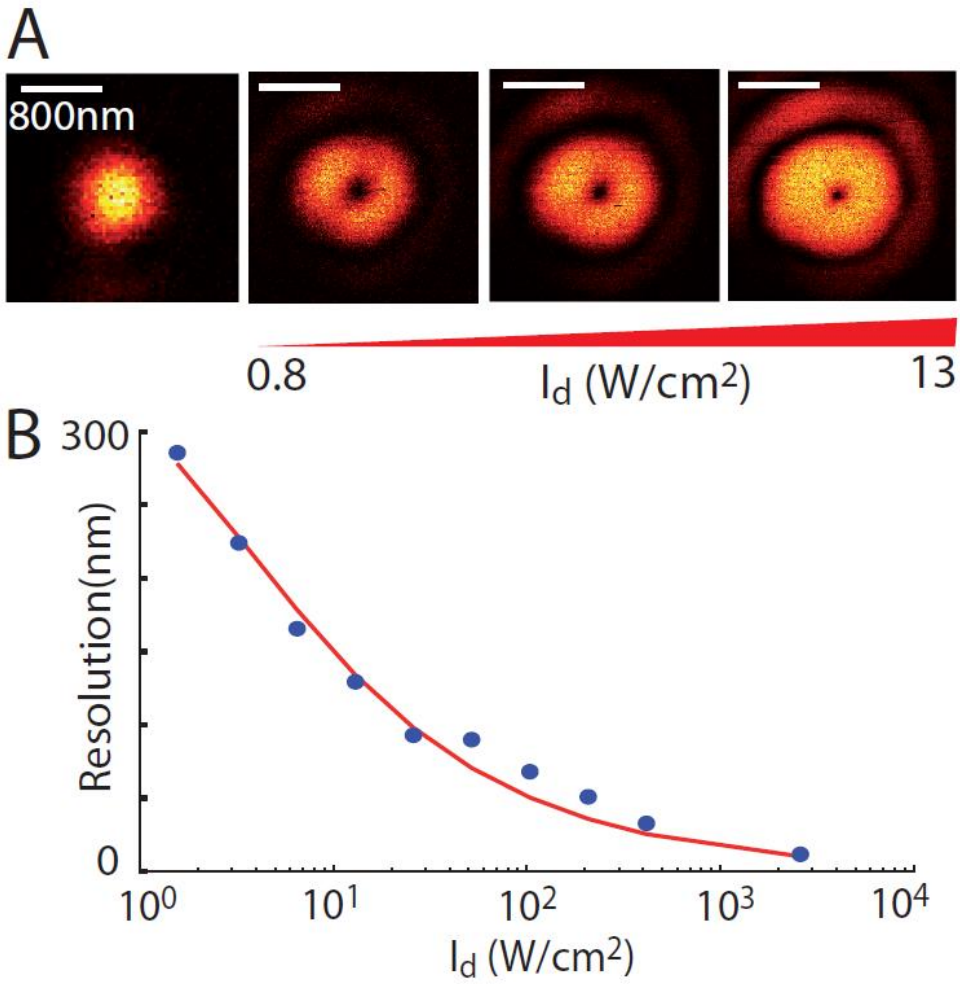

Figure 3.19: Experimental resolution obtained with direct-ESSat Microscopy: (A) Image of a single DBATT molecule obtained with a Gaussian beam (first) or the doughnut beam for different laser intensities. (B) The evolution of resolution of the direct-ESSat microscopy as a function of the doughnut beam intensity, obtained using Equation 3.4. The blue spots are the experimental data, fitted with Equation. 3.4. The saturation intensity I_S is extracted as $1.3\ W/cm^2$. The experimental images obtained are clearly in accordance with the simulated images.

The best resolution we obtained with direct-ESSat microscopy is shown in Figure 3.20. Figure 3.20.A shows the image obtained by exciting the molecule with an intensity $I_D = 13\ kW/cm^2$, that is about $10^4 \times I_S$. The minimum value of the fluorescence intensity at the center is 0.4 times that of the maximal value. This is due to the residual intensity at the doughnut center. The achieved resolution is 4.4 nm, close to the predicted value with Equation 3.7, i.e., 3.9 nm. The resolution is less than a hundredth of laser wavelength (589 nm) and approaches the size of the molecule with four orders of magnitude less intensity compared to that needed for room temperature STED. In principle, it is possible to attain an even higher resolution by increasing the excitation intensity again. However, because of the limitations offered by the mechanical stability of our system, we observed displacements in the minimal fluorescence signal between successive scanning lines in images acquired at higher laser intensities.

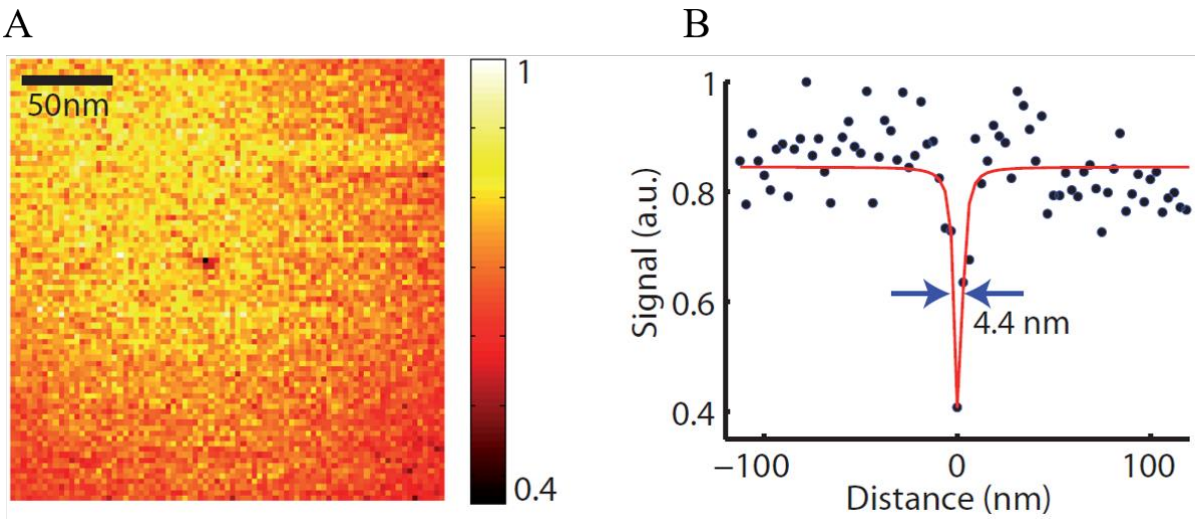

Figure 3.20: Best resolution obtained with direct-ESSat microscopy: (A) Direct-ESSat image of a single molecule excited with an intensity $I_D = 13\ kW/cm^2$. (B) Cross-sectional profile of the left image at the minimum intensity line.

We also could resolve two molecules closer than the diffraction limit by Direct-ESSat microscopy. Figure 3.21.A shows such an image. The two molecules are separated by 300 nm while the diffraction-limited limit of resolution is 380 nm. By using the fluorescence excitation spectra, we show that those molecules that are spatially close also have close optical resonances, as displayed in Figure 3.21.B. The excitation laser was tuned in frequency to the overlap of the resonances, so that both molecules are excited.

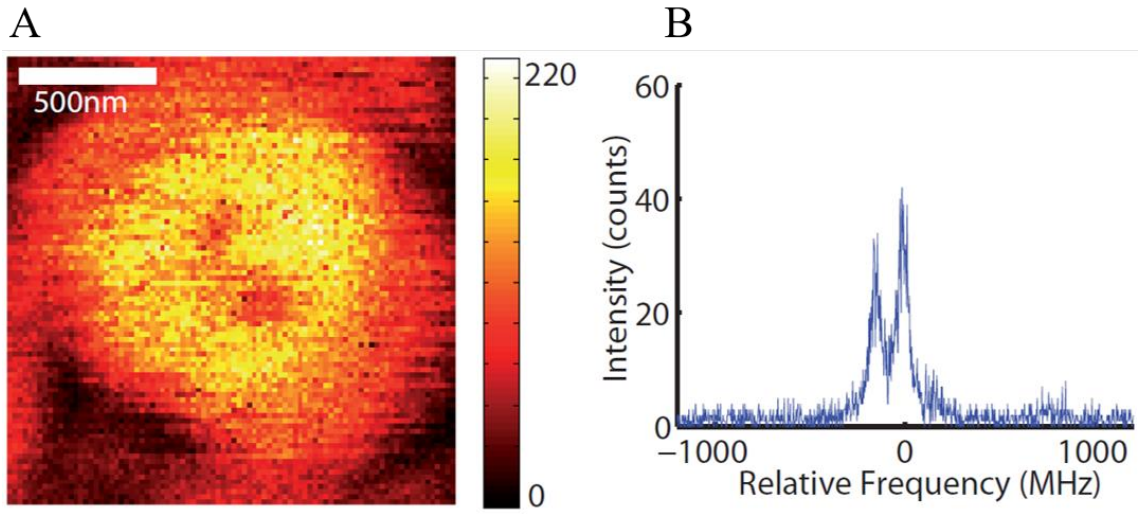

Figure 3.21: Resolving two molecules with Direct-ESSat microscopy: (A) Direct ESSat image of two molecules with $I_D = 130\ W/cm^2$. The pixel dwell times is 5 ms. (B) Fluorescence excitation spectrum of the two molecules shown in the left image ($I_D = 0.5\ W/cm^2$).

The two molecules are well resolved with two distinct minimum intensity points. However, the image has a very poor contrast, because of the background from the saturated fluorescence of each

molecule adds to the fluorescence minimum of the other one. Thus, Direct-ESSat microscopy is not an efficient method for resolving molecules. The image contrast can be improved by performing modulated-ESSat microscopy, presented in the next section.

3.6.2 Results of modulated ESSat Microscopy

Figure 3.22 shows the comparison between confocal, direct-ESSat and modulated microscopy images of the same single DBATT molecule. The direct-ESSat image gives a negative image of the molecule, where the intensity minimum denotes its position (Figure 3.22.A), while modulated-ESSat microscopy gives the "positive" signal over a dark background (Figure 3.22.B). This will drastically enhance the microscopy contrast. Still, there is some residual fluorescence present around the signal in the modulated-ESSat image. This is due to the fluorescence shot noise in the doughnut-shaped saturated fluorescence intensity. In order to improve the signal-to-noise ratio of the modulated-ESSat image, a longer acquisition time is required.

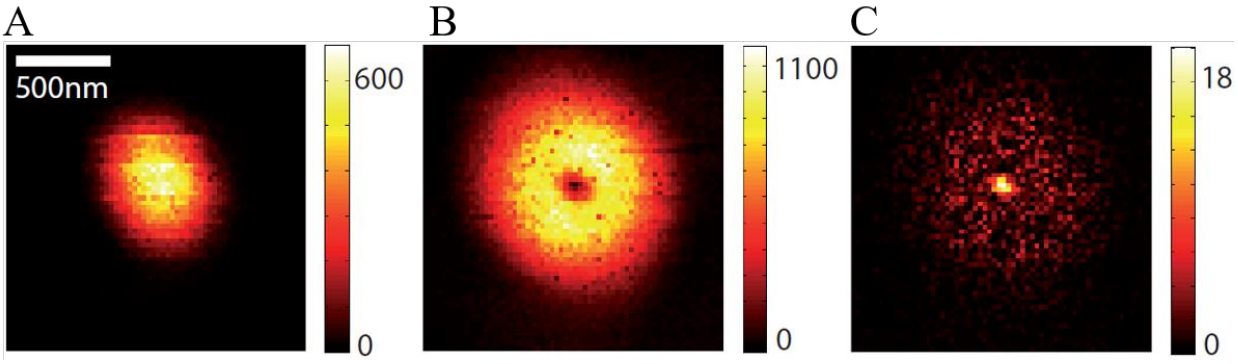

Figure 3.22: Comparison of confocal, Direct-ESSat and modulated-ESSat image of a single molecule. (A) Confocal image, $I_G = 0.7\ W/cm^2$. (B) Direct-ESSat image obtained with the doughnut beam excitation, $I_D = 26\ W/cm^2$. (C) Modulated ESSat image of the same molecule, with $I_G = 5\ W/cm^2$, $I_D = 26\ W/cm^2$, a pixel dwell time of 10 ms, and a modulation frequency of 1 kHz.

As with direct-ESSat microscopy, we can improve the resolution of the image by increasing the excitation light intensity. At $I_D = 2.2\ kW/cm^2$ and $I_G = 170\,W/cm^2$, we could achieve a resolution of 9 nm, as shown in Figure 3.23. Yet, in practice we could not achieve the same resolution as that obtained with direct-ESSat microscopy. Since modulated-ESSat images are recorded over a longer acquisition time, the images are more prone to mechanical vibrations of the system.

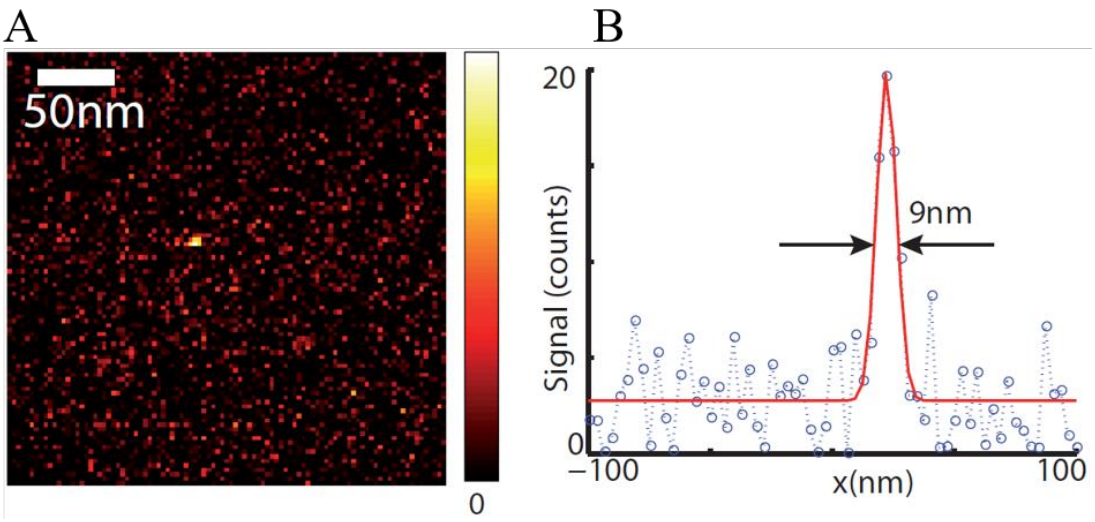

Figure 3.23: Modulated-ESSat imaging of a single molecule. (A) Modulated-ESSat image. (B) The intensity profile of the molecule and the Gaussian fit used to determine the FWHM. Pixel size: 3 nm, pixel dwell time 25 ms, $I_D = 2.2\ \mathrm{kW/cm^2}$ and $I_G = 170\,\mathrm{W/cm^2}$.

Finally, we could resolve two molecules separated by a distance smaller than the diffraction limit by modulated-ESSat imaging. As with the direct-ESSat imaging of two molecules, the two molecules are selected by taking the fluorescence excitation spectrum and by tuning the laser frequency to the frequency of maximal overlap of two molecular lines. A conventional confocal image of two molecules is shown in Figure 3.24.B. The images of two molecules overlap so that it is impossible to distinguish them. With modulated-ESSat, (Figure 3.24.C), the two molecules are resolved clearly and the image unravels the spatial separation of 200 nm between them.

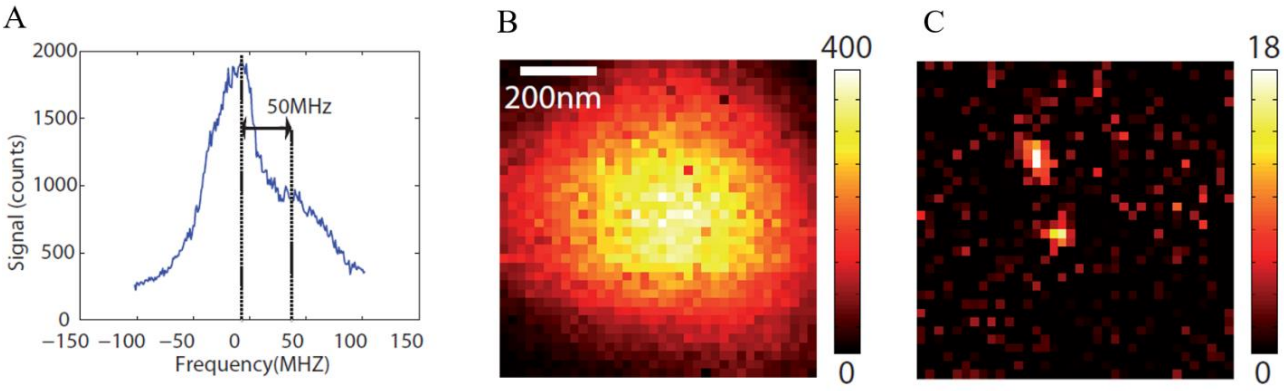

Figure 3.24: Super-resolution imaging of two molecules with modulated-ESSat microscopy. (A) Fluorescence excitation spectrum of two molecules at T = 2 K, $I_G = 1.5\,\mathrm{W/cm^2}$; (B) Confocal image, $I_G = 5\,\mathrm{W/cm^2}$, pixel dwell time: 4 ms; (C) modulated-ESSat image, $I_G = 100\,\mathrm{W/cm^2}$, $I_D = 260\,\mathrm{W/cm^2}$, pixel dwell time: 25 ms.

3.6.3 Effect of Mechanical Vibrations

One serious limitation of ESSat microscopy is the mechanical vibrations in the cryostat. The sample and the objective are placed inside the cryostat using a 60 cm long rod hanging from the top. At the bottom, it is fixed by using three springs around the insert. However, this might not provide sufficient mechanical stability for nm-resolution imaging. In addition, we have hysteresis in our open-loop piezo scanner. All these stability problems result in displacements of the minimal fluorescence signal between successive scanning lines in images acquired at high laser intensities.

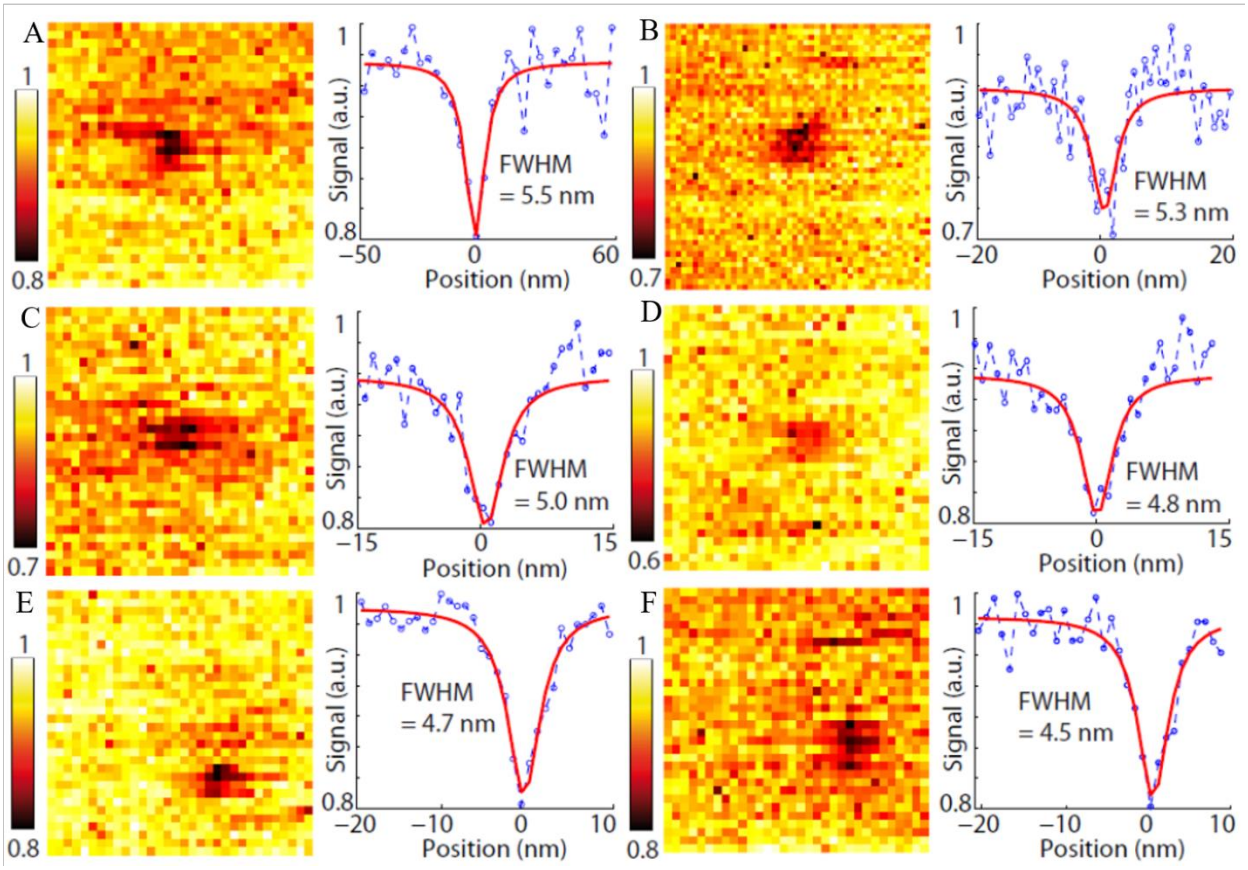

Figure 3.25: Direct-ESSat Microscopy images and their corresponding cross-sectional profiles for the same single molecule with different scans demonstrating a resolution of about 5 nm. Images are recorded at $I_D = 13\ kW/cm^2$ (A, B, E, F) and $I_D = 6.5\ kW/cm^2$ (C, D). Cross-sectional profiles are obtained by integrating several lines of the corresponding images. Number of lines averaged to derive the cross-sectional profiles: 1 (A, B), 2(C), 3 (D) and 4 (E, F). Pixel size: 1.9 nm (A) and 0.95 nm (B-F).

Figure 3.25 shows the images of a single molecule with different scans. The images do not look identical every time. There is a small displacement between successive scan lines. These displacements are due to the mechanical vibrations in the system. These displacements degrade the quality of the image and the precision of the resolution measurements while taking images with sub-ten nanometer resolution. We can decrease the effect of vibrations by decreasing the

acquisition time, but at the same time reducing the signal to noise ratio. Therefore, the next step of this work will be to improve the stability of the cryostat.

3.7 Conclusion

In this Chapter, we presented a new super-resolution imaging technique at liquid helium temperature based on the excited state saturation of single molecules, called the Excitation State Saturation (ESSat) Microscopy. ESSat microscopy could achieve a resolution of 4.4 nm, approaching the molecular size with a laser intensity of only a few tens of $\mathrm{kW/cm^2}$ and without any post-processing. The direct-ESSat microscopy gives negative images, i.e. the position of the molecule is given by a minimum of fluorescence signal position which is surrounded by a high background intensity. Therefore, the contrast is very poor when trying to resolve two or more molecules separated by sub-wavelength distances. This can be overcome with modulated-ESSat microscopy, where we add a modulated Gaussian beam along with a demodulation technique. A resolution of 9 nm can be achieved with modulated-ESSat microscopy. This modulated-ESSat approach is well suited to resolve two or more molecules below the diffraction limit. For instance, we could clearly resolve two molecules with overlapping optical resonances and separated by 200 nm, with few hundreds of $\mathrm{W/cm^2}$ intensity.

The lower resolution achieved for modulated-ESSat in comparison with direct-ESSat is due to longer acquisition times over which the mechanical vibrations of the cryostat are integrated. Such mechanical vibrations of the cryostat and the piezo scanner, as well as the residual intensity at the doughnut center, limit the resolution of ESSat microscopy. Thus, we need to try different mounting designs for the sample and the piezo scanner to get rid of the vibration issues.

The ability to achieve sub-diffraction resolution images of molecules with close optical resonances at low temperature offers the possibility to pursue different quantum optics investigations, such as coherent dipole-dipole coupling between molecules and entanglements. Yet, two-dimensional ESSat microscopy is limited since the axial resolution is that of conventional confocal microscopy, i.e. about three-times worse than the confocal lateral resolution. Extending the two-dimensional ESSat microscopy, to the axial dimension would enable to measure the exact distance between neighboring molecules with overlapping optical resonances. The next chapter is devoted to the development of three-dimensional ESSat microscopy.

Chapter 4

Three-Dimensional Excited State Saturation (ESSat) Microscopy

4.1 Motivation

Solid-state quantum emitters such as single organic molecules [227], quantum dots [228] or defect centers in diamond [229] are promising candidates for realizing quantum logic gates, quantum memories [230] or performing quantum computation [15]. Because most of the interactions between emitters occur at a very short distance, imaging these emitters at the nanometer scale level is a crucial step toward the manipulation and the control of delocalized states formed by their strong and coherent interaction [17]. However, nanometer-apart emitters are excited simultaneously by the laser and fluoresce, which prevents the use of the spectral selection to optically localize them with standard fitting methods [11] [12].

In chapter 3, we proposed a simple super-resolution optical nanoscopy method operating at cryogenic temperatures [204], which is based on the optical saturation of single fluorescent aromatic molecules (DBATT in octadecane).

In this chapter, we will describe the three-dimensional extension of Excited State Saturation Microscopy, which provides a resolution beyond the diffraction limit in both the lateral and the axial directions. We will start by detailing the phase mask we used to tailor the excitation beam profile in order to realize a 3D local intensity minimum and the associated constraints to reach a resolution of a few tens of nanometers. The principle of 3D-ESSat and the experimental details follow the upcoming sections, 4.3 and 4.4, respectively. As we will see in this chapter, the ESSat method can be also used to determine the 3D orientation of an emitting dipole. Indeed, the combination of the 3D electric field distribution and the dipole orientation will produce a unique fluorescence ESSat image, signature of the emitter. After reviewing the various existing methods [231], we will explain the procedure to obtain both the in-plane and the out of plane angles with one (or two) ESSat images. The results obtained with 3D-ESSat Microscopy will be presented in the next sections.

4.2 0-π phase plate for 3D imaging

As explained in chapter III, the Laguerre-Gaussian beam is well suited to perform two-dimensional super-resolved images [204]. However, its vanishing intensity along its optical axis prevents its use to increase the axial resolution as shown in Figure 4.1.

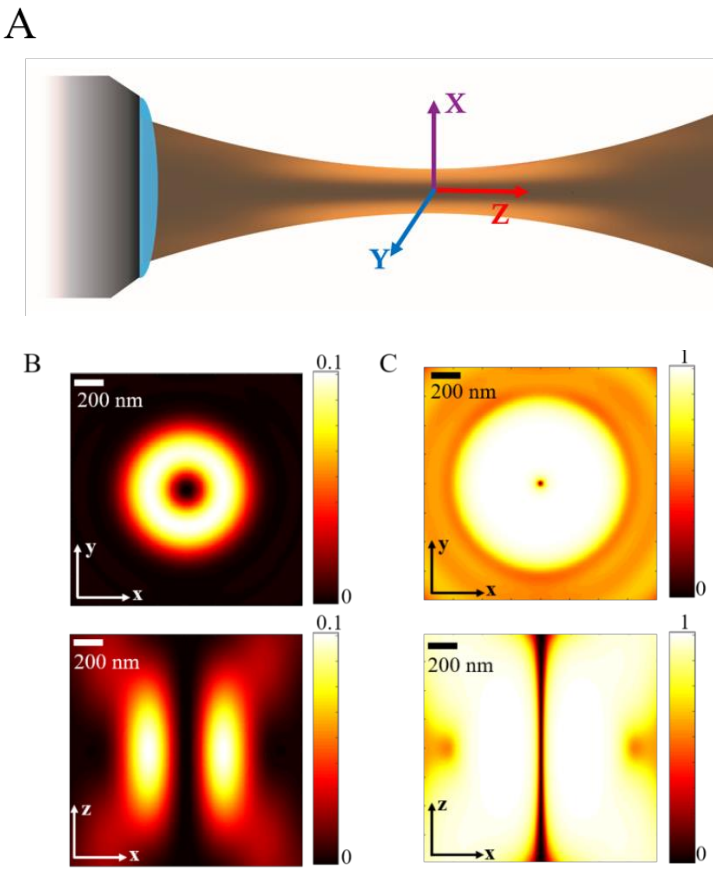

Figure 4.1: (A) Laguerre-Gaussian beam propagation close to the focal plane of an objective. The intensity distribution is zero along the optical axis. B) and C) Simulated images of a single molecule excited with a doughnut beam in the lateral direction (XY) and axial direction for different saturation parameters, I_D/I_S=0.1, (B) and (C) for I_D/I_S=100. The fluorescence signal is given in unit of R_∞. In these simulations, we average over an isotropic distribution of dipole.

To address this concern, we propose to pattern the excitation beam with a 0-π optical phase mask. This mask consists of a circular phase plate, which produces a π phase retardation on the central part of the incident beam as shown in Figure 4.2. In this configuration, a destructive interference occurs at the focal plane of the objective and leads to a zero-intensity region surrounded by two bright spots along the axial direction. The level of residual intensity in the "zero-intensity" region strongly depends on the π phase area.

To produce this phase mask, we apply to the SLM the following phase function [128],

$$\text{mask}(\theta, \psi) = \frac{\pi}{2}\text{sign}[\sin(z_0 \lambda k_0 \cos\theta)], \tag{4.1}$$

where z_0 is a real number comprised between 0.5 and 1, θ is the angle between the ray direction and the optical axis at the focus, ψ is the azimuthal angle of the exit pupil. The value of $z_0\lambda$ gives the distance between the bright spots with respect to the focal plane of the objective lens.

For a low NA objective, where the paraxial approximation is valid, the perfect destructive interference occurs when both areas, the π phase retardation and the 0-phase retardation, are equal when assuming a plane wave arriving on the SLM. However, in the case of high NA, it is not anymore valid, and the parameter z_0 has to be determined numerically by computing the electric field distribution, with the full vectorial calculation, at the focal plane of the objective.

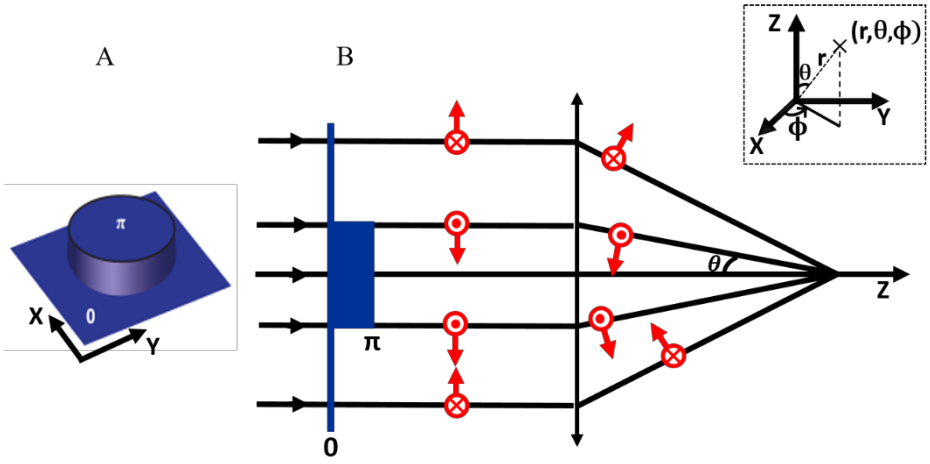

Figure 4.2: (A) 0- π phase mask. (B) Illustration of the polarization conversion of a tightly focused circularly polarized beam after passing through a 0-π phase plate. The arrows indicates the direction of the polarization of the electric field. Insert: Spherical coordinate system definition.

As in chapter III, the three electric field components and the intensity distribution are computed using the generalized vectorial Debye Integral (Equation 3.13), by replacing the helix phase mask with the expression given in Equation 4.1.

$$\mathbf{E}(r_2, \varphi, z_2) = \frac{i}{\lambda}\iint A_1(\theta, \psi).A_2(\theta).A_3(\theta, \psi).\exp[-ikr_2\sin\theta\cos(\psi - \varphi)]. \tag{4.2}$$

$$\exp(-ikz_2\cos\theta).\mathbf{a}(\theta, \varphi).\sin\theta.d\theta.d\psi,$$

where $\mathbf{E}$ is the electric field vector at (r_2, φ, z_2) expressed in cylindrical coordinates, λ is the excitation wavelength, $A_1(\theta, \psi)$ is the amplitude distribution of the input beam at the back focal plane, $A_2(\theta)$ is the apodization factor, $A_3(\theta, \psi)$ corresponds to the aberrations introduced by the optical system and $\mathbf{a}(\theta, \varphi)$ is the polarization unit vector of the excitation beam. Usually, the apodization factor is equal to $\sqrt{\cos\theta}$ to ensures the energy conservation before and after lens for an aplanatic system [209].

For the 0-π beam, $A_1(\theta, \psi)$ can be written as:

$$A_1(\theta, \psi) = \exp(i\, \mathrm{mask}(\theta, \psi)). \tag{4.3}$$

In the following, we will assume that the incoming electric field is a plane wave with a right-handed circular polarization. Figure 4.3 shows the intensity distribution in both (xy) and (xz) planes and the intensity cross-sectional plots along x- and z-direction. As expected, the destructive interference produces a zero-intensity located at the focal plane of the objective with two bright spots located symmetrically along the optical axis. Interestingly, a doughnut-shaped beam is also observable in the transverse plane. Even though the maximal intensity in this plane is about four times smaller than the maximal intensity along z, the resulting intensity gradient close to the center is not negligible and, as we will see later in this manuscript, we use the 0-π shaped beam to perform 3D ESSat images. Similarly, to the doughnut case, we define the optical resolution by the FWHM of the central dip in both lateral and the axial direction.

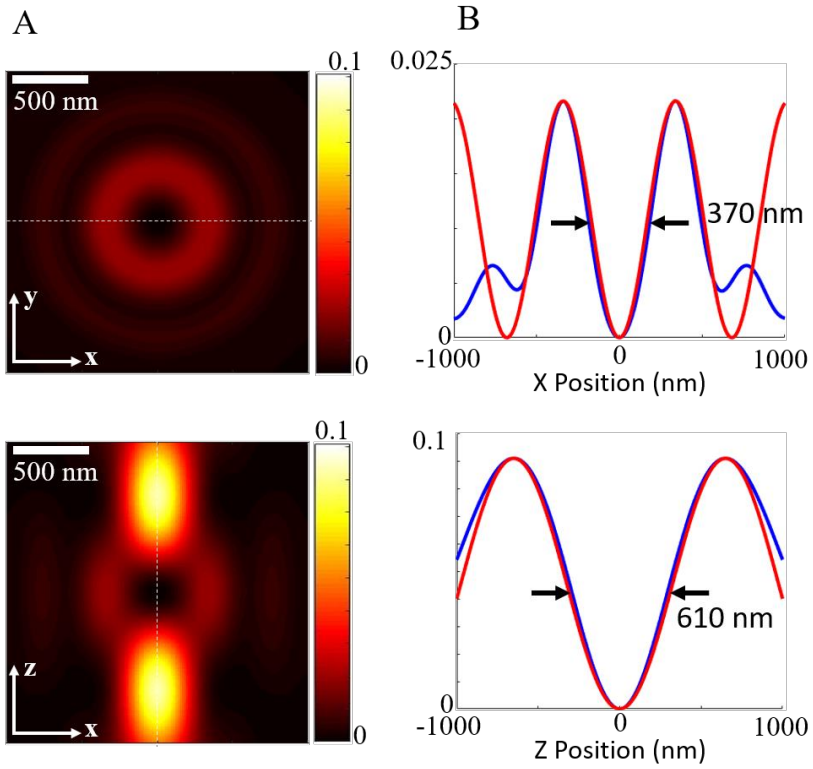

Figure 4.3: (A) Simulated images of the fluorescence intensity of a molecule excited with a 0-π beam in the lateral (XY) direction (top) and axial (XZ) direction (bottom). (B) The cross-sectional profile of the image along the dashed line in A (blue curve) and the approximating sinus function (red curve). The two profiles overlap well around the 0-π beam center. The FWHM of the blue curve determines the resolution. $I_{0-\pi} = 0.1 I_S$, where $I_{0-\pi}$ is the maximum intensity of the 0-π beam. At this low excitation intensity, the fluorescence intensity is linear with the excitation intensity and the resolution is set by the diffraction limit. The fluorescence signal is given in unit of R_∞.

4.3 Principle

4.3.1 Direct 3D-ESSat Microscopy

Three-dimensional ESSat Microscopy uses the same principle of two-dimensional ESSat. A single fluorescent DBATT molecule is scanned through the laser beam resonant on the ZPL, while its fluorescence is recorded with an avalanche photodiode. For laser intensities much smaller than the saturation intensity, the fluorescence image reproduces the beam profile intensity. At larger excitation intensities, the optical saturation leads to a broadening of the fluorescence image and a sharpening of the central dark spot and therefore to a resolution enhancement. In Figure 4.4, we plot the simulated fluorescence images of a molecule excited with the 0-π beam of wavelength 589 nm for different saturation parameters.

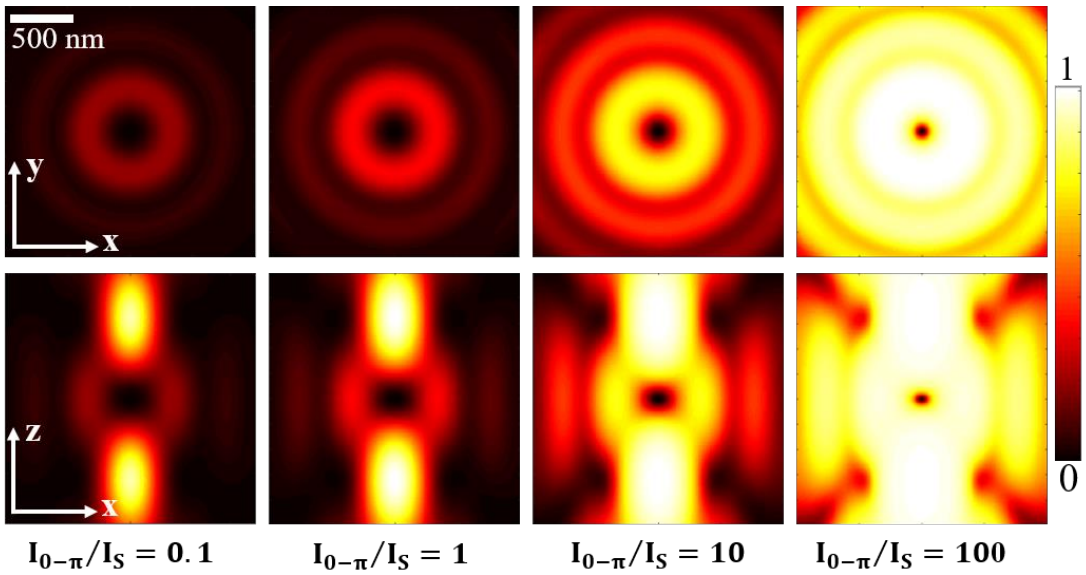

Figure 4.4: Simulated fluorescence images of molecule excited with a 0-π beam (λ = 589 nm) in the lateral (xy) and axial (xz) directions for different saturation parameters $I_{0-\pi}/I_S$. The color bar is normalized to the maximum fluorescence counts along the axial direction when $I_{0-\pi}/I_S = 100$. In these simulations, the dipole orientation of the molecule is not taken into account.

The cross-sectional profiles corresponding to the simulated images are shown in Figure 4.5. The profiles show a drastic reduction in the size of the central dip once the molecule is excited beyond the saturation intensity in both lateral and axial directions. At low intensities, for a wavelength of 589 nm, the large distances between the two axial bright spots produce a poor resolution close to 610 nm, while the lateral resolution is close to 370 nm. At larger intensities, the intensity gradient along z compensates this large distance and the resolution in the axial direction becomes better than the transverse one. In the real experiment, the ultimate resolution will be limited by the residual intensity at the central point of the PSF.

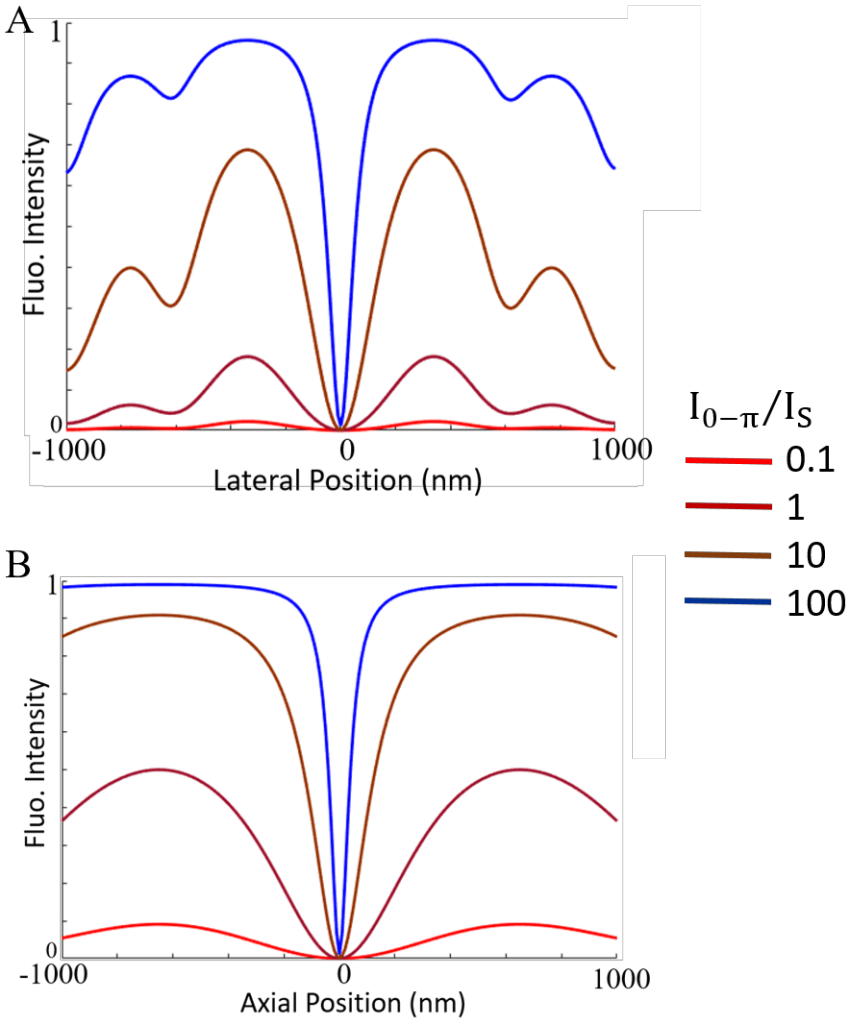

Figure 4.5: Simulated cross-sectional profiles of the fluorescence signal for different excitation intensities: A) along x, B) along z.

4.3.2 Theoretical resolution with a 0-π beam

As in chapter III, we derive the theoretical expressions of the optical resolution in both lateral and longitudinal directions by approximating the two intensity profiles near the focus by a sine function:

$$I_z(z) = I_{0-\pi}\sin^2\left(\frac{\pi z}{d_z}\right), \tag{4.4}$$

$$I_r(r) = \alpha\, I_{0-\pi}\sin^2\left(\frac{\pi r}{d_r}\right), \tag{4.5}$$

where $I_{0\text{-}\pi}$ is the maximum intensity along z and d_r and d_z the distance between the two intensity maxima. Numerically for $\lambda = 589$ nm, we found, $\alpha \simeq 0.22$, $d_r = 680$ nm and $d_z = 1300$ nm.

Therefore, the two theoretical expressions of FWHM can be written by taking the same approximation as Equation 2.31 as:

$$\mathrm{FWHM_z} = \frac{2d_z}{\pi}\arcsin\left[\frac{1}{\sqrt{2 + I_{0-\pi}/I_S}}\right], \tag{4.6}$$

$$\mathrm{FWHM_r} = \frac{2d_r}{\pi}\arcsin\left[\frac{1}{\sqrt{2 + \alpha\, I_{0-\pi}/I_S}}\right]. \tag{4.7}$$

In Figure 4.6 we plot both lateral and longitudinal FWHM as a function of the excitation intensity. At low ESSat intensities, the transverse FWHM is smaller (371 nm) than the axial FWHM (614 nm). This arises from the fact that even though I_r is much smaller than $I_{0-\pi}$, d_z is much larger than d_r. This picture drastically changes when the ESSat intensities increases. Indeed, the larger intensity gradient in the axial direction starts to dominate and the longitudinal FWHM becomes smaller than the transverse one. From this figure, we also notice that the ESSat PSF will be slightly anisotropic with an aspect ratio of 1.4 at very large excitation intensities ($I_{0-\pi} = 10^5 I_s$).

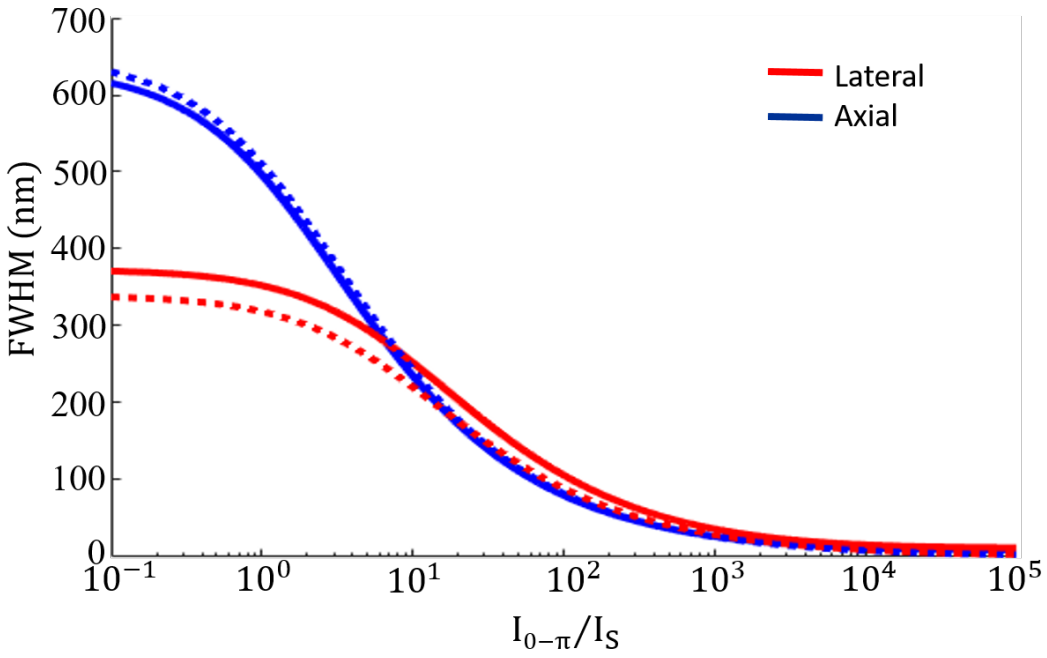

Figure 4.6: Resolution of the direct-3DESSat microscopy as a function of the 0-π excitation beam intensity of wavelength 589 nm, obtained using the sine wave approximation (dashed curves) and from the simulated images (solid curves).

The ultimate resolution, obtained for $I_{0\text{-}\pi}/I_s \rightarrow \infty$, strongly depends on the residual intensity at the PSF center. To quantitatively evaluate this effect, we derive the longitudinal FWHM by adding a residual background intensity (I_{res}) to the excitation intensity profile :

$$I(z) = (I_{0-\pi} - I_{res})\sin^2\left[\frac{\pi z}{d_z}\right] + I_{res}, \tag{4.8}$$

Following the same calculations presented before, we obtained:

$$FWHM_z = \frac{2d_z}{\pi}\arcsin\left[\sqrt{\frac{\beta + I_{res}/I_S\ (\beta - 1)}{(1-\beta)(I_{0-\pi}/I_S - I_{res}/I_S)}}\right], \tag{4.9}$$

where

$$\beta = \frac{1}{2}\left[\frac{I_{res}/I_S}{1 + I_{res}/I_S} + \frac{I_{0-\pi}/I_S}{1 + I_{0-\pi}/I_S}\right]. \tag{4.10}$$

Figure 4.7 presents the ultimate axial resolution, computed for $I_{o-\pi}=10^5 I_s$, as a function of I_{res} with a wavelength of 589 nm. As soon as $I_{res} \neq 0$, the resolution is degraded. Additionally, the amplitude of the central dip is strongly reduced at large intensities and will become hardly visible experimentally. To obtain a FWHM smaller than 20 nm, I_{res} must be smaller than $5.10^{-4} I_{o-\pi}$. This value imposes a strong constraint on the phase mask i.e. the determination of z_0. A dedicated method has been developed to minimize this residual intensity and will be presented in section 4.5.1.

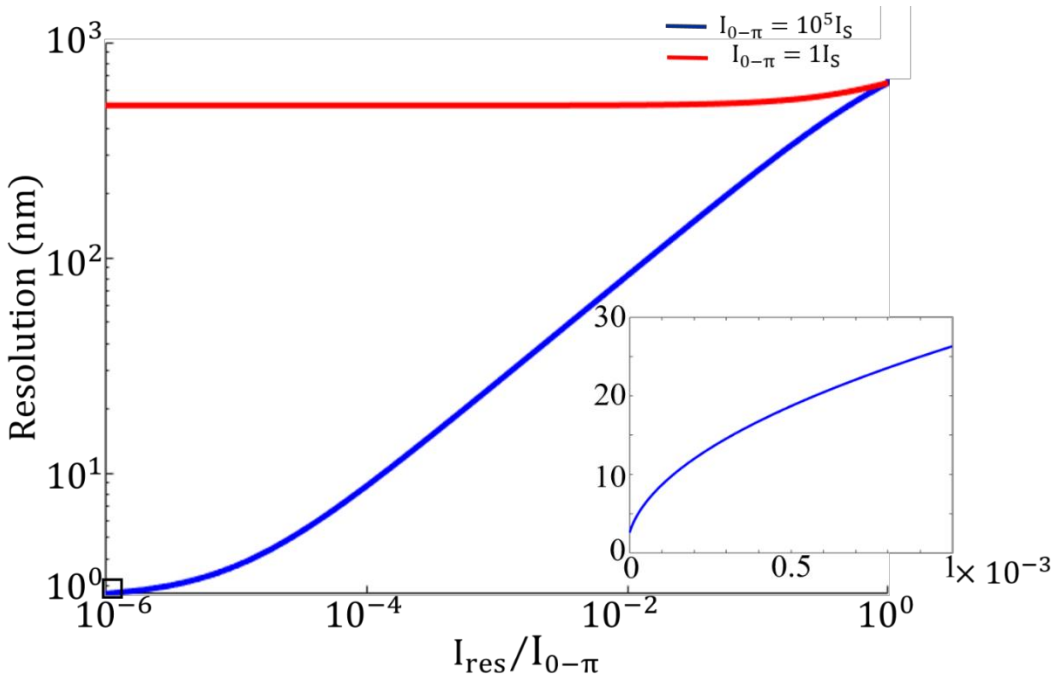

Figure 4.7: Evolution of the ultimate resolution ($\lambda = 589$ nm) as a function of the residual intensity I_{res} at the centre of the PSF for $I_{o-\pi} = 10^5 I_s$ (blue) and $I_{o-\pi} = I_s$ (red).

4.3.3 Effect of high NA objective

As we discussed in Chapter III, the scalar approximation does not hold to describe the electric field distribution at the focal plane of the objective. Therefore, the PSF will strongly depend on the incoming polarization. A special care has to be taken to determine the most appropriate one in terms of asymmetry, transverse and longitudinal intensity gradients as well as the value of I_{res}. In

this section, we will compute the PSF for different incoming polarizations with the Debye vectorial diffraction theory given by the Equation 4.2.

Figure 4.8 shows the intensity distribution in both lateral (xy) and axial (xz) planes for different incoming beam polarizations. For the two linear polarizations (along x in Figure 4.8.A and along y in figure 4.8.B), the intensity distribution in the transverse plane is not anymore invariant by rotation. Indeed, the intensity is weaker and "blurry" along the incoming beam polarization direction. Even though the residual intensity at the origin vanishes, the asymmetry of both the intensity distribution and the intensity gradients along x and y prohibits the use of such linear polarizations to produce an isotropic PSF in the transverse plane. Along the longitudinal direction, no noticeable effect is observable.

In Figure 4.8.C, which represents the case of right-handed polarization, the rotational invariance of the circular polarization produces, as expected, a symmetric intensity distribution in the transverse plane with a vanishing intensity at the focal plane. Along the longitudinal direction, the intensity profile has two symmetric lobes around the PSF center. As observed in the cross-sectional profiles (Figure 4.8.D), the longitudinal intensity profile is identical for all of the polarizations. This configuration is therefore the most favourable to perform 3D-ESSat images and will be used experimentally.

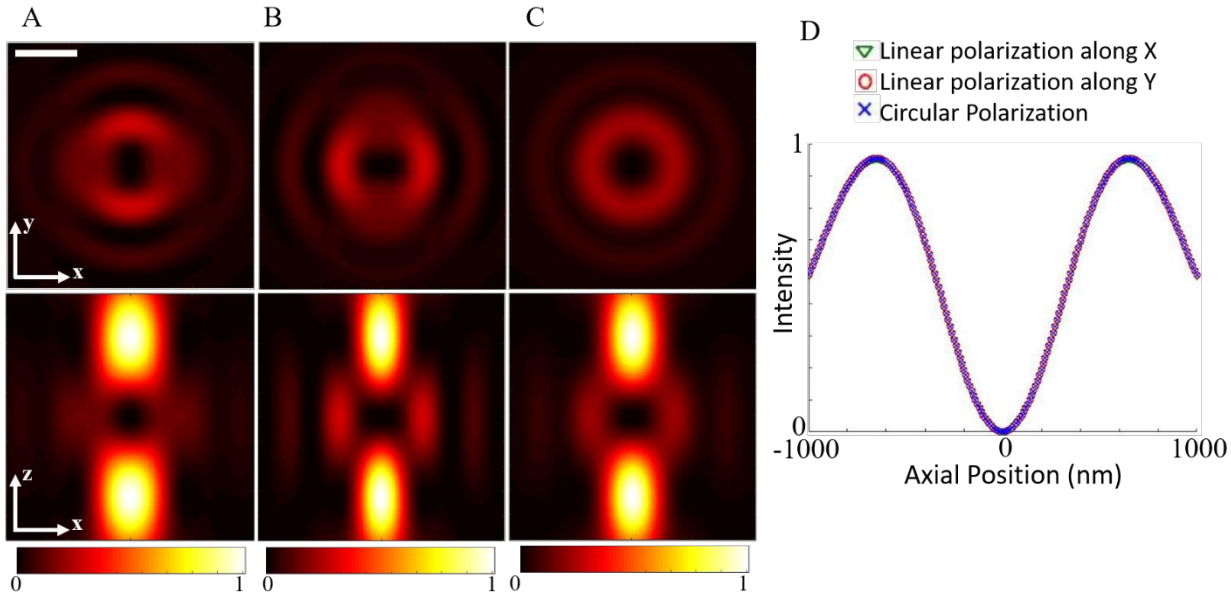

Figure 4.8: Simulated images of the 0-π beam intensity distribution with a linear polarization along x (A), along y (B) and for the right handed circularly polarization (C). NA = 0.95, λ = 589 nm. Scale bar: 500 nm. (D) Longitudinal intensity profiles for three different polarizations.

4.3.4 Modulated-3DESSat Microscopy

For a large concentration of emitters, the contrast will decrease drastically as the number of molecules (N) inside the excitation volume increases (drop of 1/N). As in reference [204] and chapter 3, we developed a modulated version of the 3D ESSat nanoscopy. The principle of modulated-3DESSat microscopy is identical to the modulated ESSat images in 2D. A 1 kHz temporally modulated weak Gaussian beam is overlapped on the 0-π excitation beam and we record the amplitude of the fluorescence signal modulation while scanning the sample through the excitation beam profile. The modulated beam polarization is set to be left-hand circular and orthogonal to the 0-π beam polarization (right-hand circular) to avoid optical interferences. Additionally, a frequency detuning of about 1 MHz (much smaller than the ZPL line-width) is applied on the modulated beam with two acousto-optical modulators (110 MHz and 109 MHz) to completely remove the interferences between the two beams. The fluorescence signal is then demodulated and the modulated image is extracted.

To compute the theoretical modulated ESSat images, we add the modulated laser beam in the time averaged scalar product $\langle \mathbf{d} \cdot \mathrm{Re}\{\mathbf{E_{0-\pi}} \exp(i\omega_1 t) + \mathbf{E_G} \exp(i\omega_2 t)\}\rangle_T$, where ω_1 and ω_2 are the optical frequency of the 0-π beam and the modulated Gaussian beam, respectively. The modulated fluorescence signal is then derived from the difference between the calculated fluorescence obtained with and without the modulated laser beam (see Figure 4.9).

The resolution of modulated-3DESSat microscopy can be obtained as a function of intensities of the 0-π beam and the Gaussian beam. The amplitude of the fluorescence intensity modulation can be written as:

$$\Delta R(r, z = 0) = R[I_r(r) + I_{Gaussian}(r)] - R[I_r(r)] \tag{4.11}$$

and

$$\Delta R(r = 0, z) = R[I_z(z) + I_{Gaussian}(z)] - R[I_z(z)]. \tag{4.12}$$

Considering the case where $r \ll d_r$ and $z \ll d_z$, we can approximate $I_{Gaussian}(r, z) \simeq I_G$, where I_G the maximum intensity of the Gaussian beam.

The resolution along the lateral direction can be defined as the FWHM of $\Delta R(r)$:

$$\Delta r = \frac{2 d_r}{\pi} \sqrt{\frac{A(I_G)}{\alpha\ I_{0-\pi}/I_S}}, \tag{4.13}$$

and along the axial direction can be defined as the FWHM of $\Delta R(z)$:

$$\Delta z = \frac{2 d_z}{\pi} \sqrt{\frac{A(I_G)}{I_{0-\pi}/I_S}}, \tag{4.14}$$

with

$$A(I_G) = \sqrt{(1 + I_G/I_S) + (1 + I_G/2I_S)^2} - (1 + I_G/2I_S). \quad (4.15)$$

We obtain the same expression as in the case of the 2D ESSat microscopy. When $I_G \gg I_S$, $A(I_G) = 1$ and the resolution of the modulated 3DESSat microscopy is the same as that of direct-3DESSat microscopy. A reduction of A by a factor of ~ 2 can be obtained using $I_G \ll I_S$. However, in the experiment a compromise has to be found between the resolution enhancement and the signal to noise ratio. Typically, we use $I_G \sim 100$ Is, for which $A(I_G) \sim 1$.

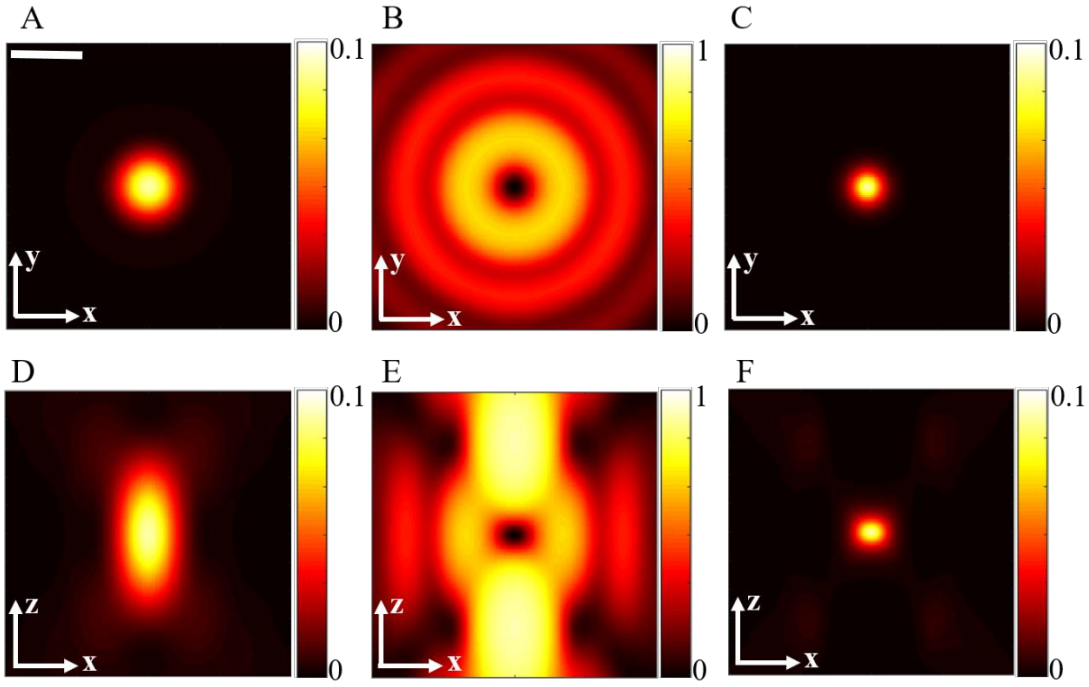

Figure 4.9: Simulations of 3D modulated ESSat imaging. (A) and (B) represent XY images of a molecule excited with a Gaussian beam and a 0-π beam respectively. (C) Modulated-ESSat XY-image. (D) and (E) represents XZ images of a molecule excited with a Gaussian beam and a 0-π beam respectively. (F) 3D modulated ESSat image in the XZ plane. $\lambda = 589$ nm, $I_G = 0.1I_S$, $I_{0-\pi} = 10I_S$. The fluorescence signal is given in the unit of R_∞. Scale bar = 500 nm.

4.4 Experimental setup

The experimental set-up for 3D-ESSat Microscopy is very similar to the 2D-ESSat version. We use the same host-guest system (DBATT embedded in octadecane) as it presents very interesting properties. First, the octadecane melting point is close to the room temperature (28°C). In such conditions, we can easily heat it and spread a drop of a highly-doped solution on a glass coverslip. By lowering the temperature back to room temperature, we obtain a thin polycrystalline layer with a thickness of about 1 µm, which is estimated from the analysis of Newton rings with a conventional microscope. The sample is then mounted on a 3D piezo scanning stage (7.5 µm×7.5

µm×2 µm), inserted in a pre-cooled cryostat and cooled down to 2K with liquid helium. As we mentioned before, we choose this host guest system because of its high photostability, a required property to perform ESSat images.

To scan the sample along the axial direction, we added to the 2D Attocube scanner (ANSxy50) a z piezo scanner (ANSz50). As a first step, we calibrate its displacement with a Michelson interferometer at room temperature. For that, we attached a gold mirror on top of the piezo stage and we use this movable mirror as one arm of the Michelson interferometer (see in Figure 4.10). For a full piezo displacement, we recorded and counted the number of fringes and we obtained a displacement of 17λ ± 0.5λ (for a wavelength of 589 nm, corresponding to 5.01 ± 0.15 µm). The z-piezo stage together with the gold mirror is then mounted on the sample holder and is inserted into the cryostat. We image the reflection of the beam on a CMOS camera for the different z piezo positions and we measure the beam divergence to calibrate the piezo excursion in the z-direction. Assuming the same beam divergence between room temperature and cryogenic temperature, we deduce the amplitude range of the piezo at 2K. We obtained a full displacement of 3.24 ± 0.13 µm at 2 K.

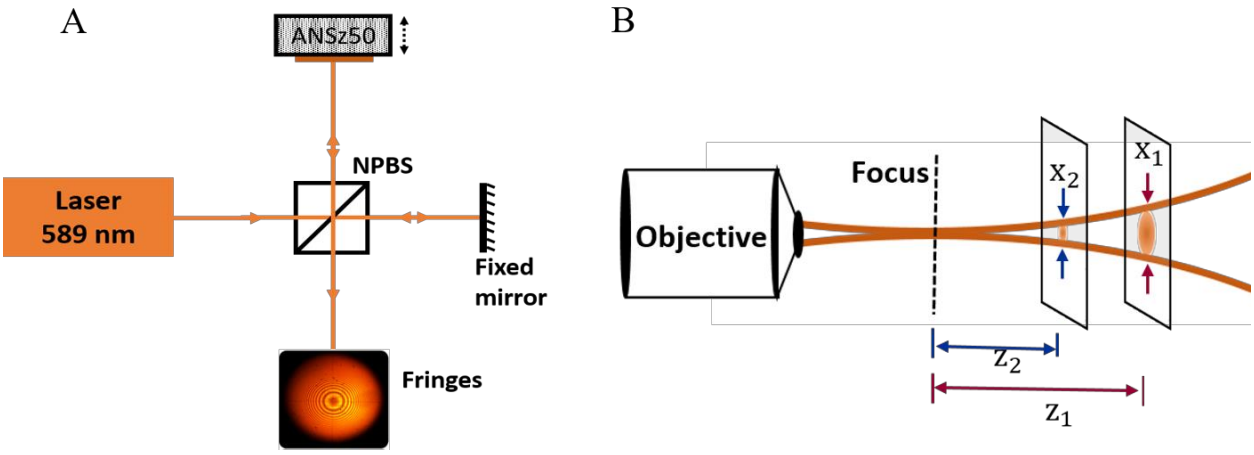

Figure 4.10: (A) Michelson Interferometer setup for the z-piezo scanner calibration. (B) Schematics of the piezo calibration from the beam divergence.

The experimental setup is depicted in Figure 4.11. The emitted photons from the molecules are filtered with a band-pass filter (centered at 629 nm, with a transmission band-width of 56 nm) and focused onto an avalanche Photodiode (active area of 200 µm). The overall magnification (x 33) in the detection path is chosen such that for any defocusing of the piezo stage during the 3D acquisitions, the variation of the detected signal is within 10%. This will avoid any artefact during the fluorescence image acquisition and reconstruction.

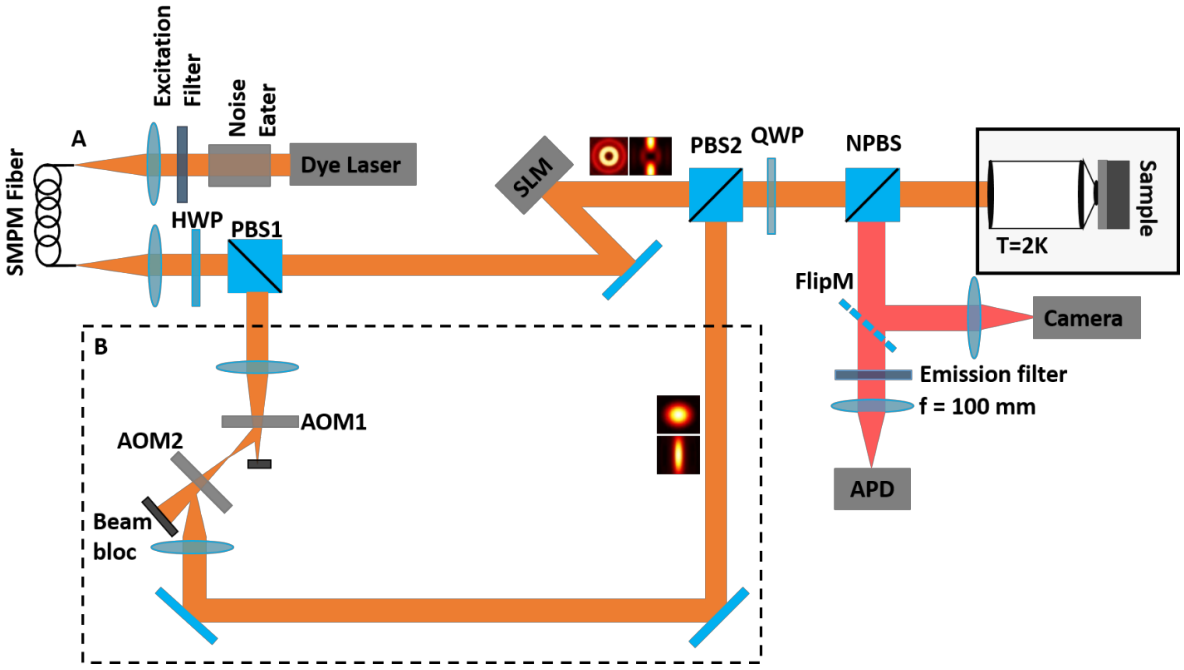

Figure 4.11: Experimental setup of a 3DESSat Microscope along with the (B) modulation part. (Excitation filter: 570/80, Emission filter: 629/56).

4.5 Characterization of the beam

4.5.1 Determination of z_0

Since the central dark spot of the PSF results from a destructive interference, its intensity strongly depends on the parameter z_0 as well as the intensity distribution on the back pupil of the objective. As we have seen before, this residual intensity strongly affects the ultimate resolution. Therefore, two questions arise: what will be the ultimate resolution in such conditions and what will be the accuracy needed on z_0 to obtain an axial resolution of 20 nm? To answer these two questions, we plot the theoretical behavior of I_{res} as a function of z_0. For this calculation, we assume that the incoming beam is a plane wave and is circularly polarized. Figure 4.12 shows this evolution and displays a minimum for $z_0 = 0.68$. For this value, the residual intensity is equal to $1 \times 10^{-7}\ I_{0\text{-}\pi}$, and is limited by the finite discretization while evaluating the integral of equation 4.2. According to Figure 4.7, this residual intensity corresponds to an ultimate resolution of 7 nm for $I_{0\text{-}\pi} = 10^5\ I_s$. Following the same arguments, the evolution of the residual intensity as a function of z_0 also permits to evaluate the mandatory accuracy to achieve a resolution of 20 nm. In such case, we obtain $z_0 = 0.68 \pm 0.01$. To determine this value experimentally, we follow the procedure described below.

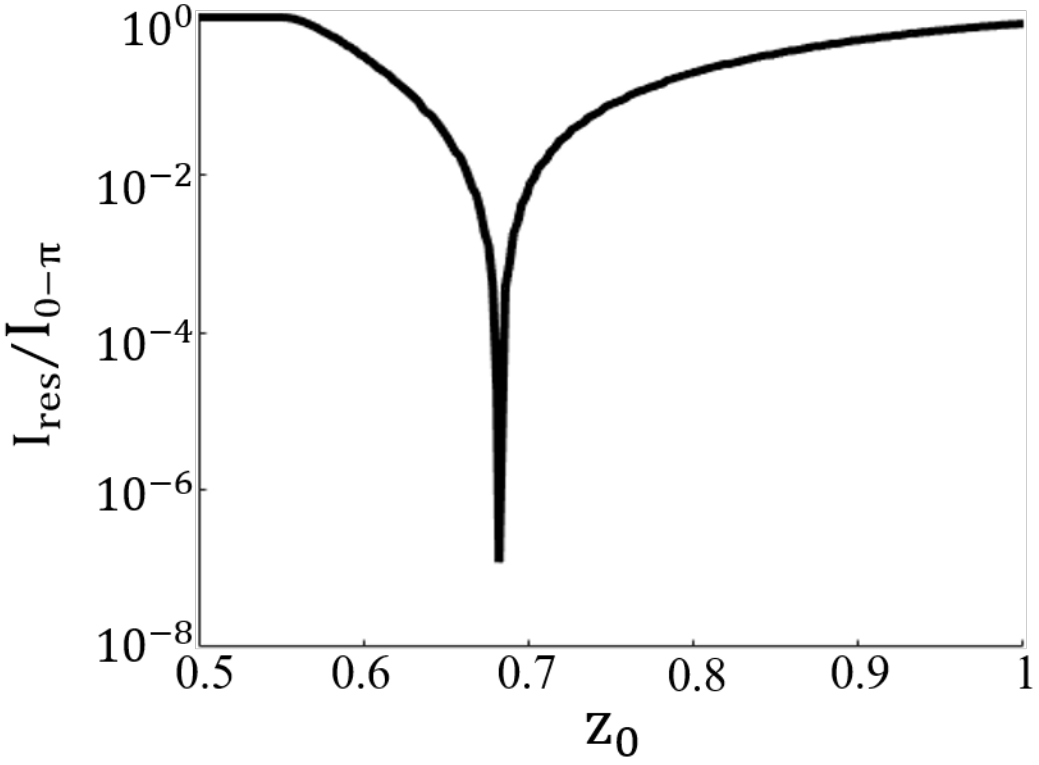

Figure 4.12: Evolution of the residual intensity I_{res} as a function of z_0. The optimal phase mask is obtained for z_0 =0.68.

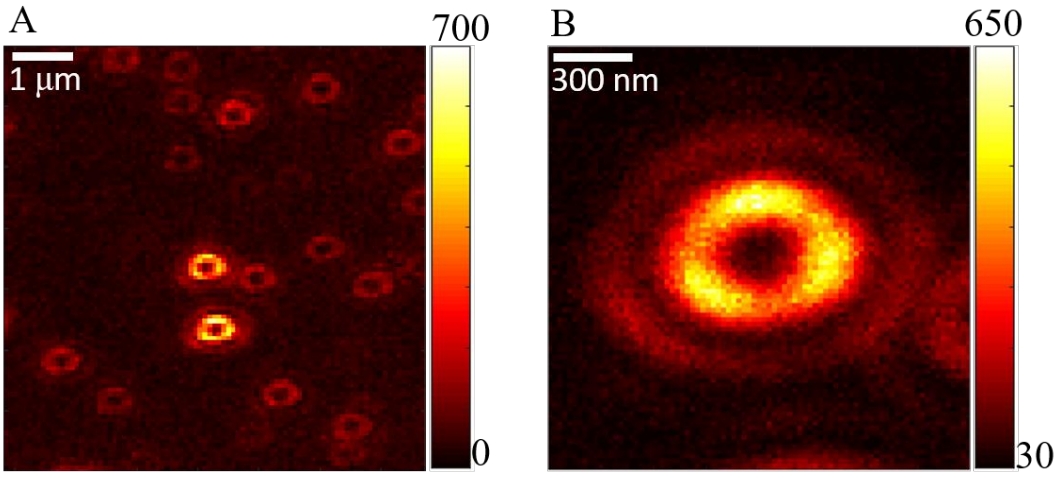

Figure 4.13: (A) and (B) XY images of crimson fluorescent beads excited with the 0-π beam at 589 nm with $z_0 = 0.69$ at room temperature. $I_{0-\pi} = 72\ W/cm^2$. Pixel dwell time: 5 ms. The color-bar corresponds to the number of detected counts per pixel dwell time.

A fluorescent molecule is scanned through the excitation PSF in different 2D XY planes. For each axial position, we measure the corresponding residual fluorescence intensity and we determine the PSF center along z and its associated I_{res}. We repeated this process for different z_0 and choose the one which minimizes the residual intensity ($10^{-4} \times I_{0-\pi}$). First, this method has been tested at room

temperature with a sample of fluorescent Crimson beads (20 nm diameter) embedded in a polymer matrix (thickness less than 100 nm). Experimentally, we found $z_0 = 0.69$, close to the theoretical value of 0.68. An example of the optimized PSF in the XY plane for z = 0, is given in figure 4.13.

We applied the same procedure at low temperatures. However, additional constraints due to cryogenics appeared and will be explained in the next paragraph.

4.5.2 Effects of aberrations at low temperature

Due to thermal constraints, the microscope objective induces a small wave-front distortion, mainly astigmatism and spherical aberrations, which alters the quality of the zero, reduces the intensity gradient, and therefore limits the ultimate resolution. We correct these aberrations by applying a set of eight well-chosen Zernike polynomials on the SLM. As the mechanical constraints are identical for both the doughnut and 0-π beams, we chose the same Zernike coefficients. To observe the beam quality, we use a gold mirror on the sample holder and image the beam reflected on the CMOS camera. Figure 4.14 shows the images after the optimisation for three different distances of the gold mirror.

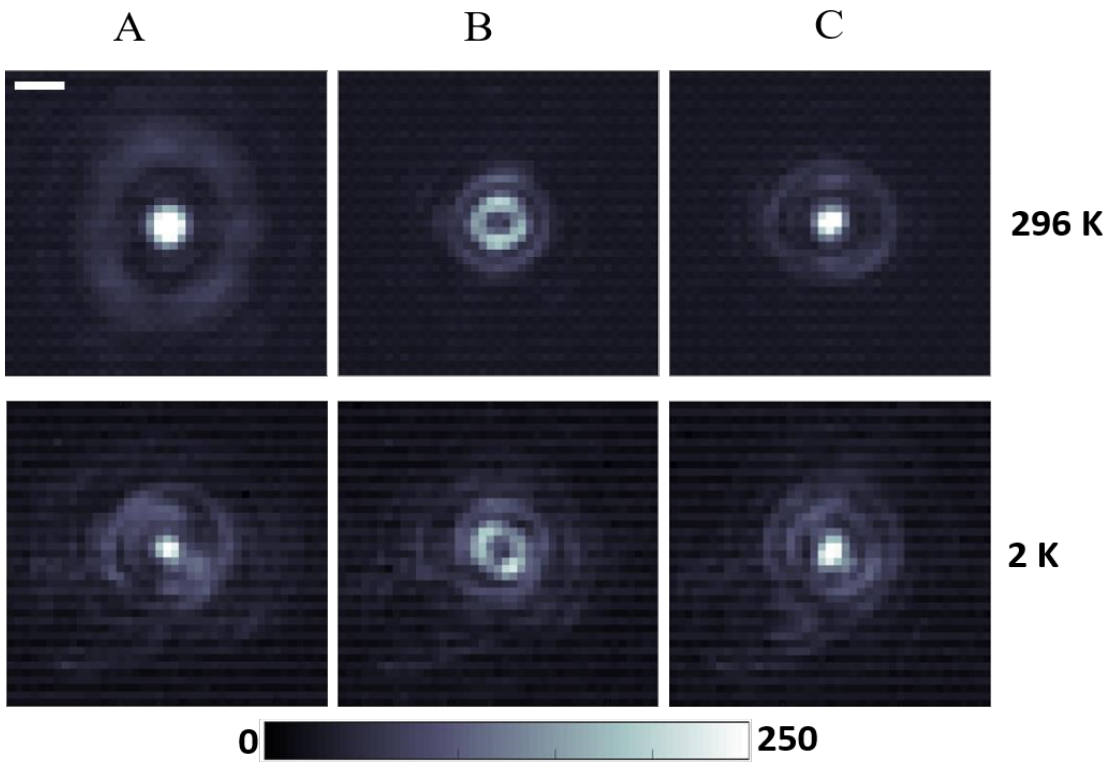

Figure 4.14: Camera images of the 0-π beam reflected on a gold mirror at room temperature (296K) and low temperature (2K). (A) and (C) Imaging each plane containing a bright spot equidistant from the focal plane. (B) Image when the gold mirror is in the focal plane. Scale bar: 1 µm. The colorbar is given in gray level.

After correcting these aberrations arising from the microscope objective, one has to take into account the propagation of the beam in the crystal before reaching the molecule axial position. Indeed, we assumed up to now that the molecules are close enough to the surface such that we can neglect the beam propagation in the crystal as well as the Fresnel coefficients occurring at the crystal surface.

For a large numerical aperture (NA = 0.95), this propagation causes spherical aberrations. With the optical design software "Oslo", we computed the wave-front distortion obtained for a propagation of 1μm in a refractive index of 1.5 and with a numerical aperture of 0.95. In these conditions, we found a wavefront distortion with an amplitude (peak to valley, P-V) of 0.3λ (Figure 4.15).

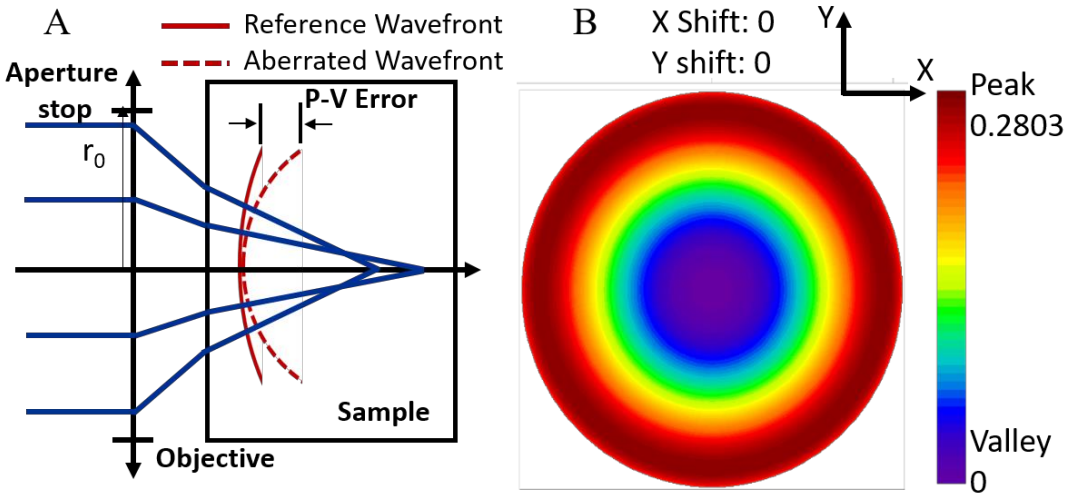

Figure 4.15: (A) Wavefront distortion arising from a spherical aberration induced by the propagation in a medium of refractive index 1.5. Marginal rays focus before the paraxial rays. r_o is the radius of the aperture stop. (B) Wavefront distortion map corresponding to a propagation of 1 μm in the sample. Colorbar in the unit of λ.

In Figure 4.16, we computed the intensity distribution in the axial plane (0xz) in presence of spherical aberration. To do so, we added to the Equation 4.2 the phase term, $\exp(-i2\pi\beta/\lambda(r/r_0)^4)$, where r_o is the pupil coordinate (defined in figure 4.15) and β the spherical aberration coefficient. We choose β such that P-V wavefront distortion corresponds to 0.3λ. As shown in Figure 4.16, the presence of spherical aberration induces a dissymmetry in the axial intensity profile (intensity difference of 15 % between the two bright spots). Moreover, the spherical aberration adds a residual intensity at the center position of the PSF. This can be explained by the fact that optical rays arising from different positions of the entrance pupil will not focus at the same z positions resulting in a non-perfect destructive interference. From Figure 4.16, we can see an increase of 20% for I_{res} at the paraxial focus for a wavefront distortion of 0.3λ. At the best focus position, located 80 nm away from the paraxial one (see figure 4.17.B), we obtained a residual intensity of 0.2%. This value will limit the ultimate resolution (to about 40 nm) and must be taken into account

experimentally. Moreover, the axial shift of the PSF center depends linearly on the spherical aberration parameter β as shown in figure 4.17.A.

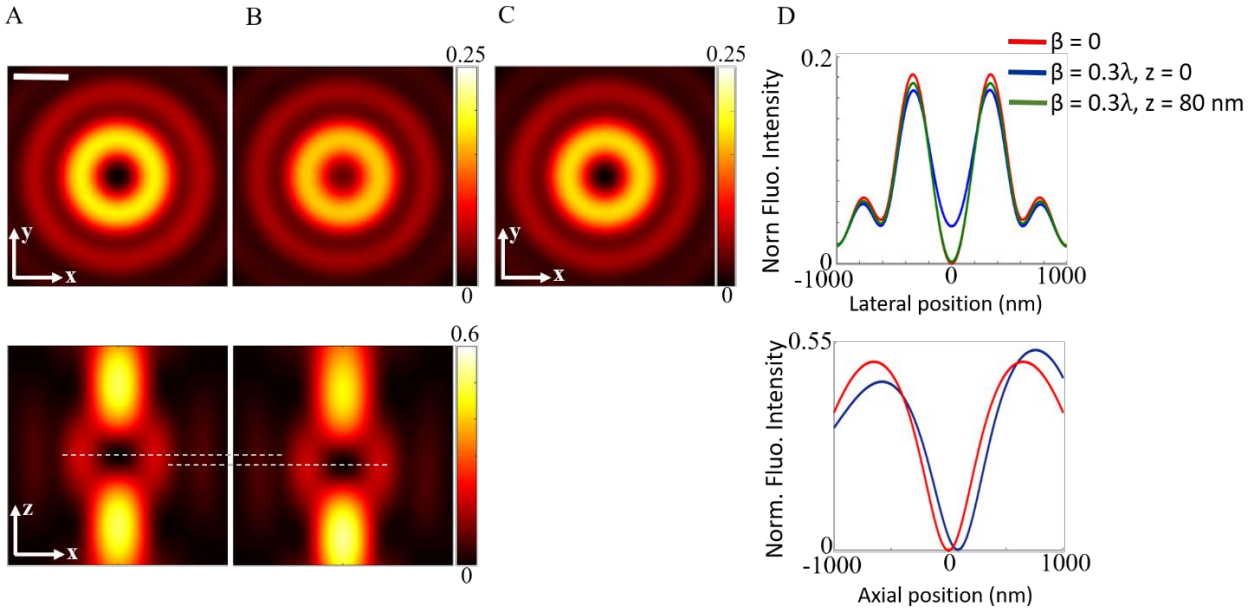

Figure 4.16: Simulated fluorescence images of a molecule located at the surface of the sample (A) and located 1µm inside the crystal at the paraxial (z = 0) position (B) and at the best axial position (z = 80 nm with respect to the paraxial position) (C). The top images are computed at the paraxial focal plane for an excitation intensity of I_s. Scale bar: 500 nm. (D) Cross-section profiles along the lateral and axial directions for spherical aberration coefficient, β = 0 (red curve), β = 0.3λ (blue curve) and for β = 0.3λ at the best axial plane (green curve). λ = 589 nm, the colorbar is given in the unit of R_∞.

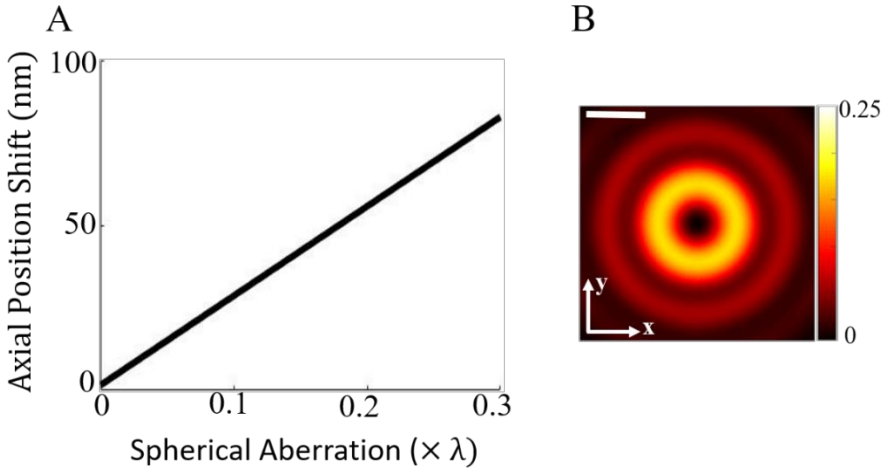

Figure 4.17: (A) axial position shift as a function of the spherical aberration coefficient. (B) Simulated fluorescence image at the best axial position (shifted by 80 nm with respect to the paraxial position). I_{res} = 0.2 % in this case. λ = 589 nm, scale bar: 500 nm.

Two examples of such spherical aberration effects are shown in Figure 4.18. Two experimental XZ fluorescence images of single molecules located inside the crystal were recorded at an intensity of 5.7 W.cm^{-2}. A noticeable asymmetry of the two axial bright spots is evidenced in the figure 4.18.B, (22% difference in fluorescence intensity), indicating the presence of spherical aberration, while the axial profile of the A molecule is almost symmetric. From the dissymmetry, we can estimate the amplitude of the spherical aberration coefficient. From a fit of the axial profile and assuming that the molecule is not saturated, we found for the B molecule, $\beta = 0.4$, which corresponds to a depth of 1.4 μm.

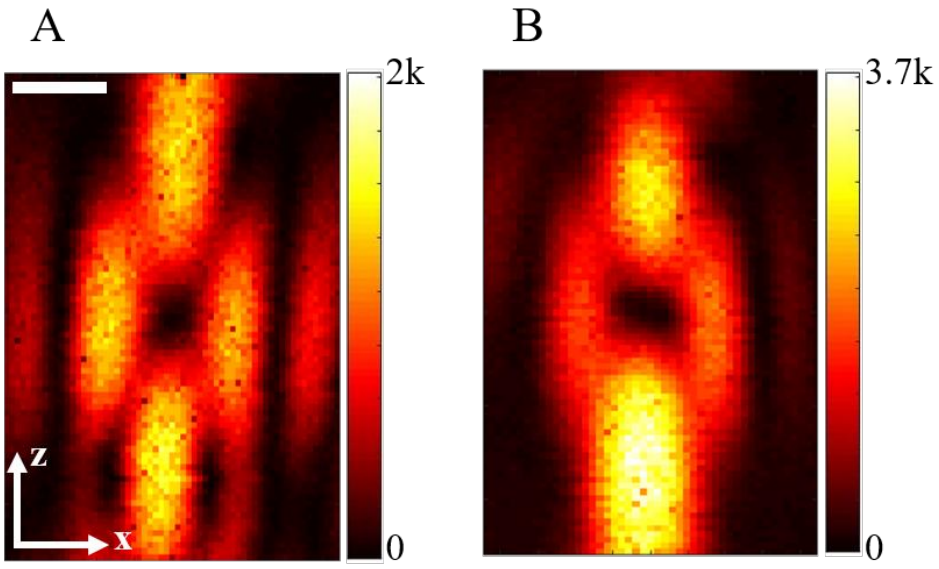

Figure 4.18: Experimental ESSat images recorded for two different molecules in the XZ plane. A) The axial profile of this molecule is almost symmetric, which reflects the absence of spherical aberration. B) For the second molecule, the clear dissymmetry of the two bright spots intensities (22%) indicates a large spherical aberration. With this ratio, we extract the spherical aberration coefficient β (0.4) and the location of the molecule position inside the crystal (1.4 μm). For image A) : the unit of the colorbar is in counts per 5 ms, $I_{0\text{-}\pi} = 8$ W.cm^{-2}, scale bar: 500 nm. For image B): the unit of the colorbar is in counts per 10 ms, $I_{0\text{-}\pi} = 5.7$ W.cm^{-2}, scale bar: 500 nm.

In Figure 4.19, we plot the residual intensity I_{res} as a function of β. We observe a cubic increase of I_{res} and I_{res} reaches $2.10^{-3} I_{0\text{-}\pi}$ for $\beta = 0.3\lambda$. Figure 4.19. B shows the axial cross-section fluorescence intensity profiles for $\beta = 0$ and 0.3λ for two $I_{0\text{-}\pi}$ intensities. We see a clear axial shift (80 nm) of the minimum position and an increase of the $FWHM_z$ in the best imaging plane (figure C). For $\beta = 0.3\lambda$, the ultimate resolution is equal to 32 nm (computed for $I_{0\text{-}\pi} = 10^5 I_s$).

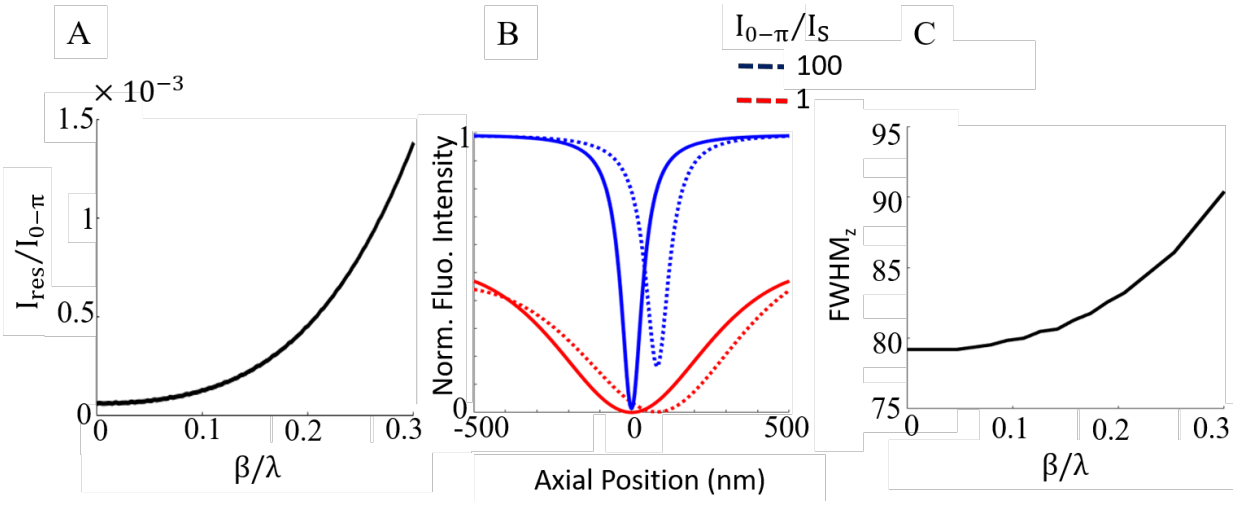

Figure 4.19: (A) Evolution of the residual intensity as a function of the spherical aberration coefficient at the best imaging plane. (B) Axial cross-sectional fluorescence intensity profiles for a single molecule excited at $I_{0-\pi}/I_S = 1$ and 100, in presence (dashed line) or absence (solid line) of spherical aberration (0.3λ). (C) Evolution of the axial FWHM with the spherical aberration coefficient at the best focus plane for $I_{0-\pi}/I_S$ =100.

In the host matrices, the molecules are immobile with fixed dipole orientations. In such conditions, the effects of dipole orientation could not be neglected. In the next section, we will study this effect in detail.

4.6 Effect of molecular dipole orientation

4.6.1 Methods to determine the dipole orientation

Various techniques have been developed, over the last two decades, to measure fixed or time-dependent single molecule dipole orientations [232] [233] [234]. These techniques are divided in three main categories:

- The first one employs standard wide-field illumination configuration to excite the emitters with linearly polarized light and deduce the dipole orientation from the fluorescence intensity by rotating the excitation polarization [235] [236].
- The second one is based on the analysis of the spatial distribution of the light emitted by a fluorescent molecule [237] [238].
- The third is based on the scanning of the dipole into the PSF of a tightly focused beam (by high NA objective) [239].

The first method is the most simple and straightforward. Generally, this solution is combined with the detection of the fluorescence signal in two orthogonal polarizations to map the evolution of the linear dichroism of the emitters. However, the non-unicity of this problem (determination of ϕ) as well as the missing information to determine the polar angle limit this method. Upgraded versions using four detection channels at 0°, 45°, 90°, and 135° can break this degeneracy [240].To

efficiently measure the dipole orientation along z, Goldman and co-workers [232] proposed to use, in addition to the previous illumination scheme, a TIRF illumination. In this latter case, the z component of the electric field is larger and the molecules with smaller polar angles can be measured with a better accuracy.

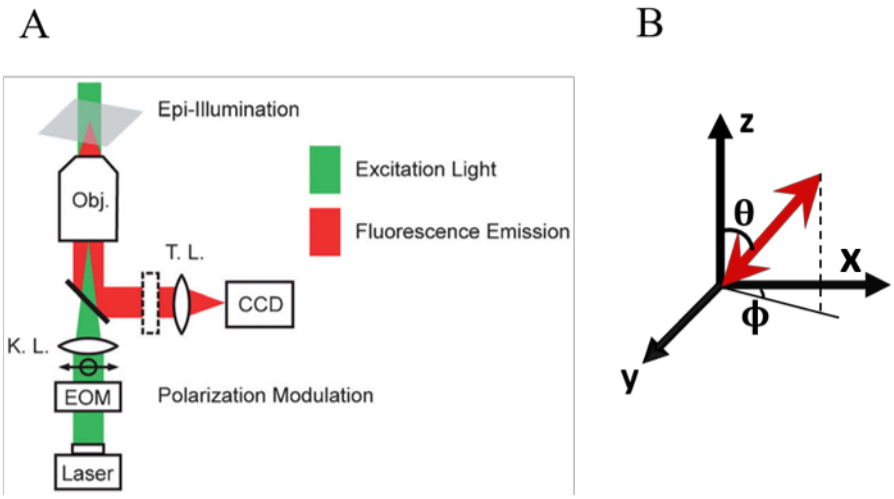

Figure 4.20: (A) Polarized illumination/detection method: The polarization of the illumination light (green beam) is modulated with an electro optic modulator (EOM). A Kohler lens (K.L.) is used to focus the beam at the back focal plane of the microscope objective (Obj.). The fluorescence emission from the sample is then collected and detected on a CCD camera. A polarizer (indicated by the dashed box) can be added in the detection path to perform emission polarization measurement. Figure extracted from [231]. (B) Schematics of molecular dipole with parameters θ (polar angle) and ϕ (azimuthal angle).

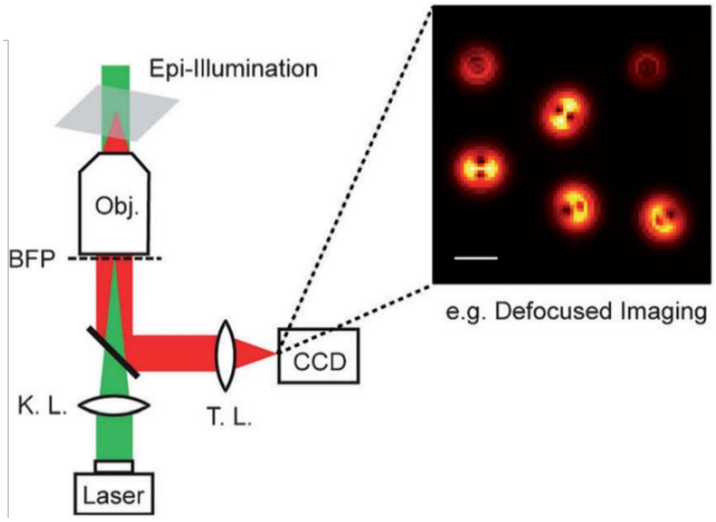

Figure 4.21 details a typical experimental setup used for the dipole orientation measurement with the non-uniform emission pattern technique. The spatial distribution of the single emitter emission pattern is then recorded with a defocused camera. From this unique signature, one can find the dipole orientation. Figure extracted from [231].

The second category exploits the property of the non-uniform emission pattern of a single emitter. In the far field, the emission dipole is well approximated by a classical dipole whose radiation pattern is proportional to $\sin^2(\delta)$, where δ is the angle between the Poynting vector and the dipole orientation. Since the objective acts as a spatial frequency low pass filter, only a subset of emitting rays will be collected by the objective and the resulting image pattern will depend on the orientation of the molecule (see Figure 4.21). This method has been firstly demonstrated by Sepiol et al. with terrylene molecules embedded in a polymer at cryogenic temperatures [237].

The third method makes the use of the distinct spatial patterns of the polarized fields at the focus of a microscope objective with a large numerical aperture. As we have seen in this chapter, the large NA will lead to a significant mixture of the three electric field components close to the focus [239]. The amount and direction of polarization mixing of each ray entering the objective is highly dependent on the angular and radial coordinates of the ray relative to the aperture. This results in specific intensity patterns of each polarization component in the focal plane. Thus, the intensity pattern of a single emitter directly indicates its 3D orientation. Different configurations have been used so far such as annular illumination [241] [206], bone-shaped amplitude/phase mask [242], azimuthally or radially polarized doughnut modes or double helix-PSF–based measurements [243].

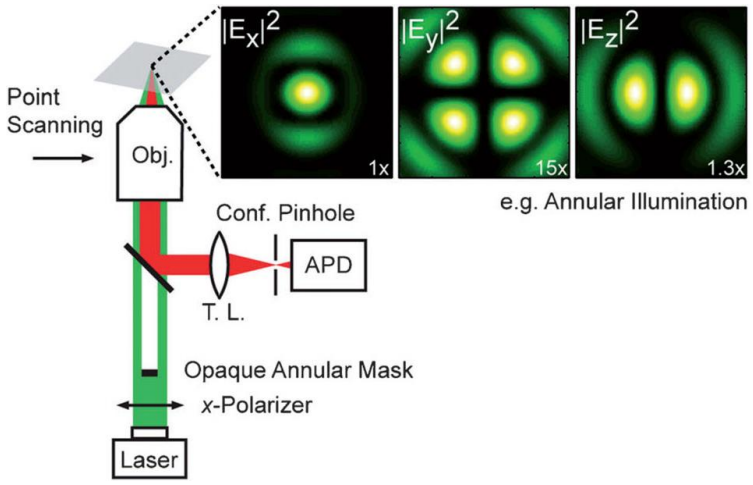

Figure 4.22: A typical experimental setup used for the dipole orientation measurement using a structured light illumination for different incoming polarizations. In this example, an x-polarized illumination light passes an annular mask before being focused by the objective. The intensity patterns are shown for each incident polarization. Confocal scanning will directly provide the orientation of the molecular dipole: a molecule with an arbitrary orientation will be displayed with patterns that are linear combination of these patterns [241]. Figure extracted from [231].

We propose to go even further by applying the same kind of method and using the 3DESSat microscopy to measure both θ and ϕ of a given dipole orientation.

4.6.2 Dipole orientation using ESSat

Taking a circularly polarized 0-π beam, the spatial distributions of the intensities for the x, y and z polarizations are shown in Figure 4.23. The anisotropy of the intensity patterns for the x and y

polarization components in the focal plane, as well as the presence of a z polarization component, are due to the polarizing mixing that occurs under high NA (0.95) focusing. Since a molecule can only be excited with the polarization component that is parallel to its absorption dipole moment, a single molecule with an arbitrary dipole orientation will be imaged with a specific linear combination of the spatial patterns. The analysis of fluorescence images of single molecules with ESSat microscopy will thus directly reveal their 3D-dipole orientation.

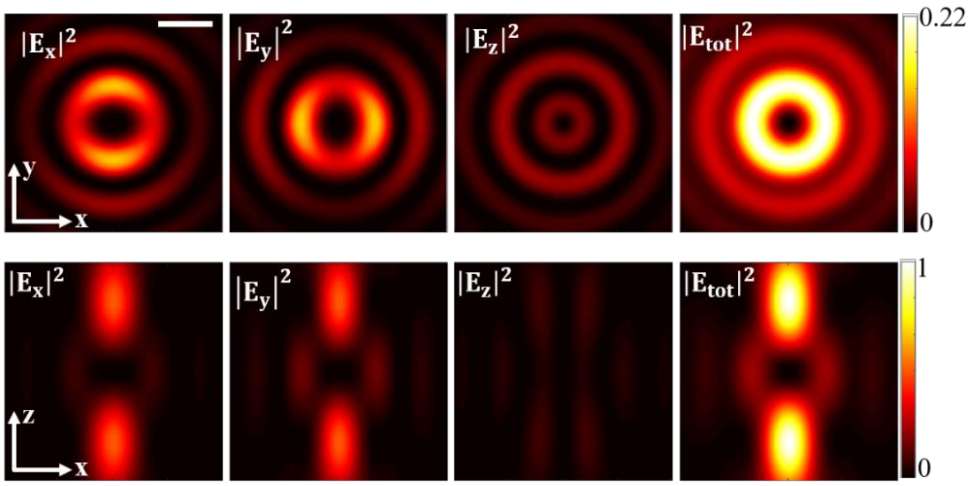

Figure 4.23: Intensity patterns of the x, y, z polarization components of a circularly polarized 0-π beam illumination light in the xy and xz planes. The colorbar is normalized to the maximum intensity in the respective plane. λ = 589 nm, NA = 0.95, scale bar: 500 nm.

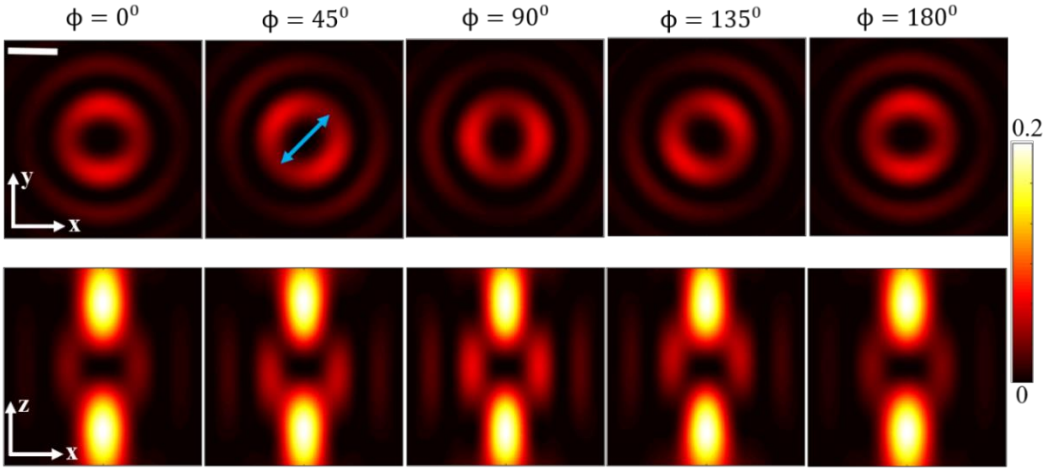

Figure 4.24: Simulated 3D ESSat images for θ=90°, and for different values of ϕ. The blue arrow indicates the dipole orientation in the case of ϕ =45°. Images computed for $I_{0\text{-}\pi} = I_s$, λ = 589 nm, NA = 0.95, scale bar: 500 nm.

First, let's consider the case of in-plane dipole orientations, (i.e. θ = 90°). Figure 4.24 shows a selection of simulated xy and xz images obtained for different ϕ angles. It is easy to determine the in-plane dipole orientation by fitting the central part of the image with an ellipse. The dipole

orientation is then directly given by the direction of the major axis of the ellipse. For the xz images, a slight dependence of the PSF shape with ϕ is observable in Figure 4.24. As we will show in the next paragraph, the choice of the axial imaging plane will play an important role in the determination of the complete 3D dipole orientations.

Now, let us consider the case of a dipole whose projection in the xy plane is aligned along x (i.e. $\phi = 0^0$). Figure 4.25 shows a selection of xy, xz and yz images computed for different θ. Starting from $\theta = 90^0$, the central region of the PSF in the xz imaging plane becomes distorted when θ decreases and the iso-intensity contours are well approximated by an ellipse. The tilt of the ellipse long axis with respect to the x-axis increases to reach its maximum value (90°) at $\theta = 90°$. When $\theta = 0°$, the dipole only feels the longitudinal component of the electric field, which vanishes along the optical axis. No axial resolution enhancement is therefore possible in this configuration. To determine the link between the dipole orientation and the ellipse tilt, we extract an iso-intensity contour close to the PSF center at $3.10^{-4}I_{0\text{-}\pi}$, fit this contour with an ellipse and determine the orientation of its major axis. The evolution of the ellipse major axis angle as a function of θ (see Figure 4.26) shows that these angles are equal. This striking property will provide a straightforward way to determine θ from the experimental XZ images. It is worth noting that, this relationship is not linear anymore when the dipole is not contained in the axial plane imaged.

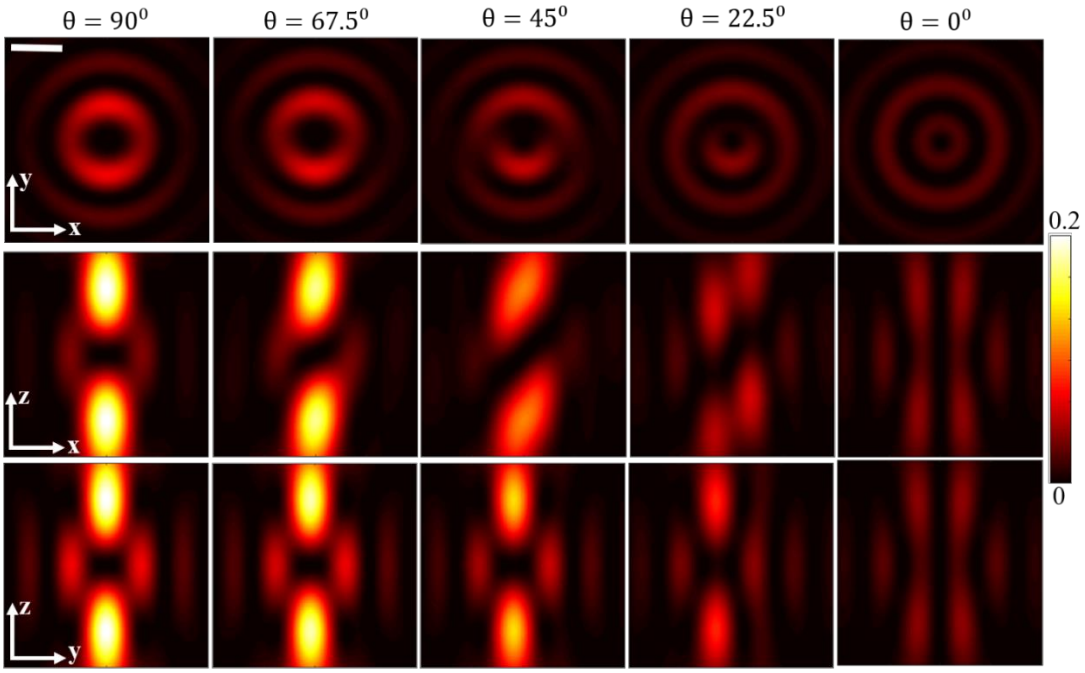

Figure 4.25: Simulated direct-ESSat images of a molecule with a dipole oriented with different values of θ in the XY plane, XZ plane and in the YZ plane (c). These images are computed for $I_{0-\pi} = I_s$ and $\phi = 0°$, $\lambda = 589$ nm, NA = 0.95, scale bar: 500 nm.

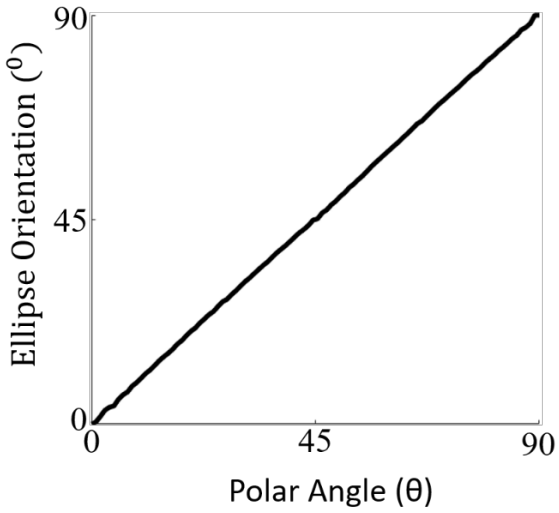

Figure 4.26: Evolution of the ellipse tilt as the function of the polar angle θ. This curve has been obtained for a thresholding at 3.10^{-4} R_∞ and for $\phi = 0°$.

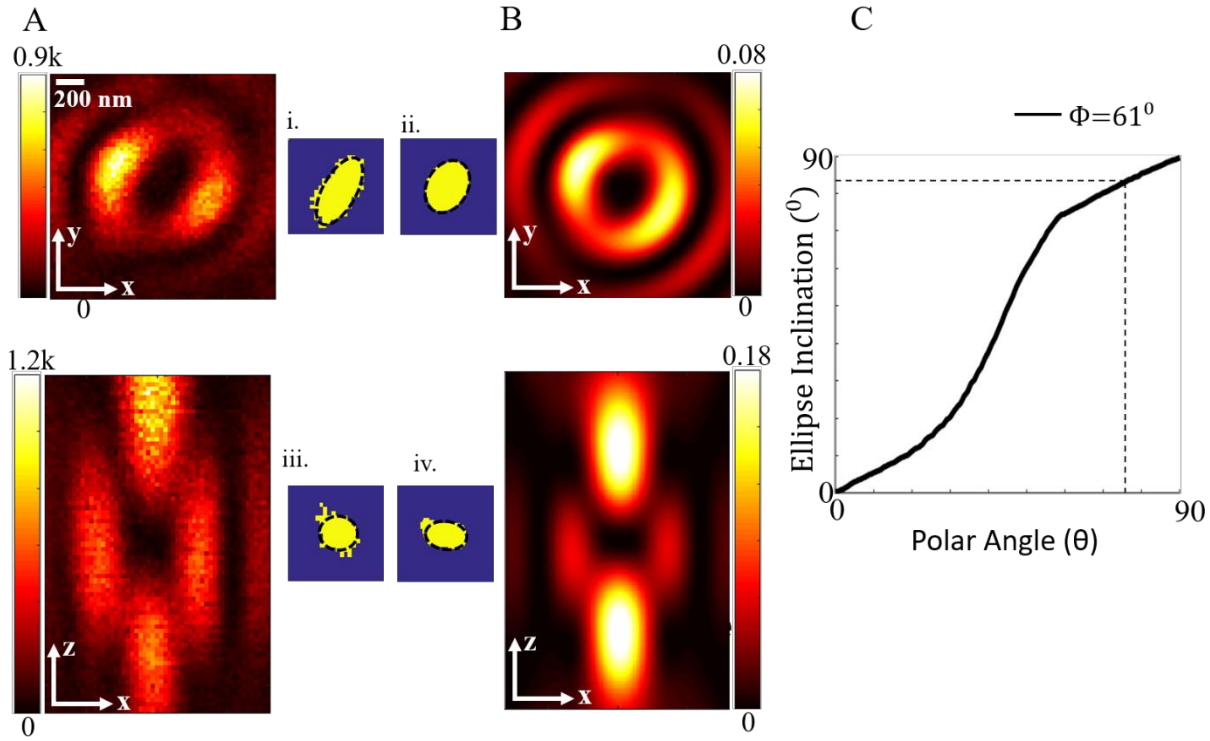

Figure 4.27: Comparison between the fitting and the iterative methods. A) Experimental ESSat images taken in the XY plane and in the XZ plane. Pixel dwell time: 10 ms. i) and iii) show the extracted ellipse by thresholding the ESSat image at R = 80 counts per dwell time. B) Simulated images obtained with the ellipse fitting method reproducing the experimental data. The colorbar is in the unit of R_∞. ii) and iv) are the corresponding extracted ellipses by thresholding at 0.005 and 0.01 for lateral and axial images, respectively. (C) Evolution of the ellipse tilt as the function of the polar angle for $\phi = 61^0$ by thresholding at 5.10^{-4} R_∞.

Figure 4.27 shows a comparison between the experimental fluorescence images and the simulated ones, with the corresponding ellipse fitting used to obtain the θ and ϕ values. We fit the ellipse at the iso-intensity contour of the experimental images by thresholding the intensity distribution of the ESSat image at R = 80 counts per 10 ms. The fit of the two ellipses gives the inclination of the major axis of the ellipses $\phi_{ellipse} = 61.4°$ (xy – image) and $\theta_{ellipse} = 83.2°$ (xz-image). Since the xz image plane does not contain the molecular dipole ($\phi_{ellipse} \neq 0$), the ellipse tilt of the axial image is not equal to the polar angle, θ. Therefore, we plot the evolution of the ellipse tilt as a function of the polar angle for $\phi = 61.4^0$. The polar angle corresponding to an axial ellipse inclination of 83.2° is found out for $\theta = 76 \pm 2°$. The simulated lateral and axial images for these values of θ and ϕ are shown in figure 4.27.B and have a close resemblance with the experimental ones. Overall, we show that it is possible to retrieve both the in-plane and the out of plane dipole orientations with two well-chosen ESSat images. The sensitivity of the ellipse fitting method is increased at large excitation intensity and corresponds to less than two degrees for $I=10I_s$.

For a molecule located deeply inside the crystal, the depth-induced spherical aberration has little effect on the PSF (a global shift along the axis and a dissymmetry in the axial intensity profile, as discussed in section 4.5.2). Figure 4.28 shows an example of simulated images for $\phi = 0^0$, $\theta = 0^0$ and for $\phi = 0^0$, $\theta = 45^0$ with zero spherical aberration and with a spherical aberration of $\beta = 0.3\lambda$. The images look identical for both values of β, which demonstrates that spherical aberration does not add any systematic error on the determination of ϕ and θ.

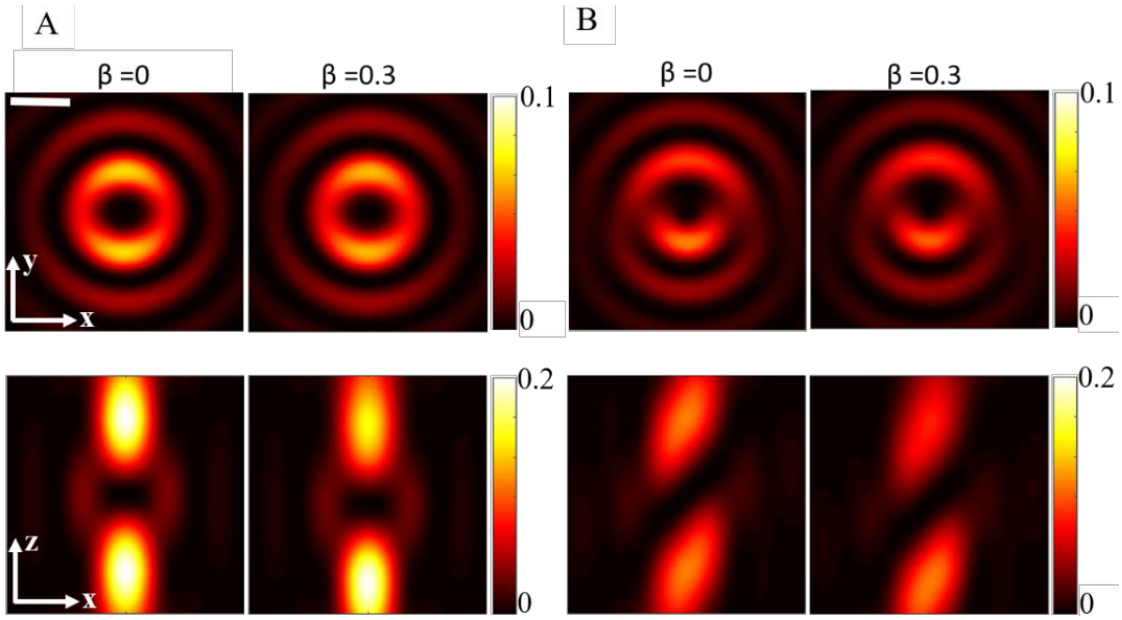

Figure 4.28: Comparison between simulated fluorescence images obtained with and without spherical aberration ($\beta = 0.3\lambda$) in two cases: A) in plane dipole $\theta = 90^0$ and $\phi = 0^0$ and B) $\theta = 45^0$ and $\phi = 0^0$. For $\beta = 0.3\lambda$, the xy images are taken in the plane with minimal central intensity.

4.7 3D-ESSat Microscopy: Experimental results

4.7.1 3D Imaging with direct 3D-ESSat microscopy

Figure 4.29 displays three direct 3D ESSat images of a single DBATT molecule recorded with a 0-π beam for three different laser intensities in two different planes (XY and XZ). The spatial distribution of the fluorescence intensity is in a good agreement with the previous simulations (see figure 4.4). As the excitation intensity increases, both the lateral and the axial resolutions are enhanced as expected. For $I_{0\text{-}\pi}$ = 82 W.cm^{-2}, we fit the axial and lateral fluorescence intensity profiles with two lorentzian curves and we find a FWHM of 205 nm (along X) and 263 nm (along Z). In this image, we see that the (XY) component of the dipole orientation is oriented along y.

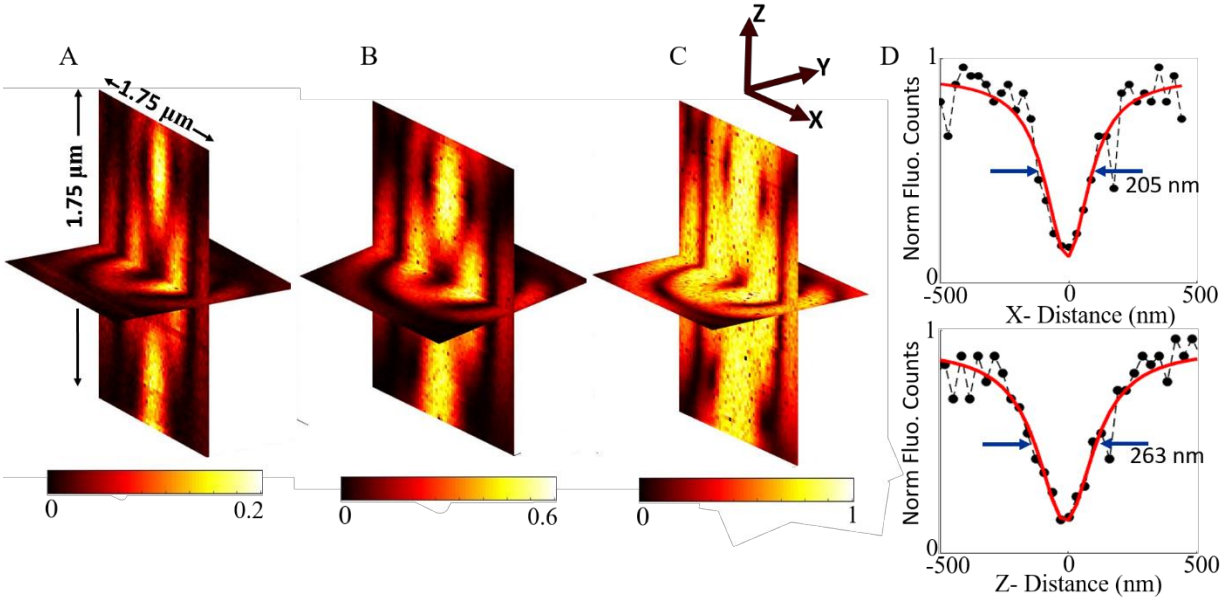

Figure 4.29: Experimental fluorescence images of a single DBATT molecule obtained with direct-3DESSat microscopy for three different excitation intensities: (A) 0.4 W.cm^{-2}, (B) 16 W.cm^{-2} and (C) 82 W.cm^{-2}. Pixel dwell time: 5 ms. Colorbar is normalized to the maximum fluorescence counts of figure (C). (D) Cross sectional profiles along x and z of figure C.

At even larger intensity ($I_{0\text{-}\pi}$ = 163 W.cm^{-2}), we obtained the XZ image shown in Figure 4.30.A, with a contrast of 0.47, given by the ratio of the fluorescence at the center and the maximal measured fluorescence intensity. This value corresponds to a residual intensity of less than I_{res} = 5.10^{-3} $I_{0\text{-}\pi}$. The resolution is improved to 151 nm in the lateral direction and 221 nm in the axial direction. For another molecule, for which the residual intensity is smaller, with ten times higher excitation intensity ($I_{0\text{-}\pi}$ = 1.6 kW.cm^{-2}), we could achieve better lateral and axial resolutions of 79 nm and 38 nm, respectively. These values have been obtained from a lorentzian fit of the profiles along the white dotted lines of the image.

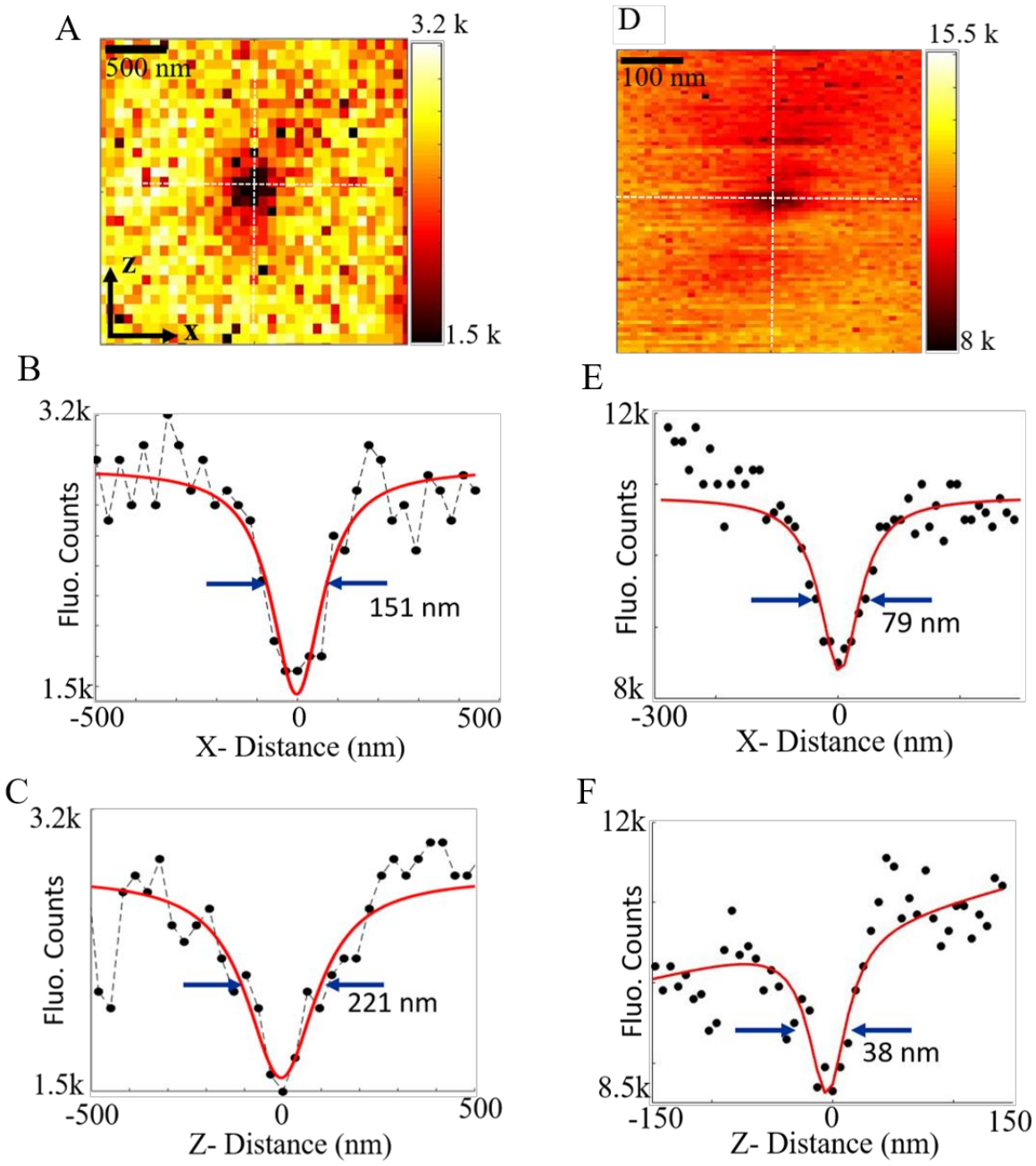

Figure 4.30: Direct-3D ESSat images of two molecules (A is the same molecule as in Figure 4.29) and their cross-section profiles. (A) The central region of the image of the molecule of Figure 4.29. (B) Cross-section profile along the lateral direction of the image. (C) Cross-section profile along the axial direction of the image. Pixel dwell time: 10 ms. $I_{0-\pi} = 1.6\,\mathrm{kW/cm^2}$. (D) The central region of the image of another molecule. (E) and (F) are the corresponding cross-section profiles along the lateral direction and axial direction (white dotted lines), respectively. Pixel dwell time: 10 ms.

4.7.2 3D-imaging with Modulated-ESSat Microscopy

In modulated 3D-ESSat microscopy, the images are taken by overlapping a 0-π beam with a modulated Gaussian beam as in 2D-ESSat microscopy. Figure 4.31 shows the modulated 3D-ESSat image of a single molecule for three different excitation intensities: (A) $I_{0\text{-}\pi}$ = 16 W.cm^{-2}, I_G = 6 W.cm^{-2} (B) $I_{0\text{-}\pi}$ = 78 W.cm^{-2}, I_G = 6 W.cm^{-2} and (C) $I_{0\text{-}\pi}$ = 163 W.cm^{-2}, I_G = 6 W.cm^{-2}. As the 0-π beam intensity increases, the size of PSF strongly decreases.

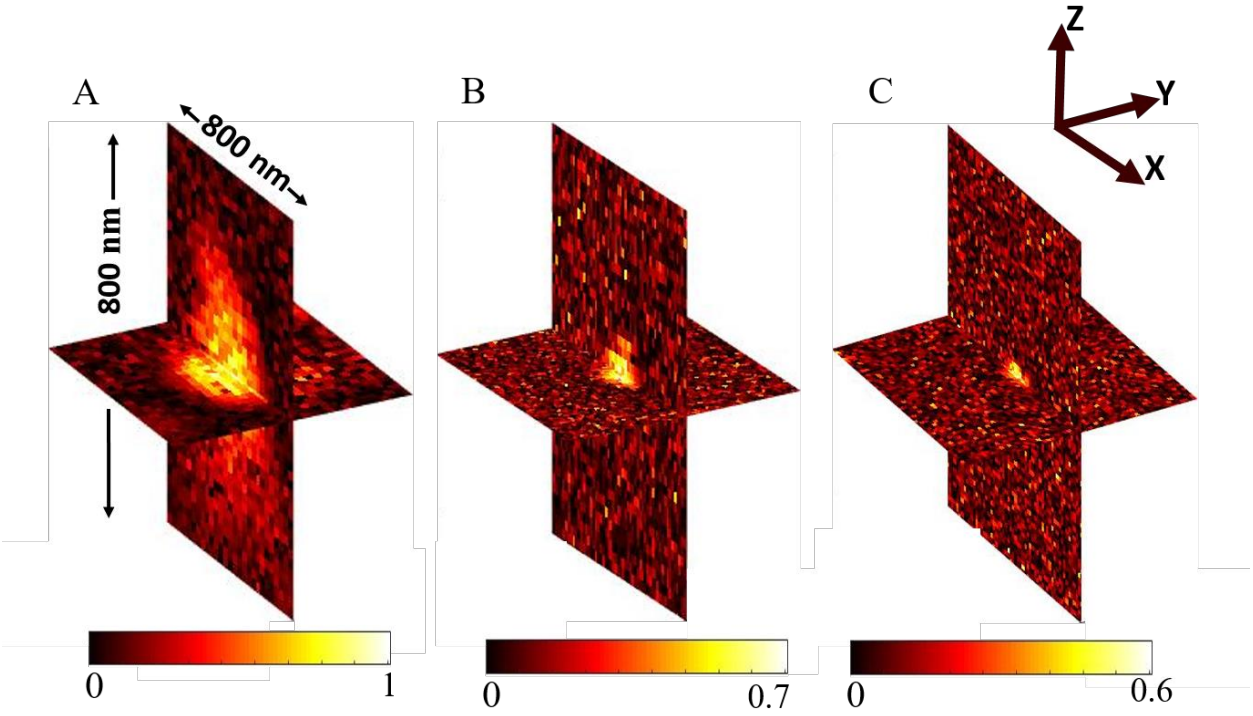

Figure 4.31: Modulated 3D-ESSat imaging: (A) $I_{0\text{-}\pi}$ = 16 W.cm^{-2}, I_G = 6 W.cm^{-2}, (B) $I_{0\text{-}\pi}$ = 78 W.cm^{-2}, I_G = 6 W.cm^{-2} and (C) $I_{0\text{-}\pi}$ = 163 W.cm^{-2}, I_G = 6 W.cm^{-2}. Scale bar: 200nm. The colorbar is normalized to the maximum fluorescence counts of (A). λ = 589 nm, pixel dwell time: 5 ms.

Figure 4.32 presents two experimental modulated ESSat images of the same molecule recorded in the xy and xz planes for I_G = 6 W.cm^{-2} and $I_{0-\pi}$ = 163 W.cm^{-2}. Along the white dotted lines, we plot the three cross-sectional profiles along x, y and z. We fit these three profiles with lorentzian curves and obtain a FWHM of 88 nm in the x-direction, 42 nm in the y-direction and 48 nm in the z-direction. The asymmetry in the resolution is due to the dipole orientation.

.

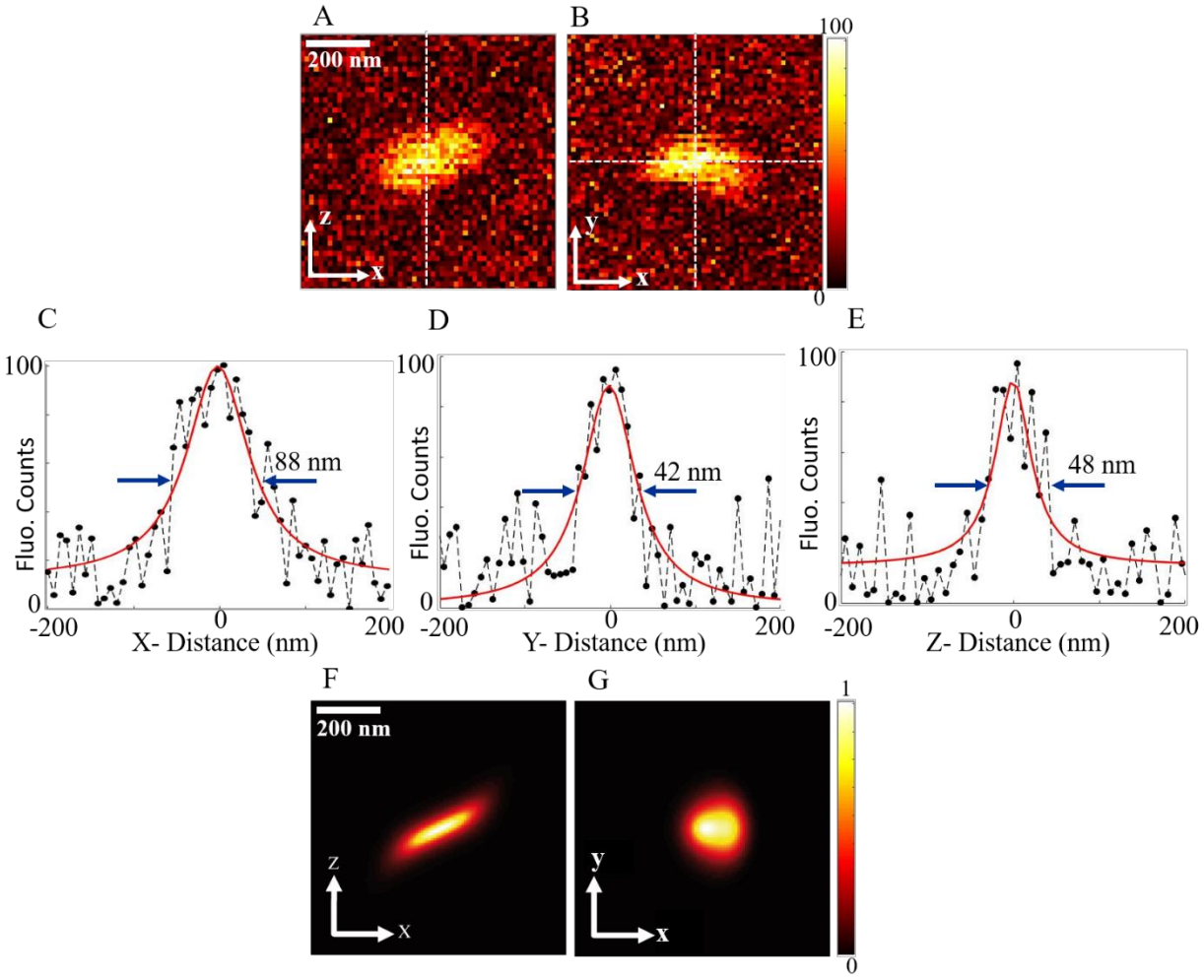

Figure 4.32: Modulated ESSAT images of a single DBATT molecule embedded in octadecane matrix, in the xz plane (A) and in xy plane (B). These two images have been recorded at $I_{0-\pi} = 163$ W.cm^{-2} and $I_G = 6$ W.cm^{-2}. Colorbar in counts per 10 ms. C), D) and E) cross sectional profiles along the three white lines and their associated lorentzian fits (solid lines). $FWHM_x$ = 88 nm; $FWHM_y$ =42 nm and $FWHM_z$ = 48 nm. F) and G) are the corresponding simulated images for the same excitation parameters and for a dipole orientation of $\phi = 0°$ and $\theta = 66^0$. The colorbar is given in unit of R_∞.

As in the case of the unmodulated images, the orientation of the PSF in the XZ plane allows the determination of the z component of the dipole orientation. From the fit of the ellipse tilt, we derive $\theta = 66^0$. We compare this result with the corresponding simulated modulated ESSat images. A good agreement with the experimental data is shown in Figure 4.32.F and 4.32.G.

4.7.3 Super resolution of two molecules

To increase the probability of finding two spatially and spectrally close molecules, we record a confocal image at larger excitation intensity. For hot spots having a large count rate, we can expect that more than one molecule is present in the excitation volume with similar optical resonances. For such an event, we recorded the excitation spectrum at I_G= 12 W.cm^{-2}. With a Gaussian excitation beam presented in Figure 4.33, we found two resonances, separated by 360 MHz, confirming the presence of two emitters. To super-resolve these two molecules, we set the laser frequency in between the two molecular frequencies and we recorded the modulated 3D ESSat image for I_G= 6 W.cm^{-2} and $I_{0\text{-}\pi}$ = 163 W.cm^{-2} as shown in Figure 4.33. According to Figure 4.33, both emitters are excited. We observe two hot spots on this image, well below the diffraction limit. In the transverse plane, the distance between the two molecules is estimated by pointing the two maxima. We found, d = 60 ± 10 nm. At this ESSat intensity, the axial PSF has a FWHM below 50 nm which gives an upper bound for the separation of the two emitters of 80 nm. The decrease in the fluorescence signal of the first molecule while scanning is attributed to the spectral diffusion.

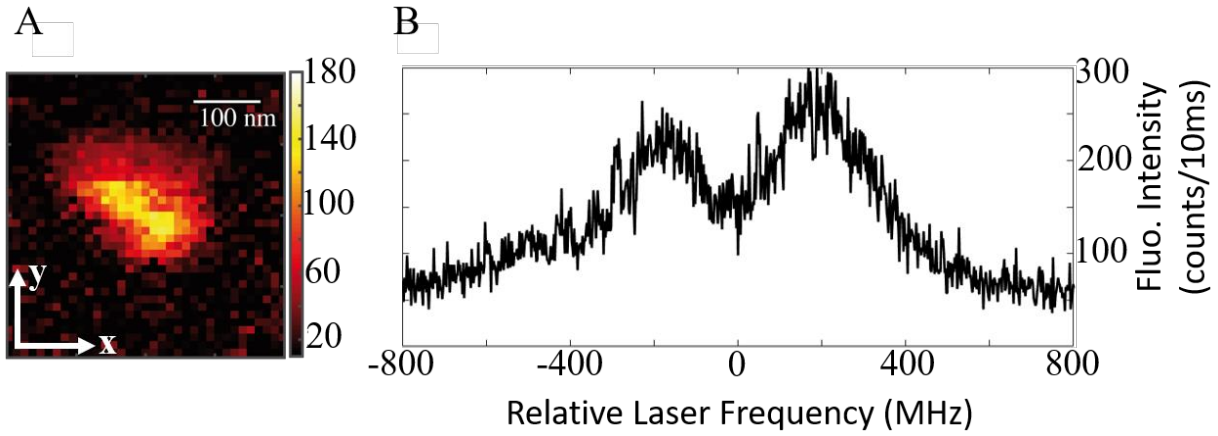

Figure 4.33: A) XY modulated ESSat image recorded at an intensity $I_{0\text{-}\pi}$ = 163W.cm^{-2} and I_G = 6 W.cm^{-2}) of single emitters embedded in octadecane. Two molecules are observable and separated by a distance of 60 nm in the xy-plane. At this ESSat intensity, the axial PSF has a FWHM below 50 nm, which gives an upper bound for the distance between the two emitters of 80 nm. B) Excitation spectrum recorded at an intensity close to the saturation intensity. Two resonances are observable confirming the presence of two molecules. Scale bar: 150 nm.

To go further, we need to achieve a complete z-stack of xy-plane images. A highly stable sample holder is therefore needed to avoid any spatial drifts during the measurement (approx. 10 min). In these conditions, we decided to improve the sample holder stability as seen in the next section.

4.8 Overcoming mechanical vibrations

4.8.1 Upgrade of the sample holder

The mechanical vibrations of the sample holder inside the cryostat limit the best achievable resolution and it is crucial to minimize them. During my PhD thesis, we engineered a new version of the sample holder. Figure 4.34.A shows the schematics of the previous version of the sample can. The sample can contain three steppers (x, y and z), three piezo scanners (x, y and z), the sample plate and the microscope objective. All of the elements are hanged on a long rod. The rod is connected to the upper part of the cryostat. Small vibrations occurring at the end of the rod are amplified and induce oscillations of the sample. An oscillation of the sample rod with an amplitude of only 3×10^{-3} mrad will produce a molecule displacement of 10 nm in an image. As a first modification, we decided to use an electromagnet to detach the sample can from the rod once it is inserted into the cryostat (as seen in Figure 4.34.B). A ring magnet located at the bottom of the can is used to fasten the sample holder to the cryostat windows on which another ring magnet is glued. Three additional clamps, located at the top of the sample can, are also used to maintain the holder in position.

Moreover, the change in refractive index due to turbulences caused by the Helium gas flow ($\Delta n/n = 3\times10^{-5}$) degrades the beam shape and moves the beam position with respect to the molecule location. This small effect becomes noticeable for sub-ten nanometer super resolved single molecule images. To minimize this problem, we decided to cover the sample holder with four metallic windows (see Figure 4.34.C) and bring the objective closer to the bottom window to decrease as much as possible the optical path in the helium gas.

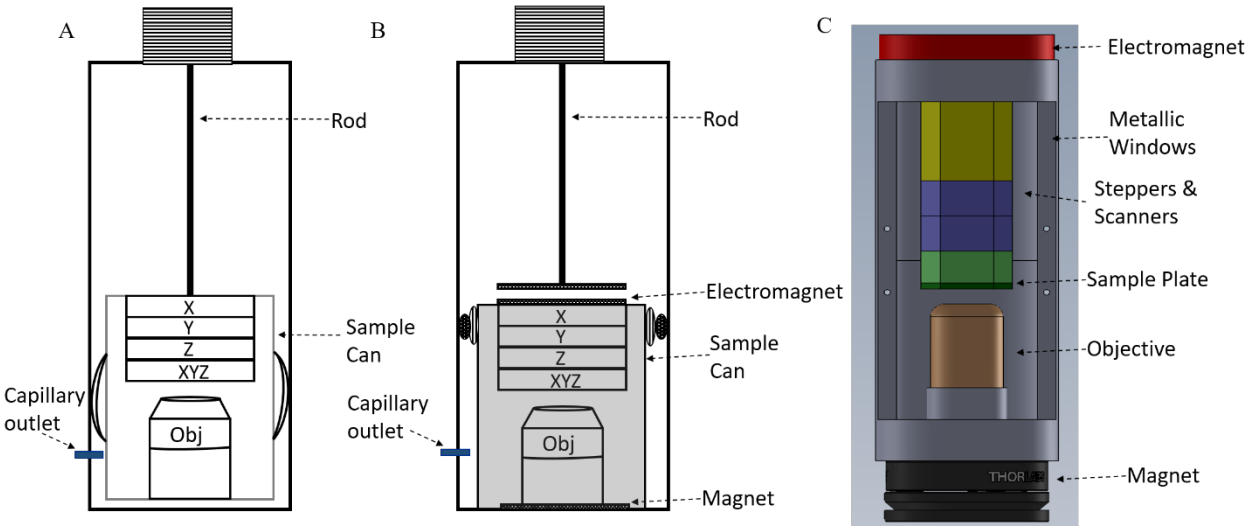

Figure 4.34: Schematics of the A) initial version of the sample holder. The can is rigidly attached to the upper part of the cryostat through a long rod. (B and C) New version of the sample holder (for details see text).

4.8.2 Results

We decided to test this new sample holder with the 3D modulated ESSat method. As we expect a better optical resolution, obtained at higher excitation intensities, we decided to use a more stable, host/guest system: DBATT in naphthalene. This system, with no spectral diffusion at liquid Helium temperature, exhibits a zero phonon line at 618 nm with a spectral linewidth of 20 MHz limited by the lifetime of the excited state[244]. The molecular structure of host/guest is shown in Figure 4.35.

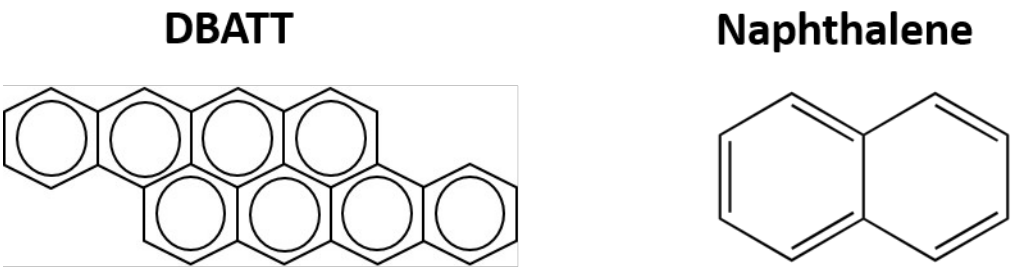

Figure 4.35: Molecular structures of the aromatic fluorescent DBATT molecule and the naphthalene matrix.

The naphthalene is a very volatile substance and solid at room temperature. To prepare a thin layer (<1 μm), we heat a highly doped piece of naphthalene sandwiched between two coverslips. After pressing the sample, we cool it down quickly by putting it in liquid nitrogen. This ensures a good insertion of the DBATT molecules in the naphthalene. As for the other sample, we observed the Newton rings to estimate the thickness. A layer of PVOH (poly-vinyl alcohol) is spin coated over the sample to limit the naphthalene sublimation. The coverslip is then taped onto the sample holder and inserted into the pre-cooled cryostat. In the optical setup, we replaced the band pass excitation filter by a short pass filter (cutting edge at 633 nm) and the emission filter by band pass filter centered at 700 nm with a transmission window of 100 nm.

The images presented in Figure 4.36 show the 3D reconstruction of the point spread function surface, at half maximum, recorded in confocal configuration with a TEM_{00} beam (I_G =1.2 W.cm^{-2}) and with the modulated ESSAT method (I_G = 60 W.cm^{-2} and $I_{0\text{-}\pi}$ =3.1 kW.cm^{-2}). The confocal image corresponds to the diffraction limit (lateral size: 375 nm and axial size: 900 nm). The axial and lateral FWHM of the confocal PSF are in agreement with the theoretical simulated intensity profiles (370 nm and 840 nm) obtained with the equation 4.2. In the case of modulated 3D-ESSat (Figure 4.36.B), the lateral resolution is 55 nm and the axial resolution 29 nm. This 30 times better resolution is achieved with an excitation 0-π beam intensity of $I_{0\text{-}\pi}$ =3.1 kW.cm^{-2} and with a Gaussian beam intensity, I_G =60 W.cm^{-2}. Finally, we could achieve an axial resolution of 22 nm and a transverse resolution of 28 nm for another molecule excited at $I_G = 75\ W/cm^2$ and $I_{0-\pi} = 9.8\,kW/cm^2$ (see Figure 4.37). This axial resolution is thus more than 50 times smaller than the diffraction limit.

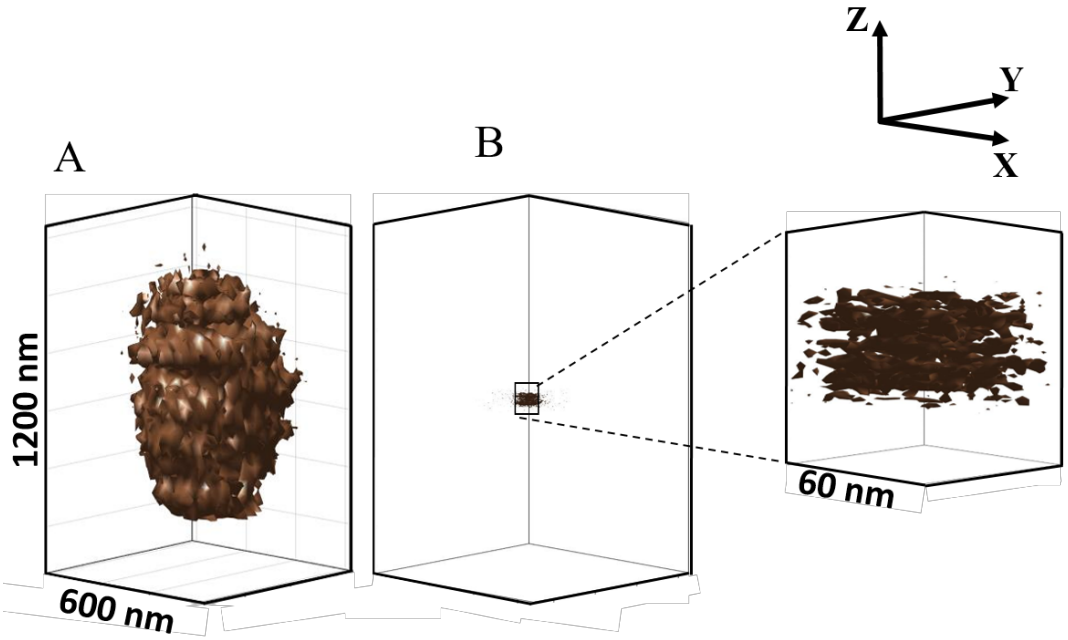

Figure 4.36: A) 3D reconstruction of the point spread function surface (at half maximum) recorded with a confocal TEM_{00} excitation beam (I_G= 1.2 W.cm^{-2}). The axial and lateral are in agreement with the theoretical FWHM values computed with the propagation of a Gaussian beam using equation 4.2. B) Modulated 3D ESSat PSF reconstruction obtained for the same molecule at $I_{0-\pi} = 3.1\,kW/cm^2$ and $I_G = 60\ W/cm^2$.

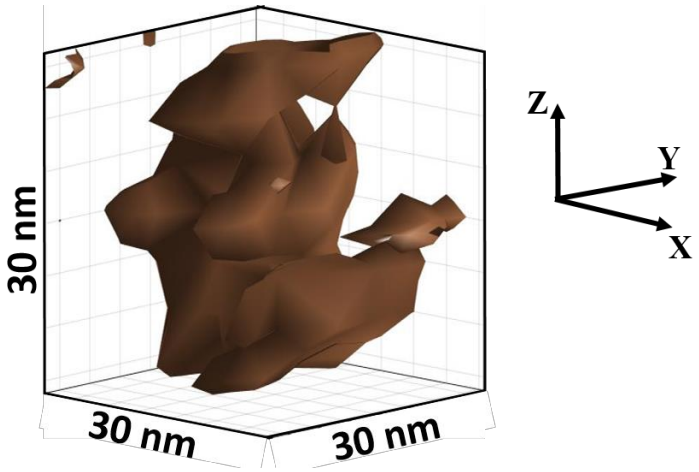

Figure 4.37: 3D reconstruction of the point spread function surface using the 3D modulated ESSat technique. An ultimate axial and lateral resolutions of 22 nm and 28 nm are obtained respectively. Experimental parameters: $I_G = 75\ W/cm^2$ and $I_{0-\pi} = 9.8\,kW/cm^2$. Modulation Frequency 1 kHz, Pixel dwell time: 10 ms.

4.9 Conclusions

In this chapter, we presented the 3D extension of 2D ESSat microscopy using a 0-π excitation beam. We show that the design of the phase mask is critical to produce the optimal electric field distribution at the focal plane and the determination of z_0 has to be done carefully. We developed an experimental method, to achieve such sensitivity and we obtained a residual intensity of $10^{-4}I_{0-\pi}$. Systematic effects induced by the vectorial behavior of light, which mainly shift the positions of the intensity minimum can be compensated and the 3D positions of the molecule can be derived accurately.

The mechanical vibrations of the piezo scanners limit the ultimate achievable optical resolution of the 3D-ESSat microscopy. We improve the stability of the system by building a new sample holder (steppers, piezos, and sample plate) fixed at the bottom of the cryostat and free from the top. In such conditions, an axial resolution of 38 nm is achieved with direct-ESSat microscopy and of 22 nm with modulated-ESSat microscopy for an excitation intensity $I_{o-\pi}$ of less than 10 kW.cm^{-2}. We could also resolve two spectrally close (180 MHz) molecules separated by a distance of 60 nm in the lateral plane and less than 50 nm in the axial direction.

One other advantage of 3D-ESSat microscopy is the possibility to determine the dipole orientation with only one lateral and one axial ESSat images with an accuracy of few degrees.

The 3D ESSAT method, developed during my PhD work, could be also used to localize emitters in the close vicinity of nano-objects such as metallic nanoparticles and study their coupling. The next step of this work will be to study the coherent optical dipole-dipole coupling between two individual molecules located few tens of nanometer apart and image them with the ESSat method.

Summary and Outlook

This Ph.D. thesis is devoted to the optical nanoscopy of single molecules at low temperature. We developed a super-resolution scanning confocal imaging technique called the Excited State Saturation (ESSat) Microscopy. ESSat microscopy is a cryogenic technique based on the optical saturation of the first singlet excited state of a single fluorescent molecule. The excitation beam is shaped such that it contains an isolated intensity zero at the focus of the microscope objective, around which a large intensity gradient develops.

In a first step, we developed a 2D super-resolution method, using a Laguerre Gaussian (donut-shaped) excitation beam. At liquid helium temperatures, we achieved a lateral optical resolution of 4.4 nm with an excitation intensity of 13 $kW.cm^{-2}$. The limitation of the maximal attainable resolution is mainly due to the mechanical instabilities in the cryostat system. The next step was to make the necessary modifications in the cryostat holder, in order to reduce the effect of the mechanical vibrations on the sample and the piezo scanners. The "negative" images, which present fluorescence dips in the saturated fluorescence background, have a poor contrast and therefore are unsuitable for resolving two close by molecules. Hence, we introduced a demodulation technique with the application of a modulation Gaussian beam along with the excitation beam. A lateral resolution of 9 nm is achieved by the modulated ESSat microscopy.

In order to achieve 3D super-resolution, the excitation beam is shaped using a phase mask with a circular central area inducing a π-phase retardation. In the focal plane, it presents a ring-shaped profile with a dark center, while symmetric bright spots apart from the focus are formed along the optical axis. With direct-ESSat microscopy, we achieved a 3D super resolution of single molecules with an axial resolution of 38 nm and a lateral resolution of 79 nm with an excitation intensity of 1.6 kW/cm^2. In order to improve the image contrast, we incorporated the demodulation technique into 3D super-resolution as well. We attained an axial resolution of 22 nm and a lateral resolution of 28 nm with an excitation 0- π beam intensity of 9.8 $kW.cm^{-2}$ and modulated-Gaussian beam intensity of 75 $W.cm^{-2}$, i.e. with an intensity $\sim 10^5$ times smaller than that needed to saturate optical transitions at room temperature in STED-based methods. We could also determine the dipole orientation of single molecules from their spatial fluorescence pattern. Moreover, we could also resolve two molecules with overlapping optical resonances separated by 60 ± 10 nm, well below the optical resolution offered by conventional confocal microscopy.

With higher excitation intensities of few tens of $kW.cm^{-2}$, it will be possible to resolve single molecules that are separated spatially by few tens of nanometers. Such 3D nanoscopic imaging of molecules is crucial to study the coherent dipole-dipole coupling interaction between them. Ongoing experimental efforts in our lab are in progress for this realization. We first find molecules

that are spectrally as well as spatially close with the ESSat method. The coupling interaction between the molecules is confirmed by checking the presence of a two-photon transition at higher excitation intensities, say a hundred times the saturation intensity of the molecules. Typical fluorescence excitation spectra showing the evolution of the two-photon feature with increasing excitation intensities is shown in Figure I.

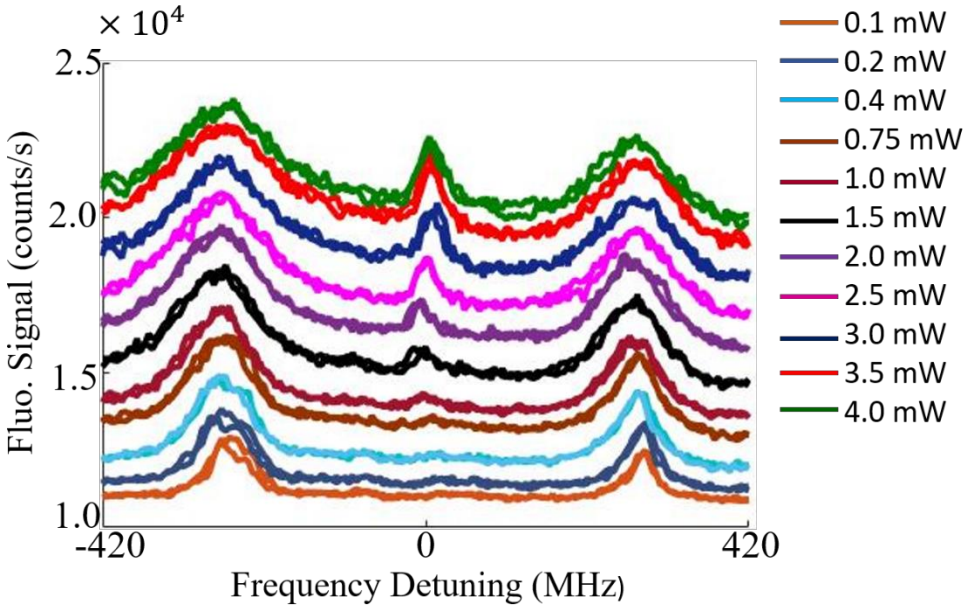

Figure I: Evolution of the fluorescence excitation spectrum of a two-molecule coupled-system with increasing excitation intensities. At low excitation powers, the two peaks correspond to the two intermediate transitions. At high laser powers, a third peak shows up in the center of the spectrum, as a signature of an optical dipole-dipole coupling. This feature arises when two photons populate the upper state of the coupled system, where both molecules are simultaneously excited.

Since the emission of the coupled molecules is delocalized, it is not possible to observe the molecules independently. However, ESSat microscopy provides a unique opportunity to record the rich spatial and spectral features of the coupled system. Such images can provide information about the position as well as the dipole orientation of the individual molecules as well as the coupling parameters.

Further improvement in the ESSat method can be made by combining the doughnut-shaped beam with the 0-π beam excitation pattern as in the case of 3D STED microscopy [129]. This can give a 3D isotropic hollow focal spot and offer a better lateral resolution for the 3D-ESSat microscopy. It is also possible to use the Stark effect to spectrally tune molecules that are spatially close in order to manipulate the degree of entanglement between them. These experiments pave the way to characterize quantum entanglement and should help developing new research directions in quantum information processing.

Bibliography

[1] E. Abbe, "Beitrage zur Theorie des Mikroskops und der mikroskopischen Wahrnehmung," *Archiv für mikroskopische Anatomie*, **9,** 413 (1873).

[2] Moerner, W. E., and Fromm, D. P., "Methods of single-molecule fluorescence spectroscopy and microscopy", *Review of Scientific Instruments* **74,** 3597 (2003).

[3] Minsky, M., "Memoir on inventing the confocal scanning microscope", *Scanning* **10,** 128 (1988).

[4] Helmchen, F., and Denk, W., "Deep tissue two-photon microscopy", *Nature Methods* **2,** 932 (2005).

[5] Axelrod, D., 2008 "Total Internal Reflection Fluorescence Microscopy", *Methods in Cell Biology* **89,** 169 (2008).

[6] Schmidt, R., Engelhardt, J., and Lang, M., "4Pi microscopy", *Methods in Molecular Biology* **950,** 27 (2013).

[7] Gustafsson, M. G. L., "Surpassing the lateral resolution limit by a factor of two using structured illumination microscopy", *Journal of Microscopy* **198,** 82 (2007).

[8] Farahani, J. N., Schibler, M. J., and Bentolila, L. A., "Stimulated Emission Depletion (STED) Microscopy: from Theory to Practice", *Microscopy: Science, Technology. Applcations and Education* **2,** 1539 (2010).

[9] Hofmann, M., Eggeling, C., Jakobs, S., and Hell, S. W., "Breaking the diffraction barrier in fluorescence microscopy at low light intensities by using reversibly photoswitchable proteins", *Proceedings of the National Academy of Sciences of the United States of America* **102,** 17565 (2005).

[10] Gustafsson, M. G. L., "Nonlinear structured-illumination microscopy: Wide-field fluorescence imaging with theoretically unlimited resolution", *Proceedings of the National Academy of Sciences of the United States of America* **102,** 13081 (2005).

[11] Betzig, E., Patterson, G. H., Sougrat, R., Lindwasser, O. W. W., Olenych, S., Bonifacino, J. S., Davidson, M. W., Lippincott-Schwartz, J., and Hess, H. F., "Imaging intracellular fluorescent proteins at nanometer resolution", *Science* **313,** 1642 (2006).

[12] Hess, S. T., Girirajan, T. P. K., and Mason, M. D., "Ultra-High Resolution Imaging by Fluorescence Photoactivation Localization Microscopy" *Biophysical Journal* **91,** 4258 (2006).

[13] Giannone, G., Hosy, E., Sibarita, J., Choquet, D., and Cognet, L., "High content Super-Resolution Imaging of Live Cell by uPAINT", *Methods in Molecular Biology* **950,** 95 (2013).

[14] Zhang, Y., Luo, Y., Zhang, Y., Yu, Y. J., Kuang, Y. M., Zhang, L., Meng, Q. S., Luo, Y., Yang, J. L., Dong, Z. C., and Hou, J. G., "Visualizing coherent intermolecular dipole-dipole coupling in real space", *Nature* **531,** 623 (2016).

[15] Nielsen, M. A., and Chuang, I. L., *Quantum computation and quantum information,* Cambridge University Press (2010).

[16] Rios Leite, J. R., and De Araujo, C. B., "Lineshape of cooperative two-photon absorption by atom pairs in solids", *Chemical Physics Letters* **73,** 71 (1980).

[17] Hettich, C., Schmitt, C., Zitzmann, J., Kuhn, S., Gerhardt, I., and Sandoghdar, V., "Nanometer resolution and coherent optical dipole coupling of two individual molecules", *Science* **298,** 385 (2002).

[18] Ladd, T. D., Jelezko, F., Laflamme, R., Nakamura, Y., Monroe, C., and O'Brien, J. L., "Quantum computers", *Nature* **464,** 45 (2010).

[19] Hartshorne, V. N. H., "The Microscopy of liguid crystals", *The Microscopy Series* **17,** 280 (1974).

[20] Winchell, A. N., and Winchell, H., *"The microscopical characters of artificial inorganic solid substances: Optical properties of artificial minerals",* Academic Press (1964).

[21] Cordes, T., and Blum, S. A., "Opportunities and challenges in single-molecule and single-particle fluorescence microscopy for mechanistic studies of chemical reactions", *Nature Chemistry* **5,** 993 (2013).

[22] Axelrod, D., "Total internal reflection fluorescence microscopy in cell biology", *Traffic* **2,** 764 (2001).

[23] Osten, P., and Margrie, T. W., "Mapping brain circuitry with a light microscope", *Nature Methods* **10,** 515 (2013).

[24] Strano, A. J., "Light microscopy of selected viral diseases (morphology of viral inclusion bodies)", *Pathology Annual* **11,** 53 (1976).

[25] Wilt, B. A., Burns, L. D., Ho, E. T. W., Ghosh, K. K., Mukamel, E. A., and Schnitzer, M. J., "Advances in light microscopy for neuroscience", *Annual Review of Neuroscience* **32,**

451 (2009).

[26] Spoplet, V., Desmet, R., and Melnyk, O., "Imaging of protein layers with an optical microscope for the characterization of peptide microarrays", *Journal of Peptide Science* **13,** 451 (2007).

[27] Stipe, B. C., Rezaei, M. A., and Ho, W., "Single-molecule vibrational spectroscopy and microscopy", *Science* **280,** 1732 (1998).

[28] Jaiswal, J. K., Goldman, E. R., Mattoussi, H., and Simon, S. M., "Use of quantum dots for live cell imaging", *Nature Methods* **1,** 73 (2004).

[29] Hoshino, K., Gopal, A., Glaz, M. S., Vanden Bout, D. A., and Zhang, X., "Nanoscale fluorescence imaging with quantum dot near-field electroluminescence", *Applied Physics Letters* **101,** 043118-1 (2012).

[30] Brouri, R., Beveratos, A., Poizat, J-P., and Grangier, P., "Photon antibunching in the fluorescence of individual color centers in diamond", *Optics Letters* **25,** 1294 (2000).

[31] Arroyo-Camejo, S., Adam, M. P., Besbes, M., Hugonin, J. P., Jacques, V., Greffet, J, J., Roch, J. F., Hell, S. W., and Treussart, F., "Stimulated emission depletion microscopy resolves individual nitrogen vacancy centers in diamond nanocrystals", *ACS Nano* **7,** 10912 (2013).

[32] Ovak, M. A., Surwade, S., Prokop, J., Bolotin, K., Hone, J., Nuckolls, C., and Liu, H., "Visualizing Individual Carbon Nanotubes with Optical Microscopy", *Journal of the American Chemical Society* **136,** 8536 (2014).

[33] Liu, K., Hong, X., Zhou, Q., Jin, C., Li, J., Zhou, W., Liu, J., Wang, E., Zettl, A., and Wang, F., "High-throughput optical imaging and spectroscopy of individual carbon nanotubes in devices", *Nature Nanotechnology* **8,** 917 (2013).

[34] Betzig, E., Trautman, J. K., Harris, T., D., Weiner, J. S., and Kostelak, R. L., "Breaking the Diffraction Barrier: Optical Microscopy on a Nanometric Scale", *Science* **251,** 1468 (1991).

[35] Betzig, E., and Trautman, J. K., "Near-field optics: Microscopy, spectroscopy, and surface modification beyond the diffraction limit", *Science* **257,** 189 (1992).

[36] Taylor, R. S., and Hnatovsky, C., "Trapping and mixing of particles in water using a microbubble attached to an NSOM fiber probe", *Optics Express* **12,** 916 (2004).

[37] Gustafsson, M. G., "Extended resolution fluorescence microscopy", *Current Opinion in Structural Biology* **9,** 627 (1999).

[38] Bernstein, L. H., "Development of super-resolved fluorescence microscopy", Leaders in Pharmaceutical Business Intelligence LPBI Group, *http://pharmaceuticalintelligence.com*

/2014/10/12/development-of-super-resolved-fluorescence-microscopy/, (2014) .

[39] Attwood, D., *"X-rays and Extreme Ultraviolet Radiation: Principles and Applications",* Cambridge University Press (1999).

[40] Oldfield, R. J., "*Light Microscopy - An Illustrated Guide",* Wolfe (1994).

[41] Axelrod, D., Long, J. C., and Davidson, M. W., "High Numerical Aperture Objectives", *http// www.olympusmicro.com/ primer/ java/tirf/highnaobjective/index.html.*

[42] Parry-Hill, M., and Davidson, M. W., "Microscope objectives: Immersion oil and refractive index", *http://www.microscopyu.com/* (2008).

[43] Mansfield, S. M., and Kino, G. S., "Solid immersion microscope", *Applied Physics Letters* **57,** 2615 (1990).

[44] Vamivakas, A. N., Younger, R. D., Goldberg, B. B., Swan, A. K., Ünlü, M. S., Behringer, E. R., and Ippolito, S. B., "A case study for optics: The solid immersion microscope", *American Journal of Physics* **76,** 758 (2008).

[45] Wu, Q., Ghislain, L. P., and Elings, V. B., "Imaging with solid immersion lenses, spatial resolution, and applications", *Proceedings of the IEEE* **88,** 1491 (2000).

[46] Spring, K. R., and Davidson, M. W., "Introduction to Fluorescence Microscopy", *Nikon's MicroscopyU.,www.microscopyu.com/techniques/fluorescence/introduction-to-fluorescence-microscopy.*

[47] Moerner, W. E., and Fromm, D. P., "Methods of single-molecule fluorescence spectroscopy and microscopy", *Review of Scientific Instruments* **74,** 3597 (2003).

[48] García-Parajó, M. F., Veerman, J. A., Bouwhuis, R., Vallée, R., and van Hulst, N. F., "Optical probing of single fluorescent molecules and proteins", *ChemPhysChem* **2,** 347 (2001).

[49] Peterman, E. J. G., Sosa, H., and Moerner, W. E., "Single-Molecule Fluorescence Spectroscopy and Microscopy of Biomolecular Motors", *Annual Review of Physical Chemistry* **55,** 79 (2004).

[50] Conchello, J-A., and Lichtman, J. W., "Optical sectioning microscopy", *Nature Methods* **2,** 920 (2005).

[51] Paddock, S. W., Fellers, T. J., and Davidson, M. W., "Introductory Confocal Concepts", *Nikon MicroscopyU., www.microscopyu.com/techniques/confocal/introductory-confocal-concepts.*

52] Light Microscopy Core Facility: "Introduction to Microscopy | Duke Light Microscopy

Core Facility", http://*microscopy.duke.edu/introduction-microscopy.*

[53] Sheppard, C. J. R., and Choudhury, A., "Image Formation in the Scanning Microscope", *Optica Acta: International Journal of Optics* **24,** 1051 (1977).

[54] Denk, W., Strickler J. H., Webb, W. W., "Two-Photon Laser Scanning Fluorescence Microscopy", *Science* **248,** 73 (1990).

[55] Denk, W., Delaney, K. R., Gelperin, A., Kleinfeld, D., Strowbridge, B. W., Tank, D. W., and Yuste, R., "Anatomical and functional imaging of neurons using 2-photon laser scanning microscopy", *Journal of Neuroscience Methods* **54,** 151 (1994).

[56] Choi, S. M., Kim, W. H., Côté, D., Park, C-W., and Lee, H., "Blood cell assisted in vivo Particle Image Velocimetry using the confocal laser scanning microscope", *Optics Express* **19,** 4357 (2011).

[57] Moens, P. D. J., Gratton, E., and Salvemini, I. L., "Fluorescence correlation spectroscopy, raster image correlation spectroscopy, and number and brightness on a commercial confocal laser scanning microscope with analog detectors (Nikon C1)", *Microscopy Research and Technique* **74,** 377 (2011).

[58] Shao, L., Isaac, B., Uzawa, S., Agard, D. A., Sedat, J. W., and Gustafsson, M. G. L., "I5S: Wide-Field Light Microscopy with 100-nm-Scale Resolution in Three Dimensions", *Biophysical Journal* **94,** 4971 (2008).

[59] Neil, M. A. A., Juškaitis, R., and Wilson, T., "Method of obtaining optical sectioning by using structured light in a conventional microscope", *Optics Letters* **22,** 1905 (1997).

[60] Gustafsson, M. G. L., Shao, L., Carlton, P. M., Wang, C. J. R., Golubovskaya, I. N., Cande, W. Z., Agard, D. A., and Sedat, J. W., "Three-Dimensional Resolution Doubling in Wide-Field Fluorescence Microscopy by Structured Illumination", *Biophysical Journal* **94,** 4957 (2008).

[61] Tinnefeld, P., Eggeling, C., and Hell, S. W., *"Far-Field Optical Nanoscopy",* Springer Series on Fluorescence 14 (2014).

[62] Axelrod, D., "Cell-substrate Contacts Illuminated by Total-Internal Reflection Fluorescence", *Journal of Cell Biology* **89,** 141 (1981).

[63] Reichert, W, M., and Truskey, G. A., "Total Internal Reflection Fluorescence Microscopy I. Modelling. cell contact region fluorescence", *Journal of Cell Science* **96,** 219 (1990).

[64] Funatsu, T., Harada, Y., Tokunaga, M., Saito, K., and Yanagida, T., "Imaging of single fluorescent molecules and individual ATP turnovers by single myosin molecules in aqueous solution", *Nature* **374,** 555 (1995).

[65] Mattheyses, A. L., Simon, S. M., and Rappoport, J. Z., "Imaging with total internal reflection fluorescence microscopy for the cell biologist", *Journal of Cell Science* **123,** 3621 (2010).

[66] Koen, K. A., Weber, M. L., Mayer, K. M., Fernandez, E., and Willets, K. A., "Spectrally-resolved polarization anisotropy of single plasmonic nanoparticles excited by total internal reflection", *Journal of Physical Chemistry C* **116,** 16198 (2012).

[67] Hell, S. W., Schmidt, R., and Egner, A., "Diffraction-unlimited three-dimensional optical nanoscopy with opposing lenses", *Nature Photonics* **3,** 381 (2009).

[68] Hell, S., and Stelzer, E. H. K., "Properties of a 4Pi confocal fluorescence microscope", *Journal of the Optical Society of America A* **9,** 2159 (1992).

[69] Bailey, B., Farkas, D. L., Taylor, D. L., and Lanni, F., "Enhancement of axial resolution in fluorescence microscopy by standing-wave excitation", *Nature* **366,** 44 (1993).

[70] Gugel, H., Bewersdorf, J., Jakobs, S., Engelhardt, J., Storz, R., and Hell, S. W., "Cooperative 4Pi Excitation and Detection Yields Sevenfold Sharper Optical Sections in Live-Cell Microscopy", *Biophysical Journal* **87,** 4146 (2004).

[71] "Fluorescence Microscopy." Comparing Protein Sequence and Structure, *http://www.ks.uiuc.edu/Research/microscope/.*

[72] Patterson, G., Davidson, M., Manley, S., and Lippincott-Schwartz, J., "Superresolution Imaging using Single-Molecule Localizatio", *Annual Review of Physical Chemistry* **61,** 345 (2010).

[73] Shroff, H., Galbraith, C. G., Galbraith, J. A., and Betzig. E., "Live-cell photoactivated localization microscopy of nanoscale adhesion dynamics", *Nature Methods* **5,** 417 (2008).

[74] Egner, A., Geisler, C., von Middendorff, C., Bock, H., Wenzel, D., Medda, R., Andresen, M., Stiel, A. C., Jakobs, S., Eggeling, C., Schönle, A., and Hell, S. W., "Fluorescence Nanoscopy in Whole Cells by Asynchronous Localization of Photoswitching Emitters", *Biophysical Journal* **93,** 3285 (2007).

[75] Huang, B., Wang, W., Bates, M., and Zhuang, X., "Three-Dimensional Super-Resolution Imaging by Stochastic Optical Reconstruction Microscopy", *Science* **319,** 810 (2008).

[76] Rustm, M. J., Bates, M., and Zhuang, X., "Sub-diffraction-limit imaging by stochastic optical reconstruction microscopy (STORM)", *Nature Methods* **3,** 793 (2006).

[77] Bates, M., Huang, B., Dempsey, G. T., and Zhuang, X., "Multicolor Super-Resolution Imaging with Photo-Switchable Fluorescent Probes", *Science* **317,** 1749 (2007).

78] Yildiz, A., Forkey, J. N., McKinney, S. A., Ha, T., Goldman, Y. E., and Selvin, P. R.,

"Myosin V Walks Hand-Over-Hand: Single Fluorophore Imaging with 1.5-nm Localization", *Science* **300,** 2061 (2003).

[79] Juette, M. F., Gould, T. J., Lessard, M. D., Mlodzianoski, M. J., Nagpure, B. S., Bennett, B. T., Hess, S. T., and Bewersdorf, J., "Three-dimensional sub–100 nm resolution fluorescence microscopy of thick samples", *Nature Methods* **5,** 527 (2008).

[80] Pavani, S. R. P., Thompson, M. A., Biteen, J. S., Lord, S. J., Liu, N., Twieg, R. J., Piestun, R., and Moerner, W. E., "Three-dimensional, single-molecule fluorescence imaging beyond the diffraction limit by using a double-helix point spread function", *Proceedings of the National Academy of Sciences of the United States of America* **106,** 2995 (2009).

[81] Shtengel, G., Galbraith, J. A., Galbraith, C. G., Lippincott-Schwartz, J., Gillette, J. M., Manley, S., Sougrat, R., Waterman, C. M., Kanchanawong, P., Davidson, M. W., Fetter, R. D., and Hess, H. F., "Interferometric fluorescent super-resolution microscopy resolves 3D cellular ultrastructure", *Proceedings of the National Academy of Sciences of the United States of America* **106,** 3125 (2009).

[82] Bates, M., Jones, S. A., and Zhuang, X., "Stochastic optical reconstruction microscopy (STORM): A method for superresolution fluorescence imaging", *Cold Spring Harbor Protocols* **8,** 498 (2013).

[83] Zhuang, X., "Nano-imaging with STORM", *Nature Photonics* **3,** 365 (2009).

[84] Rainey, A. M., Gines, T. B., and Davidson, M. W., "Education in microscopy and digital imaging", *http://zeiss-campus.magnet.fsu.edu.*

[85] Bates, M., Huang, B., and Zhuang, X., "Super-resolution microscopy by nanoscale localization of photo-switchable fluorescent probes", *Current Opinion in Chemical Biology* **12,** 505 (2008).

[86] Lippincott-Schwartz, J., and Patterson, G. H., "Photoactivatable fluorescent proteins for diffraction-limited and super-resolution imaging", *Trends in Cell Biology* **19,** 555 (2009).

[87] Kanchanawong, P., Shtengel, G., Pasapera, A. M., Ramko, E. B., Davidson, M. W., Hess, H. F., and Waterman, C. M., "Nanoscale architecture of integrin - based cell adhesions", *Nature* **468,** 580 (2010).

[88] Giannone, G., Hosy, E., Levet, F., Constals, A., Schulze, K., Sobolevsky, A. I., Rosconi, M. P., Gouaux, E., Tampe, R., Choquet, D., and Cognet, L., "Dynamic Superresolution Imaging of Endogenous Proteins on Living Cells at Ultra-High Density", *Biophysical Journal* **99,** 1303 (2010).

[89] Cognet, L., Coussen, F., Choquet, D., and Lounis, B., "Fluorescence microscopy of single autofluorescent proteins for cellular biology", *Comptes Rendus Physique* **3,** 645 (2002).

[90] Willig, K. I., Rizzoli, S. O., Westphal, V., Jahn, R., and Hell, S. W., "STED microscopy reveals that synaptotagmin remains clustered after synaptic vesicle exocytosis", *Nature* **440,** 935 (2006).

[91] Hell, S. W., and Wichman, J., "Breaking the diffraction resolution limit by stimulated emission: stimulated-emission-depletion fluorescence microscopy", *Optics Letters* **19,** 780 (1994).

[92] Hell, S. W., "Increasing the Resolution of Far-Field Fluorescence Light Microscopy by Point-Spread-Function Engineering", In: Lakowicz J.R. (eds), *Topics in Fluorescence Spectroscopy* **5**, Springer, Boston, MA (2002).

[93] Hell, S. W., "Microscopy and its focal switch", *Nature Methods* **6,** 24 (2009).

[94] Westphal, V., and Hell, S. W., "Nanoscale resolution in the focal plane of an optical microscope", *Physical Review Letters* **94,** 143903–1 (2005).

[95] Hein, B., Willig, K. I., and Hell, S. W., "Stimulated emission depletion (STED) nanoscopy of a fluorescent protein-labeled organelle inside a living cell", *Proceedings of the National Academy of Sciences of the United States of America* **105,** 14271 (2008).

[96] Hell, S. W., "Toward fluorescence nanoscopy", *Nature Biotechnology* **21,** 1347 (2003).

[97] Huang, B., Bates, M., and Zhuang, X., "Super-Resolution Fluorescence Microscopy", *Annual Review of Biochemistry* **78,** 993 (2009).

[98] Wildanger, D., Patton, B. R., Schill, H., Marseglia, L., Hadden, J. P., Knauer, S., Schönle, A., Rarity, J. G., O'Brien, J. L., Hell, S. W., and Smith, J. M., "Solid immersion facilitates fluorescence microscopy with nanometer resolution and sub-Ångström emitter localization", *Advanced Materials* **24,** 309 (2012).

[99] Hell, S. W., "Far-field optical nanoscopy" *Science* **316,** 1153 (2007).

[100] Hell, S. W., Sahl, S. J., Bates, M., Zhuang, X., Heintzmann, R., Booth, M. J., Bewersdorf, J., Shtengel, G., Hess, H., Tinnefeld, P., Honigmann, A., Jakobs, S., Testa, I., Cognet, L., Lounis, B., Ewers, H., Davis, S. J., Eggeling, C., Klenerman, D., Willig, K. I., Vicidomini, G., Castello, M., Diaspro, A., and Cordes, T., "The 2015 super-resolution microscopy roadmap", *Journal of Physics D: Applied Physics* **48,** 443001–1 (2015).

[101] Hell, S. W., and Kroug, M., "Ground-state-depletion fluorescence microscopy: a concept for breaking the diffracition resolution limit", *Applied Physics B: Lasers and Optics* **60,** 495 (1995).

[102] Lakowicz, J. R.,*"Topics in Fluorescence Spectroscopy",* Kluwer Academic Publishers **5**, Maryland (2002).

[103] Hell, S. W., Jakobs, S., and Kastrup, L., "Imaging and writing at the nanoscale with focused

visible light through saturable optical transitions", *Applied Physics A: Material Science and Processing* **77,** 859 (2003).

[104] Dyba, M., and Hell, S. W., "Focal spots of size λ/23 open up far-field fluorescence microscopy at 33 nm axial resolution'' *Physical Review Letters* **88,** 163901–1 (2002).

[105] Hell, S. W., "Strategy for far-field optical imaging and writing without diffraction limit", *Physics Letters, Section A: General, Atomic and Solid State Physics* **326,** 140 (2004).

[106] Hell, S. W., Dyba, M., and Jakobs, S., "Concepts for nanoscale resolution in fluorescence microscopy", *Current Opinion in Neurobiology* **14,** 599 (2004).

[107] Yang, B., Przybilla, F., Mestre, M., Trebbia, J-B., and Lounis, B., "Massive Parallelization of STED Nanoscopy Using Optical Lattices", *Optics Express* **22,** 5581 (2014).

[108] Chmyrov, A., Keller, J., Grotjohann, T., Ratz, M., Este, E., Jakobs, S., Eggeling, C., and Hell, S. W., "Nanoscopy with more than 100000 'doughnuts '", *Nature Methods* **10,** 737 (2013).

[109] Cragg, G. E., and So, P. T. C., "Lateral resolution enhancement with standing evanescent waves", *Optics Letters* **25,** 46 (2000).

[110] Heintzmann, R., Jovin, T. M., and Cremer, C., "Saturated patterned excitation microscopy—a concept for optical resolution improvement", *Journal of the Optical Society of America.A* **19,** 1599 (2002).

[111] Rittweger, E., Wildanger, D., and Hell, S. W., "Far-field fluorescence nanoscopy of diamond color centers by ground state depletion", *EPL, A Letters Journal Exploring the Frontiers of Physics* **86,** 14001–1 (2009).

[112] Balzarotti, F., Eilers, Y., Gwosch, K. C., Gynnå, A. H., Westphal, V., Stefani, F. D., Elf, J., and Hell, S. W., "Nanometer resolution imaging and tracking of fluorescent molecules with minimal photon fluxes", *Science* **355,** 606 (2017).

[113] Lew, M. D., Backlund, M. P., and Moerner, W. E., "Rotational mobility of single molecules affects localization accuracy in super-resolution fluorescence microscopy", *Nano Letters* **13,** 3967 (2013).

[114] Kao, H. P., and Verkman A, S., "Tracking of Single Fluorescent Particles in Three Dimensions : Use of Cylindrical Optics to Encode Particle Position", *Biohysical Joumal* **67,** 1291 (1994).

[115] Holtzer, L., Meckel, T., and Schmidt, T., "Nanometric three-dimensional tracking of individual quantum dots in cells", *Applied Physics Letters* **90,** 053902-1 (2007).

[116] Prabhat, P., Ram, S., Ward, E. S., and Ober, R. J., "Simultaneous imaging of different focal

planes in fluorescence microscopy for the study of cellular dynamics in three dimensions", *IEEE Transactions on Nanobioscience* **3,** 237 (2004).

[117] Pavani, S. R. P., and Piestun, R., "Three dimensional tracking of fluorescent microparticles using a photon-limited double-helix response system", *Optics Express* **16,** 22048 (2008).

[118] Pavani, S. R. P., Greengard, A., and Piestun, R., "Three-dimensional localization with nanometer accuracy using a detector-limited double-helix point spread function system", *Applied Physics Letters* **95,** 201103–1 (2009).

[119] Fischer, R. S., Wu, Y., Kanchanawong, P., Shroff, H., and Waterman, C. M., "Microscopy in 3D: A biologist's toolbox", *Trends in Cell Biology* **21,** 682 (2011).

[120] Santi, P. A., "Light Sheet Fluorescence Microscopy: A Review", *Journal of Histochemistry and Cytochemistry* **59,** 129 (2011).

[121] Selchow O and Huisken J 2013 "Light sheet fluorescence microscopy and revolutionary 3D analyses of live specimens", *Photonik International* **1,** 44 (2013).

[122] Galland, R., Grenci, G., Aravind, A., Viasnoff, V., Studer, V., and Sibarita, J., "3D high- and super-resolution imaging using single-objective SPIM", *Nature Methods* **12,** 641 (2015).

[123] Mudry, E., Moal, E. Le., Ferrand, P., Chaumet, P. C., and Sentenac, A., "Isotropic diffraction-limited focusing using a single objective lens", *Physical Review Letters* **105,** 203903 (2010).

[124] Moal, E. Le., Mudry, E., Chaumet, P. C., Ferrand, P., Sentenac, A., "Isotropic Single Objective (ISO) microscopy : Theory and Experiment", *Journal of the Optical Society of America A* **28,** 1586 (2011).

[125] Le Moal, E., Mudry, E., Chaumet, P. C., Ferrand, P., and Sentenac, A., "Two-photon fluorescence isotropic-single-objective microscopy", *Optics Letters* **37,** 85 (2012).

[126] Matsuda A, Shao L, Boulanger J, Kervrann C, Carlton P M, Agard D and Sedat J W 2010 "Condensed Mitotic Chromosome Structure at Nanometer Resolution Using PALM and EGFP- Histones", *PLoS One* **5,** 1 (2010).

[127] Wildanger, D., Medda, R., Kastrup, L., and Hell, S. W., "A compact STED microscope providing 3D nanoscale resolution", *Journal of Microscopy* **236,** 35 (2009).

[128] Li, S., Kuang, C., Hao, X., Gu, Z., and Liu, X., "Generation of a 3D isotropic hollow focal spot for single-objective stimulated emission depletion microscopy", *Journal of Optics* **14,** 085704-1 (2012).

[129] Harke, B., Ullal, C. K., Keller, J., and Hell, S. W., "Three-dimensional nanoscopy of colloidal crystals", *Nano Letters* **8,** 1309 (2008).

[130] Schmidt, R., Wurm, C. A., Jakobs, S., Engelhardt, J., Egner, A., and Hell, S. W., "Spherical nanosized focal spot unravels the interior of cells", *Nature Methods* **5,** 539 (2008).

[131] Agard, D. A., and Sedat, J. W., "Three-dimensional architecture of a polytene nucleus", *Nature* **302,** 676 (1983).

[132] Gould, T. J., Myers, J. R., and Bewersdorf, J., "Total internal reflection STED microscopy", *Optics Express* **19,** 13351 (2011).

[133] Grover, G., Rama, S., Pavani, P., and Piestun, R., "Performance limits on three-dimensional particle localization in photon-limited microscopy", *Optics Letters* **35,** 3306 (2010).

[134] Shao, L., Kner, P., Rego, E. H., and Gustafsson, M. G. L., "Super-resolution 3D microscopy of live whole cells using structured illumination", *Nature Methods* **8**, 1044 (2011).

[135] Schermelleh, L., Carlton, P. M., Haase, S., Shao, L., Winoto, L., Kner, P., Burke, B., Cardoso, M. C., Agard, D. A., Gustafsson, M. G. L., Leonhardt, H., and Sedat, J. W., "Subdiffraction Multicolor Imaging of the Nuclear Periphery with 3D Structured Illumination Microscopy", *Science* **320,** 1332 (2008).

[136] Moerner, W., and Kador, L., 1989 "Optical detection and spectroscopy of single molecules in a solid", *Physical Review Letters* **62,** 2535 (1989).

[137] Orrit, M., and Bernard, J., "Single pentacene molecules detected by fluorescence excitation in a p-terphenyl crystal", *Physical Review Letters* **66,** 2716 (1991).

[138] Wang, D., Kelkar, H., Martin-Cano, D., Utikal, T., Götzinger, S., and Sandoghdar, V., "Coherent coupling of a single molecule to a scanning Fabry-Perot microcavity", *Physical Review X* **7,** 1 (2017).

[139] Wen, J. D., Lancaster, L., Hodges, C., Zeri, A. C., Yoshimura, S. H., Noller, H. F., Bustamante, C., and Tinoco, I., "Following translation by single ribosomes one codon at a time", *Nature* **452,** 598 (2008).

[140] Gautier, A., Gauron, C., Volovitch, M., Bensimon, D., Jullien, L., and Vriz, S., "How to control proteins with light in living systems", *Nature Chemical Biology* **10,** 533 (2014).

[141] Querard, J., Markus, T. Z., Plamont, M. A., Gauron, C., Wang, P., Espagne, A., Volovitch, M., Vriz, S., Croquette, V., Gautier, A., Saux, T. Le., and Jullien, L., "Photoswitching kinetics and phase-sensitive detection add discriminative dimensions for selective fluorescence imaging", *Angewandte Chemie International Edition* **54,** 1 (2015).

[142] Li, J. R., Yu, J., Lu, W., Sun, L. B., Sculley, J., Balbuena, P. B., and Zhou, H. C., "Porous materials with pre-designed single-molecule traps for CO2 selective adsorption", *Nature Communications* **4,** 1538 (2013).

[143] Nirmalraj, P., Thompson, D., Molina-Ontoria, A., Sousa, M., Martín, N., Gotsmann, B., and Riel, H., "Nanoelectrical analysis of single molecules and atomic-scale materials at the solid/liquid interface", *Nature Materials* **13,** 947 (2014).

[144] Vaigu, A., Porrovecchio, G., Chu, X-L., Lindner, S., Smid, M., Manninen, A., Becher, C., Sandoghdar, V., Götzinger, S., and Ikonen, E., "Experimental demonstration of a predictable single photon source with variable photon flux", *Metrologia* **54,** 218 (2017).

[145] Chu, X-L., Götzinger, S., and Sandoghdar, V., "A single molecule as a high-fidelity photon gun for producing intensity-squeezed light", *Nature Photonics* **11,** 58 (2016).

[146] Moerner, W. E., "Examining Nanoenvironments in Solids on the Scale of a Single, Isolated Impurity Molecule", *Science* **265,** 46 (1994).

[147] Moerner, W. E., and Orrit, M., "Illuminating single molecule in condensed matter", *Science* **283,** 1670 (1999).

[148] Tamarat, P., Maali, A., Lounis, B., and Orrit, M., "Ten Years of Single-Molecule Spectroscopy", *Journal of Physical Chemistry A* **104**, 1 (2000).

[149] Basche, T., Moerner, W. E., Orrit, M., Wild, U. P., *Single-molecule optical detection, imaging and spectroscopy",* VCH (1996).

[150] Brunel, C., Tamarat, P., Lounis, B., Woehl, J. C., and Orrit, M., "Stark effect on single molecules of dibenzanthanthrene in a naphthalene crystal and in a n-hexadecane Shpol'skii matrix", *Journal of Physical Chemistry A* **103,** 2429 (1999).

[151] Weiss, S., "Fluorescence Spectroscopy of Single Biomolecules", *Science* **283,** 1676 (1999).

[152] Ishijima, A., Yanagida, T., "Single molecule nano-bioscience", *Trends in Biochemical S ciences* **26,** 438 (2001).

[153] Brunel, C., Lounis, B., Tamarat, P., and Orrit, M., "Triggered Source of Single Photons based on Controlled Single Molecule Fluorescence", *Physical Review Letters* **83,** 2722 (1999).

[154] Lounis, B., and Moerner, W., E., "Single photons on demand from a single molecule at room temperature", *Nature* **407,** 491 (2000).

[155] Westphal, V., Kastrup, L., and Hell, S. W., "Lateral resolution of 28 nm (λ/25) in far-field fluorescence microscopy", *Applied Physics B: Lasers and Optics* **77,** 377 (2003).

[156] Heilemann, M., Herten, D. P., Heintzmann, R., Cremer, C., Müller, C., Tinnefeld, P., Weston, K. D., Wolfrum, J., and Sauer, M., "High-resolution colocalization of single dye molecules by fluorescence lifetime imaging microscopy", *Analytical Chemistry* **74**, 3511 (2002).

[157] Köhler, J., Disselhorst, J. A. J. M., Donckers, M. C. J. M., Groenen, E. J. J., Schmidt, J., and Moerner, W. E., "Magnetic resonance of a single molecular spin", *Nature* **363,** 242 (1993).

[158] Wrachtrup, J., Vonborczyskowski, C., Bernard, J., Orrit, M., and Brown, R., "Optical-Detection of Magnetic-Resonance in a Single Molecule", *Nature* **363,** 244 (1993).

[159] Beams, R., Cançado, L. G., Jorio, A., Vamivakas, A. N., and Novotny, L., "Tip-enhanced Raman mapping of local strain in graphene", *Nanotechnology* **26,** 175702 (2015).

[160] Masia, F., Langbein, W., Watson, P., and Borri, P., "Triply surface-plasmon resonant four-wave mixing imaging of gold nanoparticles", *SPIE Proceedings* **7911,** 79110Y-1 (2011).

[161] Meixner, A. J., Jäger, R., Jäger, S., Bräuer, A., Scherzinger, K., Fulmes, J., Krockhaus, S. zur O., Gollmer, D. A., Kern, D. P., and Fleischer, M., "Coupling single quantum dots to plasmonic nanocones: optical properties", *Faraday Discussion* **184,** 321 (2015).

[162] Skoff, S. M., and Rauschenbeutel, A., "Quantum nonlinear optics: Focus on a single molecule", *Nature Photonics* **10,** 438 (2016).

[163] Maser, A., Gmeiner, B., Utikal, T., Götzinger, S., and Sandoghdar, V., "Few-photon coherent nonlinear optics with a single molecule", *Nature Photonics* **10,** 1 (2015).

[164] Gerhardt, I., Wrigge, G., Hwang, J., Zumofen, G., and Sandoghdar, V., "Coherent nonlinear single-molecule microscopy", *Physical Review A* **82,** 063823 (2010).

[165] Ambrose, W. P., and Moerner, W. E., "Fluorescence spectroscopy and spectral diffusion of single impurity molecules in a crystal", *Nature* **349,** 225 (1991).

[166] Gagliardi, R. M., and Karp, S., "M-ary Poisson detection and optical communications", *IEEE Transactions on Communication Technology* **17,** 208 (1969).

[167] Dovichi, N. J., "Attogram detection limits using laser induced fluorescence", *Trends in Analytical Chemistry* **3,** 55 (1984).

[168] Hungerford, J. M., and Christian, G. D., "Statistical Sampling Errors Solutions as intrinsic limits on detection in dilute solutions", *Analytical Chemistry* **58,** 2567 (1986).

[169] Debye, P., "Interferenz von Rontgenstrahlen und Warmebewegung", *Annals of Physics* **348,** 49 (1913).

[170] Waller, I., "Zur frage der einwirkung der warmebewegung aud die interferenz von rontgenstrahlen", *Zeitschrift fur Physik A (in German).* **17,** 398 (1923).

[171] Franck, J., and Dymond, E. G., "Elementary processes of photochemical reactions", *Transactions of the Faraday Society* **21,** 536 (1925).

[172] Condon, E. U., “A theory of intensity distribution in band systems”, *Physical Review* **28,** 1182 (1926).

[173] Condon, E. U., "Nuclear motions associated with electron transitions in diatomic molecules”, *Physical Review* **32,** 858 (1928).

[174] Lakowicz, J. R., *"Principles of Fluorescence Spectroscopy ",* Springer, New York (2006).

[175] Wu, S., and Dovichi, N. J., “High-sensitivity fluorescence detector for fluorescein isothiocyanate derivatives of amino acids separated by capillary zone electrophoresis”, *Journal of Chromatography A* **480,** 141 (1989).

[176] Fauré, M., Lounis, B., and Buzdin, A. I., “Single-molecule spectroscopy as a possible tool to study the electric field in superconductors”, *Europhysics Letters* **77,** 17005–1 (2007).

[177] Tian, Y., Navarro, P., and Orrit, M., “Single molecule as a local acoustic detector for mechanical oscillators”, *Physcs Review Letters* **113,** 135505–1 (2014).

[178] Hochstrasser, R. M., and Agranovich, V. M., *“Spectroscopy and Excitation Dynamics of Condensed Molecular Systems”,* New York: North-Holland: Elsevier Science Publishing Company, (1983).

[179] Plakhotnik, T., Donley, E. A., and Wild, U. P., “Single-molecule Spectrocsopy” *Annual Review of Physical Chemistry A* **104,** 181 (1997).

[180] Moerner, W. E., “Fundamentals of single-molecule spectroscopy in solids”, *Journal of Luminescence* **60–61,** 997 (1994).

[181] Platt, U., and Stutz, J.,*“Differential Optical Absorption Spectroscopy: principles and applications”,* Springer (2008).

[182] Ambrose, W. P., Basché, T., and Moerner, W. E., “Detection and spectroscopy of single pentacene molecules in a p -terphenyl crystal by means of fluorescence excitation”, *Journal of Chemical Physics.* **95,** 7150 (1991).

[183] Kummer, S., Mais, S., and Basché, T., “Measurement of Optical Dephasing of a Single Terrylene Molecule with Nanosecond Time Resolution”, *Journal of Physical Chemistry* **99,** 17078 (1995).

[184] Plakhotnik, T., Moerner, W. E., Palm, V., and Wild, U. P., “Single molecule spectroscopy: maximum emission rate and saturation intensity”, *Optics Communications* **18,** 83 (1995).

[185] Metcalf, H. J., and Straten, P., van der, *“Laser cooling and trapping”,* New York: Springer-Verlag (1999).

[186] Brown, R., Wrachtrup, J., Orrit, M., Bernard, J. and von Borczyskowski, C., “Kinetics of optically detected magnetic resonance of single molecules”, *Journal of Chemical Physics*

100, 7182 (1994).

[187] Basché, T., Kummer, S., and Bräuchle, C., "Direct spectroscopic observation of quantum jumps of a single molecule", *Nature* **373,** 132 (1995).

[188] Moerner, W. E., "Those blinking single molecules", *Science* **227,** 1059 (1997).

[189] Basché, T., "Fluorescence intensity fluctuations of single atoms, molecules and nanoparticles", *Journal of Luminescence* **76–77,** 263 (1998).

[190] Dickson, R. M., Cubitt, B., Tsien, R. Y., and Moerner, W. E., "On/off blinking and switching behaviour of single molecules of green fluorescent protein", *Nature* **388,** 355 (1997).

[191] Zondervan, R., Kulzer, F., Orlinskii, S. B., and Orrit, M., "Photoblinking of rhodamine 6G in poly(vinyl alcohol): Radical dark state formed through the triplet", *Journal of Physical Chemistry A* **107,** 6770 (2003).

[192] Widengren, J., and Schwille, P., "Characterization of Photoinduced Isomerization and Back-Isomerization of the Cyanine Dye Cy5 by Fluorescence Correlation Spectroscopy", *Journal of Physical Chemistry A* **104,** 6416 (2000).

[193] Christ, T., Kulzer, F., Bordat, P., and Basché, T., "Watching the photo-oxidation of a single aromatic hydrocarbon molecule", *Angewandte Chemie International Edition* **40,** 4192 (2001).

[194] Meixner, A. J., and Weber, M. A., "Single molecule spectral dynamics at room temperature", *Journal of Luminescence* **86,** 181 (2000).

[195] Boiron, A-M., Tamarat, P., Lounis, B., Brown, R., and Orrit, M., "Are the spectral trails of single molecules consistent with the standard two-level system model of glasses at low temperatures", *Chemical Physics* **247,** 119 (1999).

[196] Reilly, P. D., and Skinner, J. L., "Spectral diffusion of single molecule fluorescence: A probe of low-frequency localized excitations in disordered crystals", *Physics Review Letters* **71,** 4257 (1993).

[197] Reilly, P. D., and Skinner, J. L., "Spectral diffusion of individual pentacene molecules in P-terphenyl crystal: Stochastic theoretical model and analysis of experimental data", *Journal of Chemical Physics* **102,** 1540 (1995).

[198] Eggeling C., Widengren J., Rigler R., and Seidel C.A.M., "Photostability of Fluorescent Dyes for Single-Molecule Spectroscopy: Mechanisms and Experimental Methods for Estimating Photobleaching in Aqueous Solution", In: Applied Fluorescence in Chemistry, Biology and Medicine. Springer, Berlin, Heidelberg (1999).

[199] Davidovich, L., "Sub-Poissonian processes in quantum optics", *Reviews of Modern Physics*

68, 127 (1996).

[200] Loudon, R., *"The Quantum Theory of Light",* Oxford: Oxford University Press (1983).

[201] Walls, D. F., and Milburn, G. J., "*Quantum Optics"* Springer (2008).

[202] Lounis, B., and Orrit, M., "Single-photon sources", *Reports on Progress in Physics* **68,** 1129 (2005).

[203] Andrews, D. L., *"Structures light and its applications: An introduction to phase-structured beams and nanoscale optical forces",* Elsevier: Academic Press (2008).

[204] Yang, B., Trebbia, J., Baby, R., Tamarat, P., and Lounis, B., "Optical nanoscopy with excited state saturation at liquid helium temperatures", *Nature Photonics* **9,** 658 (2015).

[205] Pampaloni, F., and Enderlein, J., "Gaussian, Hermite-Gaussian, and Laguerre-Gaussian beams: A primer", *arXiv:physics/0410021* (2004).

[206] Gu, M., *"Advanced optical imaging theory",* Melbourne: Springer Series in Optical Sciences (1999).

[207] Wolf, E., "Electromagnetic Diffraction in Optical Systems. I. An Integral Representation of the Image Field" *Proceedings of the Royal Society A* **253,** 349 (1959).

[208] Marathay, A. S., and McCalmont, J. F., "Vector diffraction theory for electromagnetic waves", *Journal of Optical Society of America A* **18,** 2585 (2001).

[209] Davidson, N., and Bokor, N., "High-numerical-aperture focusing of radially polarized doughnut beams with a parabolic mirror and a flat diffractive lens", *Optics Letters* **29,** 1318 (2004).

[210] Ganic, D., Gan, X., and Gu, M., "Focusing of doughnut laser beams by a high numerical-aperture objective in free space" *Optics Express* **11,** 2747 (2003).

[211] Bokor, N., Iketaki, Y., Watanabe, T., and Fujii, M., "Investigation of polarization effects for high-numerical-aperture first-order Laguerre-Gaussian beams by 2D scanning with a single fluorescent microbead", *Optics Express s* **13,** 10440 (2005).

[212] Zhang, Z., Pu, J., and Wang, X., "Focusing of partially coherent Bessel–Gaussian beams through a high numerical-aperture objective'' *Optics Letters* **33,** 49 (2008)

[213] Chen, B., Zhang, Z., and Pu, J., "Tight focusing of partially coherent and circularly polarized vortex beams", *Journal of Optical Society of America A* **26,** 862 (2009).

[214] Mawardi, A., Hild, S., Widera, A., and Meschede, D., "ABCD-treatment of a propagating doughnut beam generated by a spiral phase plate", *Optics Express* **19,** 21205 (2011).

[215] Padgett, M., Courtial, J., and Allen, L., "Light's Orbital Angular Momentum", *Physics*

Today **57,** 35 (2004).

[216] Weiner, A. M., "Femtosecond pulse shaping using spatial light modulators", *Review of Scientific Instruments* **71,** 1929 (2000).

[217] Bekshaev, A., Orlinska, O., and Vasnetsov, M., "Optical vortex generation with a 'fork' hologram under conditions of high-angle diffraction", *Optics Communications* **283,** 2006 (2010).

[218] Beijersbergen, M. W., Allen, L., van der Veen, H. E. L. O., and Woerdman, J. P., "Astigmatic laser mode converters and transfer of orbital angular momentum", *Optics Communications* **96,** 123 (1993).

[219] Willig, K. I., Harke, B., Medda, R.. and Hell, S. W., "STED microscopy with continuous wave beams", *Nature Methods* **4,** 915 (2007).

[220] Bazhenov, V. Y., Soskin, M. S., and Vasnetsov, M. V., "Screw Dislocations in Light Wavefronts", *Journal of Modern Opitics* **39,** 985 (1992).

[221] Leach, J., Yao, E., and Padgett, M. J., "Observation of the vortex structure of a non-integer vortex beam", *New Journal of Physics* **6,** 1 (2004).

[222] Kaufmann, R., Hagen, C., and Grunewald, K., "Fluorescence cryo-microscopy: Current challenges and prospects", *Current Opinion in Chemical Biology* **20,** 86 (2014).

[223] Born, M., and Wolf, E., "Principles of optics: Electromagnetic Theory of Propagation, Interference and Diffraction of Light" *Pergamon Press* 1–952 (1999).

[224] Rahbar, K., Faez, K., and Attaran, K. E., "Phase wavefront aberration modeling using Zernike and pseudo-Zernike polynomials", *Journal of the Optical Society of America A* **30,** 1988 (2013).

[225] Tango, W. J., "The circle polynomials of Zernike and their application in optics", *Applied Physics* **13,** 327 (1977).

[226] Tyson, R. K., *"Topics in Adaptive Optics",* Intech Open (2012).

[227] Moerner, W. E., and Orrit, M., "Illuminating single molecule in condensed matter", *Science* **283,** 1670 (1999).

[228] Berezovsky, J., Mikkelsen, M. H., Stoltz, N. G., Coldren, L., and Awschalom, D. D., "Picosecond coherent optical manipulation of a single electron spin in a quantum dot", *Science* **320,** 349 (2008).

[229] Jelezko, F., and Wrachtrup, J., "Single defect centres in diamond: A review", P*hysica Status Solidi (A) Applications and Materials Science* **203,** 3207 (2006).

[230] Brennen, G., Giacobino, E., and Simon, C., "Focus on Quantum Memory", *New Journal of Physics* **17,** 9 (2015).

[231] Backlund, M. P., Lew, M. D., Backer, A. S., Sahl, S. J., and Moerner, W. E., "The role of molecular dipole orientation in single-molecule fluorescence microscopy and implications for super-resolution imaging", *ChemPhysChem* **15** 587 (2014).

[232] Forkey, J. N., Quinlan, M. E., and Goldman, Y. E., "Measurement of single macromolecule orientation by total internal reflection fluorescence polarization microscopy", *Biophysical Journal* **89,** 1261 (2005).

[233] Forkey, J. N., Quinlan, M. E. and Goldman, Y. E., "Protein structural dynamics by single-molecule fluorescence polarization" *Progress in Biophysics and Molecular Biology* **74,** 1 (2000).

[234] Beausang, J. F., Shroder, D. Y., Nelson, P. C., and Goldman, Y. E., "Tilting and wobble of Myosin v by high-speed single-molecule polarized fluorescence microscopy", *Biophysical Journal* **104,** 1263 (2013).

[235] Sosa, H., Peterman, E. J., Moerner, W. E., and Goldstein, L. S., "ADP-induced rocking of the kinesin motor domain revealed by single-molecule fluorescence polarization microscopy", *Nature Structural and Moelcular Biology* **8,** 540 (2001).

[236] Peterman, E. J., Sosa, H., Goldstein, L. S., and Moerner, W. E., "Polarized fluorescence microscopy of individual and many kinesin motors bound to axonemal microtubules", *Biophysical Journal* **81,** 2851 (2001).

[237] Sepioł, J., Jasny, J., Keller, J., and Wild, U. P., "Single molecules observed by immersion mirror objective. The orientation of terrylene molecules via the direction of its transition dipole moment", *Chemical Physics Letters* **273,** 444 (1997).

[238] Dickson, R. M., Norris, D. J. and Moerner, W. E., "Simultaneous Imaging of Individual Molecules Aligned Both Parallel and Perpendicular to the Optic Axis", *Physics Review. Letters* **81,** 5322 (1998).

[239] Richards, B., and Wolf, E., "Electromagnetic Diffraction in Optical Systems. II. Structure of the Image Field in an Aplanatic System", *Proceedings of the Royal Society A: Mathematical, Physical and Engineering Sciences* **253,** 358 (1959).

[240] Fourkas, J. T., "Rapid determination of the three-dimensional orientation of single molecules", *Optics Letters* **26,** 211 (2001).

[241] Sick, B., Hecht, B., Wild, U. P., and Novotny, L., "Probing confined fields with single molecules and vice versa", *Journal of Microscopy* **202,** 365 (2001).

[242] Débarre, A., Jaffiol, R., Julien, C., Nutarelli, D., Richard, A., Tchénio, P., Chaput, F., and Boilot, J. P., "Quantitative determination of the 3D dipole orientation of single molecules",

European Physical Journal D **28** ,67 (2004).

[243] Backlund, M. P., Lew, M. D., Backer, A. S., Sahl, S. J., Grover, G., Agrawal, A., Piestun, R., and Moerner, W. E., "Simultaneous, accurate measurement of the 3D position and orientation of single molecules", *Proceedings of the National Academy of Sciences of the United States of America* **109,** 19087 (2012).

[244] Jelezko, F., Lounis, B.. and Orrit, M., "Pump – probe spectroscopy and photophysical properties of single di- benzanthanthrene molecules in a naphthalene crystal", *Journal of Chemical Physics* **107,** 1692 (1997).